Joost Buitink

CAPTURING HYDROLOGICAL VARIABILITY

Spatio-temporal aspects of the Rhine basin

Propositions

1 | Including long-term variability in short-term simulations is worth the added complexity.
(this thesis)

2 | Conceptual hydrological models are too “bucket”-oriented.
(this thesis)

3 | Controversial ideas are only taken seriously when coming from an established scientist.

4 | Scientists should get rewarded for minimising, and not maximising, their carbon footprint.

5 | Salaries should only be communicated in their net values.

6 | Describing motorsport as "going round in circles" is like describing science as "staring at a screen".

Propositions belonging to the thesis, entitled

Capturing hydrological variability
— Spatio-temporal aspects of the Rhine basin

Joost Buitink
Wageningen, 20 October 2021

Capturing hydrological variability

Spatio-temporal aspects of the Rhine basin

Joost Buitink

Thesis committee

Promotor
Dr A. J. Teuling
Associate professor, Hydrology and Quantitative Water Management Group
Wageningen University & Research

Co-promotor
Dr L. A. Melsen
Assistant professor, Hydrology and Quantitative Water Management Group
Wageningen University & Research

Other members
Prof. Dr J. Vila-Guerau de Arellano, Wageningen University & Research
Prof. Dr K. Stahl, University of Freiburg, Germany
Dr J. Larsen, University of Birmingham, United Kingdom
Dr M. Hrachowitz, Delft University of Technology

This research was conducted under the auspices of the Graduate School for Socio-Economic and Natural Sciences of the Environment (SENSE).

Capturing hydrological variability

Spatio-temporal aspects of the Rhine basin

Joost Buitink

Thesis
submitted in fulfilment of the requirements for the degree of doctor
at Wageningen University
by the authority of the Rector Magnificus,
Prof. Dr A. P. J. Mol,
in the presence of the
Thesis Committee appointed by the Academic Board
to be defended in public
on Wednesday 20 October 2021
at 4 p.m. in the Aula.

J. Buitink
Capturing hydrological variability
– Spatio-temporal aspects of the Rhine basin,
v+244 pages.

PhD thesis, Wageningen University, Wageningen, The Netherlands (2021)
With references, with summaries in English and Dutch

ISBN 978-94-6395-872-1
DOI 10.18174/549338

Contents

1

Introduction

Capturing hydrological variability, despite being only three words, very concisely summarises all contents of this thesis. Since I use these words throughout the entire thesis, it is important to clarify the definition and interpretation of each word. Following the Cambridge Dictionary, each word is defined as:

Capturing "to represent or describe something"

Hydrological "relating to the study of water on the earth"

Variability "the quality or fact of being variable"

As definitions of words are prone to different interpretations, I briefly describe how I interpret these definitions in order to clarify their usage throughout this thesis. *Hydrological* is prone to the least interpretations, and I refer here to the different components and processes of the terrestrial water cycle. *Variability* occurs as a result of spatial variation in catchment characteristics, spatial and temporal variations in hydrological processes, and how these characteristics and processes vary under changing conditions. Finally, the hydrological variability is *captured* through analysis of observations and hydrological representation in models. As this likely still sounds abstract, the following sections will give more details and background to further clarify the meaning of these three words.

"I know the falls that the water face
I know it's over, an ocean awaits for a storm
The sun on snow, rivers in rain
Crystal ball can foresee a change"

—Coldplay, *Fun* (2015)

1.1 | Hydrological variability

Much of the current research in hydrology is driven by hydrological variability, ranging from the development of new observation techniques to the refinement of model grids. However, before diving into the details of hydrological variability, let's take a step back and view hydrology at its most basic level: the hydrological cycle. As the name already suggests, this is often visualised as a circle, with arrows indicating the "flow" of water through air, soil, rivers, and oceans. Four main fluxes are identified, and generally move in the following direction: precipitation, runoff generation, evaporation, and from condensation back to precipitation (Viessman & Lewis, 2012). A very basic visualisation of the hydrological cycle is presented in Figure 1.1a. This type of visualisation is very commonly used in applications ranging from education to policy. Despite the many issues related to this basic illustration (Abbott et al., 2019), it still nicely depicts how water interacts with the Earth's surface. An important note: this thesis does not cover all these four main fluxes of the hydrological cycle, but focuses on the generation of runoff, evaporation, and (the type of) precipitation.

1.1.1 | Spatial variability

In reality, each arrow in Figure 1.1a represents a multitude of different local processes. All of these processes can vary within a basin, driven by spatial and temporal variations in climate or catchment characteristics, giving cause for hydrological variability (see Figure 1.1b). This variability can translate through the whole hydrological system, enhanced by the fact that the input of water (precipitation) is also highly variable, both in space and time. This variability is induced by the spatial variation within precipitation events, meaning that some regions receive more precipitation than other regions, even within a catchment. Variability in precipitation has considerable effects on the internal states of a hydrological system (e.g. Schuurmans & Bierkens, 2007; Sapriza-Azuri et al., 2015). The elevation of the land surface is one of the factors controlling the amount of precipitation falling in a catchment. Due to the cooling of air when being forced over high elevated regions, water vapour condenses and falls as rain. As a result, high elevated regions generally receive more precipitation resulting from this orographic effect (Roe, 2004;

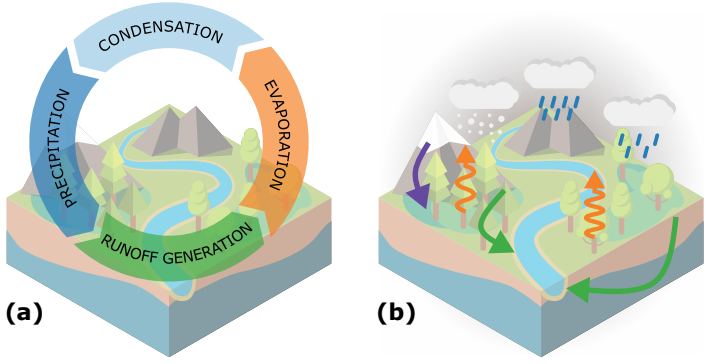

Figure 1.1 | Conceptual overview of a hydrological system. Panel **a** visualises a very basic interpretation of the global water cycle, with arrows indicating the typical direction of water movement. Panel **b** shows a typical variability these different processes impose on a hydrological system.

Napoli et al., 2019). Furthermore, whether precipitation falls as rain or snow is another cause for hydrological variability, as it influences the behaviour of water through a catchment (explained in more detail below). The division of precipitation between rain or snow is considered a threshold process, where a temperature threshold influences whether precipitation falls as snow or rain. While this threshold is typically assumed to be around 0°C, a study by Jennings et al. (2018) showed that it actually varies across the globe.

When precipitation has fallen, the resulting water can follow many different pathways (runoff generation in Figure 1.1a) depending on the type of precipitation, climate conditions, and catchment characteristics. A basic visualisation of this is shown in Figure 1.1b. For example, the type of precipitation determines when the water becomes available for runoff generation. If fallen as snow, it remains stored as snow pack on the land surface. When sufficient energy is available to melt this snow pack, it becomes available to the runoff generating processes. If fallen as liquid precipitation, it becomes almost immediately available to the runoff generating processes. These processes entail all mechanisms that transport precipitation to the river network, such as surface runoff, percolation, baseflow, et cetera. Due to differences in hydro-

logical conditions, catchment characteristics, and/or seasonality, these processes vary both in space and time, with spatial hydrological variability as a result. Eventually, water is transported via rivers to the oceans. Once in the ocean, but also during runoff generation, water is evaporated back into the atmosphere. Evaporation occurs via different processes, of which evaporation from open water and transpiration from plants are two examples.

Spatial variability can also result from heterogeneity in catchment characteristics. For example, variations within a basin in elevation, slope, soil type and land cover all influence the hydrological response. The study by Karlsen et al. (2019) describes the role of catchment characteristics and storage on streamflow recession. They showed that slope and elevation were the main controls during high flows, but that catchment area was the main factor during low flows. Furthermore, they highlight that these relations are dependent on the hydrological conditions. The importance of elevation was also described by Rottler et al. (2021), who showed how snow melt occurs in elevation bands and hence played an important role in the generation of runoff. Land cover is often found to be an important factor controlling different patterns. Mastrotheodoros et al. (2020) showed how the Alpine region responds to warm and dry summers using a high resolution model. They concluded that the change in evaporation differed per land cover type, where forested regions even showed an increase in evaporation despite the reduction in precipitation. These studies show how varying characteristics within a basin can influence the hydrological response. A correct representation of these characteristics is vital in order to have a correct understanding of the hydrological response of a basin.

However, correctly representing, or even observing, hydrological characteristics is highly dependent on the scale of the study. A famous example of spatial variability is related to measuring the hydrological conductivity. Hydrological conductivity is highly influenced by the scale and location of the measurement (Sobieraj et al., 2004). The observed value can vary largely depending on the local characteristics, such as preferential pathways resulting from biological activity. These local differences have a large effect on the local hydrological response. Furthermore, this also means that a representative conductivity value is a function of the required scale or study area. This scaling

issue is a widely discussed and longstanding topic in hydrology (e.g. Peters-Lidard et al., 2017; Gentine et al., 2012; Sivapalan et al., 2004; Blöschl, 2001), and has implications for the parameterisation of models used to simulate discharge response of river basins (see Section 1.2).

1.1.2 | Temporal variability

Hydrological variability occurs not only in space, but also in time. Temporal variability can occur on a range of different scales: from daily to seasonal to decadal variations. Typical examples of these three scales are presented in Figure 1.2. For example, Figure 1.2a shows a positive trend in yearly precipitation, where precipitation is steadily increasing over the entire period. Trends in precipitation can have several causes, such as a change in large weather systems. Despite the increase in precipitation, the yearly discharge remains rather constant, and even shows a declining trend during the 1990s (see Figure 1.2a). The latter is caused by an opposite trend in evaporation, which could result from changes in temperature. Long term variations can have different sources, two examples of these sources are explained below.

The most common example of long term temporal variation is the warming of the climate. This change in climate is expected to intensify the hydrological cycle (Huntington, 2006), leading to more extreme floods and droughts. Besides, a change in climate can establish or strengthen certain positive feedback loops. For example, Teuling (2018) showed how dry conditions during heatwaves further increase temperature through the lack of evaporation. Additionally, an increase in temperature can trigger processes at different moments in time, and/or cause a shift in the seasonal patterns. For example, Rottler et al. (2020) showed that over the last century, there has been a decrease in the runoff seasonality of snow dominated rivers. Changes in snow cover shifted the discharge peak resulting from snow melt earlier in the year, leading to a reduction in discharge during summer and autumn. Correct understanding of how temperature interacts with the hydrological cycle is of vital importance, especially with further expected increase in global temperatures.

Another example of long term variability is the “global dimming and bright-

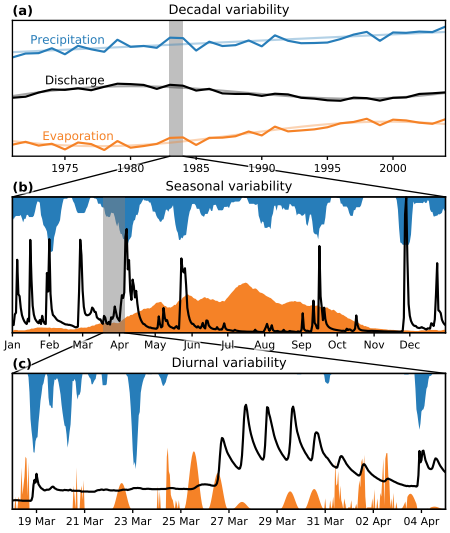

Figure 1.2 | Example of typical temporal variability in three main hydrological variables at three temporal scales. Decadal time series (**a**) are synthetic time series, based on observations from the global dimming and brightening event. Seasonal (**b**) and diurnal (**c**) time series are based on observations from the research catchment Rietholzbach, Switzerland.

ening": over the period 1950–1980, a considerable decrease in the amount of surface solar radiation has been observed, followed by a partial recovery since the 1980s (Wild, 2009). This dimming and brightening has been linked to fluctuations in aerosol and air pollution emissions, and the regulation of these emissions. These fluctuations in aerosols affected the amount of incoming radiation. As a result, these trends are reflected in evaporation of large river basins in the Northern hemisphere (Teuling et al., 2009a), as evaporation largely depend on the amount of incoming energy. Ultimately, this has also led to similar—but opposite—trends in river discharge (Gedney et al., 2014), as is also visualised in Figure 1.2a. Despite the substantial influence of these trends on river discharge, they are typically not accounted for in hydrological models. As these long-term fluctuations occur on decadal time scales,

and are therefore rather constant on shorter time scales, they are typically captured using a constant value. While this can be valid for short term forecasts, it can add significant uncertainties for long term predictions.

As mentioned earlier, temporal variability also occurs on shorter time scales than decadal. For example, most river basins experience seasonal patterns, driven by seasonal variations in e.g. precipitation, temperature and/or sunshine duration. The example shown in Figure 1.2b shows a strong seasonal pattern in evaporation, with higher evaporation rates during summer. Precipitation does not show a strong seasonal pattern, but the type of precipitation does ultimately influence the discharge; as explained below. Resulting from this strong seasonal variability in evaporation, discharge values are typically lowest during the summer months. Additionally, seasonal (or even diurnal) variability in temperature controls the type of precipitation, and when it will be discharged. A delayed discharge response is visible in Figure 1.2c, where the discharge peaks occur later than the precipitation events, caused by the melting of snow. The strong daily cycle is explained by the daily variation in temperature, which exceeds melting point during daytime, but drops below this point during nighttime. Hence, it is essential to have a correct understanding and representation of temporal variability at all scales.

Linking back to the long term variability, as presented in Figure 1.2a, it is important to understand the underlying causes and interactions causing these trends. While there is good understanding of the events occurred in the past, it is vital to understand how and which feedbacks might arise in the future. Changes in precipitation, evaporation and runoff processes all influence discharge, where shifts in the occurrence of hydrological extremes can have large (societal and/or economical) impacts. For example, global temperatures have and will continue to rise in response to an increase in atmospheric CO_2 concentrations (Stocker et al., 2013). Higher temperatures will increase potential evaporation and potentially shift the melting season to a moment earlier in the year. The interactions between these components ultimately affect the hydrological response, and hence the occurrence of extremes. Furthermore, changes in atmospheric concentrations of CO_2 are known to influence several aspects of vegetation. However, it is unclear how these different aspects interact and affect the discharge of large river basins. Therefore, to

correctly understand change in hydrological regimes, it is vital to quantify both the temporal and spatial aspects of the relevant variabilities across the hydrological cycle.

The previous paragraphs highlight that the various causes of hydrological variability are rather well studied. Additionally, their direct effects on each specific part of the hydrological cycle are also well understood. The interplay, however, of multiple different components of the hydrological cycle and their combined effect on large river basins is currently not well understood. Therefore, there is a need to improve our understanding of—and ultimately predicting (*capturing*)—the *hydrological* response resulting from *variability* within different components of the hydrological cycle.

1.2 | Capturing hydrology

Due to the size and complexity of typical river basins, fully controlled experiments are not feasible. Therefore, hydrological studies are restricted to investigating past events using observations, or to testing the response of a basin under hypothetical conditions using hydrological models. Naturally, understanding past events is limited by the availability of observations. While models can be used to study hypothetical conditions, they still need to be calibrated to ensure the simulations are in line with the real response of a basin. Both types of "experiments" have their own advantages and disadvantages, as will be explained below.

Extraordinary events provide the perfect foundation to understand how a hydrological system behaves. These extraordinary events can originate from both spatial and temporal variability. For example, an extreme precipitation event was used to understand how the combined response of different parts and processes within a lowland catchment (e.g., soil moisture, groundwater, surface runoff) lead to a flash flood (Brauer et al., 2011). Additionally, by applying special filter techniques to local observations, Geertsema et al. (2018) quantified typical discharge wave durations and lag times, in order to understand how a confluence of two rivers influences the behaviour of floods. As mentioned earlier, these studies are limited by the availability of data. The vast majority of basins around the globe are however ungauged (Blöschl

et al., 2013a), making local observation-based studies in many regions impossible. Luckily, the use of spaceborn sensors is rising as more sensors, filtering techniques, and algorithms are discovered (Schmugge et al., 2002). Remotely sensed observations still have some challenges regarding the representability, such as measuring soil moisture that is representative for the entire rootzone (Mohanty et al., 2017). This requires in-depth comparisons with high-quality observations, before they can be interpreted on a larger (global) scale.

One way to validate remotely sensed observations, is to use smaller regions which are equipped with sufficient high-quality sensors. Several smaller catchments around the globe are specifically used as research catchments, and are used to answer these fundamental questions. Additionally, due to the high density of high-quality observations, they can be used to study specific processes. Two examples of such research catchments are the Hupsel catchment, situated in the Dutch lowland area (Brauer et al., 2018), and the Rietholzbach, a Swiss pre-Alpine catchment (Seneviratne et al., 2012). However, these catchments are rather small, which raises the question on how to extrapolate their results to large river basins. Further explorations on the link between remotely sensed data and in situ observations will help to understand the interactions and processes occurring within large river basins.

As previously described, models can be used to study hypothetical conditions. Most often, models are used to study the potential effects of climate change on river discharge. Models are also used to study past events—similarly as described before—where observations were lacking, or to test whether our current understanding of a hydrological systems is correct. Moreover, models are used to create "reanalysis data": local observations are used to force and constrain a model to create a dataset that optimally blends observations and models, whereby the model is used to interpolate optimally in space and time between available observations (such as the ERA5 dataset, Hersbach et al., 2018). The wide range of model applications mentioned here, and the ambiguity of the term "model" suggests—correctly—that there is a wide range of models available. Generally, these models can be grouped in three types: black box models, parametric or conceptual models, and physically-based models. These types are classified from least to

most complex, respectively. Here, black box models are often determined on an empirical basis, or use neural networks to simulate the hydrological response. In contrast, physically-based models are often based on our understanding of the physics behind a hydrological process (such as Richards' equation for the unsaturated zone). Conceptual models sit between these two types, and generally simplify hydrological processes using reservoirs and fluxes connecting these reservoirs. This type of model (rainfall-runoff models) is widely used due to the relative low data requirements and ease in setting up. However, despite their simplicity, conceptual rainfall-runoff models are not flawless.

One of the main problems with conceptual rainfall-runoff models is their requirement to be calibrated. The simplification of hydrological processes using reservoirs often results in equations with tuneable parameters. Tuning of these parameters is required to ensure realistic and reliable model output, and is referred to as calibration. Typically, the difference between observed and simulated discharge is minimised using optimisation algorithms. Even when following a calibration protocol, de Boer-Euser et al. (2017) showed how subtle differences in calibration techniques and different model structures can have substantial effects on the resulting simulated discharge. A follow-up study by Bouaziz et al. (2021) showed how the different models had additional differences in their "internal" states (e.g., evaporation, storage and snow processes). Not only does calibration (and model selection) influence the resulting output, other subjective decisions made by the modeller (such as spatial resolution, parameter boundaries, performance metric) were proven to have large influences on the simulation of floods and droughts (Melsen et al., 2019).

One of these subjective modelling decisions was the choice of spatial resolution. Recently, it has become more feasible to run models at higher spatial resolutions, due to increases in computational power and advances in data availability (Hersbach et al., 2018). However, as space and time are linked in hydrology (Blöschl & Sivapalan, 1995), an increase in spatial resolution should be accompanied by an increase in temporal resolution. This is not always the case, as either underlying concepts are not designed for a smaller time step, or the smaller time step would lead to very high computational demand. For

example, the simulations performed by Mastrotheodoros et al. (2020) were ran on a 250×250 meter spatial resolution and an hourly time step, and required more than six million CPU hours. There is a need for a model that is able to simulate the hydrological response at both high spatial and high temporal resolutions, without requiring the user to resort to computation clusters of high performance computers.

1.3 | Objectives and research questions

The goal of this thesis is to capture the hydrological variability across the different components of the hydrological cycle, and evaluate how this ultimately affects the discharge. By using a combination of studies largely driven by observations and studies driven by simulations, this thesis improves the understanding of the variability and interactions within the hydrological cycle. To achieve this, I focus on the Rhine basin, which is one of the main river basins in Europe (see Figure 1.3a). The Rhine has major economic and societal importance, as many sectors such as industry, agriculture, and drinking water depend on the water generated in this basin. As a consequence, both too high and too low discharges can have large economic impacts. Additionally, the Rhine basin consists of a large variety of land cover types, ranging from mountainous regions in the Swiss Alps to the Dutch lowlands. Different land cover types typically indicate different hydrological responses, meaning that a correct understanding of the hydrological variability is important for accurate discharge projections. The main goal of this thesis is split into the following objectives and questions:

1. **Understand how variability within and between different hydrological variables influence drought frequency** (Chapter 2)

   Droughts propagate through the hydrological system, generally starting with a lack of precipitation. As regions are typically heterogeneous in terms of elevation, land use, soil type and/or geology, typical drought signals likely respond different to the same lack of precipitation. Additionally, the different hydrological fluxes have different processes with varying response times. Droughts are often defined based on frequency-of-occurrence, yet it is unclear how this inter- and

intra-variability in the different fluxes affects the actual occurrence of droughts. This led to the following questions:

- How often and where do droughts occur in each component of the hydrological cycle?
- Does the definition of drought match the actual frequency of droughts?
- Are different drought types overlapping, and if so, how often?

2. **Evaluate the interaction between soil moisture and vegetation productivity during the 2018 summer drought** (Chapter 3)

   Soil moisture and vegetation dynamics are inherently linked. Despite this, both variables often show different signals. Additionally, reduced vegetation productivity can have large impacts through e.g. a reduction in crop yields. By using local soil moisture observations together with satellite observations of plant productivity, the following questions are raised:

   - How do soil moisture and vegetation productivity signals differ during long periods with low precipitation?
   - What is the interaction between soil moisture and vegetation productivity during periods with extremely low precipitation?
   - How does the critical soil moisture content vary with depth?

3. **Quantify the impact of model resolution during seasonal hydrological extremes** (Chapter 4)

   Spatial model resolution is an important factor controlling the representation of spatial variations in models. As two typical modelling practices (regional scale and global scale) often result in typical spatial resolutions ($\pm$500 m$\times$500 m and 0.5°$\times$0.5°), this raises several questions on the representability of the model output:

   - How well does a large model grid cell represent a collection of small grid cells?
   - What is the difference between the range in anomalies at high resolution and the single anomaly of the low resolution model?

- How do these results compare between different Alpine and pre-Alpine basins?

4. **Create a simple and efficient, yet versatile, hydrological model to simulate catchments at high spatio-temporal resolution with low computational demand** (Chapter 5)

   As more datasets become available at high spatial resolution, modelling at high spatial resolution becomes more and more feasible. However, through the link of time and space, the temporal resolution should be increased when increasing the spatial resolution. The simple dynamical systems approach (Kirchner, 2009), a concept proven at high spatio-temporal resolutions, is used to define a new distributed hydrological model. The following questions are raised:

   - How can the simple dynamical systems approach be transformed in order to be applied in a distributed fashion?
   - How can the model be implemented in a computationally efficient manner?
   - How well does this new model perform in the spatially complex basin, such as the Thur basin in Switzerland?

5. **Understand how temperature-driven changes in snow and evaporation affect the discharge** (Chapter 6)

   Current and projected changes in climate all show increases in temperature. Higher temperatures increase the energy available for both evaporation and snow melt. Furthermore, higher temperatures lead to less snowfall and more rain, leading to a more direct runoff response. The exact interplay of these two variables and their effect on the discharge is currently not well understood, leading to the following questions:

   - How have past changes in temperature influenced the discharge?
   - How can changes in discharge be attributed to changes in evaporation, changes in type of precipitation and changes in melt dynamics?
   - With step-wise temperature increments, how does the typical seasonal discharge response change?

6. **Understand how CO_2-induced feedbacks in vegetation and temperature influence evaporation and discharge** (Chapter 7)

   The already observed and projected changes in climate are largely being driven by the increasing CO_2 concentration in the atmosphere. Besides an increase in temperature, a change in atmospheric CO_2 concentration also influences two important aspects in vegetation. A change in stomatal resistance and a change in leaf area index both affect the transpiration of plants, which is a major component in the hydrological cycle. This leads to the following questions:

   - What is the influence of changes in stomatal resistance, leaf area index, and temperature on the hydrological response?
   - How are low flows, such as during the summer drought of 2018, affected by these three changes?
   - How sensitive is the discharge of the Rhine to these changes?

Each research objective investigates different parts of the Rhine basin. The exact study area used in each chapter is motivated and explained in more detail in the corresponding chapters.

1.4 | Thesis outline

The chapters in this thesis follow the major steps in a typical hydrological study: from observing and determining relations, to conceptualising and building models, to exploring and understanding hydrological behaviour in hypothetical yet realistic cases using these models. A conceptual overview of the different chapters and their relations is presented in Figure 1.3b.

Chapter 2 and Chapter 3 both focus on the hydrological response during droughts. Firstly, Chapter 2 provides an overview of the behaviour of all major hydrological components during drought conditions, and describes how the drought definition influences the actual drought occurrence. In Chapter 3, the interaction between soil moisture and vegetation is described in more detail, using the drought of 2018 as a case study. Next, the effect of spatial model resolution is quantified by comparing two common model resolutions in Chapter 4. Chapter 5 describes how the simple dynamical sys-

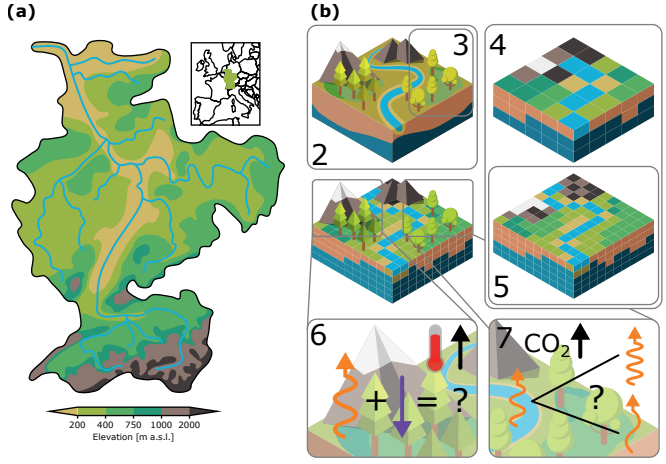

Figure 1.3 | Schematic overview of the contents of this thesis. Left hand side (**a**) shows the Rhine basin and its location in Europe, coloured based on the elevation. Right hand side (**b**) shows a graphical overview of the relation between the different chapters, where the numbers indicate the corresponding chapter. Orange arrows indicate evaporation, and purple arrow represents melt from snow and ice.

tems approach is used to develop a spatially distributed, yet computationally efficient hydrological model. Finally, this model is used to simulate the Rhine basin. The changes induced by increasing temperatures are quantified in Chapter 6. Chapter 7 describes how CO_2-induced changes in vegetation and temperature affect evaporation and discharge. In the final chapter (Chapter 8), conclusions from all studies are summarised, leading to the overall conclusion. Additionally, this chapter outlines opportunities for future research directions, which hopefully ultimately improves the understanding and representation of hydrological variability in future studies even further.


2

Hydrological systems complexity and a drought frequency paradox

---

This chapter is based on:

Buitink, J., van Hateren, T. C., and Teuling, A. J. (2021). Hydrological system complexity induces a drought frequency paradox, *Frontiers in Water*, 3, 42, doi:10.3389/frwa.2021.640976.

Droughts occur as a result of a lack of water compared with normal conditions. Whilst this appears trivial, the exact definition of drought is not. Especially since different drought types exist, resulting from the different variables in a hydrological system, each with unique characteristics. We use a common drought definition, the percentile score, and apply the same definition across all drought types, to study whether the actual occurrence of droughts matches the definition. We focus on the data-rich Dutch province of Gelderland, to study droughts from observations across five major components of the terrestrial hydrological cycle. When a percentile threshold of 20% is used as drought definition, corresponding to a mild drought, droughts anywhere in the system occur at least 3 times more frequently (73% of the time). On the other hand, the situation where drought occurs across all components of the terrestrial hydrological cycle is more than 4 times less likely than the drought threshold of 20% (namely 5% of the time). This can be attributed by both (1) the different responses across the hydrological system, and (2) the spatial variability present within each component of the hydrological system. In this chapter, we show the existence of the drought frequently paradox: although droughts are seen and defined as rare from a scientific perspective, when viewed from a societal or operational water management perspective in typical hydrological systems subject to spatial variability and other system complexity, droughts become common, rather than rare. This paradox is a consequence of an inconsistent use of the percentile score drought definition between research and operational water management, and better communication between the two domains is needed in search for a universally accepted drought definition.

"I thought that I was in the green
But it turns red every time"

—The Wombats, *Bee-Sting* (2018)

2.1 | Introduction

Droughts are among the extreme natural events with the most widespread impact, both on socio-economic sectors as well as on natural ecosystems. Due to the strong coupling between drought and heat, the impacts of drought are expected to worsen with climate change (Teuling, 2018; Miralles et al., 2019). In spite of the relevance of drought, its exact definition has been, and still is, subject to debate (Dracup et al., 1980). In a review on the use of drought indices in the U.S., Heim (2002) provides several possible and widely used definitions: drought can be defined as a "prolonged absence or marked deficiency of precipitation", a "deficiency of precipitation that results in water shortage for some activity or for some group", or a "period of abnormally dry weather sufficiently prolonged for the lack of precipitation to cause a serious hydrological imbalance". More recently, van Loon et al. (2016) argued that drought "is ... simply an exceptional lack of water compared with normal conditions", to allow for the possibility that drought is induced by human activity rather than rainfall deficiency. Additionally, different drought types are identified, corresponding to different components of the hydrological system: meteorological (precipitation, evaporation), agricultural (soil moisture, vegetation) and hydrological drought (groundwater, surface water) (van Loon, 2015). A general feature of these different drought definitions is the notion that drought is a deviation from normal, and relatively rare.

As these definitions are more descriptive of the cause of droughts, they do not help with classifying certain events as droughts. Within drought classifications, two main perspectives can be distinguished: a more research-oriented perspective which sees drought as a multivariate phenomenon, and a operational water management perspective were drought is treated as a univariate phenomenon. In the research perspective on drought, drought is usually defined using drought indices. Developments in the use of drought indices reflect the changing attitude towards drought definition. Whereas early drought indices were often based on absolute values of precipitation characteristics (Heim, 2002), the use of standardised indices has become commonplace over the past decades (Hayes et al., 2011). It is believed that standardisation facilitates the comparison of drought impact between climates and seasons. In terms of standardised indices, drought conditions

typically start whenever the standardised index falls below minus one standard deviation, or −1.5 for moderate drought. On the other hand, drought is defined as a rare event in water management practise, as it is often related to its impacts. Typically, multiple univariate drought indicators are used to monitor drought conditions. However these indicators reflect physical drought impacts in various sectors that cannot easily be weighted or aggregated. As a result, droughts might be felt in different sectors at different times, and the effective drought frequency might be at odds with the definition of drought as extreme event.

The typical complexity and variability found in hydrological systems causes different drought types to show diverging dynamics. A first example of this is the relation between precipitation deficit and evapotranspiration and vegetation productivity. Because of the nonlinear relation between soil moisture and evapotranspiration, the latter will respond to absolute values of soil moisture (i.e. below a critical soil moisture content, see Denissen et al., 2020) rather than anomalously low precipitation. This is reflected in the observation that in the humid Central-Western Europe, total evapotranspiration during drought summers might show positive anomalies—in response to increased energy due to reduced cloud cover and high temperatures—rather than negative anomalies due to low soil moisture (Teuling et al., 2013). Similar findings of increased evapotranspiration and vegetation productivity during drought in (pre-)Alpine regions were reported in Chapter 4 and by Jolly et al. (2005) and Mastrotheodoros et al. (2020). The complex and climate-dependent relation between soil moisture and vegetation provides an argument to consider vegetation and soil moisture separately in analyses of agricultural drought (van Hateren et al., 2021). Hydrological drought dynamics also differ from meteorological drought. Because of the large size of most groundwater systems, meteorological drought is often delayed and attenuated with timescales involved ranging from several months to over a year. However, an analysis for Germany and the Dutch province of Gelderland revealed that the transformation is subject to considerable spatial variability, and that even a locally optimised transformation of the precipitation signal is a poor predictor of groundwater drought (Kumar et al., 2016). Adding to the complexity of hydrological droughts is the situation in which a region receives surface water that depends on non-local weather conditions. This is

typical for downstream lowland and delta regions where most of the global agricultural production takes place, and where the impact of a drought can be large. These downstream regions can experience a hydrological drought in the surface water, even when local precipitation has been normal. Clearly, hydrological systems complexity poses a challenge to drought identification and effective regional water management when drought observations cover a limited number of drought types, or when spatial variability is not taken into account.

Typically, drought is classified using different drought types, which represent different components of the hydrological system: meteorological, agricultural, vegetation, and hydrological drought (for an overview of the different drought types, see Wilhite & Glantz, 1985; van Loon, 2015). Spatial complexity and different drought characteristics ensure that each drought type has a unique drought occurrence. When we classify the hydrological system to be in drought conditions when at least one of these types is classified as a drought, the spatial complexity might cause droughts to occur a lot more frequently when the entire system is considered. A visualisation of this is presented in Figure 2.1, which shows a typical hydrological response across five different components of a hydrological system. We hypothesise that a drought frequency paradox exists: even though drought events are generally considered to be relatively rare, drought occurrence could become relatively common when viewed across the hydrological system due to inherent spatial variability and complexity. The last panel in Figure 2.1 highlights that the hydrological system is in drought conditions for the majority of the time. As commonly used indices are likely to show this signal, we investigate the existence of a possible drought frequency paradox. Specifically, we aim to identify the effective frequency at which drought conditions might occur within any of the possible drought types. The existence of this paradox has consequences for the perception of drought frequency by e.g. stakeholders and public attention. We investigate this paradox for the Dutch province of Gelderland. This region has not only experienced recent droughts (including the 2018 European summer drought, see Chapter 3), but in addition has typical variability in soil, vegetation, and drainage properties, while being located in the downstream part of three river basins. While past studies covering all different drought types were limited by spatial or temporal coverage,

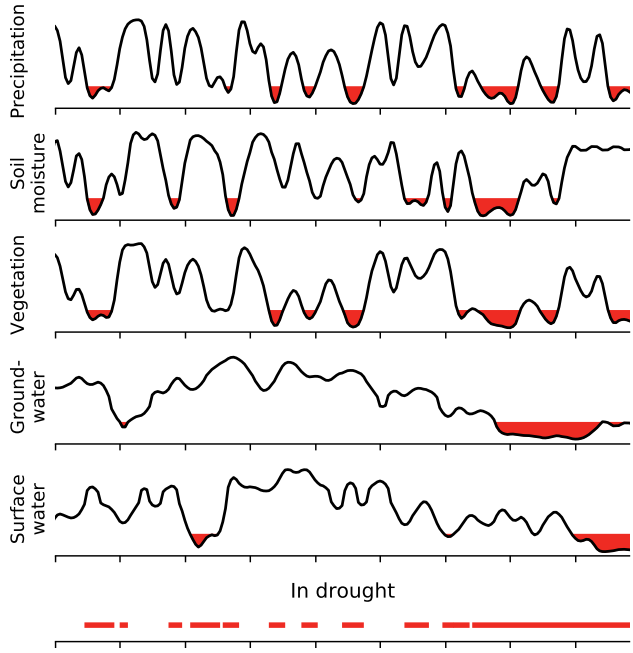

Figure 2.1 | Conceptual illustration of drought propagation. Time series can be interpreted as percentile values for each particular month. Red areas indicate periods below the drought threshold (here 20% reflecting mild drought and worse). Note that propagation increases the fraction of time that any of the variables is in drought to more than 20% (lower panel).

we were able to combine a large number of local precipitation, surface water and groundwater observations with climate records of vegetation greenness and soil moisture derived from Earth observation. This resulted in a combined dataset that allows for the first time to study different drought types and their spatial variability in a historical perspective, solely from observations.

2.2 | Methods and Data

2.2.1 | Study area

In this chapter, we focus on a single data-rich region in the Netherlands: the province of Gelderland (see Figure 2.2). As mentioned earlier, this region experienced the recent droughts of 2018 and 2019 that affected much of Western Europe. The region is small enough for the meteorological drought conditions to be fairly homogeneous (so spatial variability in other drought types is not induced by spatial variability in precipitation), yet large enough to have considerable variation in soil, vegetation and drainage properties. The extensive groundwater system under the Veluwe Massif, where the depth to the groundwater table can reach tens of meters (Kumar et al., 2016) is an important resource for drinking water and irrigation (van Engelenburg et al., 2018), while its location downstream of three river basins (the Rhine, Meuse and Berkel) makes it an important hub for shipping and surface water management. The three river systems vary considerably in size: 900 km^2 for the Berkel, 34,500 km^2 for the Meuse, and 185,000 km^2 for the Rhine. The Rhine is the largest river entering both Gelderland and the Netherlands, and the country largely depends on water from this river. The southwestern region of Gelderland is dominated by floodplains of the large Rhine and Meuse rivers, the northwestern part is dominated by a sandy moraine, and the northeastern part is dominated by sandy soils.

2.2.2 | Data

We investigate drought across five major components of the hydrological cycle: precipitation, soil moisture, vegetation greenness, groundwater and surface water. Below, we describe the data of each component.

Precipitation data were obtained from the Royal Netherlands Meteorological Institute (KNMI), and seven stations were selected based on their location in or near the study area (blue squares in Figure 2.2). Daily precipitation values were summed to obtain total monthly precipitation.

Groundwater levels were obtained from the Dutch institute TNO (www.dinoloket.nl), and selected based on available data (purple dots

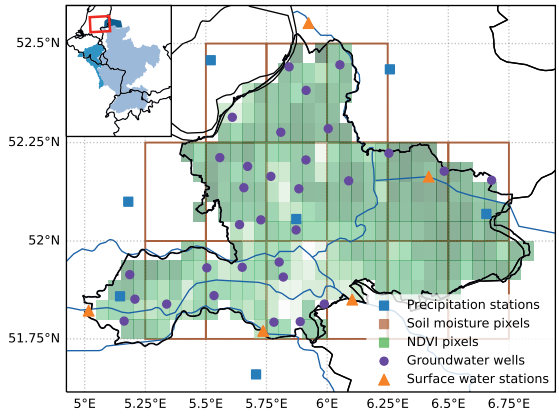

Figure 2.2 | Map of the study region and measurement locations. Inset figure shows the location of the main panel, including the three river basins corresponding to the water level and discharge stations: the Rhine (light blue), Meuse (medium blue) and Berkel (dark blue). Both soil moisture and NDVI products are gridded datasets. NDVI pixels are shaded based on their mean value over the entire period, ranging from 0.5 to 0.75.

in Figure 2.2). We selected groundwater wells such that they had sufficient data to cover the period 2000–2019, and measured data at regular temporal intervals. Data records were averaged to obtain monthly mean groundwater levels.

Surface water observations were obtained from the Directorate-General for Public Works and Water Management, and from the water board Rijn en IJssel (orange triangles in Figure 2.2). These observations cover three river systems, varying in size. The catchment areas of these systems are presented in the inset in Figure 2.2: Berkel, Meuse and Rhine (from smallest to largest). These were selected to cover the different types of river systems present in the study area. The most eastern surface water station is situated in the Berkel river, the most southern station in the Meuse, and the three remaining stations in branches of the Rhine river. For stations located in the downstream areas of the Rhine and Meuse basins, surface water levels were ob-

tained. For the Berkel, however, no surface water level observations were available, so discharge observations were used instead. The surface water records were averaged to obtain monthly mean values.

Both soil moisture content and vegetation greenness were based on remotely sensed data. Soil moisture data were obtained from the ESA Climate Change Initiative soil moisture data set (CCI SM v05.2, Gruber et al., 2017; Dorigo et al., 2017; Gruber et al., 2019). These data are available on a monthly $0.25° \times 0.25°$ resolution (brown squares in Figure 2.2). The most southwestern pixel was omitted due to insufficient data. We selected the Normalised Difference Vegetation Index (NDVI) to represent vegetation greenness. Monthly $0.05° \times 0.05°$ NDVI data were retrieved from the MODIS/Terra Vegetation indices data set (MOD13C2 v006, Didan, 2015), as indicated by the shaded pixels in Figure 2.2. As mentioned earlier, NDVI had the shortest period of available data (2000–2019).

2.2.3 | Drought definition

We investigate the spatio-temporal variability in five different drought types to cover all major components of the hydrological cycle: precipitation, soil moisture, vegetation greenness, groundwater and surface water levels (or discharge, we assume no difference in percentile scores between the two). To understand the different drought types and their spatial variability, we have split the analysis in two parts. First, we investigate the recent severe droughts of 2018 and 2019 to understand the general behaviour of, and interaction between the five variables. Next, we use the longest available period of overlapping records to understand how different drought thresholds affect the resulting frequency of droughts.

The period of overlapping records was limited by the data product to measure vegetation greenness (see more in Section 2.2.2), which was limited to 2000–2019, yielding 20 years of monthly data. Many different drought indicators are available (Zargar et al., 2011), ranging from standardised variable-specific indices (such as the Standardised Precipitation Index) to non-variable-specific indices (such as percentiles). In this study, we selected the percentile score for our drought metric based on two important factors.

Firstly, we want to compare droughts across different components of the hydrological system. By using the same index for all variables, we minimise any deviations caused by different index calculations for different variables Secondly, our data period covers 20 years of data, which is considerably shorter than the period typically used for robust determination of standardised indices. With our shorter period, we cannot ensure to correctly define the underlying distributions that are required for standardised indices. These two arguments considered, we decided to use the percentile score as our drought indicator. A similar approach is commonly used in typical retrospective drought analysis studies (e.g. Gibbs & Maher, 1967; Steinemann, 2003; Steinemann et al., 2015; Kumar et al., 2016), where a drought threshold is set based on a percentile score. This threshold (the 20^{th} percentile, for example) is based on observation time series, and each value can be compared to be above or below this threshold. In our study, as we are investigating the link between drought threshold and resulting frequency, we invert this method: for each data point we calculate the matching percentile score. This implies that this data point would classify as a drought when the drought threshold matches the percentile score. To account for seasonal variability (especially present in vegetation data), values were grouped by month, and the percentile score is calculated based on these 20 monthly values. The percentile score is calculated over the time series of each station/pixel using the following equation:

$$\phi = \frac{C}{N} \cdot 100, \tag{2.1}$$

where ϕ is the percentile score, C is the number of values equal or less than the value of interest, and N is the total number of values considered. This is in line with the variable threshold approach used in many hydrological drought analyses (e.g. van Huijgevoort et al., 2014). It should be noted that the 20 year record length in combination with a variable threshold approach results in percentile scores only being defined in steps of 5% (1/20).

With the percentile score for each time step, we need to define a drought threshold. We defined a location to be in drought when the percentile score is at or below 20%. This threshold corresponds to mild drought, and is a typical value in drought studies (van Loon, 2015; van Huijgevoort et al., 2013;

Corzo Perez et al., 2011; Sheffield et al., 2009; Tallaksen et al., 2009; Fleig et al., 2006; Andreadis et al., 2005; Hisdal et al., 2001). As each variable has multiple stations or pixels, an additional threshold is required to determine whether that variable is in drought conditions. For this threshold, we defined that at least 20% of the stations/pixels should be in drought conditions. As not all variables had the same number of stations/pixels, exactly 20% of the stations was not possible for all variables (e.g. precipitation with 7 stations). To account for this, we calculate the value corresponding to the 20% quantile range. The value is calculated based on linear interpolation in the case when this point sits between two stations, as is explained in more detail by Schoonjans et al. (2011). This should correspond to a value where 20% of the stations are in drought, when sufficient stations are available. This way, we account for any outliers within each variable (i.e. drought conditions in a single groundwater well would not indicate regional groundwater drought, but several would), while respecting the spatial variability.

Finally, to test whether there is a change in drought frequencies between the first and second 10 years of our study period, we split the dataset into two 10 year periods. This way, we can compare the relative drought frequencies, both for droughts within each variable, as for the number of simultaneous droughts.

2.3 | Results

We first illustrate how the recent severe droughts of 2018 and 2019 have impacted the different parts of the hydrological system in Gelderland. To understand the severity and duration of the drought impact, we compare the time series with the long term average of the entire data period (see Figure 2.3). Only for visualisation purposes, the groundwater and surface water data are normalised, to be able to ensure meaningful comparisons between the different stations. For all variables, we see deviations from the climatology during those two years, but the deviations vary in timing, duration and severity. Precipitation (Figure 2.3a) was not only extremely low during July 2018, but was also below the mean monthly precipitation for the majority of the months in 2018. Precipitation volumes recovered during 2019, but were

below mean monthly volumes again during spring and summer.

Surface soil moisture values seem to follow the climatology during most parts of the year, except for July 2018 where they show a sharp decline (Figure 2.3b). Soil moisture remained below the 20% climatology quantile for several months, but did not show a clear deviation from normal during 2019. Similarly to the soil moisture, NDVI shows a reduction during the summer of 2018 (Figure 2.3c). However, NDVI recovers quickly to the monthly mean values, and even remained above the 80% climatology quantile during the winter months. During the summer of 2019 values were again reduced below the 20% climatology quantile, but the anomaly was not as large as in 2018. Both groundwater (Figure 2.3d) and surface water (Figure 2.3e) show similar responses: starting from relatively high water levels in early 2018, dropping to nearly two standard deviations below the mean at the end of the year. These low values continue into 2019, where the anomalies in surface water levels were not as severe as the groundwater level anomalies. Interestingly, even though the surface water level stations are situated in different river basins, they all show a similar response during this drought.

While Figure 2.3 provides an important first insight into the differences in temporal drought evolution, it does not provide insight into the underlying spatial variability at the regional scale. The evolution of the spatial drought distributions in 2018 and 2019 are visualised in Figure 2.4. Here, the months surrounding the meteorological drought peak are depicted, as this is when the drought was generally most severe. This figure shows how the drought propagates through the hydrological cycle, starting from a slight reduction in precipitation in May 2018. When precipitation reaches its minimum in July 2018 (Figure 2.3a), both the soil moisture and NDVI follow quickly. However in the preceding months, both variables did not respond directly to the reduced precipitation, indicating the flexibility and buffering capacity of these variables. Additionally, in response to the low precipitation during July 2018, a direct anomaly in both groundwater and surface water levels is present. Both variables remain on the lower end of the percentile score, while the soil moisture and NDVI values slightly recover towards the end of 2018.

Similar to 2018, precipitation values showed low percentile scores in July

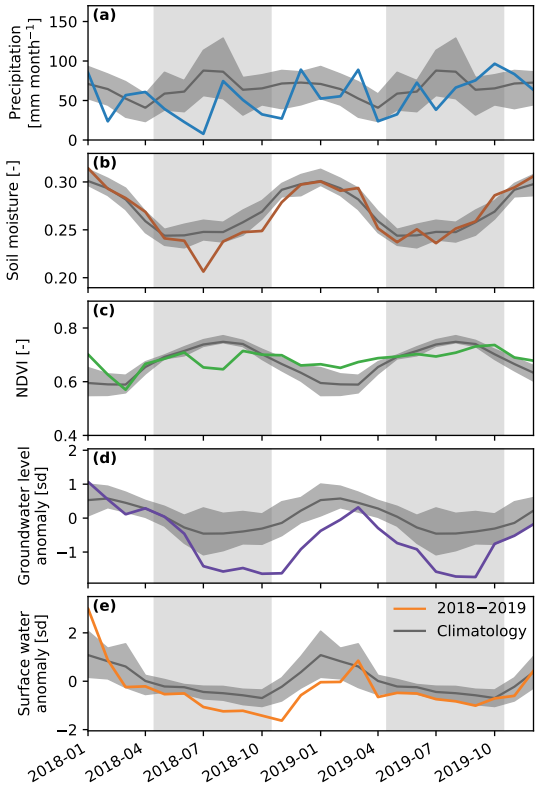

Figure 2.3 | Temporal evolution of the drought over 2018–2019 for the different variables. The grey line shows the monthly mean over the entire period, where the coloured line represents the mean time series for 2018 and 2019. The grey shaded area shows the monthly temporal variability, using the 20–80% quantile range. Precipitation (**a**), soil moisture (**b**) and NDVI (**c**) are shown as their observed values. Groundwater (**d**) and surface water levels (**e**) are normalised using the mean and standard deviations of each station. The two highlighted areas indicate the periods used in Figure 2.4.

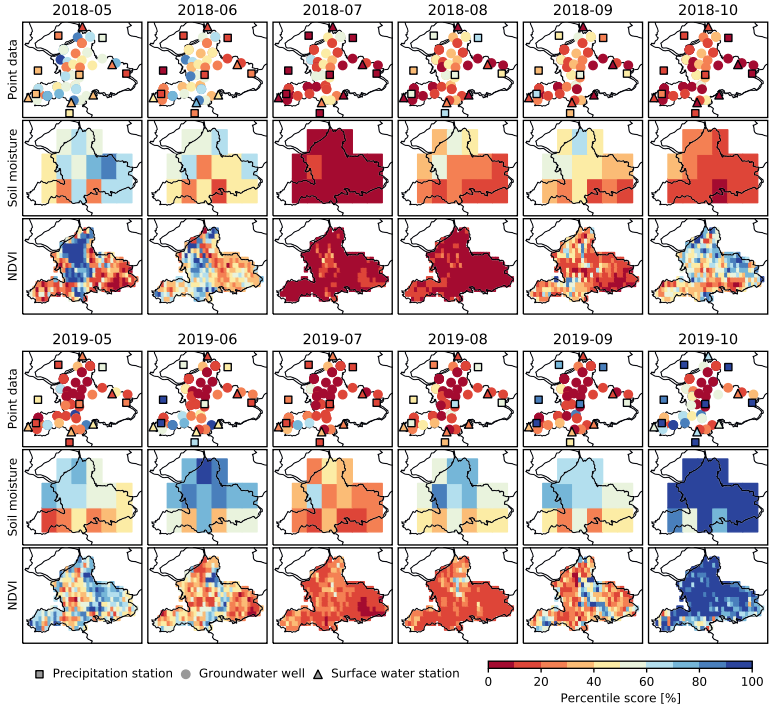

Figure 2.4 | Spatio-temporal evolution of the drought during May-October in 2018 and 2019.

2019, and both soil moisture and NDVI reached low percentile scores in the same month. Groundwater levels, on the other hand, were already low at the start of 2019, as they had not yet recovered from the drought of the previous year (also visible in Figure 2.3). Despite higher precipitation values in September and October 2019, the majority of the groundwater levels did not recover and remained below the 20% percentile score. Surface water shows a similar response as the groundwater, starting already at low percentile scores in May 2019. Only in October 2019, the percentile scores for the large rivers start to recover, while the Berkel river was still showing low percentile scores.

The complete time series for all variables and measurement stations/pixels are presented in the left column of Figure 2.5. These panels not only show both the spatial and temporal variability within the different stations/pixels of a single variable, but also show the interaction between the five variables. Overall, all variables show relatively low variability between the stations, but show substantial differences in terms of temporal variability. Most striking is the temporal variability in precipitation (Figure 2.5a): percentile scores can jump from extremely high percentile scores to extremely low percentile scores, from one month to the next. Soil moisture and NDVI show a more smooth temporal signal. This is as expected, as these variables have a 'memory' and are therefore unlikely to move from one end of the spectrum to the other in a single month. It is noteworthy that the relatively high soil moisture values around 2010 are not matched with high NDVI values in the same period, but rather the opposite. Likewise, NDVI shows high values around 2014–2016, while soil moisture values show a rather dry signal. The drought of 2018 is clearly visible in both, while the drought of 2019 is only clearly visible in the NDVI signal. Both groundwater and surface water percentiles again show similar dynamics. Both start relatively wet at the early years of our analysis, and move towards predominantly low percentile values at the end of the time series. Both variables stay longest in drought conditions during 2018 and 2019, as is also visible in Figure 2.3.

The right column of Figure 2.5 shows the value where 20% of the stations have a value equal or lower to this value. A variable is in drought conditions whenever at least 20% of the stations of that variable are in drought conditions, resulting in Figure 2.6a. Resulting from the spatial variability, all variables are more frequently in drought conditions than the percentile score suggests: ranging between 27–38% of the time, while the percentile score suggests 20% of the time. The fact that the drought frequency is higher than the percentile score, indirectly indicates that there is variability between measurement stations/pixels.

Panel b in Figure 2.6 shows the percentage of time that x variables are meeting the drought condition. Despite that the drought threshold is set to be at a percentile score of 20%, the study area is considered to be in drought conditions for 73% of the time. This can be attributed to the different vari-

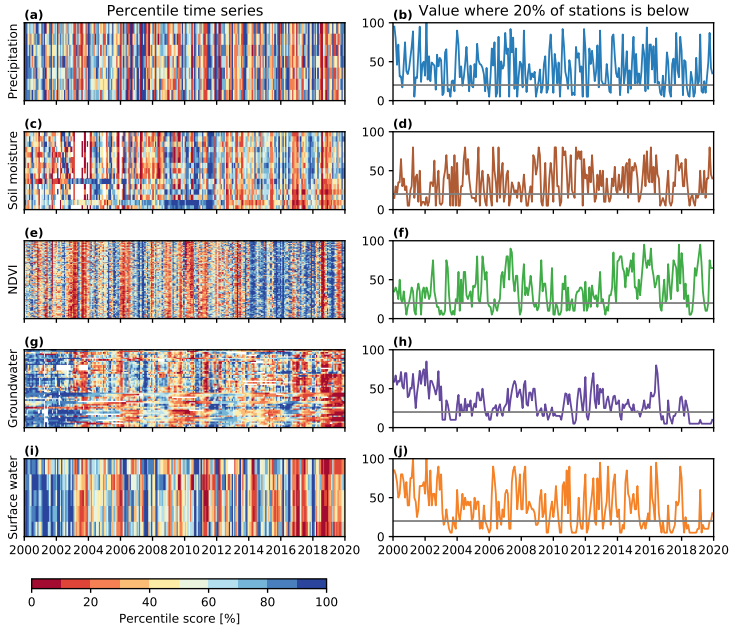

Figure 2.5 | Spatial and temporal variability in percentile scores across all variables. Left column of panels (**a**, **c**, **e**, **g**, **i**) shows the time series of all stations over the entire data period, where each row in each panel represents an individual measurement point/pixel. Right column of panels (**b**, **d**, **f**, **h**, **j**) show the value that represents the point where 20% of the stations/pixels in that variable are below this value.

ables considered, which do not always have overlapping droughts. The percentage of time in drought is reduced when more variables have overlapping droughts. In order to match the percentage of time in drought with the drought threshold, three to four variables need to have overlapping droughts. When all five variables have overlapping droughts, the region is only considered to be in drought conditions for 5% of the time.

The results in Figure 2.6, where the number of droughts seems to have increased in recent years, raise the question whether there has been a change

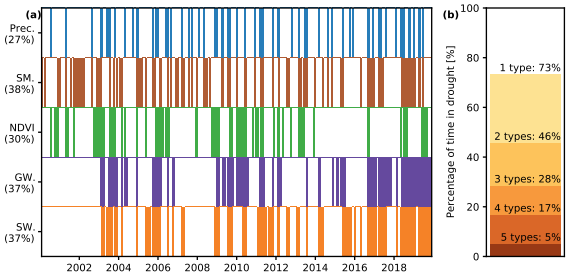

Figure 2.6 | Temporal evolution of drought conditions over the entire study period. Panel **a** highlights the months where the variable is considered to be in drought conditions. Percentages on the y-axis indicate the percentage of time that each variable is in drought conditions. Panel **b** shows the percentage of time the study area is in drought conditions, depending on how many variables are below the drought threshold.

in the frequency of co-occurring droughts within our study period (see Figure 2.7). The number of droughts in both groundwater and surface water increased substantially, mostly due to the 2018 and 2019 droughts (Figure 2.6a). The highlighted green bar in Figure 2.7 shows that the droughts of 2018 and 2019 can partly be attributed to this increase. The last 10 years also had more frequent co-occurrences of droughts, with the years 2018 and 2019 again playing a substantial role. Even without these years, 2010–2019 had more frequent droughts where at least 4 variables were in drought conditions.

When plotting the percentile threshold to define drought against the percentage of time that the data is below this threshold, we see that this relation is consistent across all threshold values (Figure 2.8). In this figure, we plot the percentile threshold from 0 to 100% for completeness, but percentile thresholds above roughly 30% would not be relevant for drought studies. However, showing the entire range facilitates the understanding of how the drought threshold and percentage of time in drought relate. In Figure 2.8a, we see that groundwater levels deviate farthest from the 1:1 line, followed by NDVI and soil moisture values. Both precipitation and surface water show a similar deviation from the 1:1 line. As mentioned earlier, this deviation can be attributed to variation between the different measurement stations/pixels.

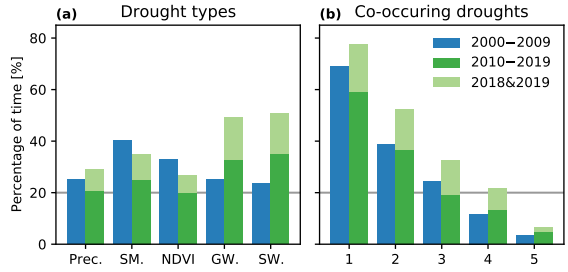

Figure 2.7 | Change in drought frequency between 2000–2009 and 2010–2019. Panel **a** shows the percentage of time each variable is below the drought threshold, and panel **b** shows the percentage of time at least x variables are in drought conditions. The horizontal line corresponds with the expected frequency based on the 20% percentile threshold. The entire green bar represents the 2010–2019 period, and the highlighted green bar represents the contribution of the recent droughts over the last two years.

Plotting the values from Figure 2.6b as a function of the percentile threshold to define drought, we get the results in Figure 2.8b. At a percentile threshold of just above 30% percent, there is at least one variable in drought conditions nearly 90% of the time. At the more commonly used 20% threshold, this number reduces somewhat to 73% of the time. This confirms our hypothesis that droughts are occurring more often than the threshold would suggest, when multiple variables in the hydrological cycle are considered. When a threshold of 20% is used as drought definition, droughts anywhere in the system occur at least 3 times more frequently. On the other hand, the situation where drought occurs across all components of the terrestrial hydrological cycle is 4 times less likely than the drought threshold of 20% (namely 5%).

2.4 | Discussion

In this chapter, we investigate droughts in five different variables in the hydrological cycle: precipitation, soil moisture, vegetation, groundwater and surface water. We show how these variables interact, and how the propagation and spatial variability of each of these variables influence the occurrence

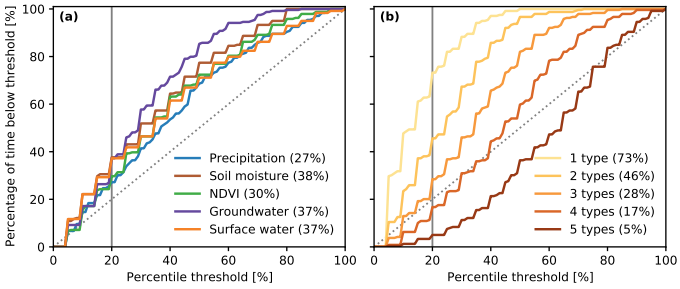

Figure 2.8 | Relation between drought threshold and percentage of time in a drought. Panel **a** shows the percentage of time each variable is below the corresponding threshold. Panel **b** shows how often the area is in drought conditions for a different number of variables considered. The dotted line in both panels shows the 1:1 line. Value between brackets shows the percentage of time each variable in in drought conditions at the 20% percentile threshold.

of drought and the effective drought frequency in Gelderland, the Netherlands. Our results show that droughts, when viewed across a complex hydrological system, are common rather than rare. This is of course dependent on the exact definition of a drought. In our study, we used the 20th percentile as drought threshold, meaning that mild droughts are included as well. This could potentially entail that events without clear impacts are classified as droughts, something that was highlighted as a challenge in drought definition by Stahl et al. (2020). Despite this, our drought definition still reflects common practices in water management, and we therefore emphasise that this practice is susceptible to a drought frequency paradox. Given our results, two obvious questions can be raised: are the results representative for other regions, and what are possible solutions for drought monitoring?

At first glance, the Dutch province of Gelderland is a unique region in the Netherlands, with geomorphological features ranging from floodplains to the sandy moraine (the Veluwe Massif), and substantial regions that are used for agriculture. Additionally, it is situated in the downstream areas of several rivers. While this may perhaps be unique for the Netherlands, the general features that influence drought are less unique. The majority of agricultural

production occurs in downstream regions of river systems, due to the relatively flat land and availability to water, and it is in these regions that drought is highly relevant since agriculture could be impacted by both local droughts (e.g. soil moisture), but also by drought occurring upstream of the river basin, through its impact on river discharge. Furthermore much of the signal is caused by spatial variability in the groundwater response to drought. But in the study by Kumar et al. (2016), also partly in Gelderland, similar variability in groundwater response was found for many regions in Germany. And while we did not investigate the dependency of our results on the size of the study region, we expect that most regions with variability in soil, vegetation, and depth to the groundwater table will show similar behaviour. At larger scales, possible spatial variability in meteorological drought conditions might even become an additional factor that contributes to a higher frequency of co-occurring droughts.

As for the monitoring of droughts, several attempts have been made to either extend or improve common indices. Meteorological drought indicators are most frequently used (Bachmair et al., 2016), as meteorological drought is typically the driver of the other drought types, has usually longer available data records, and is generally easiest to measure. However, our results show that meteorological droughts do not correctly represent droughts in the four other considered variables. This is in line with other studies. For example, Kumar et al. (2016) used SPI to estimate the Standardised Groundwater Index (SGI). They found that long SPI accumulation times were required to reach high correlation with SGI, but failed to correctly predict the actual SGI values. Furthermore, Bachmair et al. (2018) conclude that using meteorological indices to represent agricultural and forest droughts highly varied with climate. Stagge et al. (2015) created a model using meteorological drought data as input to predict different drought types. They show promising results, but also note that their model needs to be re-calibrated for different regions. Given the conclusions of these studies, and the results in this chapter, we stress the importance of drought monitoring across all relevant components of the hydrological cycle. Even if meteorological drought could be used for extrapolation to other drought types, correct understanding of the link between these drought types—and hence the monitoring—is a requirement.

A possible solution to this paradox would be the use of compound drought indices. Two approaches are possible here, although they both have important disadvantages. In the first approach, a compound index can be calculated similar to our current approach, i.e. identify a drought whenever there are serious drought conditions in one or more parts of the hydrological system. The disadvantage of this approach is that the effective drought frequency might increase to levels that are incompatible with current drought definitions that define drought as a rare event. In the second approach, a compound drought index can be transformed such that the effective drought frequency is exactly the pre-defined value. While this approach might seem intuitive, it likely will require local calibration and an (arbitrary) weighing between different parts of the hydrological system and the relative impact of drought on certain economic sectors. The above suggests that tailor-made solutions remain necessary for effective drought monitoring and management at regional scales. Furthermore, the impact of a drought does not necessarily correspond with the occurrence of a drought as measured with an index, as this also depends on the socio-economic value. Therefore, we stress the importance of monitoring all relevant variables in the area of interest, involving both satellite remote sensing (West et al., 2019) and local observations, in close collaboration with stakeholders to quantify the impacts. Impacts are ultimately the most relevant aspect of droughts from a societal or operational water management perspective, which implies that a drought index should reflect the impacts rather than raise an unwanted drought frequency paradox.

2.5 | Conclusions

An overview of five major variables in the hydrological cycle (precipitation, soil moisture, vegetation greenness, groundwater and surface water levels) allows us to study a possible drought frequency paradox. The analysis focused on the Dutch province of Gelderland. Using the recent droughts of 2018 and 2019 as case studies, we show that each variable operates with typical temporal and spatial variability. Precipitation is rather homogeneous in space, but highly variable in time. Soil moisture and NDVI both are more spatially variable, but their temporal signal is smoother with respect to precip-

itation. Despite difference in underlying processes and scale, groundwater and surface water levels show very similar responses during these droughts. Inter- and intra-variability of these five variables causes different types of droughts in different parts of both space and time.

With a percentile score of 20% as the drought threshold at the pixel/point level, we show that each variable can be considered to be in drought at the regional scale for 27–38% of the time depending on the variable, which is more frequent than the 20% of the time the percentile threshold suggests. When all relevant variables are considered, at least one variable is in drought conditions for 73% of the time. Both of these values can lead to a perception of a drought frequency paradox, where drought occurs much more frequently than would be expected based on the used main drought threshold. The percentage of time matches the drought (frequency) threshold only when three to four variables are in drought conditions. We showed that the usage of a common drought definition (albeit for mild droughts) can lead to a perception of a drought frequency paradox. This might not be representative for the actual drought conditions, and we therefore stress the importance of close collaboration between scientists, water managers and stakeholders to ensure correct drought detection within a hydrological system. This can be achieved through correctly calibrated compound indices, as multiple univariate indices can lead to a drought frequency paradox.


3

Interaction between soil moisture and vegetation during drought

---

This chapter is based on:

Buitink, J., Swank, A. M., van der Ploeg, M., Smith, N. E., Benninga, H.-J. F., van der Bolt, F., Carranza, C. D. U., Koren, G., van der Velde, R., and Teuling, A. J. (2020). Anatomy of the 2018 agricultural drought in the Netherlands using in situ soil moisture and satellite vegetation indices, *Hydrology and Earth System Sciences*, 24, 6021–6031, doi:10.5194/hess-24-6021-2020.

The soil moisture status near the land surface is a key determinant of vegetation productivity. The critical soil moisture content determines the transition from an energy-limited to a water-limited evapotranspiration regime. This chapter quantifies the critical soil moisture content by comparison of in situ soil moisture profile measurements of the Raam and Twente networks in the Netherlands, with two satellite-derived vegetation indices (near-infrared reflectance of terrestrial vegetation, NIRv, and vegetation optical depth, VOD) during the 2018 summer drought. The critical soil moisture content is obtained through a piece-wise linear correlation of the NIRv and VOD anomalies with soil moisture on different depths of the profile. This non-linear relation reflects the observation that negative soil moisture anomalies develop weeks before the first reduction in vegetation indices: 2–3 weeks in this case. Furthermore, the inferred critical soil moisture content was found to increase with observation depth, and this relationship is shown to be linear and distinctive per area, reflecting the tendency of roots to take up water from deeper layers when drought progresses. The relations of non-stressed towards water-stressed vegetation conditions on distinct depths are derived using remote sensing, enabling the parameterisation of reduced evapotranspiration and its effect on gross primary productivity in models to study the impact of a drought on the carbon cycle.

"Sunsets never were so bright
And the skies, never so blue"

—Mayday Parade, *Jamie All Over* (2007)

3.1 | Introduction

Droughts can have wide environmental and socio-economic impacts, ranging from their effects on climate, the carbon cycle, and food security to water availability. Droughts are typically induced by a lack of precipitation and/or an above-average atmospheric demand for evapotranspiration (ET), which leads to an associated reduced availability of soil moisture in the root zone (Seneviratne et al., 2010; Teuling, 2018). The former is typically referred to as meteorological drought, whereas the latter is referred to as agricultural drought. Reduced soil moisture limits water uptake and ET from the plant, which leads to an increase in sensible heat flux relative to latent heat flux. This establishes a positive feedback, by further increasing temperature and vapour pressure deficit (Seneviratne et al., 2010; Miralles et al., 2019; Lansu et al., 2020). Furthermore, reduction in ET through the closing of plants' stomata also affects the carbon cycle by reducing gross primary productivity (GPP) (van der Molen et al., 2011; Reichstein et al., 2013). This can turn ecosystems from carbon sinks to sources, such as during the 2003 European summer drought and heatwave in which GPP was reduced by as much as 30% (Ciais et al., 2005). While meteorological droughts are generally well understood since they can be monitored by routine meteorological observations, quantifying the links between soil moisture, ET, and vegetation during agricultural droughts is more challenging. This is the aim of this chapter, in which we focus on the record-breaking drought of 2018 in Europe (Bakke et al., 2020).

Typically, two ET regimes are distinguished: an energy-limited and a water-limited regime. This is often conceptualised and parameterised as a bilinear function of soil moisture, separating the regimes at the so-called critical soil moisture content (Seneviratne et al., 2010). There is considerable evidence that a strong non-linearity is typical for most regions and conditions. This makes it key to i) predict the onset of drought impact on ET and ii) predict the timescale of ET decay during drought (Teuling et al., 2006; Boese et al., 2019). In early field experiments, it was already observed that the actual ET fell below the potential only at lower levels of soil moisture, and that the value at which this occurred depended on the potential ET (Denmead & Shaw, 1962). In more recent studies at larger scales, it has been observed that ET over the summer increased rather than decreased in parts of central-western

Europe during drought (Teuling et al., 2013) and that vegetation productivity in Alpine regions also increased during the 2003 summer drought (Jolly et al., 2005). In a recent study on vegetation-soil moisture coupling using satellite observation products (Denissen et al., 2020), it was found that the critical soil moisture is located at the lower rather than higher part of the soil moisture range. However, the remote sensing products used in this chapter are subject to significant limitations, mainly caused by the limited penetration depth of the sensors. Since vegetation may take up water from much deeper soil layers, it makes critical soil moisture estimations using remote sensing highly uncertain.

The impact of drought has been studied extensively using ecosystem-level information obtained from eddy covariance sensors (i.e. FLUXNET), satellite-derived observations (van der Molen et al., 2011), or terrestrial biosphere modelling (van Schaik et al., 2018). This has provided valuable insight into the timing and impact of drought on GPP (Sippel et al., 2018; Stocker et al., 2019). Several studies have shown that spatio-temporal patterns of GPP are correlated with solar-induced chlorophyll fluorescence (SIF), a satellite product which measures the re-emission of light by chloroplasts during photosynthesis (Frankenberg et al., 2011; Koren et al., 2018; Li et al., 2018). Badgley et al. (2017, 2019) found that SIF correlates strongly with satellite obtained near-infrared reflectance of terrestrial vegetation (NIRv) and proposes to use this as a proxy for GPP. Another satellite-derived observation of GPP is vegetation optical depth (VOD) (Konings et al., 2016; Teubner et al., 2018, 2019; Moesinger et al., 2020). Both NIRv and VOD have a high temporal resolution, in contrast to SIF data. This allows for a more precise analysis of how plant productivity is related to soil moisture.

Ecosystem flux observations and satellite observations of vegetation can provide valuable insight into the ecosystem response to drought. However, they do not provide direct insight into processes that occur below the surface, in particular the timing, location, and strategy of plant water uptake in the root zone. The parameterisation of root water uptake during drought is thus a major source of uncertainty in models (Braud et al., 2005; Teuling et al., 2006; Kumar et al., 2015; Combe et al., 2016). For example, a recent study showed how different vegetation types employ different strategies during

the drought of 2018 (Kleine et al., 2020). It is well known that, generally, plants take up water from the upper soil layers first. They can compensate for a developing lack of moisture near the surface by increasing their uptake deeper in the profile to values much higher than can be expected based on the root density (Sharp & Davies, 1985; Green & Clothier, 1995). Currently, many studies rely on the use of surface soil moisture to diagnose drought processes. This is problematic because surface soil moisture that can be measured by satellite-derived observations might become decoupled from soil moisture deeper in the profile where it is taken up by plants (Capehart & Carlson, 1997; Carranza et al., 2018), and they might not represent the dynamics of processes deeper in the root zone (Bassiouni et al., 2020).

The availability of a growing number of relatively accurate low-cost soil moisture sensors (Mittelbach et al., 2011) has led to an increasing number of regional soil moisture networks, where soil moisture is measured at a large number of sites and at several depths in the profile. Such networks, in combination with satellite-derived observations, can provide a unique insight into the link between vegetation stress, root water uptake, and soil moisture profiles. Two of those networks, the Twente and Raam networks in the Netherlands, are located in the region that suffered from the 2018 European summer drought.

High-impact extreme events such as flash floods are often associated with sloping or upland terrain (Marchi et al., 2010). However floods and droughts can have considerable impact in lowland areas as well, even though the main hydrological processes can differ. For the 1976 summer drought in the Hupsel Brook catchment (Brauer et al., 2018), it was found that soil moisture anomalies develop progressively deeper over the course of the drought, reflecting a strong link to the presence of a relatively shallow groundwater table (Teuling et al., 2013). For the same catchment, it was found that the link between soil moisture and the groundwater table at near-saturated conditions played an equally important role in determining the onset of saturation excess runoff and flash flood response following the August 2010 extreme precipitation (Brauer et al., 2011). In larger lowland rivers, low topographic and hydraulic gradients can induce flooding due to backwater effects (Geertsema et al., 2018). Due to the strong human influence of hydrological processes

on, for instance, changes in drainage density and/or land use, lowland areas might also be sensitive to changes in hydrological extremes (Pijl et al., 2018).

In this chapter, we combine data from the Twente and Raam soil moisture networks located in the Netherlands with satellite-derived vegetation indices (NIRv and VOD). Using these datasets, we study the regional-scale development of the 2018 agricultural drought in a lowland area during the summer months June, July, and August. Specifically, we aim to i) analyse the temporal evolution of drought in the unsaturated zone in relation to the non-drought years of 2016 and 2017, ii) link dynamics of vegetation productivity to soil moisture, and iii) infer the critical soil moisture content and its dependency on depth.

3.2 | Methods

The Raam and Twente soil moisture networks in the Netherlands (see Figure 3.1) were originally installed as validation sites for satellite-derived data products (Benninga et al., 2018; Dente et al., 2011). The Raam network faces—by Dutch standards and in comparison to the Twente network—substantial water shortages during normal summers (Benninga et al., 2018). This can be mainly attributed to the mostly sandy soils in the Raam network, whereas the Twente network is located in an area with sandy to more loamy soils. Both areas have a land cover consisting of cultivated or natural grassland, agricultural fields (maize, onion, chicory, sugar beets), and some forested sites (though these are not instrumented). Both networks are positioned between 10–30 meter above sea level. The average spacing between the soil moisture sensors is 6.2 km for Twente and 3.5 km for Raam. For further details on the network and sites, we refer to the relevant papers (Benninga et al., 2018; Dente et al., 2011).

Soil moisture observations for both networks were available for 2016–2018 at discrete depths below the soil surface (5, 10, 20, 40 cm for Raam and Twente and additionally 80 cm for Raam), from which daily averaged volumetric soil moisture (θ, in m^3_{water} m^{-3}_{soil}) was obtained. The 31 days moving means of 2016 and 2017 were averaged to represent baseline conditions (referred to as climatology hereafter). The anomaly is defined as the difference

between 2018 and the climatology. We assumed that measurements at 5, 10, 20, 40, and 80 cm represent the soil column between 2.5–7.5, 7.5–12.5, 12.5–27.5, 27.5–52.5, and 52.5–107.5 cm depth respectively. Stations were selected based on maximum available daily averaged data between May 2016 and September 2018 (filled circles in Figure 3.1c, d).

For the meteorological conditions, daily precipitation and potential ET (calculated by the Royal Netherlands Meteorological Institute (KNMI) with Makkink (1960)) were obtained from the KNMI stations in Volkel (06375) and Twenthe (06290; see locations in Figure 3.1c, d). Gridded precipitation was obtained from E-OBS, at 0.1°×0.1° and daily resolution (v20.0e; Cornes et al., 2018). Comparing yearly average values of 2016 and 2017 with the mean over 1990–2019 shows that temperature, precipitation, and potential evaporation were all close to the long-term mean values (in brackets): temperatures were 10.4 °C (10.1 °C), precipitation 791 mm (782 mm), and potential ET 584 mm (573 mm). This supports the years 2016 and 2017 being used as baseline conditions.

Photosynthetically active radiation normalised solar-induced fluorescence (SIF; v27) was used as a proxy for GPP and obtained from the GOME-2B instrument on board the MetOp-B satellite as described in Joiner et al. (2013, 2016) on a monthly average and with 0.05°×0.05° spatial resolution. Daily NIRv was obtained using the following calculation:

$$\mathrm{NIRv} = \mathrm{NDVI} \cdot \mathrm{NIR_T}, \tag{3.1}$$

where NDVI represents the normalised difference vegetation index, and $\mathrm{NIR_T}$ represents the total scene near-infrared reflectance (Badgley et al., 2017). Both are obtained from the merged MODIS Aqua and Terra satellites' product, available at a 0.05°×0.05° spatial resolution (Schaaf & Wang, 2015). The $\mathrm{NIR_T}$ was BRDF-adjusted (bidirectional reflectance distribution function), and all values below 0 were removed.

The NIRv product has a higher spatial and temporal resolution than the SIF dataset. Although the NIRv product is relatively new, several studies have highlighted the usability of this dataset. Badgley et al. (2019) showed that the relationship between NIRv and GPP was consistently linear across all values

of GPP, both during drought events and during acute stress events at short timescales. Additionally, Baldocchi et al. (2020) concluded that NIRv is able to correctly represent photosynthesis across different temporal scales.

Vegetation optical depth (VOD) values were obtained from Moesinger et al. (2019). VOD is a measure for above-ground vegetation water content (Konings et al., 2016; Moesinger et al., 2020), derived from space-borne microwave sensors (SSM/I, TMI, AMSR-E, WindSat, and AMSR2). VOD is available at a spatial resolution of $0.25 \times 0.25°$, and at a daily time step (though not every day has 100% coverage). VOD is used for comparison with NIRv values and to test the robustness of our analysis. For our analysis, we selected the C band to calculate the anomalies. The climatology and anomaly of precipitation, SIF, NIRv, and VOD were calculated similarly to θ.

To infer the critical soil moisture (θ_{critical}), the NIRv anomaly as a function of θ was fitted by employing a piece-wise linear function, which renders an inflection point indicating the transition from an energy-limited to a water-limited evapotranspiration regime (Seneviratne et al., 2010). We focus on the period during which the soil moisture anomalies show a downward trend (June and July, highlighted in Figure 3.2). Using bootstrapping, we determined the 5–95% uncertainty range of the inferred critical soil moisture value at each integration depth.

3.3 | Results

The strong reduction in precipitation over June and July that was centred around the Netherlands (Figure 3.1a) coincided with strong negative anomalies in vegetation productivity. Coarse-scale estimates of productivity based on solar-induced fluorescence (Figure 3.1b) show large negative anomalies, in particular in the eastern part of the country where soils are more sandy and groundwater tables are deeper. Higher resolution NIRv imagery shows a similar pattern, including slightly larger negative anomalies in Twente compared to more moderate anomalies in the Raam (Figure 3.1c, d). This shows that the soil moisture networks were located at a prime location to monitor the impact of the 2018 drought.

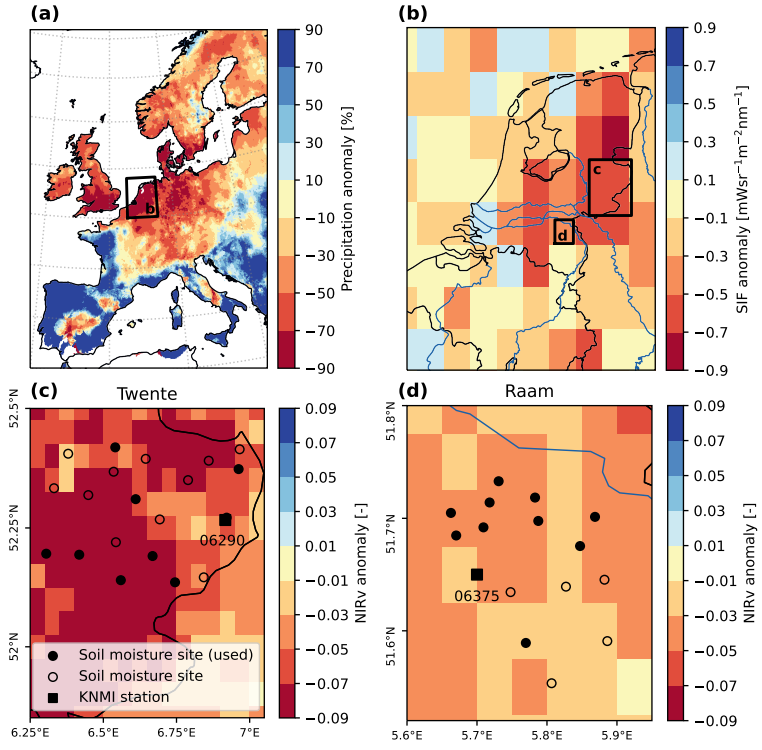

Figure 3.1 | Distribution of the 2018 summer drought and vegetation productivity with respect to 2016 and 2017. Drought distribution in western Europe (**a**) is expressed by the relative June-July precipitation anomaly (E-OBS), showing that the eastern part of the Netherlands was one of the worst hit areas. This is confirmed by a similar pattern in GOME-2 SIF anomalies (**b**). MODIS NIRv (**c**, **d**) shows a similar distribution but at much higher spatial resolution, for Twente (**c**) and Raam (**d**). The circles indicate in situ soil moisture measurement sites with (filled) and without data of sufficient availability (open); when filled these are included in the analyses. KNMI stations Twenthe (06290) and Volkel (06375) are indicated by black squares.

The temporal dynamics of the vegetation productivity and soil moisture reveals considerable complexity in the response to the drought. During initial stages of the drought, NIRv kept pace with, or even sometimes exceeded, the climatological values in both networks (Figure 3.2a, b). In the beginning of summer, the NIRv anomalies are around zero for Twente and slightly positive for Raam and are followed by a sharp decline in productivity in late June. At the end of July, maximum NIRv anomalies correspond to −30% (Twente) and −25% (Raam). In contrast to the NIRv anomalies, soil moisture observations reveal a steady decline from the beginning of summer up to the end of July. Anomalies are found to be largest at the end of July. NIRv and soil moisture anomalies remain strongly negative in Twente until the beginning of October, whereas the Raam shows a faster recovery. VOD shows a similar response to NIRv; yet the VOD anomalies exceed the climatological values during the start of the summer. The moment at which the anomalies decline matches NIRv; yet the VOD anomalies recover later in the year than the NIRv anomalies.

When the dynamics of the vegetation indices during the 2018 drought are evaluated against soil moisture averaged over different depths, a strong non-linear response becomes apparent (Figure 3.3). The response is described by a piecewise linear model with a right-hand part with zero slope (i.e. assuming no stress). This three-parameter model describes the response better than a two-parameter linear model, as indicated by consistently higher values for the adjusted R^2 (average R^2 of 0.82 versus 0.63; see Table 3.1). Due to the difference in dynamics in VOD, we removed the first days of June, as the VOD anomalies were still increasing over this period (see Figure 3.2). Over the selected period, VOD anomalies show no clear trend, and the average value (and period) can be found in Figure 3.2. Initially, NIRv and VOD anomalies remain roughly at a constant level, while soil moisture decreases considerably. It took 3 weeks before NIRv anomalies showed a decrease and 2 weeks for VOD. Next, this constant phase is followed by a second phase in which NIRv and VOD anomalies decrease approximately linearly with soil moisture, indicating a strong drought impact on vegetation productivity. The non-linearity is present when soil moisture is evaluated over different depths ranging from a shallow top layer (0–5 cm) to most of the root zone (0–80 cm), using the representative soil column thickness (see Methods) to correct the soil mois-

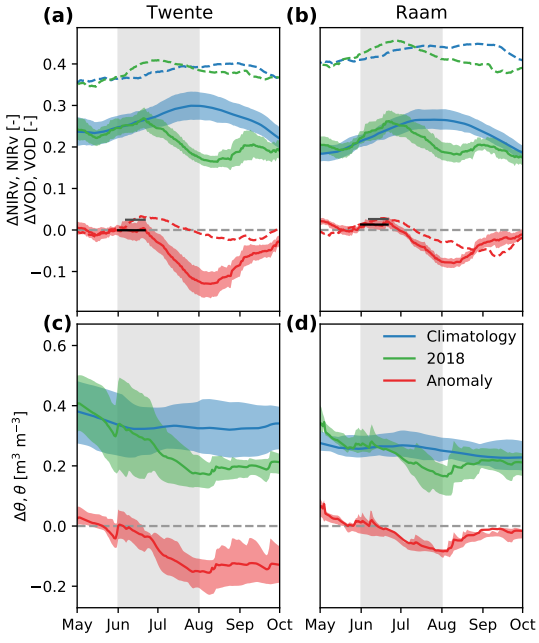

Figure 3.2 | Temporal evolution of the 2018 agricultural drought over the study regions. Top panels (**a**, **b**) show NIRv (solid) and VOD (dashed), and bottom panels (**c**, **d**) the soil moisture conditions over the growing season for Twente (**a**, **c**) and Raam (**b**, **d**). Soil moisture is the average observed at 40 cm depth. Horizontal lines in panels **a** and **b** indicate the non-stressed NIRv (black) and VOD (grey) values used in Figure 3.3. Coloured shaded areas represent spatial variability within the regions and are calculated in the 20–80% range. Grey shading highlights the period used in Figure 3.3.

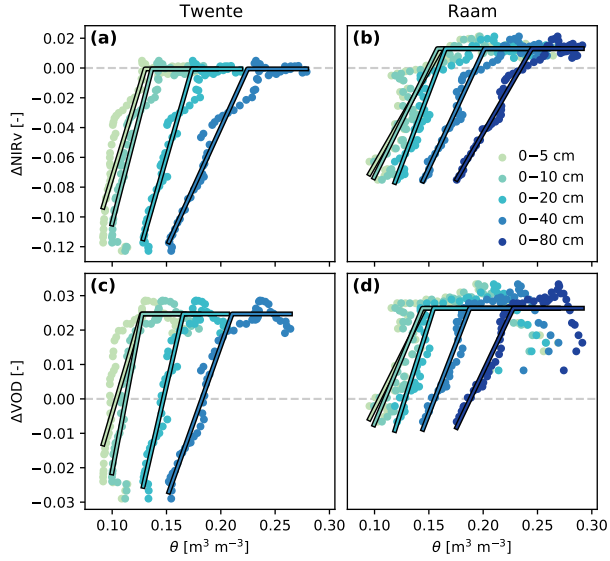

Figure 3.3 | Relation between regional anomalies in vegetation indices and soil moisture (dots) and the piecewise linear fit (lines) for Twente (**a**, **c**) and Raam (**b**, **d**), for both NIRv (**a**, **b**) and VOD (**c**, **d**). The horizontal part of the piecewise fit was set at the average vegetation index anomaly value in the first part of the summer period (corresponding to the horizontal line in Figure 3.2a, b). Note that all values represent average values over the regions, as shown in Figure 3.2.

ture values. However, soil moisture values, including the transitional point marking the start of the drought impact on vegetation productivity, are generally lower, with a difference in volumetric water content between 0.05 and 0.10 for both sites. The point separating the two phases of non-stressed and water-stressed conditions can be interpreted as the critical soil moisture content.

Further analysis of the evolution of regional-scale average soil moisture profiles (Figure 3.4) reveals the origin of the differences found in Figure 3.3. In normal years, soil moisture dries out considerably in the upper layers (down

Table 3.1 | Fit statistics and resulting critical soil moisture content based on both NIRv and VOD data. $R^2_{adjusted}$ values are shown for both the piecewise (pw) and linear (lin) fits, adjusted for the number of parameters used in the fit; the value in brackets shows the standard R^2 value. The critical soil moisture content in brackets is the value normalised between minimum and maximum moisture content values at each integration depth.

	Depth (cm)	NIRv			VOD		
		R^2pw	R^2lin	$\theta_{critical}$	R^2pw	R^2lin	$\theta_{critical}$
Raam	5	0.80 (0.81)	0.61 (0.62)	0.16 (0.24)	0.55 (0.57)	0.24 (0.27)	0.15 (0.18)
	10	0.82 (0.83)	0.65 (0.66)	0.16 (0.22)	0.58 (0.61)	0.28 (0.30)	0.14 (0.17)
	20	0.91 (0.91)	0.72 (0.73)	0.17 (0.20)	0.73 (0.74)	0.34 (0.36)	0.15 (0.16)
	40	0.96 (0.96)	0.82 (0.82)	0.20 (0.29)	0.83 (0.84)	0.46 (0.48)	0.19 (0.22)
	80	0.97 (0.98)	0.89 (0.89)	0.24 (0.37)	0.85 (0.86)	0.57 (0.58)	0.23 (0.29)
Twente	5	0.72 (0.73)	0.59 (0.60)	0.13 (0.08)	0.60 (0.63)	0.48 (0.50)	0.13 (0.08)
	10	0.86 (0.87)	0.69 (0.70)	0.14 (0.08)	0.82 (0.83)	0.62 (0.63)	0.13 (0.06)
	20	0.95 (0.96)	0.82 (0.83)	0.17 (0.11)	0.95 (0.95)	0.79 (0.80)	0.17 (0.09)
	40	0.97 (0.97)	0.88 (0.88)	0.22 (0.18)	0.97 (0.97)	0.84 (0.84)	0.21 (0.15)

to values in the range 0.15–0.20) but much less in the lower layers, where values stay around 0.30. This is partly due to the fact that in a normal summer, JJA potential evapotranspiration according to Makkink's method (2.9–3.1 mm d^{-1}) is nearly balanced by precipitation with 2.3–2.8 mm d^{-1}. This likely allows vegetation to take up most of the water in the upper part of the root zone. In 2018, the increased atmospheric demand for evaporation, as reflected in a higher potential evapotranspiration (3.6–3.7 mm d^{-1}, so a 20% increase), combined with a strong reduction in precipitation (1.3–1.4 mm d^{-1}, so a nearly 50% reduction), led to a strong initial drying of the surface layer. This is reflected in the negative anomalies which peak around the start of July (DOY 184 and 192 for Raam and Twente, respectively). Only later did strong negative anomalies develop deeper in the root zone (DOY 220 and 221 for Raam and Twente, respectively), potentially due to enhanced root water uptake to (partly) compensate for the reduced uptake in the surface layers. This contrasts sharply with normal summer conditions under which most of the uptake takes place in the surface layers. The anomalies at 40 and 80 cm depth reach their maximum only at the end of the main drought or even later. This explains the large discrepancy between surface and root zone soil moisture at the early stages of the drought.

When the critical moisture contents inferred in Figure 3.3 are evaluated against the integration depth of the soil moisture observations, we find the

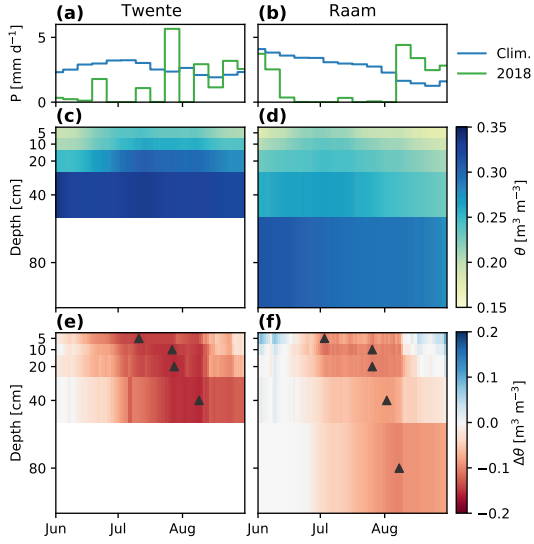

Figure 3.4 | Temporal evolution of observed precipitation and soil moisture profiles during the 2018 drought. For precipitation, the top panels (**a** and **b**) show the precipitation recorded at the KNMI stations of Twenthe and Volkel (see location in Fig. 1c/d). For soil moisture, the climatology (mean 2016–2017, panels **c** and **d**) and the 2018 anomalies (panels **e** and **f**) are shown for Twente (left panels) and Raam (right panels). The triangles in panels **e** and **f** indicate the moment of maximum negative anomaly at each depth.

results in Figure 3.5. Ideally, there should be no dependency of the critical moisture content on depth because this would facilitate the identification and use of the critical moisture content in models. However both networks show a similar, strong dependency with depth, with the inferred critical moisture content ranging from 0.13–0.16 m^3_{water} m^{-3}_{soil} for shallow soil moisture observations to over 0.20 m^3_{water} m^{-3}_{soil} when observations over most of the root zone are used. The inferred relations between critical soil moisture and depth are found to be roughly equal for the fits based on NIRv and VOD data. The uncertainty bars resulting from bootstrapping show larger uncertainty at shallower integration depths; yet the values found at shal-

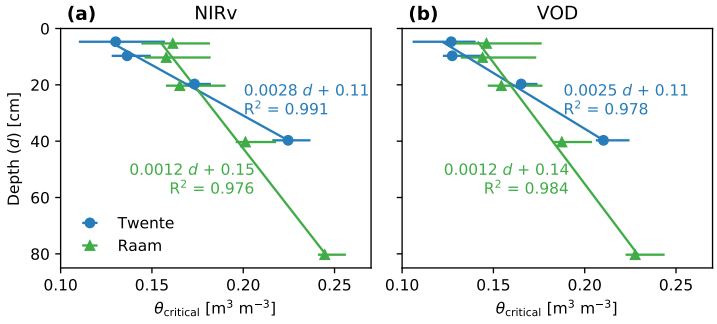

Figure 3.5 | Relation between critical soil moisture and the integration depth (denoted as d in the equation) of soil moisture used in the inference. Panel **a** shows the relation based on the NIRv data, and panel **b** shows the relation based on the VOD data. Horizontal lines indicate the 5–95% range of critical soil moisture values.

lower depths are lower than values at deeper integration depths. Given the increasing relation of critical soil moisture with depth, and since the root zone is presumably deeper than 1 m, it is possible that observations over the entire root zone will lead to even higher values. The critical soil moisture values can be found in Table 3.1. This table also shows the relative θ_{critical} determined using the minimum and maximum soil moisture values over the period 2016–2018.

3.4 | Discussion

The analysis in this chapter combined data from two Dutch soil moisture networks with high-resolution satellite vegetation indices as a novel approach to quantify agricultural drought conditions and impact. The 2018 summer drought had considerable impact in the areas where the networks were situated.

The inferred θ_{critical}—marking the transition between non-stressed (energy-limited ET) and stressed (water-limited ET) soil moisture regimes—is found to be dependent on monitoring depth. Accurate determination of the θ_{critical}

is essential for describing the relation between vegetation's response to water stress and carbon flux predictions during drought events (Boese et al., 2019; Green et al., 2019; Stocker et al., 2019) as current parametric expressions are unsuitable under droughts (Madi et al., 2018). This chapter highlights the particular value of in situ soil moisture networks, besides their purpose to calibrate and validate satellite-derived observations (Dorigo et al., 2011), to inform about θ_{critical}, as root water uptake dynamics and ET rates cannot easily be derived from satellite observations (Purdy et al., 2018).

We found a decline in NIRv and VOD to occur only once surface soil moisture had already reached its lowest level. Satellite-derived observations of the soil's subsurface can certainly serve as early predictors for drought onset (Ford et al., 2015; Otkin et al., 2018); yet drought also leads to decoupling of the soil moisture signal over depth (Carranza et al., 2018), rendering satellite-derived soil moisture or in situ surface soil moisture observations uninformative about root water uptake and drought impact status. This effect, in combination with the sandy texture of the soils in both networks, can also explain why we find values for θ_{critical} that are lower than those from recent estimates based on satellite soil moisture (Denissen et al., 2020). Assessment of vegetation response to profile soil moisture requires observations both at multiple depths and at multiple profiles to average out small-scale heterogeneities (Teuling et al., 2006).

This study determined the θ_{critical} with data that were already available. The method would in principle allow root water uptake regimes to be identified during droughts without the need for (difficult to obtain) vegetation-driven biophysical landscape interactions (e.g. Prentice et al., 2014; Warren et al., 2015; van der Ploeg et al., 2018). However, within the Raam and Twente networks, the maximum measurement depth of θ (80 and 40 cm respectively) may have been insufficient to capture the complete propagation of soil moisture anomalies in the root zone and their possible link to root water uptake dynamics. Were the measurement setups of both networks harmonised by covering the entire root zone, it would have provided a more accurate comparison of drought impacts and variability in soil moisture (Dorigo et al., 2011). When the focus of establishing a soil moisture network is not to validate satellite-derived observations—as was the case for these two networks—,

but to quantify drought effects on root water uptake, the maximum rooting depth of the vegetation near soil moisture stations should be considered, even though temporal dynamics of soil moisture and root water uptake under non-drought conditions predominantly occur in the upper 70 cm of the soil profile (Teuling et al., 2006).

Ideally, the values for θ_{critical} are considered with respect to the wilting point and field capacity because these, in concert with the rooting depth, determine the soil moisture dynamics (Albertson & Kiely, 2001). However these values themselves are highly variable spatially but also vertically over the soil profile. For sandy (Raam) to more loamy (Twente) soils, these characteristic soil moisture values are generally assumed to be in the range of a few vol. % (wilting point) and between 15 and 25 vol. % (field capacity). However, differences between various pedotransfer methods can be large (Teuling et al., 2009b). Based on the length of the time before a reduction in NIRv and VOD anomalies was first observed, it can be inferred that even in these coarse soils, a significant storage exists between field capacity and the critical moisture content that can be utilised by plants during drought onset.

This study also provides realistic environmental conditions of drought at relevant scales. In a recent meta-analysis of studies on drought impacts on ecosystems, Slette et al. (2019) concluded that drought is often poorly defined, and many supposed drought experiments take place within the normal range of climate variability rather than an extreme drought. This is problematic because drought impact is not proportional to drought severity but increases rapidly once a critical threshold has been exceeded. More research is therefore needed to identify and quantify drought thresholds and impacts across ecosystems and climate regions, especially in light of co-evolution in soil-vegetation-fauna-microbial relations, particularly the different strategies with which these relationships are adopted, modified, or adapted (Robinson et al., 2019). Failure to represent such ecosystem strategies in Earth system models might affect our ability to make reliable projections of future drought impact. The methodology presented here informs to better constrain drought-relevant parameters, such as the critical moisture content, in models.

3.5 | Conclusions

A prolonged period of no (or very low) precipitation during the summer of 2018 caused profound negative soil moisture anomalies compared to the 2 prior years in the Raam and Twente. The decrease in soil moisture proceeded into deeper layers with time as a consequence of root water uptake shifting predominantly to those layers. Subsequently, ET decreased, which is in line with the low 2018 GPP proxies SIF, NIRv, and VOD obtained via satellites throughout the growing season. Root water uptake was observed to shift to deeper layers after the first reduction in NIRv and VOD, indicating that changing root water uptake patterns can help to reduce drought impact but not to avoid it in the case of the drought of 2018. Soil moisture, ET, and GPP remained low until the end of summer.

Using a novel approach, the critical soil moisture content ($\theta_{critical}$) was derived from NIRv and VOD anomalies and soil moisture measurements at multiple depths. This non-linear relation reflects the observation that negative soil moisture anomalies develop 2–3 weeks before the first reduction in vegetation indices. The critical soil moisture content in the Raam network at 40 cm depth is found to be 0.19 and in the Twente network 0.22 (m^3_{water} m^{-3}_{soil}). The apparent critical soil moisture content increased with depth and this relationship was shown to be linear. The critical soil moisture content can serve as an indicator to mark the transition between non-stressed and stressed conditions to examine the impact on the gross primary productivity of vegetation and effect on the carbon cycle in models during droughts.

4

The role of model resolution during seasonal hydrological extremes

This chapter is based on:

Buitink, J., Uijlenhoet, R., and Teuling, A. J. (2019). Evaluating seasonal hydrological extremes in mesoscale (pre-)Alpine basins at coarse 0.5° and fine hyperresolution, *Hydrology and Earth System Sciences*, 23, 1593–1609, doi:10.5194/hess-23-1593-2019.

Hydrological models are being applied for impact assessment across a wide range of resolutions. In this study, we quantify the effect of model resolution on the simulated hydrological response in five mesoscale basins in the Swiss Alps using the distributed hydrological model Spatial Processes in Hydrology (SPHY). We introduce a new metric to compare a range of values resulting from a distributed model with a single value: the density-weighted distance (DWD). Model simulations are performed at two different spatial resolutions, matching common practices in hydrology: 500 m×500 m matching regional-scale models, and 40 km×40 km matching global-scale modelling. We investigate both the intra-basin response in seasonal streamflow and evapotranspiration from the high-resolution model, as the difference induced by the two different spatial resolutions, with a focus on four seasonal extremes, selected based on temperature and precipitation. Results from the high-resolution model show that the intra-basin response covers a surprisingly large range of anomalies, and show that it is not uncommon to have both extreme positive and negative flux anomalies occurring simultaneously within a catchment. The intra-basin response was grouped by land cover, where different dominant runoff-generating processes are driving the differences between these groups. The low-resolution model failed to capture the diverse and contrasting response from the high-resolution model, since neither the complex topography nor land cover classes were properly represented. DWD values show that, locally, the hydrological response simulated with a high-resolution model can be a lot more extreme than a low-resolution model might indicate, which has important implications for global or continental scale assessments carried out at coarse grids of 0.5°×0.5° or 0.25°×0.25° resolution.

"Make that choice to be okay
There's nothin' to it when you're makin' it rain"

—Two Door Cinema Club, *Talk* (2019)

4.1 | Introduction

In current distributed hydrological modelling, we identify two approaches at opposite ends of the scale of application. On the one hand studies are performed at global scale, and on the other hand studies are performed at regional or basin scales. The modelling approach generally affects the choice of spatial resolution, one of the key modelling decisions in hydrological modelling (Melsen et al., 2019). Most global studies are run at rather coarse spatial resolutions (often at 0.5°×0.5°) to investigate trends in the terrestrial water cycle as result of recent and projected changes in climate conditions (e.g., Luterbacher et al., 2004; Sánchez et al., 2004; Barnett et al., 2005; Beniston et al., 2007; Sheffield & Wood, 2008; Adam et al., 2009; Sheffield et al., 2012; van Huijgevoort et al., 2014; Jacob et al., 2014). These studies often rely on standardised values such as the standardised precipitation index (SPI) or standardised runoff index (SRI) in order to quantify differences between different climatic regions across the globe. Although recent global hydrological models are slowly shifting from relatively coarse resolutions to very fine resolution ("hyperresolution", ~1 km×1 km), this is not yet the state of the art (Wood et al., 2011; Bierkens, 2015; Bierkens et al., 2015). It is known that global simulations at high resolution improve predictions at small local scales (Bierkens et al., 2015). However, these global studies are limited by a lack of input data at hyperresolution or a lack of computational power (Beven & Cloke, 2012; Beven et al., 2015; Melsen et al., 2016b). As a result, most of the global studies are still performed at a relatively coarse resolution. Even when global modelling at hyperresolution becomes state of the art, the question remains as to how we should deal with simulations at these fine spatial scales, since the models parameterisations are developed on a coarser scale (Clark et al., 2017; Peters-Lidard et al., 2017).

Another type of hydrological study are those at basin or regional scales. These studies mostly use distributed hydrological models to simulate the hydrological response under climate change or climatic extremes (e.g., Middelkoop et al., 2001; Hurkmans et al., 2009; Driessen et al., 2010; Hurkmans et al., 2010; Wong et al., 2011; Immerzeel et al., 2012). Typical resolutions for these studies are similar to the previously mentioned hyperresolution or even finer. Since these studies have a narrower spatial focus than the global

simulations, high-resolution data are often more easily accessible and the computational power is less of a limiting factor. Since it is typically assumed that there is no important discrepancy between dynamics at the local scale and those at larger scale, results are often not standardised.

Both global and regional studies focus on reaching similar goals, yet with different methodologies. So far, no study has investigated how these two methodologies connect and how the modelling approach affects the results. The effect of model resolution on the simulated response has been investigated by numerous studies, either for regional climate models or for hydrological models (e.g., Haddeland et al., 2002; Leung & Qian, 2003; Carpenter & Georgakakos, 2006; Gao et al., 2006; Lucas-Picher et al., 2012; Pryor et al., 2012; Lobligeois et al., 2014; Kumar et al., 2016; Melsen et al., 2016a). The majority of these studies agree that an increased resolution leads to more realistic model results, as small-scale variability is better represented. However, no study has investigated how anomalies in the simulated hydrological response depend on the modelling approach, or what the distribution of these anomalies within complex basins looks like.

In this study, we aim to bridge the large-scale (climatological) and regional-scale (hydrological) approaches by quantifying how the simulated hydrological response depends on spatial resolution, including within-basin complexity. Despite the large body of literature addressing the problem of scaling in hydrology (e.g., Klemeš, 1983; Dooge, 1986, 1988; Blöschl & Sivapalan, 1995; Feddes, 1995; Kalma & Sivapalan, 1995; Bierkens et al., 2000; Beven, 2001; Blöschl, 2001; Sivapalan et al., 2004; McDonnell et al., 2007; Sposito, 2008), a limited number of tools to quantify this problem are proposed. Our study presents a new metric to quantify the difference between a range of values with a single value: the density-weighted distance (DWD). We use the recently developed Spatial Processes in Hydrology (SPHY) model to simulate five basins in the Swiss Alps, a region which is know for large variations in land cover and elevation (Gurtz et al., 2003; Verbunt et al., 2003; Jolly et al., 2005; Schaefli et al., 2007; Zappa & Kan, 2007; Bavay et al., 2013; Speich et al., 2015). Each basin is simulated at two resolutions: a typical resolution for regional-scale models (~500 m$\times$500 m, also matching hyperresolution), and a typical resolution for global scale models (~40 km$\times$40 km, matching a 0.5°$\times$0.5°

pixel). Model results from both resolutions are compared and differences are quantified using the DWD metric. Since many hydrological processes are nonlinear or depend on thresholds, we expect that the modelling approach can greatly affect the model results. These nonlinearities and thresholds imply that a small change in input data or initial conditions can lead to relatively large changes in hydrological response. When scaling over homogeneous catchments, the resulting nonlinear behaviour is typically preserved. However, when scaled over heterogeneous catchments, the resulting hydrological behaviour might not be trivial. For example, Blöschl et al. (2013b) investigated the 2013 flood of the Danube river caused by extremely heavy precipitation. They found that the discharge peak could have been higher, since not all precipitation fell as rain. In parts of the catchment that were high enough for the temperature to stay below 0°C, a fraction of precipitation fell as snow and did not directly contribute to the discharge. Teuling et al. (2013) showed that evaporation increased during droughts, based on data from several headwater catchments in Europe. This was explained by the lack of rainfall coinciding with reduced cloud cover and increasing net radiation, which out-weighted the effect of lower soil moisture conditions. Jolly et al. (2005) studied how vegetation responded to the extreme summer of 2003 in the Swiss Alps. They found that vegetation response was not homogeneous, but showed different responses depending on the elevation zone. Finally, catchments in the Swiss Alps are known to show complex behaviour due to the non-trivial response of snow and glaciers to extreme events (Verbunt et al., 2003; Zappa & Kan, 2007; van Tiel et al., 2018). These examples indicate the complexity of the hydrological response and the variability in time and space in these regions. Therefore, we hypothesise that the spatial resolution will play an important role in the simulated response, since many hydrological processes during extremes are inherently nonlinear combined with the fact that most of the variability occurs at scales smaller than the spatial resolution of global hydrological models.

Table 4.1 | Statistics for each catchment (FOEN, 2016).

Main river basin	Reuss	Rhone	Inn	Emme	Thur
FOEN station ID	2056	2346	2403	2155	2181
Name outlet station	Seedorf	Brig	Cinuos-chel	Wiler	Halden
Outlet elevation (m a.s.l.)	438	667	1680	458	456
Surface area (km^2)	832	913	736	940	1085
Mean elevation (m a.s.l.)	2010	2370	2467	860	910
Glaciation (%)	9.5	24.2	8.5	0.0	0.01
Mean annual precipitation (mm)	1729	1339	1501	1745	1084

4.2 | Methods, model and data

4.2.1 | Basins

For this study, we selected five mesoscale basins in the Swiss Alps. Not only is the response of these basins relevant at regional scale, these basins also contribute considerable amounts to large rivers in Europe. For example, the discharge of the Rhine consisted of almost 40% meltwater from the Swiss Alps during the warm and dry summer of 2003 (Wolf et al., 1999; Stahl et al., 2016). While not all basins are tributaries to the Rhine, they nonetheless provide important insight into our understanding of the behaviour of mountainous catchments. The basins for our study were selected based on size (roughly corresponding to the $0.5° \times 0.5°$ pixel size), elevation range, land cover, data availability and minimal human influence (as the model simulates the basins without reservoirs). Figure 4.1 shows the locations and digital elevation models of all catchments. Please note that the entire river basin is not always chosen; see Table 4.1 for the names, station identifiers used by Swiss Federal Office of the Environment (FOEN) and other characteristics. Two basin categories can be distinguished: high-elevation catchments with glaciers (Reuss, Rhone and Inn) and lower-elevation catchments without glaciers (Emme and Thur). We will refer to those basin categories as Alpine and pre-Alpine, respectively.

4.2.2 | Data

The model is forced with daily precipitation and temperature from MeteoSwiss (MeteoSwiss, 2013, 2016). All forcing data are provided at a resolution

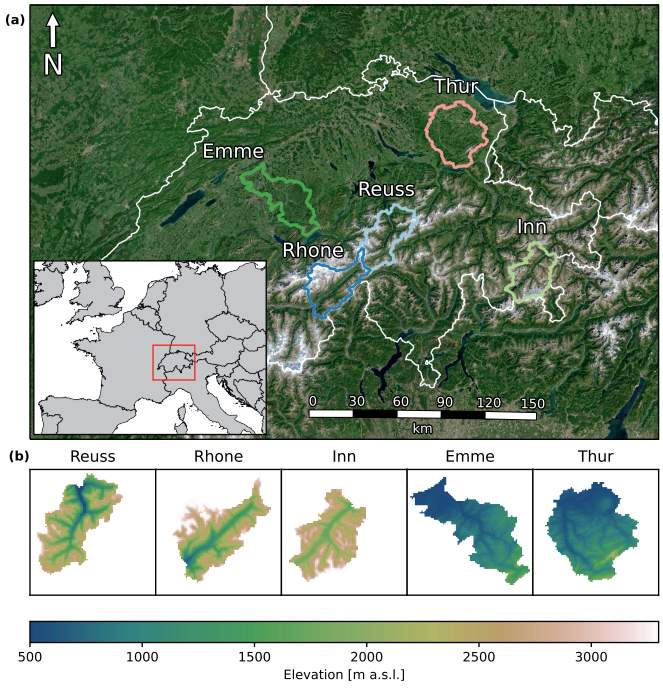

Figure 4.1 | Overview of the location (**a**) and elevation (**b**) of the five basins used in this study. Names of the main river basin are plotted above the catchment border in panel **a**. Each box in panel **b** corresponds to an area of ~40 km×40 km.

of approximately 2 km×2 km. We focus on the period from 1993 to 2014, and selected four seasons with unusual precipitation and/or temperature values (winter of 1995, spring of 2007, summer of 2003 and autumn of 2002; see Section 4.3.1 for more details). Land cover data were obtained from WSL (2016) and grouped into four classes: forest, grass, glacier and other. The latter class combines all sparse vegetation types, bare soil and rocks. Discharge observations are obtained from FOEN (2016). Catchment elevation, delineation and stream network are derived from the digital elevation model of Jarvis et al. (2008).

4.2.3 | Hydrological model

The SPHY model was used to simulate each basin at both resolutions. SPHY is a spatially distributed conceptual hydrological model, including representations of rainfall–runoff, cryosphere, evapotranspiration and soil moisture processes, as well as their nonlinearities and thresholds (Terink et al., 2015). The model runs on a daily time step and a user-defined spatial resolution. Subgrid variability is taken into account via cell fractions, but only for snow and glacier fractions. SPHY has been applied in several studies around the globe, yet the study area of most studies are situated in the Himalayas (Lutz et al., 2013, 2014; Terink et al., 2015; Lutz et al., 2016; Hunink et al., 2017; Wijngaard et al., 2017; Terink et al., 2018). A schematic overview of the model concept is presented in Figure 4.2. Based on the daily average temperature, SPHY determines whether precipitation will fall as snow or rain. The liquid precipitation will fall on the land surface, where part of the water can be directed to the river as surface runoff, depending on the volume of water already present in the root zone. The remainder infiltrates into the root zone, where it is subject to evapotranspiration based on the type of land cover. Water in the root zone can either percolate to the subzone, or be transported to the river network as lateral flow. From the subzone, water can either move upward into the root zone as result of capillary rise, or can percolate to the groundwater layer. Water in the groundwater layer will contribute to the river discharge as baseflow. Solid precipitation is added to the snow storage, where melting of snow is diverted to the stream network as snow runoff. Finally, part of the grid cell can consist of glaciers. A fraction of the melted ice is added to the groundwater storage, and another fraction is transported to the river as glacier runoff. The glaciers in SPHY are fixed in space and time, so glaciers cannot extend and retreat. More information about the model structure and parameterisations are provided by Terink et al. (2015).

4.2.4 | Model setup and calibration

SPHY was applied to each basin at two different resolutions: at ~500 m$\times$500 m (corresponding to the regional-scale resolution, and hyperresolution), and at ~40 km$\times$40 km (corresponding to the global scale resolution of 0.5°$\times$0.5°). This latter resolution implies that each basin

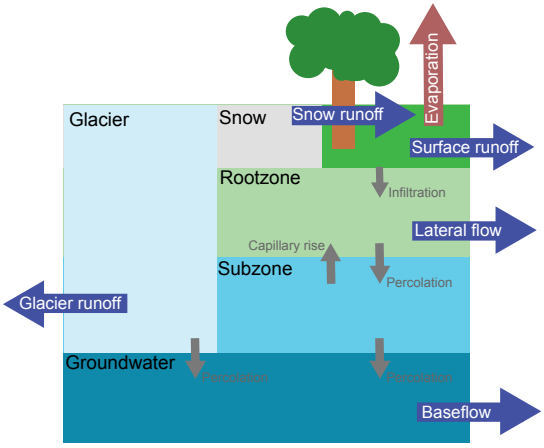

Figure 4.2 | Schematic overview of the conceptualisation in SPHY. Blue arrows represent fluxes contributing to total runoff generated in each model cell and small grey arrows represent fluxes between the different reservoirs. Overview is based on the more detailed concept by Terink et al. (2015).

was simulated as a single pixel. All input data were resampled to match the spatial resolution of the hydrological model. For the high-resolution model we used bilinear interpolation to resample the forcing data for the high-resolution model, and we averaged all cells within the 40 km$\times$40 km pixel for the low-resolution model. SPHY was calibrated individually for both resolutions and all basins using the L-BFGS-B algorithm (Zhu et al., 1997), by minimising the sum of squares of the residuals between monthly simulated and observed discharge. SPHY was calibrated over a period of 5 years (1997-2001), where the preceding year was used as spin-up period. These years were chosen to include both a relatively wet year (1999) and two relatively dry years (1997 and 1998). Four parameters were selected for calibration, all of which were found to influence the monthly discharge: root zone depth, degree-day factor for snow melt, a parameter determining the fraction of water that can refreeze in the snow pack, and the critical temperature describing the point where precipitation falls as snow. Since

the L-BFGS-B algorithm is highly sensitive to the initial parameter guess, 10 different starting parameters sets were generated using Latin hypercube sampling to cover the parameter space (McKay et al., 1979). The calibration resulted in 10 new parameter sets per region and model type, and we selected the parameter set with the highest Kling–Gupta efficiency (Gupta et al., 2009). Using this parameter set, SPHY was run from 1993 to 2014, where the first year was used as a spin-up period, resulting in 21 years of data used for analysis.

4.2.5 | Anomalies and metrics

In this study, we only focus on the runoff and actual evaporation responses. We averaged all model output over 3 months, grouping the hydrological response according to season: December, January and February for winter (DJF); March, April and May for spring (MAM); June, July and August for summer (JJA); and September, October and November for autumn (SON). Standardised anomalies are used to quantify the magnitude of the deviation within each season and are calculated for each individual model cell, using the following equation:

$$Z_{xi}^{S} = \frac{x_i^S - \mu_x^S}{\sigma_x^S}, \tag{4.1}$$

where Z_{xi}^{S} is the dimensionless standardised anomaly of variable x for year i in season S, x_i^S is the value of variable x for year i in season S, μ_x^S is the mean of variable x in season S, and σ_x^S is the standard deviation of x based on the same period. We note that most often climatologies are calculated based on time series of 30 years or more. We were not able to generate 30 years of data, because we only had sufficient data for the period 1993–2014. Since the focus of this chapter is not on the absolute values, but on the patterns and relations, we do not expect different conclusions when longer time series would have been used.

Since the goal of this chapter is to compare results from a high-resolution model with results from a low-resolution model, we require a suitable metric to quantitatively evaluate the difference between those results. Based on the previously discussed methodology, the high-resolution model outputs a distribution of values, which needs to be evaluated against a single

value from the low-resolution model. Ideally, the metric provides robust information regardless of the shape of the distribution of the results from the high-resolution model. A common option would be to calculate the percentile score of the low-resolution model result within the high-resolution model results. However, the percentile score does not provide information about the size of the error between the high- and low-resolution models. Another option would be the root mean square error (RMSE). The RMSE can be rewritten in terms of mean and variance, resulting in the following equation:

$$\text{RMSE} = \sqrt{\sigma^2 + (\mu - Z_{\text{low\_res}})^2}, \tag{4.2}$$

where σ^2 and μ are the variance and mean of the (normalised) high-resolution model results and $Z_{\text{low\_res}}$ is the low-resolution model result. However, when working with skewed or bimodal data (as visible in Figure 4.10), the mean and variance are not sensible measures to describe the distribution of values.

Therefore we propose a new metric, which provides a measure of the distance between a single point and a distribution of values, regardless of the shape of the distribution. This metric includes information not only on the difference in mean or median, but also on the width of the underlying distribution that the single value tries to represent. We call this new metric the density-weighted distance. DWD measures the distance between a single point and a range of values, weighted by the density of data that are present between the single point and the extent of the range of values. The extent is measured using the 5−95% range to exclude the outliers, and the distances between the single point and the minimum and maximum extent are multiplied by the percentile of data within this distance. DWD is defined as follows:

$$DWD = W_{\text{lower}} \cdot d_{\text{lower}} + W_{\text{upper}} \cdot d_{\text{upper}}, \tag{4.3}$$

$$W_{\text{lower}} = \max\left(0, \min\left(1, \frac{P_{\text{low\_res}} - P_{\text{lower}}}{P_{\text{upper}} - P_{\text{lower}}}\right)\right), \tag{4.4}$$

$$W_{\text{upper}} = \max\left(0, \min\left(1, \frac{P_{\text{upper}} - P_{\text{low\_res}}}{P_{\text{upper}} - P_{\text{lower}}}\right)\right), \tag{4.5}$$

$$d_{\text{lower}} = Z_{\text{low\_res}} - Z^{5\%}_{\text{high\_res}}, \tag{4.6}$$

$$d_{\text{upper}} = Z^{95\%}_{\text{high\_res}} - Z_{\text{low\_res}}, \tag{4.7}$$

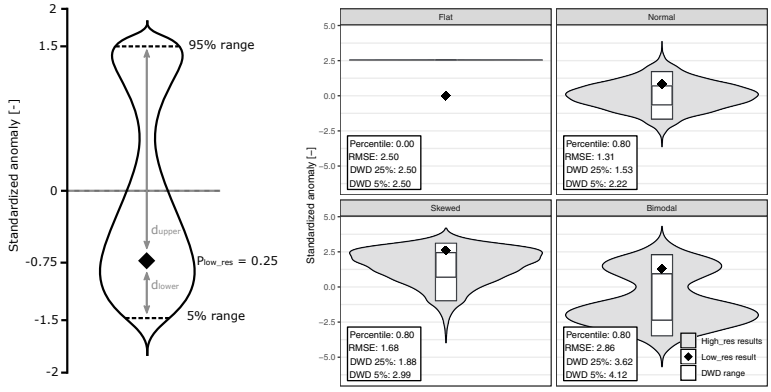

(a) (b)

Figure 4.3 | The concept behind density-weighted distance (**a**) and comparison between different metrics (**b**). Substituting the values from panel **a** into Equation (4.3) gives the following result: DWD ≈ 1.92. The violin plots in panel **b** represent the distribution of the high-resolution model results and the diamond the single low-resolution data point. The large box in panel **b** represents the 5–95% data range, and the smallest box the 25–75% data range.

where W_{lower} and W_{upper} are the weights used to weigh the distances d_{lower} and d_{upper}. $P_{\text{low\_res}}$ is the percentile of $Z_{\text{low\_res}}$ within $Z_{\text{high\_res}}$. Both weights are corrected for the selected extent of the data (P_{lower} and P_{upper}, default to 5% and 95%), and corrected between 0 and 1 if the $P_{\text{low\_res}}$ is outside the selected extent. The DWD concept is visualised in Figure 4.3a. A property of this formulation is that high DWD values can mean two things: either that the low-resolution model result is outside the range of values simulated with the high-resolution model, or that the high-resolution model results have high internal variability. This metric is aimed to measure the latter. We advise to always interpret DWD results together with the violin plots, to more easily identify cases where the low-resolution model result is outside the range of the results from the high-resolution model .

The DWD can be interpreted as the difference in terms of number of standardised anomalies. DWD is zero when the high-resolution data have zero

variability, and when the difference with the low-resolution model results is also zero. If the high resolution data have zero variability, but the result from the low-resolution model is outside of this range, DWD will give the distance between the low- and high-resolution data, measured in the number of standardised anomalies (see the "Flat" subplot in Figure 4.3b.).

In order to illustrate the concept behind DWD and compare it to the previously mentioned metrics, Figure 4.3b shows the different metrics using four synthetic example. The example with the "Flat" distribution assumes no variability in the high-resolution model results. As a consequence, the violin plot is a horizontal line. Since there is no variability in the high-resolution model results, RMSE and DWD give the same values. The percentile value is equal to zero, since the low-resolution model result is outside of the high-resolution model results. The three other examples in Figure 4.3b illustrate that the percentile score does not give sufficient information to draw conclusions about the performance of the low-resolution model, since they all received the same percentile score. The RMSE is able to catch the differences between the last two cases, but it does not accurately display the distance between the range of data from the high-resolution model and the single point from the low-resolution model. Furthermore, when working with skewed or bimodel data, the mean and variance are not the best indicators for the distribution of values. In contrast, DWD combines the spread of the high-resolution results with the density of data points, resulting in a more sensible measure when dealing with skewed or bimodal data. We also compared the effect of selecting a different data range: 25–75% instead of 5–95%. We conclude that this mostly influences results in terms of absolute size, but does not alter the relative differences much. We expect that when using the 25–75% range, low-resolution model results will be more often outside of this range than when using the 5–95% range. Furthermore, we assume that all grid cells in the high-resolution model are equally important and will therefore use the largest data range to calculate the DWD, only excluding the outer 10% to remove any undesired behaviour resulting from outliers.

4.3 | Results and discussion

4.3.1 | High-resolution simulations

The key focus of this work is the catchment response to extreme seasons. To identify those extreme seasons, standardised precipitation and temperature anomalies are calculated for each season and basin (see Figure 4.4). Since patterns are similar across the two catchment types, the results of only two basins are shown in this figure. It should be noted that due to averaging values over 3 months, it is very likely that extreme events with a shorter duration are averaged out in this 3-monthly time step.

The highlighted dots in Figure 4.4 show the extreme seasons selected for this study, for which the hydrological response is analysed. The seasons were selected based on unusual precipitation and/or temperature values: winter of 1994–1995, spring of 2007, summer of 2003, autumn of 2002. Brönnimann et al. (2007) and MeteoSwiss (2017) both mention the high temperature during the spring of 2007 in Switzerland. The extremely warm and dry summer of 2003 is known to be the most extreme summer in at least the last 500 years (Luterbacher et al., 2004; Zappa & Kan, 2007; Seneviratne et al., 2012). The extremely heavy precipitation during November 2002 caused mudflows in eastern Switzerland (Schmidli & Frei, 2005). No literature reference was found for the unusually wet winter of 1994–1995.

The colours of the circles indicate the discharge anomalies. Discharge anomalies in the pre-Alpine basin seem to follow a distinct pattern, where high precipitation values often coincide with high positive discharge anomalies, and vice versa. Temperature also seems to influence discharge anomalies in the pre-Alpine basin, but this relation is less evident. The Alpine basin shows a much more random pattern, without any clear relation between temperature and/or precipitation. This indicates that the runoff-generating processes are not consistently driven by either precipitation or temperature, but by a combination of both.

The calibration results for each basin are presented in Figure 4.5a. This figure shows high Kling–Gupta efficiencies for all basins, indicating good model performance. In all basins, the high-resolution model shows higher KGE val-

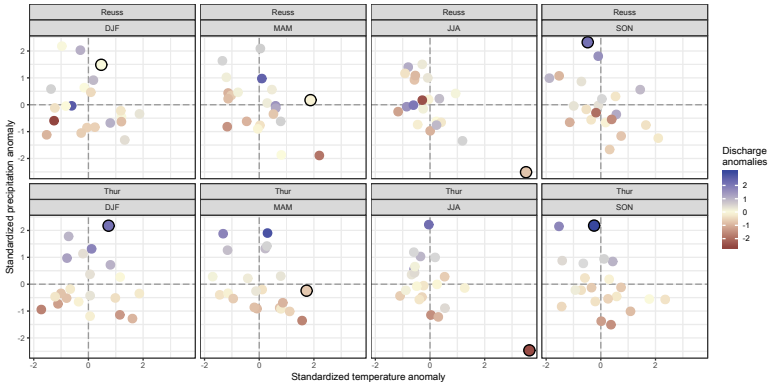

Figure 4.4 | Relation between climate anomalies and observed discharge anomalies. Each dot represents a single season and is coloured with the corresponding standardised observed discharge anomaly. Dots with a black outline represent the selected extreme seasons (winter of 1995, spring of 2007, summer of 2003 and autumn of 2002).

ues than the low-resolution model, yet the values for the low-resolution model still show relatively good performance. Only the winter discharge in the Alpine basins is underestimated by the model, at both resolutions. Discharge observations show an almost constant outflow during winter, which is most likely the result of human interference (reservoirs) (Fatichi et al., 2015). SPHY is not able to simulate this constant outflow and simulates discharge values close to zero. As a means of validating the model, we presented the spread (monthly standard deviation) around the monthly average discharge in Figure 4.5b, excluding the years used for calibration. The high-resolution model again shows better values than the low-resolution model, and the spread around the mean matches better than the low-resolution model. Overall, the low-resolution model is able to accurately simulate these basins, yet the lack of spatial variability ensures that the high-resolution model is able to reach better performance.

Hydrological response maps for the two main hydrological fluxes (actual evapotranspiration, ET, and generated runoff) during each extreme season are presented in Figure 4.6. Grid cells are coloured by their cell-specific stand-

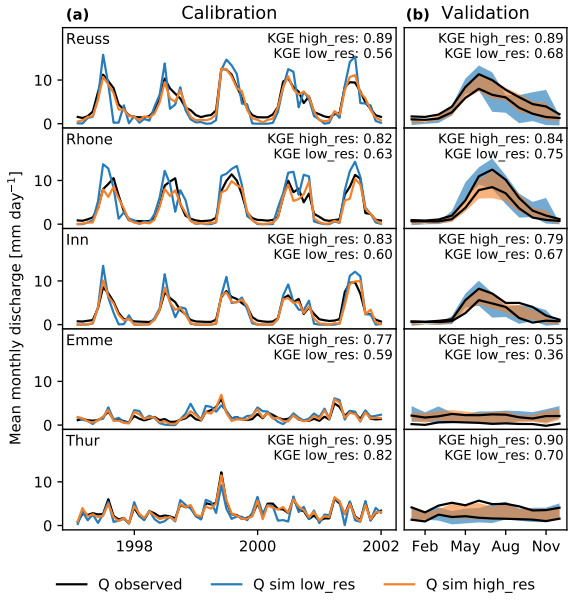

Figure 4.5 | Discharge observations compared with discharge simulations for (**a**) the calibration period and (**b**) validation based on the monthly average discharge. In the top right corner of each subplot in panel **a** the Kling–Gupta efficiency (KGE) is presented. The range in panel **b** is plotted as the standard deviation around the mean monthly discharge, where the black lines indicate the lower and upper (mean ± standard deviation) observed monthly discharge. Kling–Gupta efficiencies in these subplots are calculated over the entire simulation period, excluding the calibration years.

ardised anomalies. ET anomaly maps are only shown for spring and summer periods, when this flux is most important. During the two other seasons, large parts of the basins are covered with snow, where the model assumes no ET to occur. The same maps on a monthly time step can be found in Appendix A. To validate how well these values represent the actual hydrological response, we compared the output from the high-resolution model with observations from the research catchment Rietholzbach, situated within the

Table 4.2 | Comparison between anomalies simulated with SPHY and observed anomalies in the Rietholzbach, anomalies are based on the entire simulation period. Winter and autumn values for evaporation are in italic type, since they are not the focus of this study due to the fact that SPHY does not allow for evaporation during snow-covered periods.

Event	Runoff		Evaporation	
	Observed	Simulated	Observed	Simulated
DJF 1995	1.68	2.34	*0.86*	*0.53*
MAM 2007	-0.52	-0.27	1.61	0.98
JJA 2003	-2.15	-2.17	1.66	3.61
SON 2002	2.65	2.62	*-1.76*	*-0.26*

Thur basin (see the black dot in Figure 4.6). Evaporation observations were obtained from a long-term research lysimeter, and runoff was obtained from discharge observations from this catchment (Seneviratne et al., 2012). Both discharge and evaporation from the corresponding pixel were extracted from SPHY, to compare with the observations. We calculated the anomalies over the entire simulation period. The comparison between the observed and simulated anomalies can be found in Table 4.2. This table shows that the simulated anomalies agree well with the direction and magnitude of the observed anomalies. Winter and autumn values for evaporation are in italics, since they are not the focus of this study due to the fact that SPHY does not allow for evaporation during snow-covered periods. There is a slight mismatch between the evaporation anomalies during the summer of 2003, yet both describe unusually high values. This mismatch can be attributed to the scale difference between the lysimeter and a single high resolution SPHY pixel, and the fact that SPHY does not account for all factors influencing evaporation since it uses the temperature-based Hargreaves method.

In Figure 4.6, all basins show roughly the same ET response to the warm spring conditions in 2007. In the areas with a standardised anomaly of exactly zero, no evapotranspiration was simulated since the cells were covered with snow. Cells close to this region show a particularly high standardised anomaly. These cells are free of snow only for a limited time during spring, distorting the mean and standard deviation used to calculate the standardised anomaly. A more complex response is visible during the extremely warm

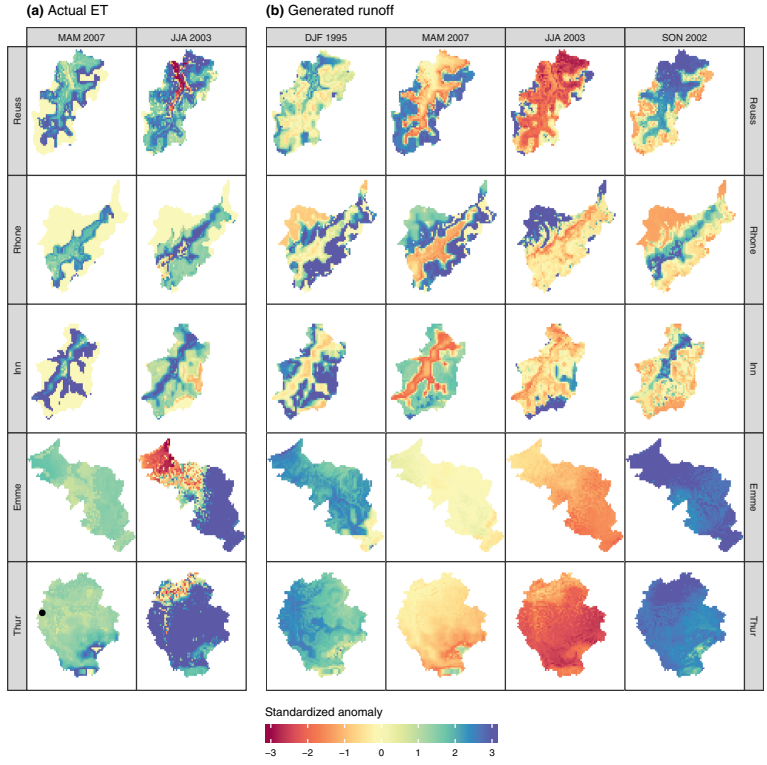

Figure 4.6 | Spatial distribution of anomalies of actual evapotranspiration (**a**) and generated runoff (**b**) during the four extreme seasons, for all basins. The location of each catchment can be found in Figure 4.1. Each box represents a size of ~40 km×40 km. The black dot in the Thur basin represents the location of the Rietholzbach research catchment.

and dry summer of 2003. In three basins, cells at low elevations show a different anomaly sign than the cells at medium to high elevations. In the entire region, higher temperatures increased the potential evapotranspiration, yet cells with a negative anomaly evaporated less water than normal. This indicates that those cells became water-limited during the course of the summer

and could no longer meet the potential ET. Cells at high elevations were able to meet the increased potential ET and evaporated a lot more water than normal. This lead to a situation in which both negative and positive anomalies are present within the same basin, even at seasonal timescale and in response to a rather homogeneous distribution of temperature anomalies. Only the Rhone and Inn basins did not show this behaviour, indicating that the low-elevation cells did not become water-limited over the course of this summer.

Anomalies in the generated runoff also show a contrasting within-basin response, in particular in the Alpine basins. Here, cells with low elevations show a different anomaly than the cells at high elevations. This dependency between anomaly and elevation is not visible in the pre-Alpine basins, where all model cells show roughly the same response. The cause of this difference between the two basin types will be further investigated below in Figure 4.8. Previously, we mentioned that the unusually wet autumn of 2002 was mainly due to a period with unusually high precipitation in November. The anomalies of the other seasons were mainly caused by a succession of multiple months with unusual temperature and/or precipitation values, so we chose to use a consistent time scale of three months throughout the chapter. We also analysed the hydrological response on a monthly timescale, but concluded that the response maps for November 2002 were not too different from the response maps for the autumn of 2002 (see Supplement).

The spatial variability (as expressed by the standard deviation, σ) of both fluxes is plotted against the average forcing for all seasons in Figure 4.7. Here the standard deviation is used as a measure of complexity, with large σ values indicating a highly spatially variable and thus complex hydrological response. This figure gives insight into how the response complexity varies with basin average forcing. The precipitation–evapotranspiration plot was excluded since the graph consisted of random scatter, without a clear relation.

Spread in the actual evapotranspiration response seems related to temperature (Figure 4.7a), where higher temperatures result in larger ET standard deviations. As mentioned earlier, potential evapotranspiration will increase

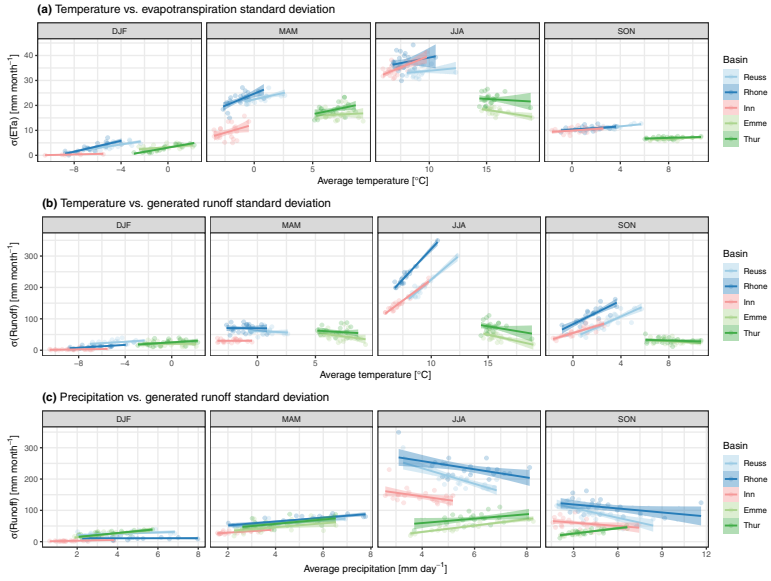

Figure 4.7 | Relation between spatial standard deviation (σ) of simulated hydrological response and basin-averaged weather conditions: temperature versus evapotranspiration σ (**a**), temperature versus runoff σ (**b**), precipitation versus runoff σ (**c**). Each point represents a single season in the 1994–2014 period. A linear regression through these points is represented as a solid line, with the shaded area indicating the 95% uncertainty range.

with higher temperatures, but so does the number of water-stressed cells. This combination increases the spatial σ for evapotranspiration and is visible in almost all basins and seasons.

Standard deviation of generated runoff seems most sensitive to temperature during summer and autumn; see Figure 4.7b. The two catchment types show a different response: the runoff σ increases with temperature in the Alpine basins, while runoff σ decreases with temperature in the pre-Alpine basins. The cause for this difference is the presence of glaciers: glacier melt will increase with higher temperatures, while regions without glaciers will

evaporate more. This contrast results in an increasing σ with temperature in the Alpine basins, and in a decreasing σ with temperature in the pre-Alpine basins. Please note that the average temperatures in both catchment types show hardly any overlap, making it difficult to identify how the basins would respond to the same temperature values.

The influence of average precipitation on the runoff σ seems smaller (Figure 4.7c). However, in the simulation period we selected, there is a correlation between temperature and precipitation. During winter, only the pre-Alpine basins show a response in runoff σ to precipitation. The lack of response in the Alpine basins is related to temperature: the average winter temperatures in these basins hardly reaches values above 0°C, where precipitation will fall as snow and does not directly contribute to runoff. A more pronounced relation between precipitation and runoff σ is visible in summer and autumn, where σ in the Alpine basins decreases with increasing precipitation and vice versa in the pre-Alpine basins. However, the Alpine regression lines are strongly influenced by the extremely warm and dry summer of 2003: without this season, the regression lines would have been much more horizontal. Since there is only one season this extreme in the 21 years of simulations, it remains difficult to separate the effects induced by temperature or by precipitation. The autumn period shows a similar response to that of the summer months, but the relation with temperature needs to be taken into account again. As is visible in Figure 4.4, seasons with unusually high precipitation are often related to lower temperatures, while seasons with less precipitation are often paired with higher temperatures, independent of the basin. This could indicate that the relation between precipitation and runoff σ might be the inverse of the temperature–runoff σ relation.

To gain a better understanding of the hydrological behaviour within each basin, the standardised anomalies of each individual grid cell are plotted against elevation in Figure 4.8. We again only show results for one basin of each catchment type, since the response patterns were similar across the different basins. The forcing anomalies show very little spread: the 95% confidence interval is almost always thinner than the plotted line, making it barely visible. Spread in runoff anomalies is bigger than the spread in forcing anomalies in both catchment types, making it impossible to explain the hy-

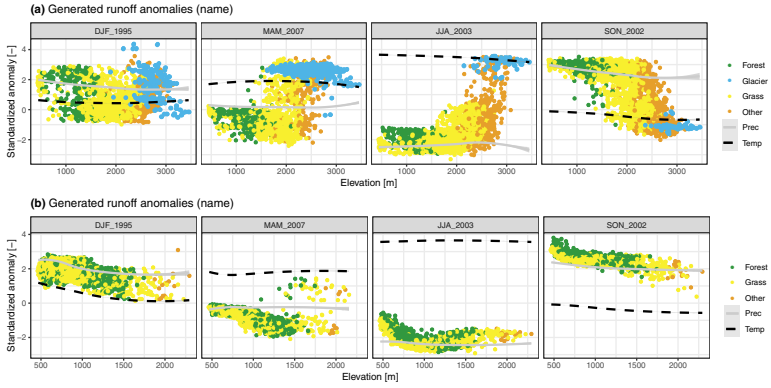

Figure 4.8 | Relation between elevation and hydrological response coloured by land cover type, presented for the Reuss (**a**) and Thur (**b**) basins. Each point represents the standardised anomaly for a single model cell, based on the data in Figure 4.6. The solid and dotted lines show the smoothed precipitation and temperature anomalies, with the shaded area showing the 5–95% data range. Land cover type "other" represents all sparse and bare vegetation types.

drological response solely by the forcing anomalies. Each dot in Figure 4.8 is coloured by land cover. Land cover shows a clear correlation with elevation, most visibly in the Alpine basin. The pre-Alpine basins did not contain any glacier cells and only a limited number of sparse or bare cells. This is explained by their more limited elevation range compared to the Alpine basins (see Figure 4.1b).

The hydrological responses can be grouped according to land cover class: "forest" and "glaciers" nearly always show a different response within the same basin and season, where "grass" and "other" are covering a gradual transition between the two groups. This grouping can be explained by the runoff-generating processes. Areas at high elevation generate runoff by melting ice and snow (if present), while areas at low altitudes rely on root zone and/or groundwater processes. The latter are mostly driven by the amount of available water (water-limited), while runoff from ice and snow is mostly dependent on the incoming energy (energy-limited). This dependency is most visible

in Figure 4.8a, where the hydrological anomalies at lower elevations coincide with the sign and size of the precipitation anomaly, while hydrological response shifts towards the temperature anomaly at higher elevations. Due to the insufficient "other" and "glacier" cells in the pre-Alpine basin, this relation is not as evident as in the Alpine basin. In the pre-Alpine basin, runoff anomalies seem to follow precipitation anomalies, indicating that the runoff-generating processes are mostly driven by available water (Figure 4.8b). This grouping of different responses matches with different zones defined by Theurillat & Guisan (2001): colline, < 700 m; montane, 700–1400 m; subalpine, 1400–2100 m; alpine, 2100–2800 m; nival, > 2800 m. These zones match with the different land cover classes defined in our study: the first class is not represented in basin Reuss, montane corresponds to the "forest" group, subalpine to the "grass" group, alpine and nival to the "other" and "glacier" groups. A study by Jolly et al. (2005) described that these zones could also be used to group vegetation responses to the extreme summer of 2003. Furthermore, Fatichi et al. (2015) showed that changes in discharge as result of climate change show a clear relation with elevation, where catchments with high average elevation are expected to see the biggest decrease in mean discharge, while catchments with low average elevation are expected to see a small increase in mean discharge. Our results combined with these studies indicate that elevation and thus vegetation cover are controlling the hydrological response to extreme seasons.

Our results may be influenced by characterisations defined within the model. For example, the limited evapotranspiration of snow-covered cells is a choice made by the developer of SPHY. One could argue whether this is realistic. Furthermore, the glaciers in SPHY are fixed in location and extent. The importance of dynamical glaciers is investigated by van Tiel et al. (2018) and they conclude that using a dynamical glacier module is most important for long-term studies. The simulation period of our study was rather short, and we therefore expect only minor differences in the location and extent of the glaciers over our time period. We do not expect any major different results and conclusions as result of those characterisations within SPHY.

4.3.2 | Impact of model resolution

With improved understanding of the hydrological response to extreme seasons when simulated at high resolution (matching the regional-scale studies), we can now compare those results to the model output when the basins are simulated on a $0.5° \times 0.5°$ resolution (matching the global-scale studies). Firstly, we compare how well the aggregated high resolution response corresponds with the low-resolution model, see Figure 4.9. All pixels within the high-resolution model are averaged and compared with the anomaly calculated for the low-resolution model. Ideally, the low-resolution model should match the aggregated high-resolution model response. This figure shows that generally both models simulate the same trend, yet the order of magnitude of the anomaly does not always match. The presented average difference represents the mean absolute difference between the high- and low-resolution model results. This value shows that the resolution difference generally causes a bigger disagreement in the Alpine basins than in the pre-Alpine basins. Overall, the runoff simulated with the low-resolution model matches the high-resolution model relatively well. This is in line with the conclusions from Kling & Gupta (2009), who stated that lumped models are able to reach similar runoff predictions to those of a distributed model. However, when investigating local responses, the prediction from the low-resolution model might not be representative.

Next, we compare how the range of values from the high-resolution model compare to the low-resolution model in Figure 4.10. In this figure, output from only two basins is shown since results were similar across basins of the same catchment type. High-resolution model responses are clearly not normally distributed, but have a bimodal or skewed distributions. Response of the pre-Alpine basin shows less variation than the Alpine basin, which was also visible in Figure 4.8. In all cases, the low-resolution model anomaly is within the high-resolution model anomaly range, but does not show a consistent position within this range. This figure makes it difficult to quantify the differences between the low- and high-resolution models.

For each hydrological flux, basin and extreme season, the DWD is calculated and presented in Table 4.3. This table shows that the runoff DWD in the Alpine

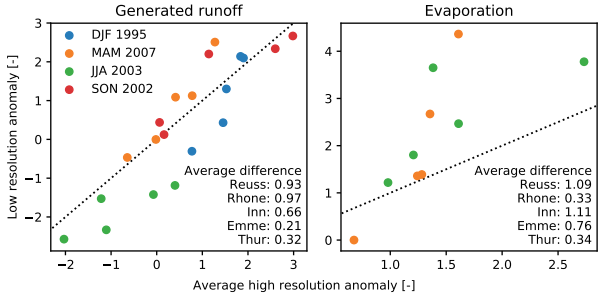

Figure 4.9 | Comparison between the average high-resolution model response and the low-resolution model response, for the generated runoff. Colours indicate the different extreme seasons, and the dotted line represents the 1:1 line.

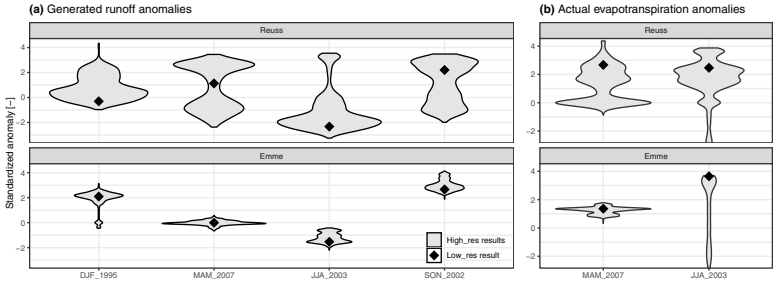

Figure 4.10 | Model response to extreme seasons for both generated runoff (**a**) and actual evapotranspiration (**b**), where violin plots represent the high-resolution model response and the diamond the low-resolution model response.

basins is generally higher than the DWD in the pre-Alpine basins (average Alpine DWD = 2.90 and average pre-Alpine DWD = 0.90). This is also visible in Figure 4.10, where the pre-Alpine runoff violin plots cover a smaller anomaly range than the Alpine violin plots. These averages indicate that the high-resolution model anomalies can deviate with 2.61 and 0.81 standardised anomalies from the low-resolution model anomaly in the Alpine and pre-Alpine basins, respectively. This illustrates that in these areas, the local hydrological

Table 4.3 | Scale mismatch between the high- and low-resolution models as measured by DWD, for both hydrological fluxes during the four extreme seasons.

Basin	**Total generated runoff**				**Actual ET**	
	DJF 1995	MAM 2007	JJA 2003	SON 2002	MAM 2007	JJA 2003
Reuss	2.63	2.31	4.81	2.58	2.44	3.70
Rhone	2.86	2.82	4.29	1.88	0.85	1.52
Inn	2.40	1.82	4.56	1.84	4.36	2.19
Emme	1.25	0.33	0.79	1.01	0.46	5.96
Thur	0.97	0.73	1.48	0.66	0.62	4.33

response can be a lot more extreme than the low-resolution model might indicate. This effect is largest in the Alpine basins, which can be explained by the wider range of elevation and land cover types.

The summer of 2003 in the Rhone basins shows a very high DWD value for the generated runoff. This is due to a combination of a relatively low percentile score (P = 0.18) and a large distance to the upper 95% anomaly (d_{upper} = 5.57). A very large portion of the high-resolution model values is close to the low-resolution model anomaly, implying that a small increase in low-resolution model anomaly would significantly increase the P_{low_res} values, which would reduce the emphasis on d_{upper}, decreasing the DWD value; see Figure 4.10b.

Another high DWD value is found for actual evapotranspiration during the summer of 2003 in the Emme basin (see Figure 4.10b). The high-resolution model results show a long tail towards negative anomalies, caused by model cells which are water-limited during this season. The low-resolution model is not able to replicate the response, since the model consisted of only a single grid cell. This cell was not water-limited during this season, since higher-than-average ET was simulated. As a result, the low-resolution model is not able to mimic basin responses which are as far as 5.66 standardised anomalies away from the low-resolution model.

Actual evapotranspiration is not only dependent on the amount of available water, but snow cover is also an important factor. For example. the high DWD value for evaporation in the Inn basin during the spring of 2007 can be attributed to this response. In the low-resolution model, the cell was free of snow, allowing the model to evaporate, while in the high-resolution model

only half the cells were free of snow. The cells covered with snow were not able to evaporate water, resulting in a large variation in anomalies and thus a large 5–95% range.

Our results are in line with numerous studies either investigating effects of model resolution or comparing the performance of lumped models with (semi-)distributed models. For example, Leung & Qian (2003) studied the sensitivity of simulation results to model resolution, and concluded that the high-resolution model was able to better represent the spatial variation than the low-resolution model. Gao et al. (2006) concluded that the simulations improved as model resolution increased, since the local dynamics are better represented in the model. However, as stated by Lucas-Picher et al. (2012) and Pryor et al. (2012), it is not given that high resolution simulations always lead to better results, as it becomes challenging to validate the model results with observations, especially at fine spatial resolutions and/or with large spatial coverage. However, they state that the model might become more physically plausible if complex processes are better represented at these scales. As shown by Lobligeois et al. (2014), correct representation of the spatial patterns in precipitation can strongly influence the quality of the simulations in basins with a lot of spatial variation in precipitation. Boyle et al. (2001) concluded that improvements in model performance were related to the spatial distribution of the model input. Koren et al. (2004) reached a similar conclusion, stating that their distributed model outperformed the lumped model in basins with significant spatial rainfall variability. Finally, Carpenter & Georgakakos (2006) compared a lumped model with a distributed model and concluded that the gain in performance was dependent on the amount of spatial variation present in the region of interest. Our study showed that the difference between the high- and low-resolution simulations is largest in basins with large spatial variability. In our study, we show that also the dominant runoff-generating processes are an important factor for the differences between the low- and high-resolution model.

The results may be influenced by the fact that the model did not allow for subgrid variability in land use or soil types, something other models might have included. When subgrid variability is taken into account, we expect the low-resolution model results to become less extreme. However, the low-

resolution model will not be able to capture the full dynamics simulated with the high-resolution model, since landscape characteristics still need to be aggregated to a coarser resolution.

4.4 | Summary and conclusions

In this study, we investigated the hydrological response anomalies in five catchments in the Swiss Alps at two different spatial resolutions. The catchments were selected based on topography and land cover. Three out of five catchments are situated at high elevations and contain glaciers (referred to as Alpine catchments), and the two other catchments are situated at lower elevations and do not contain glaciers (referred to as pre-Alpine basins). We ran the distributed hydrological model Spatial Processes in Hydrology (SPHY) at two different spatial resolutions to match two common hydrological modelling approaches: at a high resolution of ~500 m$\times$500 m to match regional scale studies (and matching hyperresolution), and at a lower resolution of ~40 km$\times$40 km to match global scale studies performed at 0.5°$\times$0.5° resolution. Model results were aggregated per season and were analysed based on standardised anomalies. For each season, we selected one season with unusual precipitation and/or temperature values within the simulation period of 1993-2014: winter of 1995, spring of 2007, summer of 2003 and autumn of 2002.

Results from the high-resolution model show that the intra-basin response covers a large range of anomalies during the selected seasons, where contrasting anomaly signs within a single catchment are often occurring. Within-basin complexity of hydrological response was found to generally increase with the magnitude of the forcing anomaly. The low-resolution model failed to capture this diverse and contrasting response, since the entire region was covered by a single grid cell. The newly introduced density-weighted distance (DWD) was used to quantify the variability simulated with the high-resolution model that is missed by the low-resolution model. The DWD indicated that the local response differed on average by more than 2 standardised anomalies from the response simulated with the low-resolution model. Our results show that results generated with a high-resolution model are not

only more variable, but anomalies can locally be much more extreme or even of the opposite sign than a low-resolution model might indicate. This conclusion confirms previous results by Melsen et al. (2016a), who found that results of large-domain models should be interpreted with care because of a lack of spatial variability in these models. Since our low-resolution model did not represent sufficient spatial variability, this led to a large discrepancy between the high- and low-resolution model results.

The variability in simulated response was associated with the different land cover classes. We found that runoff anomalies matched the temperature anomalies when the dominant runoff-generating processes are energy-limited (snow/glaciers), and runoff anomalies matched precipitation anomalies when the dominant runoff-generating processes are water-limited (grass/forest). The two pre-Alpine basins generally showed a different response than the Alpine basins, which can be attributed to the smaller variation in elevation and land cover in these basins. The grouping of responses in our study matches the elevation classes as defined by Theurillat & Guisan (2001).


5

A new hydrological model for high resolution simulations

This chapter is based on:

Buitink, J., Melsen, L. A., Kirchner, J. W., and Teuling, A. J. (2020). A distributed simple dynamical systems approach (dS2 v1.0) for computationally efficient hydrological modelling at high spatio-temporal resolution, *Geoscientific Model Development*, 13, 6093–6110, doi:10.5194/gmd-13-6093-2020.

In this chapter, we introduce a new numerically robust distributed rainfall–runoff model for computationally efficient simulation at high spatio-temporal resolution: the distributed simple dynamical systems (dS2) model. The model is based on the simple dynamical systems approach as proposed by Kirchner (2009), and the distributed implementation allows for spatial heterogeneity in the parameters and/or model forcing fields at high spatio-temporal resolution (for instance as derived from precipitation radar data). The concept is extended with snow and routing modules, where the latter transports water from each pixel to the catchment outlet. The sensitivity function, which links changes in storage to changes in discharge, is implemented by a new three-parameter equation that is able to represent the widely observed downward curvature in log–log space. The simplicity of the underlying concept allows the model to calculate discharge in a computationally efficient manner, even at high temporal and spatial resolution, while maintaining proven model performance. The model code is written in Python in order to be easily readable and adjustable while maintaining computational efficiency. Since this model has short runtimes, it allows for extended sensitivity and uncertainty studies with relatively low computational costs. A test application shows a good and constant model performance across scales ranging from 3 km^2 to over 1700 km^2.

"It's alright
'Cause the old can feel brand new"

—The Maine, *Same Suit, Different Tie* (2015)

5.1 | Introduction

Hydrological models are essential tools for applications ranging from sensitivity analysis to impact assessment and forecasting. Generally, the aim of rainfall–runoff models is to simulate streamflow given precipitation input. Depending on factors such as the research aim and the climatological/geological setting, different model structures or process representations might be preferred. This, in combination with the inherent complexity and heterogeneity of (sub)surface hydrological processes, has led to the development of numerous different hydrological models over the past decades, each with its own focus. Examples of such rainfall–runoff models and modelling tools include, amongst many others, SWAT (Arnold et al., 1998), HBV (Lindström et al., 1997), TOPMODEL (Beven & Kirkby, 1979), VIC (Liang et al., 1994, 1996), SPHY (Terink et al., 2015), FUSE (Clark et al., 2008), SUMMA (Clark et al., 2015), PCR-GLOBWB (Sutanudjaja et al., 2018) and WALRUS (Brauer et al., 2014). Although there is an ongoing debate about whether the hydrological modelling community should move towards a community model (Weiler & Beven, 2015), different models representing a wide range of complexity and different process representations might be necessary to adequately characterise uncertainty.

Hydrological models are often classified from more conceptual to more process-based models. Conceptual models have fewer processes explicitly parametrised, and as a result their limited number of parameters makes them easier to calibrate. In conceptual models, catchments are often represented by a series of buckets or storages, which mimic processes with different response times. Their typical scale of application is that of small to medium (mesoscale) catchments, generally in a lumped fashion. Process-based models, on the other hand, contain many more parameters. These models are often applied in a distributed fashion, where many of the parameter values are based on maps of vegetation and soil properties. However, often conceptual parameters remain that require calibration or tweaking. Even though process-based models should give a better representation of the physical reality, many models can easily be beaten in performance by a simple neural network (Abramowitz, 2005), or model results can be reproduced without much loss of accuracy by models with a much smaller num-

ber of parameters (Koster & Suarez, 2001; Best et al., 2015; Liu et al., 2018). So if the research aim does not require the use of complex or specific process representation, simple models will likely outperform more complex models in many applications.

Whereas conceptual models often perform satisfactorily at the daily resolution at the lumped basin scale, they lack the ability to explicitly simulate spatially distributed processes that might be needed to accurately predict streamflow response at larger scales. In a study over a large number of basins in France, Lobligeois et al. (2014) found that (hourly) model performance markedly increased from the (lumped) basin scale to a resolution of around 10 km^2 when using aggregated radar precipitation as model input. Other studies (e.g. Ruiz-Villanueva et al., 2012) have also highlighted the importance of spatial variability of rainfall, in particular the movement of storms with respect to the channel network, for flash flood simulation. Another example of a spatially distributed process that affects streamflow is the melting of snow, which can depend both on elevation (via temperature) and aspect (via radiation). Comola et al. (2015), for example, showed that aspect needs to be considered for accurate simulation of snowmelt and runoff dynamics in mesoscale catchments. The spatial organisation of the stream network within a basin also affects the response to rainfall, as has been shown by studies based on the catchment width function or the geomorphological instantaneous unit hydrograph (Kirkby, 1976; Rodríguez-Iturbe & Valdes, 1979). Thus, a spatial resolution in the order of 1–5 km to capture effects of rainfall variability and stream network organisation, combined with a temporal resolution of 1 h or less to capture individual (convective) rain storms, is necessary for realistic rainfall–runoff modelling at larger scales.

The need to improve spatially explicit information in hydrological models aligns with the increasing availability of high-resolution continental-scale forcing datasets. These include for instance merged radar data (e.g Huuskonen et al., 2013; Winterrath et al., 2018), interpolated station data (e.g. van Osnabrugge et al., 2017; Cornes et al., 2018; van Osnabrugge et al., 2019), and atmospheric reanalysis products (e.g Albergel et al., 2018). These datasets have a spatial resolution in the order of 1 km and a temporal resolution in the order of 1 h. There is a growing need for easy-to-apply and easy-to-

adjust models that can exploit the potential of spatially distributed input data at high spatial and temporal resolution.

Conceptual models have been applied in a (semi-)distributed manner to account for spatially distributed input data: a lumped model is applied at each individual grid cell, and water is most often transferred to the outlet using a post-processing function that accounts for catchment routing. This method of running the model subsequently for each individual grid cell is, however, not necessarily the most computationally efficient way to deal with spatially distributed data, but often the result of historical developments. Whereas increased computational power has driven the application of distributed models at increasingly fine (spatial) resolution (Melsen et al., 2016b), it has also led to new challenges: many aspects of distributed modelling, such as uncertainty estimation and (spatial) parameter estimation, require a large number of runs, which further increases the computational demand. This demand is in the vast majority of cases too high to be tackled by individual computers, and thus computational infrastructure such as high-performance clusters are used. However, there are costs related to this procedure, while the "free" computational power in the individual computer could be used more optimally. A conceptual model that can deal with high-resolution gridded data to tackle these kinds of issues in an efficient manner is currently lacking.

An example of a conceptual model that, in spite of its extreme simplicity, has shown good performance for discharge simulation at the scale of smaller catchments and at fine temporal (hourly) resolution is the simple dynamical systems (SDS) approach introduced by Kirchner (2009). This concept is based on the assumption that discharge is solely dependent on the total amount of stored water in a catchment. It translates changes in storage to changes in discharge using a discharge sensitivity function, without describing internal catchment processes. This sensitivity function is typically parametrised by a two-parameter power law, however several studies have suggested a more complex downward-curving rather than linear behaviour in double-logarithmic space (Kirchner, 2009; Teuling et al., 2010; Adamovic et al., 2015). Moreover, the system parameters can be inferred from streamflow recession analysis and potentially from hillslope characteristics (Troch et al., 2003), potentially removing the need for model calibration (Melsen

et al., 2014). The model's simplicity has the important advantages that discharge can be simulated based on a single equation — which can easily be vectorised for distributed implementation — and that the model only needs to store a limited number of variables, reducing the model output fields — since storage and discharge are directly linked via the discharge sensitivity function. Especially this latter part is fundamentally different from the many "bucket-based" conceptual models, which use storage in conceptual reservoirs to determine the outflow. In the original test in the humid Plynlimon catchments (area 8.70 and 10.55 km^2), Kirchner (2009) found Nash–Sutcliffe efficiencies (NSE) exceeding 0.95 during the model validation when calibrating model parameters, and efficiencies exceeding 0.90 when parameters were obtained from recession analysis. Others have also found the concept to work well in less humid catchments. Teuling et al. (2010) found the method to generally work well in the small (3.3 km^2) Swiss Rietholzbach catchment. Although the method can be expected to work best in hilly catchments, Brauer et al. (2013) found the model to produce reasonable efficiencies after calibration in the small (6.5 km^2) Dutch Hupsel Brook catchment. Adamovic et al. (2015) reported NSE values exceeding 0.6 for most years in several Ardechian catchments in the order of 10–100 km^2. Given the simplicity and good performance of the simple dynamical systems approach at the spatial (order 10 km^2) and temporal (1 h) resolution required for optimal simulation of runoff in larger (mesoscale) catchments, combining it with simple representations of routing and snowmelt should result in a model that satisfies the required criteria outlined in the previous paragraphs. In a first attempt to apply the simple dynamical systems approach spatially, Adamovic et al. (2016) developed a semi-distributed implementation of the SDS approach (SIMPLEFLOOD), only using sub-basins to distribute the catchment and not a grid. This model, however, was not optimised for computational efficiency and/or numerical stability over a wide range of model parameters required for optimisation studies, and the code was not made available as open source.

Here, we present a flexible and computationally efficient distributed implementation and extension of the simple dynamical systems approach that can be used to investigate the spatially distributed hydrological response using data at high spatial and temporal resolution: the distributed simple dynam-

ical systems (dS2) model. Our aim was not only to create a model that is capable of computationally efficient simulations of discharge in mesoscale basins at high spatio-temporal resolutions, but also to develop a model code that is easy to use, read and modify. Therefore, the model is written in Python, although there are more computationally efficient languages available. We believe, however, that this is the optimum between model speed and code adjustability required in most hydrological model studies. In this model, the catchment is divided into smaller sections using a regular grid, and discharge is simulated according to the SDS approach for each pixel. This distributed implementation allows the concept to be applied to bigger catchments, and also allows for spatial heterogeneity, both in the forcing and in the parameters. Since the original concept consists essentially of only one differential equation, it can be applied in a computationally efficient fashion, vectorising all cells in the catchment. Snow and routing modules are added to the model to allow for application in snow-dominated regions, and to transport the water from each pixel to the catchment outlet via the drainage network. This efficient distributed implementation lowers the computational burden for high-spatial-and/or high-temporal-resolution studies, and it opens doors for extensive uncertainty studies. We will first introduce the model concept and describe the technical application. After that, we discuss the parameter sensitivity, and finally we show an application of the model.

5.2 | Model concept

5.2.1 | Simple dynamical systems approach

The simple dynamical systems approach proposed by Kirchner (2009) combines the conservation-of-mass equation (assuming a constant density) with the assumption that discharge is solely dependent on the total storage (excluding snow and ice) in the area of interest:

$$\frac{\mathrm{d}S}{\mathrm{d}t} = P - E - Q, \tag{5.1}$$

$$Q = f(S), \tag{5.2}$$

where S represents the total storage, P the precipitation, E the actual evaporation and Q the discharge. Differentiating Equation (5.2) and combining it

with Equation (5.1) results in the following equation:

$$\frac{\mathrm{d}Q}{\mathrm{d}t} = \frac{\mathrm{d}Q}{\mathrm{d}S}\frac{\mathrm{d}S}{\mathrm{d}t} = \frac{\mathrm{d}Q}{\mathrm{d}S}(P - E - Q) = g(Q)(P - E - Q), \tag{5.3}$$

where we define $\frac{\mathrm{d}Q}{\mathrm{d}S}$ as the sensitivity function $g(Q)$, describing the sensitivity of discharge to changes in storage. Note that the evaporation represents actual evaporation, as the concept does not simulate evaporation reduction as a result of, for instance, soil moisture stress during dry periods. Ideally, a soil moisture model would provide the correct actual evaporation values, or, when applying the concept to humid areas, the actual evaporation is equal to a factor times the potential evaporation. To support the latter, we introduce the evaporation correction parameter ϵ, which can correct the provided (potential) evaporation input data ($E = \epsilon \cdot E_{\text{input}}$). Additionally, to prevent numerical issues, a simple evaporation reduction switch is added, which is described in Section 5.3.2.

Originally, the SDS approach was introduced as a lumped approach to simulate discharge in small catchments of approximately 10 km^2 (Kirchner, 2009). Several studies have subsequently applied this concept to other catchments in Europe (Teuling et al., 2010; Krier et al., 2012; Brauer et al., 2013; Melsen et al., 2014; Adamovic et al., 2015). Some of the catchments in these studies had a size similar to the original scale from Kirchner (2009), yet it was also applied to catchments up to 1000 km^2 in size. One could argue whether the concept is still valid at a scale so different from the scale for which it was initially developed (Beven, 1989, 2001; Sivapalan, 2006; McDonnell et al., 2007), and whether a single sensitivity function is sufficient to capture the spatial complexity of substantially larger basins. In regions with high spatial heterogeneity, grid-based models are likely to yield more realistic results than lumped models (Lobligeois et al., 2014).

To respect the original scale of development and to capture spatial variability, we have developed a distributed implementation of the simple dynamical systems approach. Our distributed implementation builds on the original concept as proposed by Kirchner (2009) and extends this concept with simple snow and routing modules. For the distributed implementation, we assume that the SDS approach is valid for each pixel of a rectangular grid. By defining pixels with a size corresponding to the original scale (in the or-

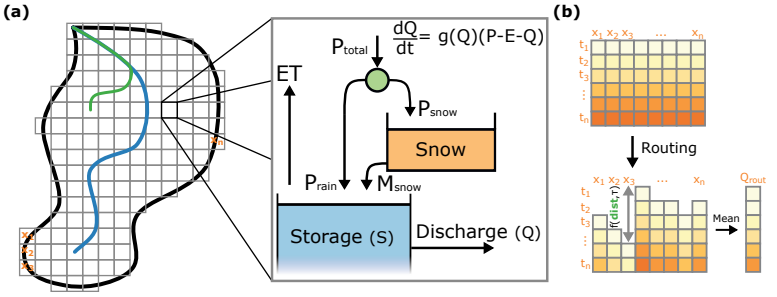

Figure 5.1 | Efficient distributed implementation of the simple dynamical systems approach, which is solved for each pixel. The left-hand side of panel **a** represents a catchment, with a regular grid covering the catchment area. The green line indicates the flow path on which the routing lag is based (green "dist" in panel **b**). Panel **b** shows how the catchment is translated to a matrix to allow for computationally efficient calculations, and how the matrix is modified in the routing algorithm, by shifting each column based on the distance to the outlet and the routing parameter τ.

der of 1 km^2), the scale of application remains similar to the original scale, and both the forcing and the model parameters can be defined for each individual pixel (see Figure 5.1). In this distributed implementation, we allow precipitation to fall as snow; see Section 5.2.3. We added a routing module to transport water from each pixel to the river outlet, by adding a time delay to each pixel based on the distance to the outlet and a travel speed parameter; see Section 5.2.4. The model can be run with different choices for Δt, yet in order to respect the spatio-temporal resolution the default time step is 1 h. This model has been built with a focus on computational efficiency, meaning that all grid cells in the catchment are stored in a single vector, allowing for vectorised computations (see Figure 5.1b). This results in a matrix with the rows and columns indicating time and space, respectively. As a result, the routing conceptualisation is a modification of this matrix, where each column is shifted to induce a temporal delay.

5.2.2 | Discharge sensitivity

As previously mentioned, the sensitivity function is required to translate changes in storage to changes in discharge. Kirchner (2009) originally presented a simple power-law version of this sensitivity function for purposes of illustration:

$$g(Q) = \frac{\mathrm{d}Q}{\mathrm{d}S} = aQ^b, \tag{5.4}$$

where a and b define the slope and intercept of the sensitivity function in log–log space. This power-law relation has been widely used in experimental and theoretical studies (e.g. Troch et al., 1993; Brutsaert & Lopez, 1998; Tague & Grant, 2004; Rupp & Selker, 2006; Lyon & Troch, 2007; Rupp & Woods, 2008). This relatively simple sensitivity function allows the translation of discharge into storage, using the following equation:

$$\int \mathrm{d}S = \int \frac{\mathrm{d}Q}{g(Q)}, \tag{5.5}$$

$$S(Q) = \begin{cases} \frac{1}{a}\frac{1}{1-b}Q^{1-b} + S_0, & b \neq 1 \\ \frac{1}{a}\ln(Q) + S_0, & b = 1, \end{cases} \tag{5.6}$$

where S_0 is the integration constant, meaning that only relative storage changes can be obtained using this method. The value of b affects the meaning of S_0, as described by Kirchner (2009). However, most catchments show recession behaviour that differs from a power-law relation between $\mathrm{d}Q/\mathrm{d}S$ and Q (Kirchner, 2009; Teuling et al., 2010; Krier et al., 2012; Adamovic et al., 2015). Therefore, a more complex formulation of the sensitivity function was also proposed by Kirchner (2009):

$$\ln(g(Q)) = c_1 + c_2\ln(Q) + c_3(\ln(Q))^2, \tag{5.7}$$

where c_1, c_2 and c_3 are the three parameters of this quadratic equation. This quadratic equation allows for a concave relation between the recession rate and the discharge in log–log space. This equation has one downside, however: since it is shaped like a parabola in log–log space, there is always an optimum in the discharge sensitivity. This implies that with an increasing Q, the system becomes less sensitive at some point. This behaviour is unrealistic and unwanted when performing automatic calibration or random

parameter sampling runs. Therefore, we have added an additional term to the original power-law equation, which accounts for the concave shape of the sensitivity function:

$$g(Q) = aQ^b \cdot e^{\gamma/Q}, \tag{5.8}$$

where a, b and γ are the three parameters describing the shape of the discharge sensitivity. However, we have rewritten this equation to include all parameters in the exponent term, as this improves computational efficiency:

$$g(Q) = e^{\alpha+\beta\cdot\ln(Q)+\gamma/Q}, \tag{5.9}$$

with $\alpha = \ln(a)$ and $\beta = b$ from Equation (5.8). In Figure 5.2, the effect of each parameter on the shape of the sensitivity function is presented. Discharge observations from Teuling et al. (2010) are also included to indicate the importance of the γ parameter. This equation has the benefit that it can be rewritten to the original power-law equation, if $\gamma = 0$:

$$g(Q) = e^{\alpha+\beta\cdot\ln(Q)} = e^{\alpha} \cdot Q^{\beta}, \tag{5.10}$$

where $a = e^{\alpha}$ and $b = \beta$ from Equation (5.4). This concept allows us to use parameters from previous studies, and to transform the discharge time series to a storage time series according to Equation (5.5). A disadvantage of this new sensitivity function is that, due to the addition of the γ/Q term, there is no longer an analytical solution, but the equation can still be integrated numerically.

5.2.3 | Snow processes

In our distributed implementation, we allow precipitation to fall as snow. Snow is treated as a separate storage (see Figure 5.1a), where snowmelt is added to the simple dynamical systems approach in the form of liquid precipitation, following the methodology of Teuling et al. (2010). We assume snowmelt to be dependent on both temperature and radiation, following the restricted degree-day radiation balance approach (Kustas et al., 1994). The

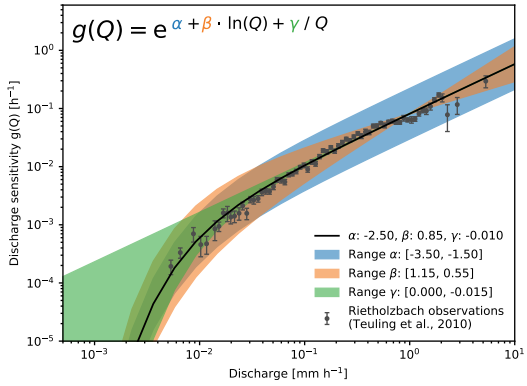

Figure 5.2 | Parametrisation of the discharge sensitivity, including the effects of the three parameters: α affects the intercept, β affects the slope and γ affects the curvature at low discharge values. Parameter values for each parameter are given in the legend as their min–max range.

snow storage is conceptualised based on the following equations:

$$\frac{\mathrm{d}S_{\text{snow}}}{\mathrm{d}t} = P_{\text{snow}} - M_{\text{snow}}, \tag{5.11}$$

$$P_{\text{snow}} = \begin{cases} P_{\text{total}} & \text{if } T <= T_0 \\ 0 & \text{if } T > T_0, \end{cases} \tag{5.12}$$

$$M_{\text{snow}} = \begin{cases} ddf \cdot (T - T_0) + rdf \cdot R_{\text{g}} & \text{if } M_{\text{snow}} \cdot \Delta t <= S_{\text{snow}} \\ \dfrac{S_{\text{snow}}}{\Delta t} & \text{if } M_{\text{snow}} \cdot \Delta t > S_{\text{snow}}, \end{cases} \tag{5.13}$$

where S_{snow} is the total snow storage in millimetres (mm), P_{snow} the precipitation falling as snow in millimetres per hour (mm h^{-1}), M_{snow} is the snowmelt in millimetres per hour (mm h^{-1}), T is the air temperature in degrees Celsius (°C), T_0 is the critical temperature for snowmelt in degrees Celsius (°C), ddf is the degree-day factor in millimetres per hour per degree Celsius (mm h^{-1} °C^{-1}), rdf is the conversion factor for energy flux density to snowmelt depth in millimetres per hour per watts per square metre (mm h^{-1} (W m^{-2})$^{-1}$), R_{g} is the global radiation in watts per square metre

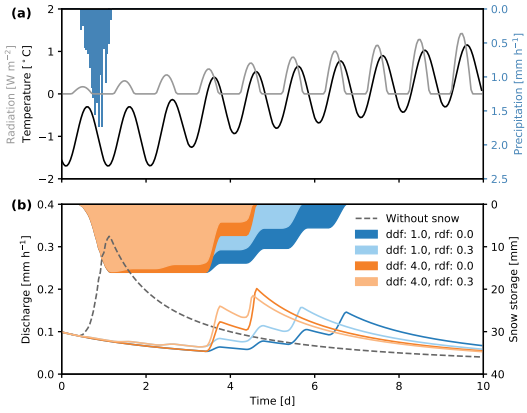

Figure 5.3 | Simulation results with and without the snow conceptualisation. Panel **a** shows the model input; panel **b** shows the model output. The four hydrographs represent runs with different snow parameter values (see legend, in mm h^{-1}). We fixed the critical temperature T_0 to 0°C. To visualise the influence of the different parameters, we used unrealistically high *ddf* and *rdf* values.

(W m^{-2}), and Δt is the time step in hours. If no radiation observations are available, the snowmelt equation is modified to the normal degree-day method.

In Figure 5.3, the effect of this snow conceptualisation is presented using synthetic forcing data. In this figure, one can see that radiation can cause snow to melt even when temperatures are still below the critical temperature (0°C in this example). If the temperature exceeds this threshold, radiation amplifies the melting of snow, resulting in an earlier depletion of the snow storage. Finally, if snow processes are not relevant in the region of interest, the snow conceptualisation can be turned off to further reduce the computational demand (see the dashed line in Figure 5.3 for the resulting discharge simulation).

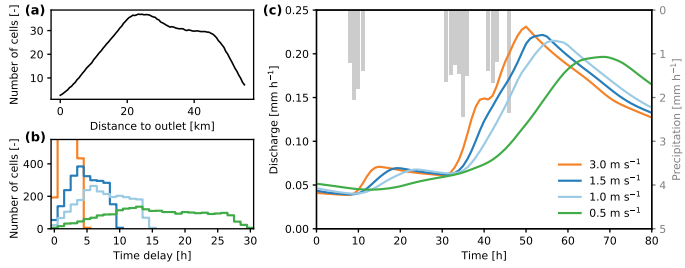

Figure 5.4 | The routing concept visualised: the width function of a synthetic catchment (**a**), the corresponding travel speed given four different τ values (**b**) and the effect of different τ values on the hydrograph (**c**).

5.2.4 | Flow routing

A simple, efficient routing conceptualisation was added to the distributed model to transport water from each grid cell to the outlet of the catchment. In most studies applying the simple dynamical systems approach, a constant delay factor was added to the generated runoff time series, in order to account for the delay caused by the river network. Since our distributed implementation has pixels at distinctly different locations, we need to account for attenuation caused by the river network. The routing concept presented here is based on the already existing width function concept (Kirkby, 1976), where it is assumed that the stream network induces a temporal delay proportional to the distance to the outlet. This can be seen as a width-function-based unit hydrograph without diffusion and goes back at least 20 years (e.g. Franchini & O'Connell, 1996). The distance to the outlet is combined with the travel speed parameter (τ) to determine the lag time for each pixel (see the green line and shifting of columns in Figure 5.1). An example of this concept is presented in Figure 5.4a.

The width function in Figure 5.4a reflects the shape and stream network of a synthetic catchment. The distance of each pixel can be translated to a time delay using the travel speed parameter τ. This delay is in discrete steps (see Figure 5.4b), determined by the time step of the model. Slower flow speeds result in larger time delays, and vice versa. The hydrograph in Figure 5.4c

shows that peaks are more attenuated with slower flow speeds. In this example, we assume homogeneous precipitation across the entire catchment, but in reality the heterogeneity of precipitation events also influences how the discharge peak is attenuated. This concept does not include diffusion of flood waves; it only incorporates advection.

5.3 | Technical aspects

5.3.1 | Model implementation

One of the main aims of this model was computational efficiency. However, we do not claim that we have built the most computationally efficient conceptual hydrological model, since we sacrificed some calculation time for the user-friendly and hugely popular Python programming language. By choosing this language, we encourage users of the model to adapt, improve and change all components of the model, in order to find answers to their research questions. The model is written in Python 3.6 and largely uses the NumPy library. NumPy uses C libraries to ensure fast computations over entire arrays, something the base functions of Python do not offer. Due to the simplicity of the simple dynamical systems approach, we need to solve only one equation (besides the snow conceptualisation). NumPy allows functions to be vectorised: receiving and outputting an array of values, while applying the same function to each individual value. This is computationally more efficient than the step-by-step application of the same function to each element in the array.

To get an idea of the computational efficiency of the model, example runtimes are presented in Figure 5.5. We ran the model for 3 months at an hourly time step using synthetic forcing data for a wide range of model cells, reflecting different catchment sizes or model resolutions, to get an idea how the computational demand scales with catchment size or resolution. We separated the time spent in the numerical solver, the I/O operations and the routing module. In the I/O operations, we include reading the settings file, reading the input data and writing the model results. The grey bars in Figure 5.5 represent the "traditional" modelling approach, where the numerical solver is called for each individual pixel and time step. This extra

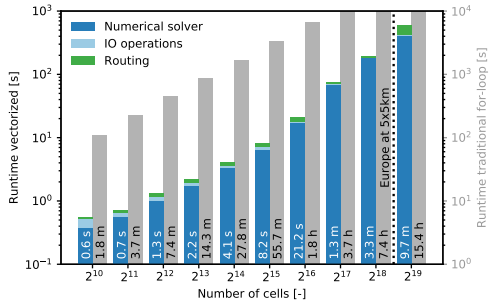

Figure 5.5 | Runtimes for a simulation of 3 months with an hourly time step with varying number of pixels, run on a single core of a normal desktop (Intel Core i7-6700, 16GB RAM). The grey bars represent model runtimes where the numerical solver is called for each individual pixel, and are keyed to the right-hand scale, making the difference in runtimes appear smaller than it really is. The dotted line represents the number of pixels when simulating Europe at 5×5 km^2 resolution.

for-loop drastically increases runtimes by a factor of more than 10 (this is also a property of Python, being an interpreted language instead of a compiled language). To demonstrate the enormous potential of this model to explore uncertainty and spatial patterns in parameters: simulating Europe for 3 months at hourly time steps and at a resolution of 5×5 km^2 (roughly $2^{18.6}$ pixels) would take approximately 5 minutes with the efficient dS2 model. The runtimes show a small inconsistency in the increase of runtimes with the increase in pixels. This is most likely the result of an internal Python or NumPy threshold. The current version of dS2 does not yet support automatic multithreading, which is expected to even further reduce runtimes, especially in large basins.

When applying the model to very large basins and/or running for very long periods, the random access memory (RAM) can become a limiting factor, as storing data in the RAM is by far most efficient. To prevent exceeding the RAM, the user can define the maximum amount of RAM the model is allowed to use, and dS2 will chunk the input and output data accordingly. For example, running the model for a basin with 1500 pixels for a period of 4 years

on a hourly time step would require approximately 800MB. Additionally, to reduce the time spent reading and writing the files on the disk, we rely on a special data format: NumPy memmap. This data file directly maps arrays to the hard drive without storing any metadata, to ensure fast reading and writing. The downside is that this format does not have any metadata, meaning the shape and data type need to be known prior to reading the file. In order to store the model output in a more common format, the model can transform the NumPy memmap data to the more commonly used NetCDF format, including metadata.

5.3.2 | Adaptive time stepping

When solving a differential equation, one would ideally opt for an analytical solution. However, many equations (including Equation (5.3)) do not have an analytical solution, so one needs to use numerical solvers to solve the differential equation. The downside of numerical methods is that they might introduce numerical errors and/or numerical instability, as they are approximations of the analytical solution. Many different numerical methods exist, varying in complexity and numerical accuracy. The importance and potential problems of numerical solutions have been described and studied extensively (Clark & Kavetski, 2010; Kavetski & Clark, 2010, 2011). For example, the most simple method is the first-order explicit Euler scheme, meaning that the value at t_{n+1} is based on the values given at t_n. This method is the simplest approximation of the value at t_{n+1}, but is as a first-order method also prone to introduce large numerical errors. A more robust and popular method is the explicit Runge–Kutta 4 scheme, which uses four estimations (fourth order) between t_t and t_{n+1} to give a more accurate estimation of the value at t_{n+1}. Furthermore, using higher-order (or implicit) solvers reduces the risk of numerical instability. Many more methods are available, which are higher order and/or use different ways to calculate the "intermediate" steps. Numerical solvers in most hydrological models are rather basic, although it is known that the numerical solver can significantly influence the model output (Schoups et al., 2010). In particular in strongly non-linear problems, a robust numerical solver is important.

Since the simple dynamical systems approach allows for non-linear reser-

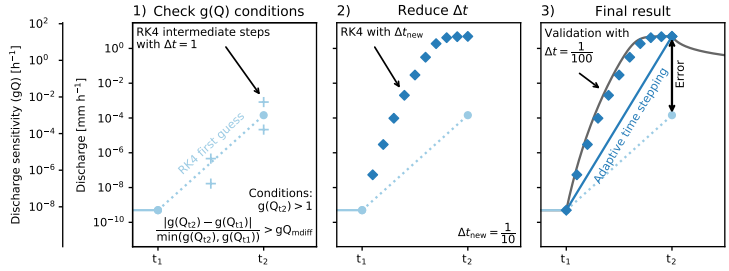

Figure 5.6 | Three steps in the adaptive time stepping scheme. Note that in extreme cases, both Q and $g(Q)$ can change over several orders of magnitude between t_1 and t_2, as can be seen from both y axes. The plus symbols in step **1** indicate the intermediate values by the RK4 solver, which combine into the blue circle at t_2. The blue diamonds in step **2** show the intermediate steps calculated with RK4 but at a smaller time step. Only the value at t_2 is stored. The error in step **3** represents the numerical error without the adaptive time stepping scheme.

voirs, the simulated response can vary over several orders of magnitude within a single time step. This non-linearity can cause numerical errors, which can be prevented by reducing the time step. Several options are available, where the Cash–Karp method is the typical textbook approach to explicitly solving differential equations (Cash & Karp, 1990). This method is based on the Runge–Kutta scheme and uses the difference between fourth- and fifth-order estimates to measure the potential numerical error. This can be used to reduce the time step if the difference exceeds a certain threshold. However, to ensure optimal computational efficiency, we decided to incorporate the knowledge about the differential equation (Equation (5.3)) to determine whether time step reduction is necessary. Therefore, we have implemented the explicit fourth-order Runge–Kutta (RK4) scheme with an adaptive time stepping scheme. We have identified cases where the RK4 scheme can become numerically unstable, and we used these cases to reduce the internal time step. These cases are explained in more detail below. This adaptive time stepping scheme is visualised in Figure 5.6.

The adaptive time stepping scheme operates in three steps. In the first step, the discharge for the next time step is calculated using the explicit Runge–

Kutta 4 scheme. For both time steps, the discharge sensitivities are calculated based on the following equation:

$$gQ_{\text{diff}} = \frac{|g(Q)_{t2} - g(Q)_{t1}|}{\min(g(Q)_{t2} - g(Q)_{t1})}, \tag{5.14}$$

where the numerator represents the absolute difference between the two discharge sensitivities, and the denominator represents the lowest discharge sensitivity to ensure the comparison also works during the falling limb of the hydrograph. The time step will be reduced whenever at least one of two conditions is met: (1) when $g(Q_{t2}) \cdot \Delta t > 1$, or (2) when gQ_{diff} exceeds a certain threshold (gQ_{mdiff}). The first condition requires a smaller time step, since values of $g(Q) \cdot \Delta t > 1$ indicate that the system is extremely sensitive and that a smaller time step is required to optimally account for this sensitivity. For this condition, the time step is reduced according to the following equation:

$$\frac{\Delta t}{\Delta t_{\text{new}}} = \max(5, \min(g(Q_{t2}) \cdot 10, 50)), \tag{5.15}$$

where the reduction in Δt is dependent on the size of $g(Q_{t2})$. We defined a lower and upper limit to the time step reduction, to ensure that the solver gains enough precision but does not spend too much time on a single time step. Both upper and lower limits can be changed by the user. The second condition is triggered when $g(Q)$ covers several orders of magnitude in a single time step. A threshold gQ_{diff} is defined, describing how many times $g(Q_{t2})$ is allowed to deviate from $g(Q_{t1})$. If this threshold is exceeded ($gQ_{\text{diff}} > gQ_{\text{mdiff}}$), a smaller time step is required since RK4 is not able to accurately solve the differential equation over this many orders of magnitude. The resulting reduced time step is based on the following equation:

$$\frac{\Delta t}{\Delta t_{\text{new}}} = \max(5, \min(gQ_{\text{diff}}^{\text{dt\_reduction}}, 50)), \tag{5.16}$$

where the reduction in Δt is dependent on the difference between $g(Q_{t1})$ and $g(Q_{t2})$, raised to the power dt_reduction, and the same lower and upper limits to the time step reduction are used. The RK4 scheme is used over these reduced time steps until the original time step (t_2) is reached. This final value is saved as output, and the intermediate steps are discarded. In Figure 5.6 step 3, we validate the adaptive time stepping scheme with an even finer

time step ($\frac{1}{100}$), which we assume approaches the analytical solution, and we conclude that the adaptive time stepping scheme yields reliable results. This figure shows that the adaptive time stepping scheme avoided a large numerical error (the difference between the two solutions: $Q_{t2} \approx 10^{0}$ mm h^{-1} vs $Q_{t2} \approx 10^{-4}$ mm h^{-1}).

During periods with low discharge and relatively high evaporation, the numerical solver can result in negative discharge amounts. To prevent this from happening, we define a threshold for discharge (which thus corresponds to a threshold storage level), below which no evaporation is allowed to occur. This mimics evaporation reduction during periods with low storage volumes, as discharge and storage are directly linked. For the pixels where the discharge is below this threshold, the evaporation rate is set to 0 mm h^{-1}. The value of the discharge threshold is currently set at 10^{-4} mm h^{-1} but can be altered by the user. All model parameters can be found in Appendix B.

5.3.3 | Closure of the water balance

The concept of this model is based on the water balance, yet it does not explicitly solve the water balance as most hydrological models do. The water balance is indirectly solved by calculating changes in storage. To check whether the model still respects the water balance, the closure of the water balance is calculated using the following equation:

$$\phi = P_t - E_t - \int_{t-1}^{t} Q - \Delta S, \tag{5.17}$$

$$\Delta S = S(Q_t) - S(Q_{t-1}), \tag{5.18}$$

where ϕ is the error in the water balance for each time step t, which ideally should result in a value of 0. The change in storage can be calculated using the storage at the beginning and at the end of the time step. The integral over Q indicates that one needs to consider the volume of water that is discharged during the time step. This depends on how the variables are considered in time within the model. Figure 5.7a explains how the different fluxes are positioned within the model. The model assumes that the precipitation and evaporation values are summations of the entire duration of a single time step. The resulting discharge values are, however, only representative at the

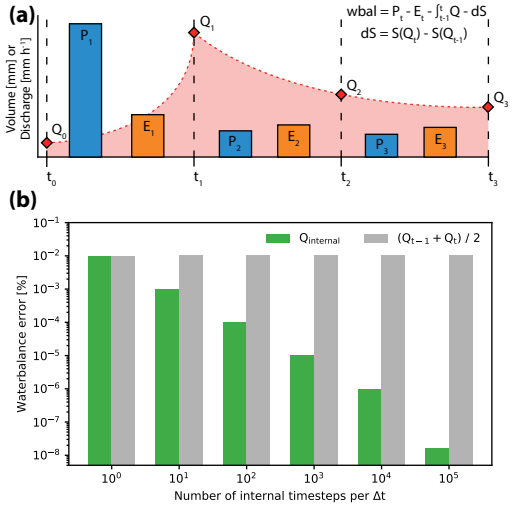

Figure 5.7 | Closure of the water balance per time step. Panel **a** shows the timing of the different variables. Red area under the dotted line indicates the total volume of water discharged per time step. Panel **b** shows the average absolute error in the water balance when the volume of water is estimated with smaller internal time steps ($Q_{internal}$), where the error is defined as the percentage of the total precipitation during the simulation period.

end of the time step, not a summation over the time step. Due to the strong non-linearity of the system, the total volume of water discharged during a single time step cannot be represented by the discharge at the end of the time step, as indicated by the dotted red line in Figure 5.7a.

To estimate the volume of water discharged during the time step, one needs a discharge value that is representative for the volume of water discharged during that time step. The easiest way to calculate this is to take the average of the discharges at time steps t and $t-1$. However, if the sensitivity function is strongly non-linear, this average might not be representative for the volume of water discharged during that time step. To improve the volume estimation, one can subdivide each time step and base the volume estim-

ation on the mean discharge of the resulting shorter steps ($Q_{internal}$). This comparison is shown in Figure 5.7b. The grey bars represent the error in the water balance when the total discharge volume is estimated using the discharge averaged over time steps t and $t-1$. This error does not reduce with an increase in internal time steps, as the discharge prediction at t changes only marginally. However, if the total discharge volume is estimated using the discharge at each internal time step, the total error in the water balance is reduced from 10^{-2} to 10^{-8}%. This indicates that the model concept is able to successfully close the water balance, given that the discharge volume per time step is accurately accounted for. Please note that this example is to show that the concept successfully closes the water balance at each time step. The current version of the model only outputs discharge at the end of the time step, as calculating $Q_{internal}$ does not add to the numerical accuracy of the discharge calculation at the end of the time step.

5.4 | Parameter sensitivity

We investigated the response of the model to the five main parameters (α, β, γ, ϵ and τ; excluding the snow parameters) by plotting the response surface over realistic parameter ranges. These ranges are based on comparing the shape of the resulting discharge sensitivity function with the previous studies that use the SDS approach. The results of this analysis are presented in Figure 5.8. We selected the Kling–Gupta efficiency (KGE) as the performance metric. We created a synthetic time series of observations based on parameters that are in the middle of each subplot, which are used to calculate the KGE. It is striking that the three discharge sensitivity parameters (α, β and γ) show large regions with similar model performance (the dark blue regions), and seem to be correlated, which Melsen et al. (2014) also showed for the α and β parameters for a lumped application. However, based on theoretical considerations (Troch et al., 1993; Brutsaert & Lopez, 1998; Tague & Grant, 2004; Rupp & Selker, 2006; Lyon & Troch, 2007; Rupp & Woods, 2008, e.g.), we can conclude that at least the α and β parameters are required to optimally capture the discharge sensitivity and, based on other studies using the simple dynamical systems approach (Kirchner, 2009; Teuling et al., 2010; Krier et al., 2012; Adamovic et al., 2015), that a third parameter (γ in this case)

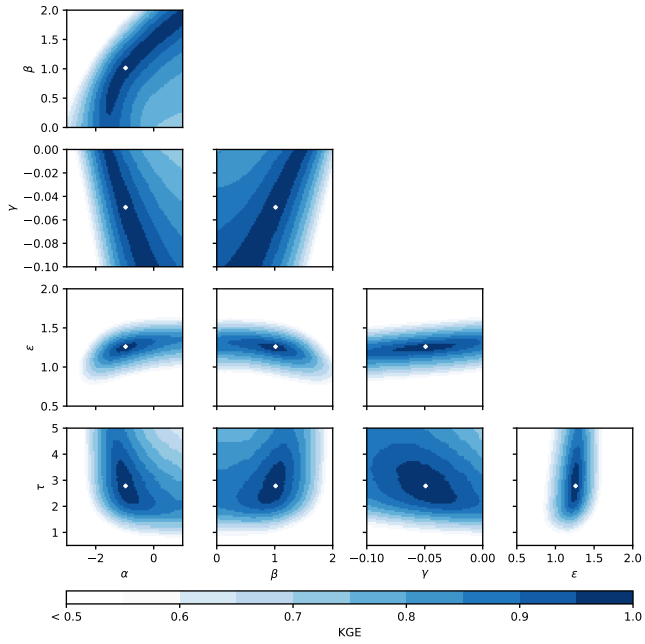

Figure 5.8 | Response surface plots for all main parameter combinations with the Kling–Gupta efficiency (KGE) as the performance metric for a synthetic experiment. The white dot in the middle of each graph represents the location where KGE is equal to 1. Each plot consists of 4900 model runs—where the model has 200 cells, and was run for 1 year on an hourly time step—and took 1 hour and 15 minutes to run on a normal desktop (Intel Core i7-6700, 16GB RAM).

is required to capture the curvature in the $g(Q)$ relation. These response surface graphs indicate that local optimisation algorithms might struggle to find the global maximum due to the large equifinality regions. We therefore recommend not to use a single parameter combination, but rather to use multiple parameter sets to account for equifinality.

Furthermore, we also analysed the parameter sensitivity according to Sobol' (2001), Saltelli (2002) and Saltelli et al. (2010). The global sensitivity ana-

lysis method is designed to analyse the sensitivity of different performance statistics to each parameter. Sobol's sensitivity analysis works optimally in a case where parameters are not correlated. Even though this condition is not fully met in our model application, we use Sobol' because it is the most widely used method to investigate parameter sensitivity. Furthermore, the aim of this sensitivity analysis is to give a first impression of the influence of the parameters on performance metrics. To perform this analysis, a set of $n \cdot (2k + 2)$ parameter combinations is required, where k is the number of parameters and n is the number of samples that sample the parameter space. We chose a sample of 1,000 and focused on the five main parameters (α, β, γ, ϵ and τ; excluding the snow parameters) resulting in 12,000 parameter sets. Usually, this is a rather computationally expensive method, but due to the computational efficiency of this model we were able to run all parameter sets in just under 6 hours (model with 100 cells, simulation period of 2 years on hourly time step, on a normal desktop with an Intel Core i7-6700 and 16GB RAM). The parameter boundaries were set to the same values as used in the response surface plots. For each parameter combination, multiple performance statistics were calculated. Next, Sobol's sensitivity analysis is able to extract the influence of each parameter on the variation in the performance statistic caused only by that parameter ("main effect"), and the influence of the parameter including all variance caused by interactions with other parameters ("total effect") (Sobol', 2001; Saltelli, 2002; Saltelli et al., 2010). The results from the analysis are presented in Figure 5.9.

It is clearly visible that parameter sensitivity depends on the performance metric used. The Nash–Sutcliffe efficiency (NSE) and Kling–Gupta efficiency (KGE) show roughly the same response, as is expected. The NSE calculated on the logarithmic discharge values shows a very different response, with γ being one of the most sensitive parameters. This is in line with our expectations, as the γ parameter describes the downward curvature of the $g(Q)$ function, where it mostly affects the lower discharge volumes. Additionally, this parameter is not very prominently visible in the NSE and KGE sensitivity plots, since these metrics tend to put more focus on higher discharges. These graphs also show that there are some parameter interactions influencing the results, indicated by the difference between the main and total effects. This was already visible in Figure 5.8, where we see correlations between the three

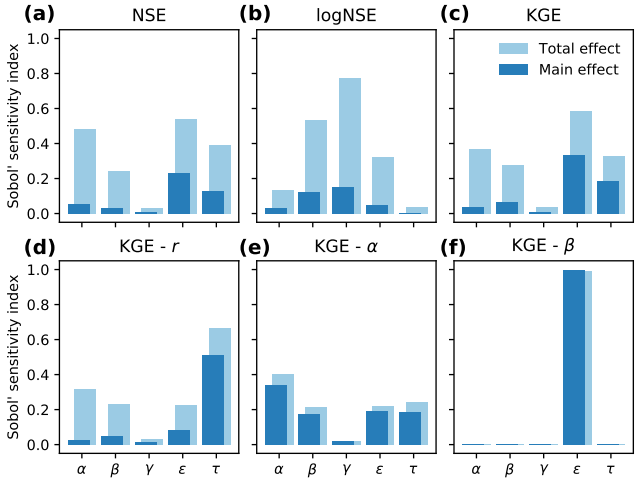

Figure 5.9 | Sobol' parameter sensitivity for a synthetic experiment, shown for different performance statistics. The main effect presents the sensitivity induced by that parameter alone, and the total effect quantifies the sensitivity when parameter interactions are taken into account as well. The top row (panels **a**, **b**, **c**) show three commonly used performance metrics. The bottom row (panels **d**, **e**, **f**) shows the three components of the Kling–Gupta Efficiency: Pearson correlation coefficient (KGE - r), ratio of variability (KGE - α) and bias (KGE - β).

$g(Q)$ parameters. Since this analysis is performed to give a first evaluation of how the parameters affect model output, we will focus on the main effect.

The most interesting patterns are visible in the bottom three subplots, where the three components of the KGE are presented. The correlation coefficient (KGE - r, Figure 5.9d) is most sensitive for the routing parameter τ, since this parameter essentially deals with the timing of discharge peaks. The ratio of variability (KGE - α, Figure 5.9e) does not show any individual parameter to be most important, yet all parameters show some degree of sensitivity. For the bias (KGE - β, Figure 5.9f), the evaporation parameter ϵ is by far the most sensitive parameter, since it determines the total volume of water that evaporates and thus the total volume of discharge. All other parameters can

only control either the response of discharge to precipitation or the timing of the peaks. Since the roles of the parameters ϵ and τ are relatively clearly defined, predominantly affecting the bias and correlation, respectively, we hypothesise that these roles can be used for more efficient optimisation procedures by reducing the number of dimensions. One could optimise the ϵ parameter only on the bias of the simulations, followed by an optimisation of the τ parameter on the correlation. Finally, the three $g(Q)$ parameters can be optimised on either the ratio of variability or the total Kling–Gupta efficiency. This reduces the optimisation from a five-dimensional problem to two one-dimensional problems and a single three-dimensional problem.

5.5 | Example application

In this section, we apply the model to the Thur, a mesoscale basin (1700 km^2) in the Swiss Alps. This basin was selected since it contains many measurement locations, where the catchment used by Teuling et al. (2010) is one of the sub-basins. Since Teuling et al. (2010) showed that the SDS concept is able to simulate the discharge at small scale, we take this opportunity to see how the model performs at different spatial extents. The model was applied at a 1 km^2 resolution, using distributed forcing. We used the same forcing data as Melsen et al. (2016a), where the data are interpolated using the pre-processing tool WINMET of the PREVAH modelling system (Viviroli et al., 2009; Fundel & Zappa, 2011). For a more detailed explanation of the basin and the data used, we refer to Melsen et al. (2016a).

For this application, we focus on three sub-basins in the Thur to validate the model at three different spatial extents (see Figure 5.10a). We used a Monte Carlo approach to generate 25,000 parameter sets to ensure good coverage in the parameter space. The parameter boundaries are based on the ranges used in Figure 5.8. We based the snow parameters on the study by Teuling et al. (2010). To capture the spread in parameters as a result of equifinality, the 100 best runs based on the KGE are selected for each sub-basin. The resulting discharge time series are presented in Figure 5.10b to Figure 5.10d.

In Figure 5.10b to Figure 5.10d the simulated discharge is compared with the observed discharge for three different basins. The three basins are ordered

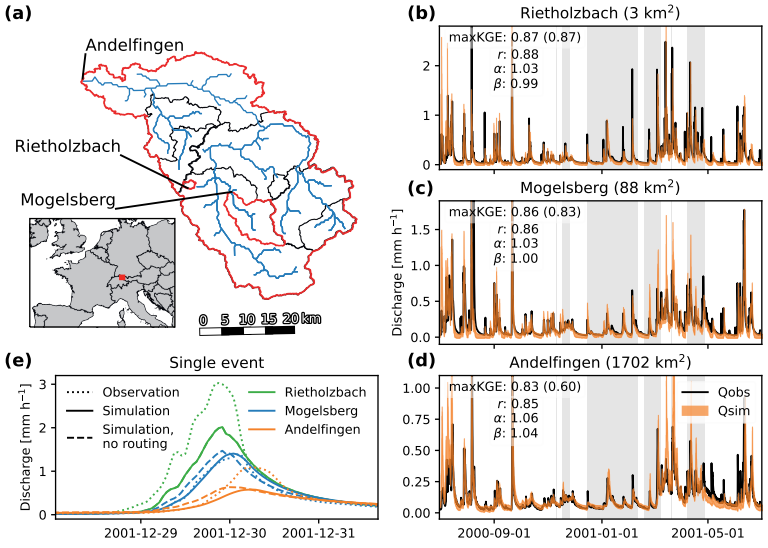

Figure 5.10 | Application of dS2 to the Thur Basin in Switzerland. Panel **a** depicts the stream network, and the catchments used in this example are highlighted in red: Rietholzbach, Mogelsberg and Andelfingen. Panels **b**, **c**, and **d** present the model output in the three basins, covering different orders of catchment size. The shaded orange region shows the minimum and maximum discharge of the 100 best runs out of 25,000, selected based on KGE value. Periods where more than 20% of the entire basin is covered with snow are indicated with the grey background. Performance values show the statistics for the best model run, with the value between brackets showing the model performance when the routing module is disabled. Panel **e** shows how a single precipitation event is translated through the different (sub-)basins, where the dotted line indicates the observed discharge, the solid line represents the simulated discharge and the dashed line represents the simulated discharge without a temporal delay induced by the routing module. Note that the simulation result without routing for Rietholzbach overlaps the simulation result with routing.

from small to large. The simple dynamical systems approach has already been applied to the Rietholzbach, the smallest of the three basins in Figure 5.10, by Teuling et al. (2010), but in a lumped fashion. We see that the distributed version of this concept is able to correctly simulate the discharge not only in this basin but also in the bigger basins. In the top left corner of each subplot, four performance statistics are presented based on the run with the highest KGE (maxKGE), Pearson correlation coefficient (r), ratio of variability (α), and bias (β). The KGE value within brackets represents the KGE without the routing module. These metrics show that there is no substantial decrease in model performance with increasing catchment size. This indicates that the model is able to correctly simulate the discharge, independent of the catchment size. We do see, however, a clear decrease in the KGE values when no temporal delay is added via the routing scheme. In the smallest basin, both KGE values show the same result, yet in the largest basin we see a substantial decrease in model performance. This indicates, in line with expectations, that the routing module is required to optimally simulate larger basins.

To elaborate this, we zoom in to a single event in Figure 5.10e. This graph shows the discharge response of the three sub-basins, and the effect of the routing module. For this event, we selected the one parameter set from the 100 sets that performed best over the period depicted in panels (b) to (d). We see that, although the magnitude of the peak is not fully captured in the Rietholzbach Basin, the timing of the peak is well simulated. Since this is a very small basin, the time lag induced by the routing module is less than 1 h, meaning that the run without the routing module gave the same result. At Mogelsberg, both the timing and magnitude of the discharge peak are well simulated by dS2. The routing module adds a correct temporal delay to the discharge peak. At the main catchment outlet (Andelfingen), we again see that the model correctly simulates the timing of the discharge but struggles to reach the correct magnitude. This is likely related to errors in the precipitation product rather than the model structure, as dS2 struggled to reach good performance in two basins in the north-western part of the catchment (Frauenfeld and Wängi). This, together with the too-low discharge peak in the Rietholzbach Basin, might explain the lack of discharge passing Andelfingen. Similar to Mogelsberg, the routing module does add a correct filter-

ing of the discharge signal due to the distribution of the stream network. Overall, the runs without the routing module indicate that the impact of the routing module depends on the size of the catchment, where the difference between these runs is largest in the biggest catchment. The differences between these runs explain the reduction in model performance in Figure 5.10b to Figure 5.10d, measured using the KGE without routing.

5.6 | Discussion

As stated in the Introduction, the aim of this chapter is not to present the best or most comprehensive conceptual rainfall–runoff model, but to develop a model that can more easily be used to perform studies that require a large number of runs, such as uncertainty or sensitivity studies. As a result, this model concept has several limitations, either linked to the original simple dynamical systems approach or linked to the (distributed) implementation of this concept.

A limitation of the simple dynamical systems approach is that it assumes that the storage–discharge relation is the same on the rising limb and on the falling limb of the hydrograph. Studies have shown that hysteresis exists in multiple basins, especially those dominated by a variable contributing area (Spence et al., 2010; Fovet et al., 2015). However, most common hydrological models do not explicitly account for hysteresis and often struggle to correctly simulate the dry-to-wet transitions (de Boer-Euser et al., 2017). In this chapter, the simple dynamical systems approach assumes a fixed storage–discharge relation, with discharge being a function only of storage. In earlier studies where the concept was applied in a lumped fashion, this did not limit the performance of the concept, especially in the studies where the $g(Q)$ parameters were retrieved from the discharge observations (Kirchner, 2009; Teuling et al., 2010). In our case study, this also did not seem to be a limiting factor. We do expect the model performance to be affected in basins exhibiting a strong hysteresis, yet we expect that one might define the $g(Q)$ function in a way that best captures the average behaviour of the rising and falling limbs.

Surface runoff as a result of either infiltration excess or saturation excess is

not explicitly accounted for. Surface runoff induced by over-saturated soils is implicitly accounted for in the discharge sensitivity function, which will reach high sensitivity values with high discharge (i.e. storage). During precipitation events with high intensity, surface runoff can also occur when the soil's infiltration capacity cannot accommodate the precipitation intensity. The model might therefore underestimate some discharge peaks resulting from infiltration excess overland flow. However, we expect that the influence of this process is minor in humid catchments. Not accounting for this process relates back to the purpose of this model, where we do not focus on correctly representing catchments' internal fluxes but instead focus on simulating the total discharge in a computationally efficient manner. It does, however, disqualify this concept for catchments with extreme precipitation events and the corresponding overland flow processes.

Furthermore, this model relies on the user to provide accurate actual evapotranspiration values as input for the model. As can be seen in Equation (5.3), evaporation is directly taken into account in determining the change in storage. Due to the simplicity of the concept, the model does not contain any evaporation reduction processes as a result of, for instance, soil moisture stress. The model disables evaporation when discharge drops below a threshold, behaving like an on–off switch, which is not how it is observed in reality. This reduction is most importantly preventing the model from calculating negative discharge values, while trying to behave like a real process.

The vectorised implementation limits the ability to transfer water between neighbouring pixels. This subsurface lateral flow is mostly driven by gravity, and is therefore expected to be most important in regions with large elevation differences. However, at the current recommended spatial–temporal scale of application ($\sim 1\,km^2$ and 1 h), we expect lateral subsurface flow to be relatively unimportant. At smaller spatial scales or longer timescales, flow between pixels can become more important. To stay in line with the original scale of the simple dynamical systems approach, we do not recommend further reducing the spatial resolution or further increasing the temporal resolution. Furthermore, most common hydrological models also do not account for flow between pixels (Liang et al., 1996; Arnold et al., 1998; Terink et al., 2015).

As proposed by Kirchner (2009), this concept can be used to "do hydrology backwards": infer precipitation from the discharge time series. Unfortunately, the distributed implementation of this concept complicates the use of this model to infer spatially distributed rainfall maps. Since the resulting discharge is an average of the integrated catchment response, it is impossible to infer the location of the precipitation event. This will become especially difficult in large basins, where the time lags induced by routing will become larger. A study by Pan & Wood (2013) describes a method to infer precipitation from streamflow observations, though it requires a relatively large number of observations. This method can potentially be applied to the model presented in this chapter.

Finally, the current technical implementation of the model implies two other limitations. First, the routing scheme only induces a time lag on the discharge peak, and it does not account for diffusion of the wave as it travels through the river network. For smaller basins, the effect of diffusion is only minor, but, when simulating larger basins such as the Rhine, diffusion of the discharge wave will play a more important role. We recommend using a more advanced routing scheme when applying the model to larger basins. The model can output a NetCDF file with runoff generated in each pixel per time step, which can easily be connected to other routing software such as SOBEK. Secondly, the current version of the model does not (yet) support multithreading, meaning that the model currently only runs on a single thread. Spreading the computational load over multiple threads is expected to further reduce the time required to run the model, especially in large basins. To make the model more efficient in single-thread mode, one can split the entire basin into several smaller sections and simultaneously run the model for each section. After the simulation is complete, the user can combine the several resulting pixel-wise runoff maps and apply a routing scheme to the entire basin.

5.7 | Conclusion

The distributed simple dynamical systems (dS2) model is a new rainfall–runoff model that aims to simulate discharge in a computationally efficient

manner. This model is based on the simple dynamical systems approach proposed by Kirchner (2009) but has been modified to be applied in a distributed fashion, written in Python. In this way, the concept can be applied to larger basins, while respecting the original spatial and temporal scale of the concept, and also make use of high–resolution data. We have extended the concept with a snow module and a simple routing module. The snow module can be turned on or off, depending on the basin of interest, and the routing module is required to transport water through the basin towards the outlet. The flexibility in the discharge sensitivity ($g(Q)$) function and the resulting strong non-linearity make this model different from more common "bucket-type" models. As a result, dS2 is able to quickly simulate hydrological response at relatively high spatial ($\sim$1 km^2) and temporal ($\sim$1 hour) resolution.

Synthetic examples demonstrate that, although dS2 solves the water balance implicitly, the model is able to accurately close the water balance. The response surface plots for all parameter combinations show that there are some correlations between the parameters, especially for the three discharge sensitivity parameters. However, we also showed that the parameters clearly influence different performance metrics, which provides the opportunity to reduce the calculation time of optimisation algorithms. Finally, we have applied the model in the Thur Basin as a case study to validate the performance of the model. Our model is able to correctly simulate discharge, both at the local scale (e.g. the Rietholzbach catchment in Switzerland, 3 km^2) and at the mesoscale (entire Thur Basin in Switzerland, 1700 km^2), without a decrease in model performance as catchment size increases.

The dS2 model has several unique strengths compared to other rainfall–runoff models: (1) it is computationally efficient even at high temporal and spatial resolutions; (2) it only has five parameters to calibrate; (3) two parameters have a clearly defined influence on the discharge time series, making them easy to identify; and (4) the Python model code is open source and easily adjustable. The computational efficiency of this model creates the opportunity to answer different research questions. Since the model is able to simulate regions in relatively short amounts of time, performing sensitivity and uncertainty analyses with a large number of samples becomes feasible.

Since the model is distributed, the sensitivity and uncertainty analyses can be performed both on a spatial and temporal basis. Furthermore, this model can be a valuable tool for educational purposes, to explain and directly show the effects of modifying parameters in distinct groups (e.g. hydrological response, snow, routing and evaporation). Overall, this makes dS2 a valuable addition to the already large pool of conceptual rainfall–runoff models, both for researchers and for practitioners interested in large sample studies.


6

The response of snow, evaporation, and discharge to higher temperatures

---

This chapter is based on:

Buitink, J., Melsen, L. A., and Teuling, A. J. (2021). Seasonal discharge response to temperature-driven changes in evaporation and snow processes in the Rhine Basin, *Earth System Dynamics*, 12, 387–400, doi:10.5194/esd-12-387-2021.

This study analyses how temperature-driven changes in evaporation and snow processes influence the discharge in the Rhine basin. Firstly, we compared two 10-year periods (1980s and 2010s) to determine how changes in discharge can be related to changes in evaporation, snowfall, melt from snow and ice, and precipitation. By simulating these periods, we can exchange the forcing components (evaporation, temperature for snowfall and melt, and precipitation), to quantify their individual and combined effects on the discharge. Around half of the observed changes could be explained by the changes induced by temperature effects on snowfall and melt (10%), temperature effects on evaporation (16%), and precipitation (19%), showing that temperature-driven changes in evaporation and snow (26%) are larger than the precipitation-driven changes (19%). The remaining 55% was driven by the interaction of these variables: e.g. the type of precipitation (interaction between temperature and precipitation) or the amount of generated runoff (interaction between evaporation and precipitation). Secondly, we exclude the effect of precipitation and run scenarios with realistically increased temperatures. These simulations show that discharge is generally expected to decrease due to the positive effect of temperature on (potential) evaporation. However, more liquid precipitation and different melt dynamics from snow and ice can slightly offset this reduction in discharge. Earlier snowmelt leaves less snowpack available to melt during spring, when it historically melts, and amplifies the discharge reduction caused by the enhanced evaporation. These results are tested over a range of rooting depths. This study shows how the combined effects of temperature-driven changes affect discharge. With many basins around the world depending on meltwater, a correct understanding of these changes and their interaction is vital.

"But rain replaces snow
and that's just pretty [...] lame"

—Chef'Special, *Birds* (2011)

6.1 | Introduction

Over the last decades, global temperatures have increased considerably (Stocker et al., 2013). The resulting change in climate is generally expected to intensify the hydrological cycle, with more frequent and more severe hydrological extremes (Huntington, 2006). As increased temperatures affect water availability in large river systems in two important ways, it is vital to understand their effects and interactions. Firstly, higher temperatures affect the cryosphere: there will be less precipitation falling as snow, and there is more energy available to enhance melt from snow and ice. As snow stores are depleted earlier in the year, it affects the timing of the snowmelt peak in the discharge signal (Jenicek & Ledvinka, 2020; Beniston et al., 2018; Baraer et al., 2012; Huss, 2011; Hidalgo et al., 2009; Collins, 2008; Takala et al., 2009). Since meltwater from "water towers" is vital for billions of people (Viviroli et al., 2007), it is important to have a correct understanding of the expected changes in the cryosphere. Secondly, higher temperatures lead to increased potential evaporation rates, since a warmer atmosphere accommodates higher transport rates (Settele et al., 2015; Wild et al., 2013; Wang et al., 2010). With increased potential evaporation rates, discharge is expected to decrease. Several recent studies have investigated the discharge response to increased temperatures and generally expect lower discharges resulting from increased evaporation and a shifted seasonality induced by the changed snow dynamics (Milly & Dunne, 2020; Mastrotheodoros et al., 2020; Rottler et al., 2020). However, the relative importance and the combined effect of evaporation and snow processes (including snowfall and snowmelt, and melt from glaciers) on discharge and its seasonal variability are currently not well understood.

Europe has experienced significant changes in evaporation, snow depth, and streamflow over the last decades. For example, Teuling et al. (2019) showed that potential evaporation has increased by about 10% over the period 1960–2010. Their study shows that both changes in precipitation and evaporation had considerable effects on the streamflow. Additionally, a study by Fontrodona Bach et al. (2018) showed that snow depth has decreased over the majority of Europe since the 1950s. Europe contains several major river basins of high socio-economic importance. One of these is the Rhine basin, with

its headwaters originating from the Alpine region. This basin covers many different types of land cover: from glaciers to lowland areas. Several studies have already investigated the response of this basin under different climate scenarios (e.g., Stahl et al., 2016; Linde et al., 2010; Hurkmans et al., 2010; Pfister et al., 2004; Shabalova et al., 2003; Middelkoop et al., 2001). Yet, none of the studies have investigated the separate and combined response of evaporation and snow processes to rising temperatures.

Spatially distributed modelling becomes increasingly viable, due to the increased computational power, gains in model performance when adding spatial information (Comola et al., 2015; Lobligeois et al., 2014; Ruiz-Villanueva et al., 2012), and increased availability of high resolution data (e.g., Huuskonen et al., 2013; Cornes et al., 2018; van Osnabrugge et al., 2017; Hersbach et al., 2018). However, the choice of spatial resolution can affect the model parameters (Melsen et al., 2016a), and the sign of the simulated anomalies (see Chapter 4). Besides, when finer spatial resolutions are used, the time step should be reduced as well, as the space and time dimensions are linked (Blöschl & Sivapalan, 1995; Melsen et al., 2016a). However, simulations run at high spatial (and temporal) resolutions usually greatly increase computational demand (for example, the study by Mastrotheodoros et al. (2020) on a 250 m resolution required more than 6×10^5 CPU hours). This not only requires the use of high-performance clusters, but also has the undesirable side-effect of increased power consumption (Loft, 2020). There is need for innovative hydrological models which can run on high spatio-temporal resolution without excessive computational demands, such as the recently developed dS2 model (see Chapter 5).

This study investigates the hydrological response to temperature-driven changes in evaporation and snow processes (snowfall and snowmelt, and melt from glaciers). We test our main hypotheses that both seasonal changes in snow processes and enhanced evaporation will aggravate low flows and that the changes will increase with temperature under realistic warming. We simulate the Rhine basin at high spatial (4 km) and temporal (1 hour) resolution using a calibrated version of the computationally efficient dS2 model, which is based on the simple dynamical systems approach (Kirchner, 2009; Teuling et al., 2010). The model was run for 2 decades, and for several scen-

arios with increased temperatures to understand both historic changes and potential changes in the future. The simulations performed at this rather unusually high temporal resolution ensure that diurnal variations—vital for evaporation and snow processes—are correctly represented. By separating the temperature-driven effects on evaporation and snow processes, we can understand and quantify the relative importance and interaction of each process.

6.2 | Methods

6.2.1 | Study area

This Rhine basin is one of the major basins situated in north-western Europe, covering several countries (see Figure 6.1, also for typical climatic values). We focus on the basin upstream of the Netherlands, as this river is of vital importance for the country (e.g. agriculture, shipping). The basin includes part of the Alps, including several glaciers. Despite this being only a small fraction of the basin (as can be inferred from the digital elevation model in Figure 6.1a), it has considerable effects on the discharge (Stahl et al., 2016). As a result, a correct understanding of temperature-driven changes is important to provide reliable discharge predictions. Despite differences in hydrological, climatic, and geological characterstics, the discharge of many basins depends on meltwater from snow and ice (Immerzeel et al., 2020). Therefore, we expect results from this study to give insight into the general hydrological response to higher temperatures.

6.2.2 | Models and data

We used the computationally efficient distributed dS2 model (see Chapter 5) to simulate discharge in the Rhine basin. The model is based on the simple dynamical systems approach (Kirchner, 2009), and is extended with snow and routing modules. As dS2 requires actual evaporation data as input, we ran a soil moisture model (BETA, Beta EvapoTranspiration Adjustment) prior to the rainfall runoff model to simulate the translation from potential evaporation (PET; calculated using the Penman–Monteith equation (Monteith, 1965)) to actual evaporation (AET). Since root zone depth is an important yet

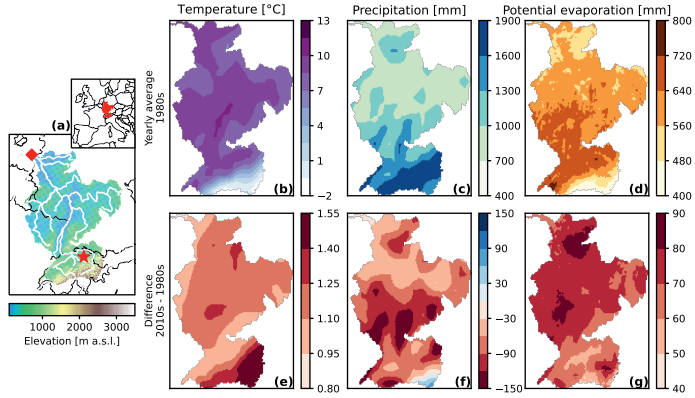

Figure 6.1 | Digital elevation model of the Rhine, and hydro-meteorological changes between the 1980s and the 2010s. Panel **a** shows the simulation domain, with white lines indicating the main river branches. The red diamond indicates the location of the main outlet, and the red star indicates the location of the Rietholzbach research catchment using for validation. Inset shows the location of the basin within Europe. Panels **b**, **c**, and **d** show the yearly average values of the 1980s for temperature, precipitation and potential evaporation respectively, and panels **e**, **f**, and **g** show the differences between the 1980s and the 2010s.

highly uncertain parameter, we included simulations with root zone depths ranging from 25 to 125 cm, with increments of 25 cm. All simulations are performed at a resolution of 4×4 km and at an hourly time step. The two models are explained in more detail below.

The input data were obtained from the ERA5 reanalysis dataset (Hersbach et al., 2018). This dataset is globally available at a $0.25 \times 0.25°$ resolution and at an hourly time step from 1979 to present. ERA5 data were interpolated to the model grid using bilinear interpolation. We selected two periods with equal length based on the maximum distance between available decades of ERA5 data: 1980-1989 and 2009-2018, referred to as the 1980s and 2010s, respectively.

Soil data were obtained from the European Soil Hydraulic Database (EU-

SoilHydroGrids ver1.0, Tóth et al., 2017). As this dataset did not contain critical soil moisture content needed by the model to distinguish between water- and energy-limited evaporation regimes (Denissen et al., 2020), it was determined as the mean between wilting point and field capacity. The hygroscopic moisture content was calculated from the moisture retention curve based on Mualem–van Genuchten parameters at -10 MPa (Laio et al., 2001; Tóth et al., 2017). The clay content of the European Soil Hydraulic Database was used to calculate the pore size distribution (b) through a linear fit of the values found in Clapp & Hornberger (1978). For the depth of the root zone, we chose a depth of 75 cm but also included simulations ranging from 25 to 125 cm with increments of 25 cm to account for the uncertainty of this parameter. The potential evaporation input data were calculated using the Penman–Monteith equation (Monteith, 1965), based on ERA5 input data.

BETA

A simple soil moisture model (BETA, Beta EvapoTranspiration Adjustment) is used to pre-process the evaporation input. This model simulates the root zone, and determines evaporation reduction based on the amount of water stored in the root zone. Actual evaporation is assumed to be a function of the available soil moisture such that

$$ET_{\text{actual}} = ET_{\text{potential}} \cdot \beta(\theta), \tag{6.1}$$

where β represents the evaporation reduction parameter as a function of soil moisture θ. β is defined using three linear relations with θ, based on Laio et al. (2001):

$$\beta(\theta) = \begin{cases} \beta_{\text{w}} \frac{\theta - \theta_{\text{h}}}{\theta_{\text{w}} - \theta_{\text{h}}} & \text{if } \theta \leq \theta_{\text{w}} \\ \beta_{\text{w}} + (1 - \beta_{\text{w}}) \frac{\theta - \theta_{\text{w}}}{\theta_{\text{c}} - \theta_{\text{w}}} & \text{if } \theta_{\text{w}} \leq \theta \leq \theta_{\text{c}} \\ 1 & \text{if } \theta_{\text{c}} \leq \theta \leq \theta_{\text{s}} \end{cases} \tag{6.2}$$

where β_{w} represents the evaporation reduction factor at wilting point (set to 0.1), θ_{h} represents the hydroscopic point, θ_{w} the wilting point, θ_{c} the critical soil moisture content, and θ_{s} the saturated soil moisture content.

Leakage from the root zone is calculated to simulate the vertical movement of water. This water is assumed to be gone from the root zone, as we do

not simulate a layer below the root zone. The leakage is based on the unit-gradient assumption in combination with the Clapp & Hornberger (1978) model for unsaturated conductivity, integrated over a time step Δt:

$$Q_{\text{leakage}} = L\theta_{\text{t}} - L\theta_{\text{s}} \left[\left(\frac{\theta_{\text{t}}}{\theta_{\text{s}}} \right)^{-2b-2} + \frac{(2b+2)k_{\text{s}}\Delta t}{\theta_{\text{s}} L} \right]^{-\frac{1}{2b+2}}, \tag{6.3}$$

where L represents the depth of the root zone, θ_{t} the soil moisture content at time step t, b the pore size distribution, and k_{s} the saturated conductivity. The value for b is calculated through the clay fraction (CF), using a linear fit based on the values in Clapp & Hornberger (1978):

$$b = 13.52 \cdot \text{CF} + 3.53. \tag{6.4}$$

Finally, the water balance for the root zone is defined as follows:

$$\theta_{\text{t}+1} = \theta_{\text{t}} + \Delta t(P_{\text{rain}} + M_{\text{snow}} - ET_{\text{actual}} - Q_{\text{leakage}}), \tag{6.5}$$

where P_{rain} is the rate of rainfall at time step t, M_{snow} the rate of snow melt at time step t, both are inferred in the same way as in the dS2 model (see below and Chapter 5).

dS2

A conceptual rainfall–runoff model is used to simulate the discharge in the Rhine basin. The dS2 model (Chapter 5) is based on the simple dynamical systems approach, as proposed by Kirchner (2009). This approach is based on the assumption that discharge is a function of storage, such that changes in storage can be related to changes in discharge via a discharge sensitivity function:

$$Q = f(S), \tag{6.6}$$

$$\frac{\text{d}Q}{\text{d}t} = \frac{\text{d}Q}{\text{d}S}\frac{\text{d}S}{\text{d}t} = \frac{\text{d}Q}{\text{d}S}(P - \text{ET} - Q), \tag{6.7}$$

where Q represents the discharge, S the storage, P and ET the precipitation and actual evaporation, respectively, and $\frac{\text{d}Q}{\text{d}S}$ the discharge sensitivity to changes in storage, referred to as $g(Q)$. This concept has been successfully

applied and validated in several catchments across Europe (Kirchner, 2009; Teuling et al., 2010; Krier et al., 2012; Brauer et al., 2013; Melsen et al., 2014; Adamovic et al., 2015). Chapter 5 describes how this concept has been modified so it can be applied in a distributed way, to allow the simulation of larger catchments, while respecting the original scale of development. A new equation to better capture the typical shape of the $g(Q)$ relation is proposed in Chapter 5, which contains three parameters:

$$g(Q) = e^{\alpha+\beta \ln(Q)+\gamma/Q}. \tag{6.8}$$

Additionally, the model has been extended with a snow module based on Teuling et al. (2010). The snow module is based on a degree-day method, adjusted to the hourly time step. This snow module is conceptualised as follows (as also described in Chapter 5):

$$\frac{\mathrm{d}S_{\text{snow}}}{\mathrm{d}t} = P_{\text{snow}} - M_{\text{snow}}, \tag{6.9}$$

$$P_{\text{snow}} = \begin{cases} P_{\text{total}} & \text{if } T <= T_0 \\ 0 & \text{if } T > T_0, \end{cases} \tag{6.10}$$

$$M_{\text{snow}} = \begin{cases} \text{ddf} \cdot (T - T_0) & \text{if } M_{\text{snow}} \cdot \Delta t <= S_{\text{snow}} \\ \frac{S_{\text{snow}}}{\Delta t} & \text{if } M_{\text{snow}} \cdot \Delta t > S_{\text{snow}}, \end{cases} \tag{6.11}$$

where S_{snow} is the total snow storage in millimetres (mm), P_{snow} is the precipitation falling as snow in millimetres per hour (mm h^{-1}), M_{snow} is the snowmelt in millimetres per hour (mm h^{-1}), T is the air temperature in degrees Celsius (°C), T_0 is the critical temperature for snowmelt in degrees Celsius (°C), ddf is the degree-day factor in millimetres per hour per degree Celsius (mm h^{-1} °C^{-1}), and Δt is the simulation time step in hours. We define separate melt factors for snow and glaciers. Partitioning of precipitation between liquid and solid precipitation (rain and snow) and melt is based on the critical temperature (set to 0°C). Routing of water is based on the width function (Kirkby, 1976), which means that lakes and other hydraulic structures are not explicitly simulated. More details on the routing module can be found in Chapter 5.

To calibrate dS2, we optimized the three discharge sensitivity parameters, the degree-day factor for both snow and glacier pixels, and an evaporation

correction factor. The evaporation correction factor is included to correct any bias errors in the forcing data. According to Boussinesq's theory of sloping aquifers (Rupp & Selker, 2006) and the results found in Karlsen et al. (2019), systems with higher slopes are expected to show higher discharge sensitivity values. Therefore, the discharge sensitivity parameters were defined as a linear function of the slope of each pixel, based on the hypothesis that regions with steeper slopes show a more responsive storage–discharge relation than regions with gentle slopes. This resulted in two fitting parameters (slope and intersect) for each of the three discharge sensitivity parameters. Latin hypercube sampling was used to gain parameter values evenly sampled across the possible parameter space. The period 2004–2008 was used for calibration. To ensure realistic model performance across the entire basin, the Kling–Gupta efficiency (KGE; Kling & Gupta, 2009) was calculated at 13 discharge measurement stations within the Rhine basin (see Appendix C for corresponding locations and performance metrics). KGE values across all stations are averaged, and the parameters from the run with the best average KGE are selected. The resulting parameter values can be found in Appendix C.

6.2.3 | Experimental setup

We have split our analysis into two parts. Firstly, we compare two decades to understand the relative impact of each forcing variable. Secondly, we increase temperature values with 0.5 degree increments to understand how an increase in temperature affects the hydrological response in the Rhine basin. We explain both experiments in more details below.

Validation

A thorough validation is required in order to ensure that models simulate the correct sign and magnitude of the trends (Melsen et al., 2018). Therefore, we validated dS2 on three variables: discharge of the total catchment and snow and evaporation dynamics. Additionally, the validation of snow and evaporation is performed at two levels: local temporal validation with point observations from the Rietholzbach research catchment (Seneviratne et al., 2012) in Switzerland (location is indicated with the red star in Figure 6.1a) and spatial validation of evaporation and snow patterns using GLEAM (v3.3, Martens et al., 2017) and the European Climate Assessment &

Data Set (ECA&D; Klein Tank et al., 2002; Fontrodona Bach et al., 2018). The Rietholzbach research catchment was selected as the data are available at a high temporal resolution (hourly), which matches our model setup. Snow observations from both the Rietholzbach and ECA&D are reported as snow depth, where dS2 simulates snow water equivalent. In the graphs, we assume a transformation factor of 0.1 (where 10 mm of snow depth represents 1 mm of snow water equivalent) but always show both axes. The ECA&D dataset only contains point observations, and no stations in France are available. Due to data availability limitations of the Rietholzbach catchment, we had to resort to our calibration period. Since dS2 was only calibrated on discharge, this can still be interpreted as validation.

Forcing swap

In the first experiment, we aim to understand how each forcing variable can explain the resulting changes in discharge, and their relative importance. To perform this, we set up the experiment according to the conceptual overview presented in Figure 6.2. The first two simulations are straightforward: using all forcing variables from either the 1980s or the 2010s to produce the corresponding discharge time series ("1980s" and "2010s"). In order to investigate how temperature influences evapotranspiration and snow processes separately, we perform model runs in which the total temperature change is separated into temperature effects on evapotranspiration ("Changed T_{evap}") and snow processes ("Changed T_{snow}"). In addition, another run is performed with only changes in precipitation ("Changed P"), so that these individual runs can be compared to a run where all changes in forcing are enabled ("2010s"). The Changed T_{evap} simulation changes the amount of evaporation which results from the new temperature time series. For the Changed T_{snow} simulation, the following snow processes are affected: type of precipitation (rain or snow), melt from snow, and melt from glaciers. This experimental setup is, to our knowledge, new and has not yet been applied in other studies. It allows us to understand changes directly driven by a change in forcing, but quantifying combined changes remains challenging (e.g. change in type of precipitation due to the interaction of precipitation and temperature). The resulting simulated discharge is compared to the 1980s run, to determine the discharge change. In this way, we can evaluate the relative impact of each forcing vari-

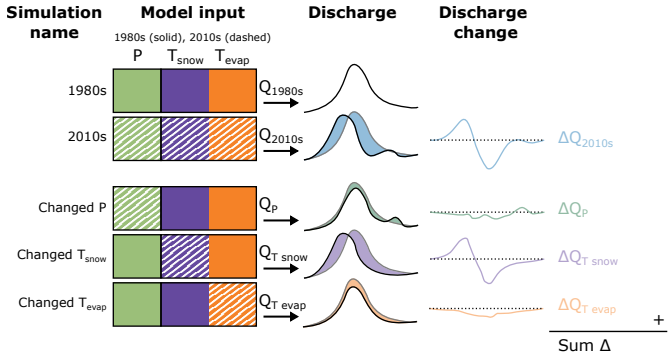

Figure 6.2 | Conceptualisation of the forcing swap experiment, showing the different simulations (rows) and steps in the analysis (columns). The different forcing variables are visualised as coloured blocks, where the solid and dashed boxes indicate forcing data from the 1980s and the 2010s, respectively.

able on the discharge.

We sum the discharge changes in the three forcing-swapped runs, to obtain $\mathrm{Sum}\Delta$ (as time series):

$$\mathrm{Sum}\Delta = \Delta Q_P + \Delta Q_{T\ snow} + \Delta Q_{T\ evap} \tag{6.12}$$

where ΔQ_x represents the discharge difference of the forcing-swapped simulations. We can use this $\mathrm{Sum}\Delta$ to study how well it explains the 2010s run, by comparing it to ΔQ_{2010s}. We hypothesise that when $\mathrm{Sum}\Delta$ is equal to ΔQ_{2010s}, the effect of the forcing is additive and together explains all differences. We will refer to this as the direct effects. In the case of a discrepancy between $\mathrm{Sum}\Delta$ and ΔQ_{2010s}, this can be attributed to the interaction between the three forcing components. We will refer to this as indirect effects. For example, temperature and precipitation are linked as the type of precipitation (rain or snow) is dependent on temperature (see Equation (6.10)): a precipitation event in the 1980s would be falling as snow with the temperature of the 1980s ($T_{\mathrm{snow}}^{1980s}$). When we swap $T_{\mathrm{snow}}^{1980s}$ with $T_{\mathrm{snow}}^{2010s}$, the same event could be classified as liquid rain leading to a direct runoff response, as opposed to the original snowfall event with snowmelt later in the year. This could also

happen vice versa or with swapped precipitation time series. The forcing-swapped simulations do not capture these interactions.

We define $\mathrm{Sum}\Delta$ to have explanatory value when it has the same sign as ΔQ_{2010s}. We calculate the contribution of the direct effects (ϕ) using the following equation:

$$\phi = \begin{cases} \frac{\min(\mathrm{Sum}\Delta, \Delta Q_{all})}{\max(\mathrm{Sum}\Delta, \Delta Q_{all})}, & \text{if } \mathrm{sign}(\mathrm{Sum}\Delta) = \mathrm{sign}(\Delta Q_{all}) \\ 0, & \text{if } \mathrm{sign}(\mathrm{Sum}\Delta) \neq \mathrm{sign}(\Delta Q_{all}) \end{cases} \tag{6.13}$$

This value can then be used to calculate the relative (direct) contribution of each forcing variable, using the following equation:

$$\phi_x = \frac{\mathrm{abs}(\Delta Q_x)}{(\mathrm{abs}(\Delta Q_P) + \mathrm{abs}(\Delta Q_{T\ snow}) + \mathrm{abs}(\Delta Q_{T\ evap}))} \cdot \phi \tag{6.14}$$

where ΔQ_x should be replaced by ΔQ_P, $\Delta Q_{T\ snow}$, or $\Delta Q_{T\ evap}$.

Increased temperatures

In the second experiment, we raise temperature in 0.5°C increments to understand how the basin responds to higher temperatures. We use the 1980s period as a baseline and increase the temperature until 2.5°C, to match realistic temperature projections. Similar to the previous experiment, we separate the effects of temperature on evaporation and snow processes: an increase in T_{evap} influences the resulting evaporation, where an increase in T_{snow} affects the type of precipitation and the melt from snow and glaciers. By separating these effects, we can understand their relative importance for each temperature increase. This is a simplified approach, as a recent study by van der Wiel & Bintanja (2021) showed that a warming climate affects not only the mean, but also the variability. The latter is not captured in our approach.

6.3 | Results

6.3.1 | Forcing comparison and validation

A first comparison of average temperature, precipitation and potential evaporation reveals considerable differences between the two periods (Figure 6.1).

Over the entire Rhine basin, yearly average temperature has increased by more than 1° C, from 8.1° C to 9.3° C between the 1980s and 2010s. The largest differences are found in the eastern Alps, where average temperature has risen by 1.5° C (Figure 6.1b, e). Average precipitation is lower in the 2010s over the majority of the Rhine basin, with the yearly average precipitation sums decreasing from 1146 mm to 1066 mm (Figure 6.1c, f). Spatial differences in precipitation are, however, less homogeneous over the basin than the changes in temperature and potential evaporation. As a result of the increased temperatures, average potential evaporation also substantially increased from 607 mm to 678 mm from the 1980s to the 2010s, with the largest increases occurring in the northern parts of the basin (Figure 6.1d, g).

Discharge validation (Figure 6.3a) shows that dS2 simulates the discharge with high KGE values in both periods. Panel b shows how the average discharge differs between the two periods, with lower discharges in the 2010s for the majority of the year. Discharge during the 2010s does not show as high discharge values in June, and shows lower discharge values occurring later in the year. Kling–Gupta efficiencies for each period and several stations within the basin can be found in Appendix C.

For the validation with data from the Rietholzbach catchment, we compare simulated actual evaporation with observed evaporation from a lysimeter and compare simulated snow storage with observed snow height measurements in Figure 6.4. Both variables are correctly represented and show similar variability as the observations, even at an hourly timescale. The simulated evaporation generally shows a smoother signal than the observations. Snow storage shows a very similar pattern. It has to be noted that snow height observations cannot be directly converted into snow water equivalent, due to, e.g., compaction. Yet dS2 simulates melt and snowfall at moments corresponding with observations, as is confirmed by the contingency table in panel b. Given that dS2 is not calibrated on these variables, and given the difference in spatial scale of the input data, this shows that dS2 is able to correctly simulate evaporation and snow processes.

This is confirmed in the spatial validation, where we compare the actual evaporation results from the BETA model with results from GLEAM (Martens

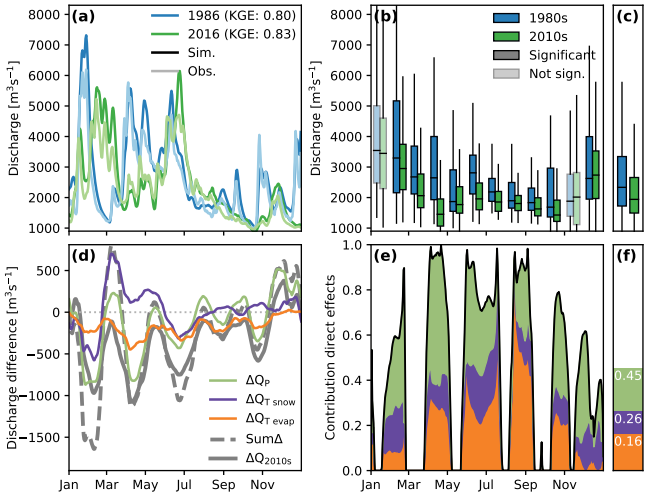

Figure 6.3 | Attribution of discharge changes between the 1980s and the 2010s. Panel **a** compares simulated (dark colours) with observed (light colours) discharge values for 1 representative year in each period. Panel **b** and **c** compare the monthly and yearly (respectively) simulated discharge values between the two periods, where fully coloured boxes are significantly different ($p<0.05$, based on independent t-test). Panel **d** shows the difference of model simulations where on the forcing time series of the 1980s has been swapped with the time series from the 2010s. Panel **e** shows the contribution of direct effects (black line), and the contribution of each forcing variable, to the total change between the two periods. Overall mean values of the time series in panel e are presented in panel **f**.

et al., 2017). We see some deviations in terms of magnitude, where BETA simulates slightly higher values than GLEAM. However, despite the differences in spatial resolution, the patterns are well represented in BETA: higher values in the southern region of the basin, with lower values in the central or northern regions. The simulated snow storage is compared with observations from the ECA&D dataset, provided by Fontrodona Bach et al. (2018). It should be noted that the observations are measured as snow height, while dS2 simulates snow water equivalent. The figure shows that dS2 simulates snow cover with a similar pattern as is observed: with high values in the Alps

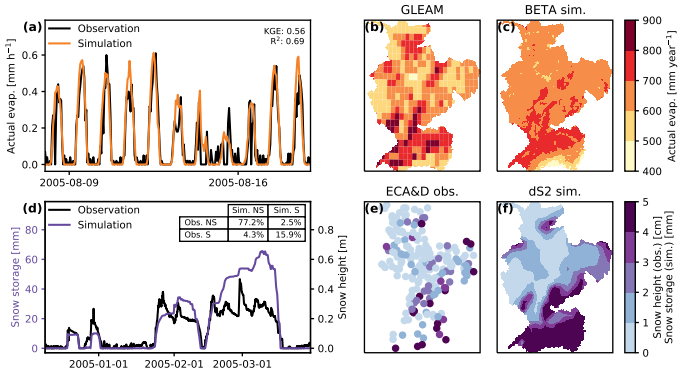

Figure 6.4 | Temporal and spatial validation of evaporation rates (**a**, **b**, **c**) and snow storage (**d**, **e**, **f**). Panels **a** and **d** show validation with observations from the Rietholzbach research catchment (location can be found in Figure 6.1a), with the table in panel **d** showing the contingency table with the percentage of occurrences with snow (S) and with no snow (NS). Note that panel **d** has two y axes: snow storage for the simulation and snow height for the observations. Panels **b** and **c** show the annual mean actual evaporation of 2005 as determined with both GLEAM and BETA (with a rooting depth of 75 cm). Panels **e** and **f** show annual mean snow heights of 2005, as observed in the ECA&D dataset (snow height in cm), and simulated with dS2 (snow storage in mm).

and south-eastern region, and low values in the central and northern parts of the basin.

6.3.2 | Forcing swap

Investigating the differences between the "forcing-swapped" runs gives insight into how each variable affects the discharge (see Figure 6.3d, e, and f). Changing the precipitation (ΔQ_P) has substantial effects on the discharge (Figure 6.3d), swinging from large negative discharge differences to positive differences. This is not unexpected, as precipitation is the factor controlling water input into the basin. Changing only the temperature related to snow processes (ΔQ_{Tsnow}, including the type of precipitation, and melt from snow and glaciers) shows discharge differences mostly in the first half of the year. The reduction in discharge in January and February is caused by overall higher

temperatures: less precipitation has fallen as snow in the preceding months (as inferred from the increased discharge at the end of the year), leading to less snowmelt in January and February. From March to May, this simulation shows higher discharge values resulting from a more direct discharge response due to more rain (instead of snow) and enhanced melt from the glaciers. From July onwards, discharge values converge back to the original 1980s simulation, indicating that the discharge regime becomes less dominated by melt from snow and ice. The simulation with evaporation from the 2010s (ΔQ_{Tevap}) shows a discharge reduction over the entire year. The higher PET leads to higher actual evaporation, decreasing the discharge.

The contribution of direct effects in Figure 6.3e-f gives an indication of the amount of interaction between the three forcing variables. Values close to 1 indicate that there is little interaction, as the sum of the differences is able to explain all changes. The contribution of direct effects is lowest during March and around October. During these periods, the storage conditions of the basin largely control the discharge response, either through snow storage or water available to generate runoff. Around March, changes in the available snow storage are the result of interactions between temperature and precipitation. Around October, discharge is controlled by water that is available for runoff generation, which is controlled by interactions of precipitation and evaporation. Additionally, since the response of a pixel is a function of its storage (through the simple dynamical systems approach), this also affects the runoff response. These interactions of forcing variables cannot be captured by simply combining the individual discharge responses, hence the relatively large contribution of indirect forcing effects during these periods. When taking the averages of the values in Figure 6.3e, the results show (Figure 6.3f) that, overall, it is possible to explain almost half of the 2010s discharge scenario by the direct forcing effects. The temperature effects of evaporation and snow (0.16 and 0.10, respectively, totalling 0.26) are just as important as the changes induced by differences in precipitation (0.19), yet due to the large role of interactions, no more than 45% can be explained using this simple addition.

6.3.3 | Increased temperatures

In the second experiment, we investigate the role of temperature increases in changes in discharge. Higher temperatures affect the hydrological cycle through evaporation, snow processes (snowfall and melt from snow and ice), or a combined effect of the two. Using the dS2 model, separate simulations of temperature effects on evaporation (Q_{Tevap}), snow (Q_{Tsnow}), and their combined effect (Q_{Tboth}) allow us to understand which variable is causing the main changes. These time series are presented in Figure 6.5a, including the 1980s run as a reference. Throughout the year, we see a near-constant reduction in discharge, without clear seasonal patterns. To investigate this further, we highlighted three periods representing typical discharge regimes: high discharge during January and February, the meltwater peak during May and June, and low discharge during September and October. For each of these periods, the change in discharge shows a roughly linear relation with temperature increase. This is in line with our hypothesis, that higher temperatures will lead to larger differences in discharges. The resulting near-linear relation is interesting, as both snow and evaporation processes are threshold processes through their relation with temperature and soil moisture, respectively. We expect to see a more non-linear response to temperature when reaching more hydrological extremes.

Surprisingly, for the periods during January-February and September-October (Figure 6.5b, d), the modified snow run shows behaviour that is the opposite of both the modified evaporation run and the combined run. In these cases, the increased discharge as result of a change in snow processes (more liquid precipitation, and more meltwater production from the glaciers) slightly offsets the negative discharge change induced by the increased evaporation. This ensures that the combined reduction in discharge is less severe than when only the reduction induced by evaporation is considered. However, during May-June (Figure 6.5c), both evaporation and snow processes show a negative discharge change, enhancing the combined negative change in discharge. During this period, less snow was available to melt, leading to a reduction in discharge. As a result, the discharge of the combined run shows an even larger reduction in discharge, where even the peak during June from the 1980s has been largely diminished (Figure 6.5a). The

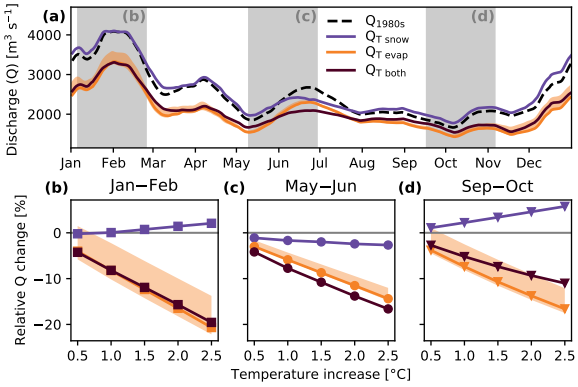

Figure 6.5 | Discharge sensitivity to temperature increase. Panel **a** shows the yearly average discharge under a 2.5°C increase, and panel **b** shows changes during typical discharge events with stepwise temperature increases. Typical discharge periods highlighted in panel **a** match the periods used to compare the mean discharges in panels **b**, **c**, and **d**. Shaded orange areas indicate the uncertainty induced by effective rooting depth (25–125 cm), where higher discharges match shallower depths and vice versa.

exact response of the type of precipitation, snow depth, cover, and melt, and melt from glaciers for each temperature increase can be found in Appendix C. A substantial influence of rooting depth on the evaporation simulation is visible (shaded orange areas in Figure 6.5), yet the trend direction with increasing temperatures remains equal. Shallower rooting depth values induce more soil moisture stress since less water is available, leading to higher average discharges.

To understand the cause of these changes, the change in generated runoff per model pixel is shown in Figure 6.6a. This figure shows that the majority of the basin produces less runoff for all three periods. Only the southern regions of the basin show a different response. During January and February, these regions produced more runoff, resulting from the increased snowmelt and increased liquid precipitation. In the other periods, only a few pixels produced more runoff. These pixels correspond to the glaciers in the Alps, which produced more meltwater resulting from the increased temperatures, and

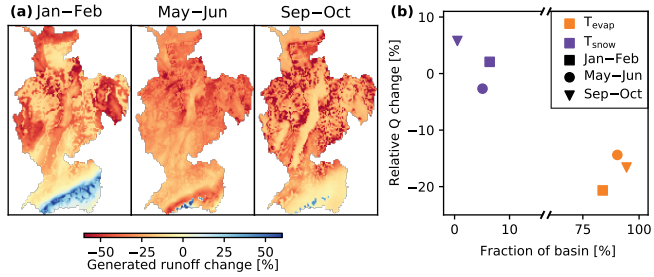

Figure 6.6 | Spatial differences in the Rhine basin under the +2.5°C scenario. Panel **a** shows the differences in generated runoff for the three periods highlighted in Figure 6.5a. Panel **b** shows the fraction of the basin where 80% of the changes could be explained by either evaporation or snowmelt and the average discharge change corresponding to each process.

explain the positive discharge change in Figure 6.5d.

In Figure 6.6b, the fraction of the basin that is dominated by one of these three options is plotted against the relative change in mean discharge for each period. As expected, the majority of the basin is mainly influenced by evaporation (84–94%). As a result, the mean discharge is reduced by $\pm$17%. By contrast, a limited fraction of the basin (1–6%) is mainly influenced by snow processes, yet still has a considerable effect on the mean discharge, varying between $-$3% and 6%, depending on the period. Pixels in the basin where neither snow nor evaporation appeared dominant take up only a very small fraction of the basin (<1%). Generally, these regions are at the transition between snow-dominated and evaporation-dominated regions. Overall, the change induced by T_{snow}—despite the small contributing area—substantially affects the discharge. More details on the response for each temperature increase can be found in Appendix C.

6.4 | Discussion

We compared two periods of 10 years to investigate the relative importance of changes in temperature, evaporation, and precipitation. Over these peri-

ods of 10 years, most interannual variability is averaged out, allowing us to objectively investigate the effect of different temperatures on the hydrological response. However, decadal variation remains present, but due to the length of these periods, it is not possible to fully contribute these changes to a change in climate.

When validating the model with data from the Rietholzbach, the simulated evaporation in the Rietholzbach showed a smoother signal than the observations. Deviations between the observations and simulations could be caused by the relatively coarse ERA5 data. Especially in the spatially heterogeneous Alps, a single ERA5 pixel could miss some local variations (such as variations in cloud cover, radiation, wind, and/or temperature), causing a smoother signal in the simulated evaporation. For the spatial evaporation validation with GLEAM, it should be noted that this is not a true validation, since GLEAM is not a completely independent observational dataset. Despite this, GLEAM is often considered as a reference for spatio-temporal validation of ET. Additionally, BETA uses a single rooting depth value for the Rhine basin.

The choice of spatial model resolution is a balance between data availability, computational time and underlying modelling concept. Here we selected a resolution of 4×4 km, so we can use the ERA5 forcing data with bilinear resampling (without adding more degrees of freedom, uncertainty, and potential errors), have short run times (simulating 10 years including all input/output operations takes just over 5 minutes on a normal desktop), and apply the model at its proven spatio-temporal scale (±10 km^2 at hourly time step). By contrast, the study by Mastrotheodoros et al. (2020) used a much finer spatial resolution but at the cost of enormous CPU times.

Several other recent studies have investigated the hydrological response to increased temperatures via either changes in evaporation and/or snow processes (snowfall and melt from snow and ice). Below, we compare our results with the results found in three of these studies. Firstly, the study by Rottler et al. (2020) showed a decrease in runoff seasonality in rivers fed by meltwater from snow, over the period 1869–2016. They found higher discharges during winter and spring and lower discharges during summer and autumn. The authors conclude that reservoir construction in these snow-dominated

rivers is likely to cause this redistribution of discharge. However, our temperature experiment shows a similar change in discharge: with higher discharges in winter and spring and lower discharges during summer. As the dS2 model does not include dams and other reservoirs, this signal can be attributed to a change in discharge production. Secondly, a recent study investigating the response of several basins in Czechia to changes in snowmelt, concluded that snowmelt started earlier in the year, which also reduced summer low flows via baseflow (Jenicek & Ledvinka, 2020). However, our study shows that low flows during September and October actually increased when only snow processes are considered. This can be explained by that fact that the Rhine basin includes glaciers, which produce more meltwater with higher temperatures (assuming the glacier is thick enough to facilitate this melt). This increase in meltwater resulted in higher discharge volumes during summer. Thirdly, Milly & Dunne (2020) showed a reduction in discharge in the Colorado river basin and conclude that this is driven by increased evaporation. This increase in evaporation is attributed to a reduction in snow cover and hence a decreased albedo. Despite the different basin, our study supports the conclusion that increased temperatures reduce discharge through both changes in snow processes, and increased evaporation. Our model does not account for changes in albedo but does allow areas previously covered in snow to evaporate water. And while differences in climate zone between the Colorado and Rhine basins make it challenging to compare the absolute numbers, the sign of the trend is equal.

Musselman et al. (2017) concluded that there was a lowering of snowmelt rates due to a shift in the melt season towards a period with lower available energy (spring instead of summer). They simulated the snowpack with a more complex energy balance rather than our degree-day method. The dS2 model does not include the radiation-driven changes, but does simulate that snowmelt occurs earlier in the year. This means that, under increased temperature scenarios, snowmelt occurs on days where previously no melt was possible. Additionally, dS2 does simulate earlier depletion of the snowpack, which also reduces snowmelt rates. Despite our different aim and approach, we believe that our study supports the findings of Musselman et al. (2017).

The glaciers used in our model are fixed in space, and no growing or shrink-

ing of glaciers is simulated. While the approach is common for shorter-timescale studies such as ours (van Tiel et al., 2018), it limits the interpretation of our results several decades into the future. The study by Lutz et al. (2014) included a glacier mass balance and showed that melt from glaciers increased before the glaciers eventually disappear. Without glaciers, increases in drought severity are expected, as less meltwater is produced during the summers (van Tiel et al., 2018; Huss, 2011). After 2050, substantial changes in summer flow resulting from the reduction in glacierised area are expected (Huss, 2011). Until this period, we expect our results to be representative.

When comparing our results with results from studies perform in the Rhine basin (e.g., Linde et al., 2010; Hurkmans et al., 2010; Pfister et al., 2004; Shabalova et al., 2003; Middelkoop et al., 2001), we see similar results. These studies focussed mainly on understanding and/or projecting the Rhine discharge under climate scenarios. Yet all these studies agree that the snowmelt peak will occur earlier in the year and that the basin is expected to transition from a mixed rain- and snow-fed river to a mostly rain-fed river. Additionally, all studies agree to expect higher evaporation rates, further reducing the discharge. This is all in line with our study, despite the fact that we did not investigate changes in precipitation in our temperature scenarios. Furthermore, the Rhine basin contains several hydraulic control measures, which are currently not represented in our model structure. Despite this, we still reach good model performance, suggesting that these structures currently do not have a very large influence on the discharge dynamics at the basin outlet. In the future, however, the management schemes and number of structures can be altered to accommodate the changes in the hydrological cycle. As these changes are a large unknown, we decided to only focus on the natural hydrological response.

6.5 | Conclusions

Temperature, evaporation, and precipitation substantially changed from the 1980s to the 2010s in the Rhine basin, reflecting changes that are typical for many larger basins around the world. In the 2010s, basin average temperature was more than 1°C higher, potential evaporation was almost 70 mm

higher, and precipitation decreased with 80 mm. Discharge between these two periods was significantly different for 10 out of 12 months. Each individual forcing variable can partly explain these discharge differences: 10% can be explained by the changed snowfall and melt dynamics, 16% is explained by the changed evaporation, and 19% by the changed precipitation, leaving 55% to be explained by the interaction of these variables. As differences in evaporation, snowfall and melt are driven by changes in temperature, the temperature effect is larger (26%) than the changes induced by changes in precipitation (19%).

With higher temperatures, discharge is expected to decrease, resulting from the positive effect of temperature on (potential) evaporation. However, snow processes (more liquid precipitation and enhanced melt from glaciers) can partially offset the negative change in discharge during the low flows in September-October, which was contrary to our expectations. The discharge response during May-June matches our hypothesis that both changes in snow processes and evaporation enhance the reduction in discharge. This is a result of the combined effect of enhanced evaporation and a reduction in snowpack leading to less snowmelt.

This study focusses on the Rhine basin, yet these results can provide insight for the many different basins around the globe, which also depend on both rain- and snowfall. With higher temperatures, changes in snow processes slightly offset the discharge reduction from enhanced evaporation over the majority of the year. However, the season where runoff generation is reduced due to smaller snow stores (and potentially smaller glaciers) should be identified in each basin, as this part of the year is impacted the most. Many regions rely on water towers for their year-round water availability (Immerzeel et al., 2020), where the mountainous regions cover varying fractions of the basin. In many basins, more of the discharge originates from these water towers than in the Rhine basin, amplifying our results. Here, higher temperatures would likely imply even stronger negative amplitudes in discharge trends during the melt season. Enhanced melt from glaciers and a shift from snow to rain can partially offset the negative change in discharge caused by the increased evaporation but can enhance the negative change when snow stores are eventually depleted earlier in the year.

7

Sensitivity of evaporation and low flows to CO_2-induced changes in temperature and vegetation

---

This chapter is based on:

Buitink, J., Melsen, L. A., and Teuling A. J. (2021). Sensitivity of evaporation and low flows to CO_2-induced changes in temperature and vegetation

The increase in atmospheric CO_2 concentration is known to influence temperature, which ultimately affects the hydrological response of a river basin through changes in evaporation. Besides changes in temperature, an increase in CO_2 concentration is also known to influence vegetation, affecting the amount of transpiration from plants. We investigate the hydrological response of the Rhine basin to CO_2-driven changes in stomatal resistance, leaf area index, and temperature. The summer drought of 2018 is used as baseline, to understand how low flows are affected for a similar event but with elevated CO_2 concentrations. We showed that potential evaporation is expected to increase with all three factors enabled. Temperature is the most dominant factor (decreasing the discharge with -17%), followed by stomatal resistance (increasing the discharge with $+4\%$). Increases in leaf area index have only very minor effects on the hydrological response. Overall, discharge is reduced over the entire year with -14%. This reduction was smaller during the summer period. This is the result of water-limited conditions, causing a relatively large reduction from potential to actual evaporation. A sensitivity study confirmed that these patterns are consistent over a range of different responses of stomatal resistance, leaf area index and temperature. This study highlights that the vegetation effects, in particular the increase in stomatal resistance, need to be considered in studies with elevated CO_2 concentrations. Not accounting for this process can lead to an annual overestimation in potential evaporation of nearly 60 mm $year^{-1}$ (7% of average 2018 potential evaporation) and an annual average underestimation in discharge of 57 m^3 s^{-1} (3% of the average 2018 discharge). This can have substantial impacts on the estimation of future low flows in basins such as the Rhine.

"Will it flow into the river
Or will it go to waste?"

—Nothing But Thieves, *Before We Drift Away* (2020)

7.1 | Introduction

The atmospheric concentration of carbon dioxide is an important factor in maintaining Earth's greenhouse effect, which is critical in supporting life. Carbon dioxide is often referred to as a "greenhouse gas", as it has the ability to absorb and re-emit long wave radiation (Hartmann et al., 2013). This warms both the atmosphere and the earth's surface. However, the concentration of CO_2 in the atmosphere has increased significantly over the last century, resulting from human activity (Stocker et al., 2013; Hartmann et al., 2013). This increase in concentration enhances the greenhouse effects, leading to a warming of the planet, and is one of the main factors responsible for climate change (Stocker et al., 2013). Additionally, the CO_2 concentration is expected to further increase in the future, making climatic changes even more prominent (Stocker et al., 2013). With this change in climate comes a change in the response of hydrological systems. In general, the hydrological cycle is expected to "intensify" (Huntington, 2006), meaning that hydrological extremes occur more frequent and are more severe. Many studies have been devoted to understand how these changes in climate affect the local hydrological response. However, these studies generally only focus on the changes in temperature (such as Chapter 6) and/or precipitation and do not include the response of vegetation to an increased CO_2 concentration.

Prior to understanding the hydrological response, we first shortly discuss the changes in vegetation and their effects on evaporation. Firstly, the physiological response of vegetation to an increase in atmospheric CO_2 concentration is a long studied subject, and rather well understood. Two main changes in vegetation to an increase in CO_2 concentration can be identified that are relevant for the hydrological response: an increase in stomatal resistance and an increase in leaf area index (LAI). Due to the increase in atmospheric CO_2 content, plants' stomata need to open less to capture the same amount of carbon, and the density of stomata is reduced: both are effectively increasing the stomatal resistance (Ball et al., 1987; Kimball et al., 1993; Medlyn et al., 2001; Ainsworth & Rogers, 2007; Lammertsma et al., 2011). As a result, less water is transported from the leaf to the atmosphere. As the second response, an increase in LAI is often observed. This is the result of higher carbon contents in the atmosphere enhancing the growth of plants (Kimball et al., 1993;

de Graaff et al., 2006). These two responses in vegetation affect the amount of transpiration: where the increased stomatal resistance reduces the transpiration, the increased leaf area enhances the amount of transpiration and rainfall interception.

The interaction of these two processes has also been widely studied across varying study regions and with slightly different conclusions. Several studies agree that on a global scale, the increase in stomatal resistance and the increase in LAI are in the same order of magnitude, and effectively counteract each other (Notaro et al., 2007; Kergoat et al., 2002; Betts et al., 2000; Douville et al., 2000; Levis et al., 2000). However, these results might not be valid on a regional scale, indicating that one of the two components can have a more pronounced impact on the resulting evaporation. For example, Keenan et al. (2016) concluded that the direct effects of stomatal resistance is much larger than the indirect effect of increased leaf area index. Additionally, Kruijt et al. (2008) compared the effects of stomatal resistance with the temperature effects of an increased CO_2 concentration. They concluded that the effects of stomatal resistance can slightly counteract the increased evaporation resulting from the higher temperatures. These studies highlight that the change in evaporation resulting from the combined response of increased stomatal resistance and increased LAI, together with higher temperatures, is not trivial.

The water balance dictates that a change in evaporation affects the hydrological response of a basin. Despite that the role of vegetation is rather well understood, their response is not always accounted for in hydrological models. Wang & Dickinson (2012) explain that the response of vegetation to CO_2 in land surface models is often based on short-term observations, meaning that the plants might not yet have fully adapted to the new CO_2 concentration. Specifically, if the process of increased stomatal resistance is not accounted for, potential evaporation estimates are likely too high (Milly & Dunne, 2016). This has major implications for the resulting discharge estimates. Recent changes in vegetation associated with the increasing atmospheric CO_2 concentration have showed to reduce the baseflow in Australia (Trancoso et al., 2017). Some other studied tried to quantify the hydrological response under potential future climate conditions. For example, Leipprand

& Gerten (2006) studied the hydrological response under a doubled CO_2 concentration. They concluded that both the changes in stomatal resistance and LAI seem to counter each other on a global scale, as they observed only very minor changes in evaporation, soil moisture and runoff. However, they also stress that the interaction between stomatal resistance and LAI can have a strong (positive or negative) sign on the regional scale, indicating that more detailed research is required. In an effort to focus on regional scales, Wu et al. (2012) studied this interaction in the Upper Mississippi river basin. They showed that, when increasing the CO_2 concentration, evaporation was reduced throughout the year (excluding the effect of temperature). A novel approach was used by Yang et al. (2019) to extract the hydrological response from Coupled Model Intercomparison Project Phase 5 models. They showed that in these models, the increased evaporation resulting from higher temperatures is almost fully offset by the increase in stomatal resistance. They did, however, not include the response of LAI to the rising CO_2 concentrations. The study by Singh et al. (2020) did include this increase in LAI, and showed that it counteracts the changes induced by the change in stomatal resistance. In conclusion, a study investigating the sensitivity of changes in stomatal resistance and LAI to changes in evaporation and discharge in a mesoscale basin is—to our knowledge—lacking.

Due to the seasonal patterns in temperature and incoming radiation, evaporation is generally highest during the summer period. In regions without strong seasonal variations in precipitation, such as northwestern Europe, discharge values are generally lowest during the summer period. As a result, a change in evaporation during its peak values can have large implications on the resulting discharge, and therefore also on the low flows. Over the past decades, Europe has experienced several widespread drought events (e.g., 2002, 2003, 2015) (van Hateren et al., 2021). Just recently, northwestern Europe experienced severe drought conditions during the summer of 2018. This period was a combination of low precipitation, high temperatures, and high incoming radiation, with high evaporation rates and low discharge values as a result, as can be seen in Figure 7.1. Vegetation was also shown to be impacted by this drought, as was inferred from a reduction in net ecosystem productivity (Bastos et al., 2020). This was mostly caused by reductions in soil moisture values (see Chapter 3, Smith et al., 2020). Northern regions

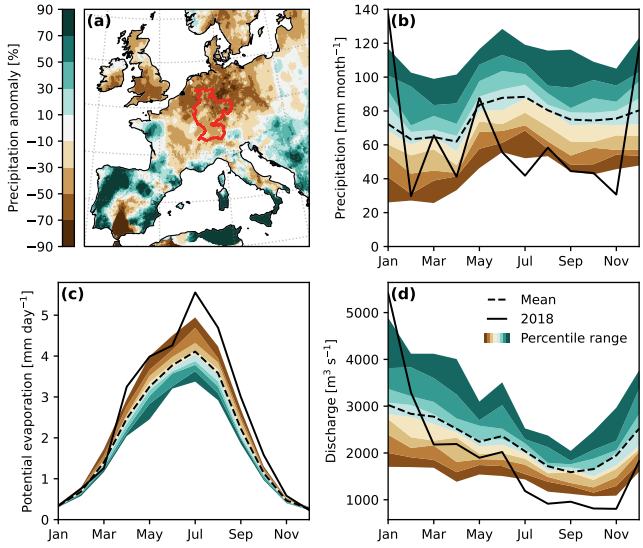

Figure 7.1 | Spatial and temporal characteristics of the 2018 summer drought. Panel **a** shows the precipitation anomaly of June, July, and August of 2018 with respect to the period 1980–2018 (based on the E-OBS v20.0e dataset; Cornes et al., 2018). Red outline shows the catchment area of the Rhine basin. Precipitation (**b**), potential evaporation (**c**), and discharge (**d**) of the Rhine basin in 2018 (solid black line) are compared with the 10–90% percentile distribution (shaded area) and the long term mean (dashed line) over the period 1980–2018.

in Europe were also affected, where anomalies in precipitation, groundwater levels and streamflow were observed (Bakke et al., 2020). Combined with climate projections (Stocker et al., 2013), these drought conditions are expected to occur more frequent in the future. As a result, it is vital to understand how evaporation and low flows are affected by CO_2-induced changes, especially during summer droughts when potential evaporation values peak. Incorrect evaporation estimates can lead to substantial errors in discharge (and water level) projections.

In this study, we quantify the sensitivity of evaporation and low flows to CO_2-

induced changes in stomatal resistance (r_s), leaf area index (LAI) and temperature (T) in the Rhine basin. We focus on the Rhine basin, as this basin is of major socio-economical importance to northwestern Europe, and covers several different land cover types. As the year 2018 provided an impression for potential future drought conditions, this year was used as a baseline to understand how the basin responds to increased CO_2 levels, translated to three factors (temperature, stomatal resistance, and LAI). This raises the question of how the Rhine basin will respond to a similar event in terms of atmospheric circulation and associated precipitation, but with an elevated atmospheric CO_2 concentration. Simulations using the dS2 model allow us to quantify the separate and combined effects of these factors on evaporation and low flows. By using different values representing the relation between increase in CO_2 concentration and r_s, LAI, and T, we quantify the sensitivity of evaporation and low flows to these changes, and address the importance of capturing these processes in long-term hydrological studies.

7.2 | Methods

7.2.1 | Study area

For this study, we focus on the Rhine basin, specifically at the catchment upstream of the Netherlands. This is one of the major basins in northwestern Europe, and is of major importance for this region for industry, agriculture, drinking water supply, and shipping. As a consequence, hydrological extremes (both floods and droughts) can have significant economical consequences. A correct understanding of the response of the Rhine basin under elevated CO_2 conditions is vital to potentially avoid large economic losses in water resources management, infrastructure, and transport.

7.2.2 | Models

For this study, we employed the same modelling setup as used in Chapter 6. Prior to running the hydrological model (dS2), we run a simple soil model (BETA) to calculate the actual evaporation. In the BETA model, potential evaporation is determined using the Penman–Montheith equation (Mon-

teith, 1965):

$$E_{pot} = \frac{0.408\Delta(R_n - G) + \gamma \frac{900}{T+273} u_2 (e_s - e_a)}{(\Delta + \gamma(1 + \frac{r_s}{r_a}))},$$

where E_{pot} is the potential evaporation in mm h^{-1}, Δ is the saturation slope vapour pressure curve at T in kPa $°C^{-1}$, R_n is the net radiation in MJ m^{-2} $hour^{-1}$, G is the soil heat flux in MJ m^{-2} $hour^{-1}$, γ is the psychrometric constant in kPa $°C^{-1}$, T is the air temperature in °C, u_2 is the wind speed at 2 meter in m s^{-1}, e_s is the saturation vapour pressure at T in kPa, e_a is the actual vapour pressure in kPa, r_s is the surface resistance in s m^{-1}, and r_a is the aerodynamic resistance in s m^{-1}.

As this study is aimed specifically to understand the hydrological response to three CO_2-driven responses (r_s, LAI, and T), we modified these variables to include a dependency on atmospheric CO_2 concentration. The relation for r_s is based on the work of Yang et al. (2019), and was taken as inspiration for the two other relations. The r_s relation was combined with the original definition from Allen et al. (1998), to include LAI into the Penman–Montheith equation. A similar relation was used for the increase in temperature. This resulted in the following three relations:

$$r_s(CO_2) = \frac{r_l}{LAI} + \Delta r_s \cdot \Delta CO_2,$$
$$LAI(CO_2) = LAI + \Delta LAI \cdot \Delta CO_2,$$
$$T(CO_2) = T + \Delta T \cdot \Delta CO_2,$$

where r_l is the bulk stomatal resistance of the well illuminated leaf in s m^{-1}, LAI is the leaf area index, Δr_s is the change in r_s as function of change in CO_2 concentration in ppm (ΔCO_2), ΔLAI is the change in LAI as function of change in CO_2 concentration in ppm, ΔT is the change in T as function of change in CO_2 concentration in ppm.

We used varying values for the Δr_s, ΔLAI, and ΔT, inferred from the studies below. Both the r_s and LAI slope values are based on the study by Yang et al. (2019). The relation between CO_2 and temperature is based on the scenario predictions made by IPCC (Stocker et al., 2013), matching the expected

Table 7.1 | Relation between vegetation characteristics, temperature and CO_2 concentration. Slope is defined as function of $x_{new} = x + \text{slope} \cdot \Delta CO_2$, similar to the approach of Yang et al. (2019)

	Slope			Value at +400 ppm CO_2		
	min	mean	max	min	mean	max
Δ r_s	$1.67 \cdot 10^{-2}$	$5.00 \cdot 10^{-2}$	$8.33 \cdot 10^{-2}$	6.67	20.00	33.33
Δ LAI	$1.02 \cdot 10^{-4}$	$3.06 \cdot 10^{-4}$	$5.10 \cdot 10^{-4}$	$4.08 \cdot 10^{-2}$	$1.22 \cdot 10^{-1}$	$2.04 \cdot 10^{-1}$
Δ T	$3.00 \cdot 10^{-3}$	$9.00 \cdot 10^{-3}$	$1.50 \cdot 10^{-2}$	1.20	3.60	6.00

temperature increase around 2100 according to the RCP 8.5 scenario. Several values for each relation (ranging between the minimum and maximum slope values in Table 7.1) are used to account of uncertainty in those values, and to understand the sensitivity of the hydrological response. We set ΔCO_2 to +400 ppm, to be in line with conditions around 2100 following the RCP8.5 scenario (Stocker et al., 2013). The resulting different PET time series are fed through the BETA and dS2 model to quantify their effects on the hydrological response.

7.2.3 | Data

Input data for both models were obtained from the ERA5 reanalysis dataset (Hersbach et al., 2018), which is globally available at a $0.25° \times 0.25°$ and hourly resolution. This data was interpolated using bilinear interpolation to the model grid (4 km$\times$4 km). We run simulations for the period 2016–2018, such that 2016 and 2017 are used as a warm-up period, and we focus on the year of 2018. As mentioned earlier, the dry conditions experienced during 2018 are expected to occur more frequent in the future (e.g. with higher CO_2 concentrations), hence we focus on the response of the basin during this year.

Soil data for the BETA model were obtained from the European Soil Hydraulic Database (EU-SoilHydroGrids ver1.0, Tóth et al., 2017). No critical soil moisture content data were available in this dataset, so it was taken as the mean between wilting point and field capacity. The moisture retention curve based on Mualem–van Genuchten parameters at -10 MPa (Laio et al., 2001; Tóth et al., 2017) was used to calculate the hygroscopic moisture content. The clay

content of the European Soil Hydraulic Database was used to calculate the pore size distribution through a linear fit of the values found in Clapp & Hornberger (1978). We chose a depth of 75 cm for the rootzone, but varied it for the sensitivity analysis (see below).

Discharge data for calibration and validation, and to determine the 10th percentile scores are obtained from the Dutch Directorate-General for Public Works and Water Management (Rijkswaterstaat). The 10th percentile is calculated for the main basin outlet (Lobith) based on monthly discharge data, covering the period 1901–2018. The hourly simulated values are compared with this threshold for each corresponding month.

7.2.4 | Simulation setup

Calibration and validation

A similar approach as used in Chapter 6 was used to calibrate dS2. We selected the period 2004–2008 for calibration, and used Latin hypercube sampling to create a sample of all required parameters. We sampled the following parameters: three discharge sensitivity parameters, degree-day factor for both snow and glacier pixels, and an evaporation correction factor. The latter is to correct any bias errors in the forcing data. The three discharge sensitivity parameters were defined as a linear function of slope, resulting in two fitting parameters (slope and intersect) for each discharge sensitivity parameter. As a result, a spatial parameter field as function of slope was created for each discharge sensitivity parameter. The Nash–Sutcliffe efficiency (NSE; Nash & Sutcliffe, 1970) was calculated based on the logarithm of the discharge, to put emphasis on the model performance during low flows. The NSE was calculated at 13 discharge measurement stations throughout the Rhine basin, to ensure good model performance across all sub-basins. The mean NSE across all stations was used to select the best performing parameter set. We validated the model for the year 2018, with a special focus on the low flow simulations.

Hydrological simulations and metrics

We focus on the hydrological response over the year 2018. As this event had major economic consequences, it is important to understand the effects of

higher atmospheric CO_2 concentrations in the Rhine basin. As the aim of this study is to quantify CO_2-driven feedbacks in evaporation, we decided to only change the evaporation time series. This allows us to elegantly quantify and describe the hydrological response to each of the three considered feedbacks in evaporation. This means that no changes in precipitation and temperature (affecting snowfall and melt from snow and ice) are considered.

To understand how the Rhine basin responds to CO_2-driven changes in r_s, LAI and T, we investigate both the individual effects and the combined effects. We run five simulations: first without any CO_2-driven changes (e.g. the baseline), three simulations with each individual effect enabled, and lastly a simulation with all changes enabled. This modelling setup allows us to investigate both the individual and combined response of the basin to each change. Additionally, we can determine the relative contribution of each effect to the total changes, by using the following equations (similarly to the approach used in Chapter 6). These equations are shown for discharge (Q), but are similar for the calculation of contribution in PET and AET. The changes in the three runs with each process separated are summed to obtain $\mathrm{Sum}\Delta$ (as time series):

$$\mathrm{Sum}\Delta = \Delta Q_{rs} + \Delta Q_{LAI} + \Delta Q_{T} \tag{7.1}$$

where ΔQ_x represents the discharge difference of each separate simulation with respect to the original 2018 simulation. By comparing $\mathrm{Sum}\Delta$ with ΔQ_{All} (the discharge difference between the simulation with all effects enables and the original 2018 simulation), we can quantify how well this approach explains the simulation with all three factors simultaneously enabled. When $\mathrm{Sum}\Delta$ is equal to ΔQ_{All}, we assume the individual effects to be additive, and can together explain all differences (referred to as direct effects). When there is a difference between $\mathrm{Sum}\Delta$ and ΔQ_{All}, we attribute these differences to the interaction between the three components, such as changes in rootzone water content (referred to as indirect effects). To quantify the contribution of each individual factor, we use the following equation. Firstly, we set $\mathrm{Sum}\Delta$ to have explanatory value when it has the same sign as ΔQ_{All}:

$$\phi = \begin{cases} \frac{\min(\mathrm{Sum}\Delta, \Delta Q_{All})}{\max(\mathrm{Sum}\Delta, \Delta Q_{All})}, & \text{if } \mathrm{sign}(\mathrm{Sum}\Delta) = \mathrm{sign}(\Delta Q_{All}) \\ 0, & \text{if } \mathrm{sign}(\mathrm{Sum}\Delta) \neq \mathrm{sign}(\Delta Q_{All}) \end{cases} \tag{7.2}$$

This value is used to calculate the direct contribution of each individual factor (ϕ) according to the following equation:

$$\phi_x = \frac{\text{abs}(\Delta Q_x)}{(\text{abs}(\Delta Q_{rs}) + \text{abs}(\Delta Q_{LAI}) + \text{abs}(\Delta Q_T))} \cdot \phi \tag{7.3}$$

where ΔQ_x should be replaced by ΔQ_{rs}, ΔQ_{LAI}, or ΔQ_T.

Sensitivity analysis

To account for uncertainty in the mean values as provided in Table 7.1, we performed a sensitivity analysis on the slope defining the relation between each process and CO_2 concentration. These values range between the minimum and maximum values presented in Table 7.1, including completely disabling the relation with CO_2. Additionally, we step-wise increased all slope values simultaneously to understand the interactions of these processes over a range of values. To account for uncertainty in the rootzone depth, all these simulations are performed over four different rootzone depths: ranging from 0.50 m to 1.25 m, with steps of 0.25 m.

The effect on discharge is investigated through two discharge metrics: the percentage of time that the simulated discharge of 2018 is below the long-term tenth percentile discharge value, and the minimum flow during 2018. For the spatial differences, we grouped the simulations by season, and compare the simulations with all components enabled with the default 2018 simulation. We investigate the response during spring and summer, as these are the periods with highest evaporation values.

7.3 | Results

7.3.1 | Effect on the hydrological response

In the first analysis, we compare the simulated discharge values with the observed discharge values over the year 2018 (see Figure 7.2a). Overall, patterns in the simulated discharge time series match the patterns found in the observations. The peak discharge during January was underestimated, yet this can be explained by the focus on low flows during the calibration procedure. The model did simulate somewhat high discharge values during Septem-

ber, but did correctly capture the lowest flow during November. Overall, the model reached a logarithmic Nash–Sutcliffe efficiency of 0.65 for 2018, indicating realistic model performance. This panel also shows the discharge time series when all three CO_2-driven relations are taken into account (according to the mean values in Table 7.1). This shows lower discharges throughout the year, yet the biggest differences are found during the first four months of the year.

The time series in Figure 7.2b show how each individual process affects the resulting discharge, presented as relative changes. Overall, we see a very limited influence of the increase in LAI, which only slightly reduces discharge values (-6.68 m^3 s^{-1}). The increase in stomatal resistance increases the amount of water discharged through the Rhine (+84.1 m^3 s^{-1}, +4% on annual average discharge), as was expected. Higher temperatures lead to lower discharge values (-365.8 m^3 s^{-1}, -17% on annual average discharge), and so does the combined response (-308.2 m^3 s^{-1}, -14% on annual average discharge). However, the combined response is lower compared to the run where only temperature is taken into account (with a difference of 57.6 m^3 s^{-1}, 3% of annual average discharge). This graph confirms that the largest discharge differences—even when looking at the relative changes—occur during the first four months, with the smallest differences during the summer period. This latter can be attributed to relatively large AET reduction factors (see Figure 7.2e), as explained below.

Potential evaporation (PET) time series show that, with all CO_2-induced changes, the evaporation is higher throughout the year (see Figure 7.2c). This is confirmed in Figure 7.2d, where we see a rather constant increase of 0.41 mm day^{-1} throughout the year. Similarly to the discharge, we see the limited influence of LAI, as the PET values are only increased by 0.01 mm day^{-1}. The effect of r_s is in line line with expectations, showing a decrease of 0.14 mm day^{-1}. The largest increase is caused by the increase in temperatures, which show an increase of 0.57 mm day^{-1}. This does highlight that when the effect of vegetation is not taken into account, PET estimates will be on average about 0.16 mm day^{-1} too high (almost 60 mm year^{-1}, or 6%).

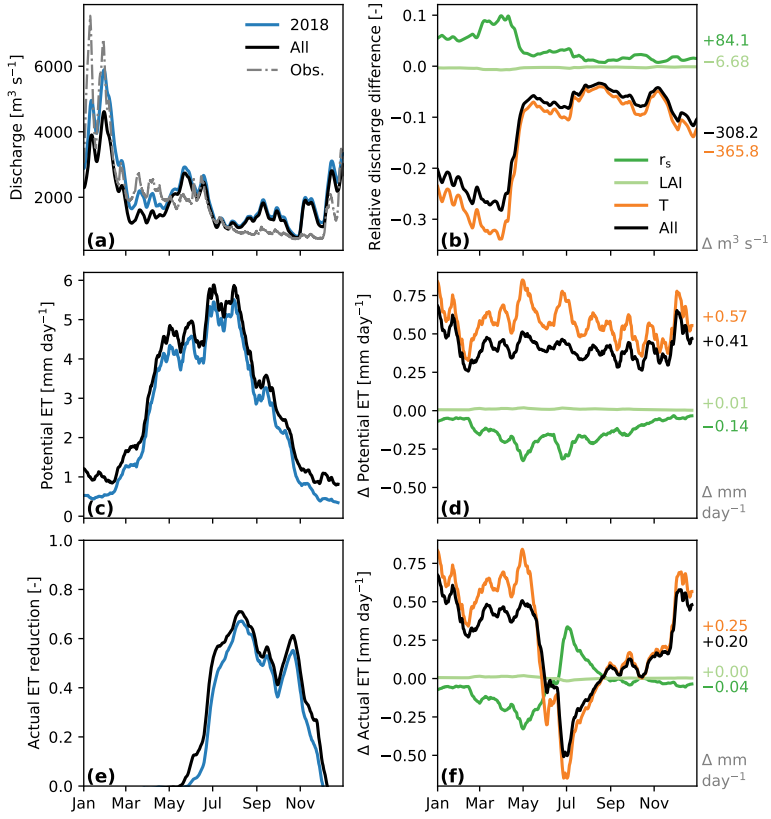

Figure 7.2 | Temporal dynamics of discharge (**a**), potential evaporation (**c**), and actual evaporation reduction factor (**e**) in response to an increase in CO_2 concentration (+400 ppm). Panels on the right (**b**, **d**, **f**) show the difference induced by the separate and combined effects of the three CO_2-driven relations. Evaporation values are smoothed using a moving average of 2 weeks to improve visualisation of the patterns. Numbers on the right hand side show mean difference over the full year with respect to the original 2018 conditions.

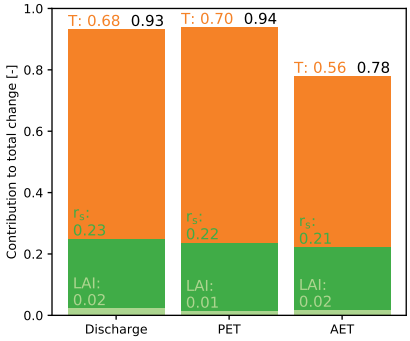

Figure 7.3 | Contribution of each component to the total change. Black numbers represent the total explained fraction, and coloured numbers the contribution of each variable.

When looking at the actual evaporation values (AET), we see a completely different response. Firstly, during the period July–November, we see rather high actual evaporation reduction factors (where this factor is defined as AET = factor · PET). With all CO_2-driven feedbacks enabled, this factor is higher than the baseline 2018 conditions. This indicates more water stressed conditions. Despite the increase in PET, the resulting AET is lower with all CO_2-driven feedbacks enabled (see Figure 7.2f), due to this higher reduction factor. When looking at the individual responses in Figure 7.2f, we again see that temperature is the largest contributing factor. Due to the increase in stomatal resistance, the AET around July is actually higher than the original 2018 time series. This can be explained by the fact that actual evaporation was lower during the preceding months, meaning that the basin was less water-limited during this period.

7.3.2 | Relative contributions

From the differences induced by the individual components, we can infer the contribution of each component to the total change. The results are presented in Figure 7.3, and are separated for discharge, potential evaporation, and actual evaporation. The total direct contribution in each variable is rather

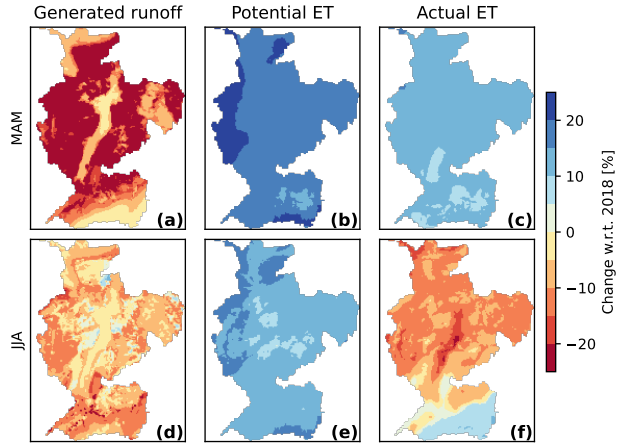

Figure 7.4 | Spatial differences during spring (**a**, **b**, **c**) and summer (**d**, **e**, **f**) between the current situation and a simulation with +400 ppm CO_2. Differences are shown for generated runoff (**a**, **d**), potential evaporation (**b**, **e**), and actual evaporation (**c**, **f**).

high, indicated by the black numbers in Figure 7.3. This means that there is limited interaction between the three components, such as a change in storage conditions leading to a different response. When this would be the case, the total direct effect would deviate further from one. Actual evaporation has the lowest total direct contribution with 0.78. This is not unexpected, as AET is highly dependent on the amount of water available in the rootzone. The relatively low direct contribution indicates that there is more interaction (indirect effects) between the three components that in the discharge and PET time series. Furthermore, these results show that temperature is by far the largest contributing factor, as was expected from the results in Figure 7.2. This is followed by the increase in stomatal resistance, and the increased LAI only has a very minor effect on the total change.

Spatial differences show some interesting patters across the three different output variables (Figure 7.4). We see a reduction in generated runoff for both seasons. However, the reduction is largest during spring. The pixels in the

middle of the basin show a smaller reduction. This part of the basin has very low (or close to zero) terrain slope angles. Following from the calibration procedure, where discharge values were related to terrain slope angles, this resulted in discharge sensitivity parameter such that these pixels have extremely low discharge sensitivity values. Consequently, a change in storage conditions leads to only a very minor change in generated runoff, hence the low values in this region.

During the summer period, generated runoff is also decreased, yet not as much as during spring. Some very small regions even generated slightly more runoff than during the original 2018 conditions. Potential evaporation shows a more homogeneous pattern, with increases of around 10% across the basin. This is in line with the time series presented in Figure 7.2. Interesting patterns appear in the actual evaporation maps. During spring, we again see an increase in actual evaporation, yet not as large as the increase in potential evaporation. However, during the summer period, we see contrasting patterns across the basin. The majority of the basin shows a decrease in AET, but the southernmost region of the basin (the Alps) show an increase in AET, despite an overall increase in PET. This can be explained by the water availability, similarly to the response in Figure 7.2f. The majority of the basin—except the southernmost region—is water limited, meaning that the soil could not meet the evaporation demand set by the increased PET. Additionally, since more water already evaporated during spring, less water was available for evaporation, leading to this overall reduction in evaporation. Interestingly, despite lower AET values, generated runoff values (and hence discharge, see Figure 7.2a, b) were still lower during the summer, also resulting from a reduction in water availability during this season.

7.3.3 | Sensitivity analysis

A sensitivity analysis was performed to understand the hydrological response across varying changes in stomatal resistance, LAI, and temperature. These results are presented in Figure 7.5. The increase in stomatal resistance seems to have only a limited effect on the fraction of time where discharge is below the tenth percentile (Q10). However, higher values generally do lead to lower fractions. A more pronounced effect is visible in the minimum flow,

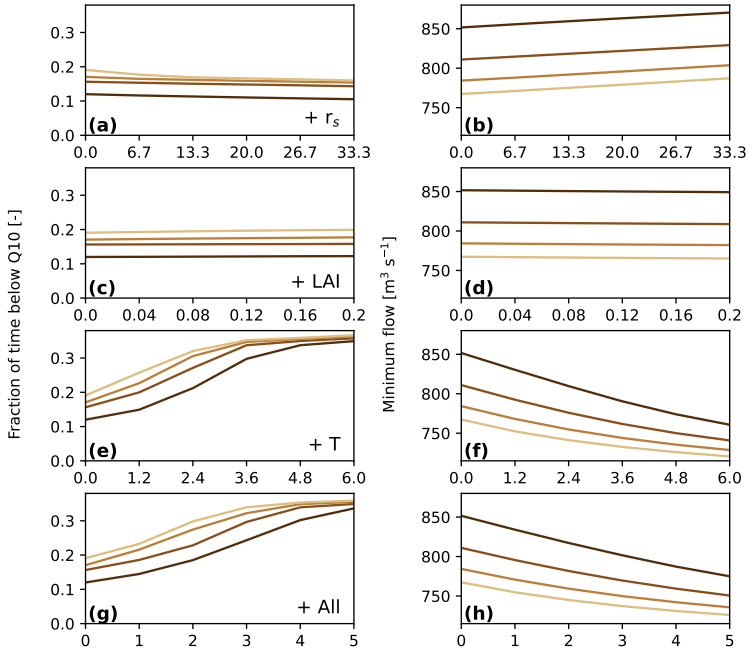

Figure 7.5 | Discharge sensitivity to each variable based on a +400 ppm CO_2 concentration. Left column of panels (**a**, **c**, **e**, **g**) shows the effect of each component to the fraction of time that the 2018 discharge is below Q10. Right column of panels (**b**, **d**, **f**, **h**) shows how the minimum flow changes resulting from each component. The bottom row (**g**, **h**) shows the results of step-wise increases of the values determining the relation with CO_2 concentration, starting from no relations at all (0) to the highest value for each relation (5). Different coloured lines indicate different depths for the rootzone, ranging from 0.50 m (darkest) to 1.25 m (lightest) in 0.25 m intervals.

where higher relation values lead to higher minimum discharge values. Similarly to previous results, the increase in LAI has only very minor effects on the discharge. It very slightly increases the fraction of time where discharge drops below Q10, and very slightly lowers the minimum flow. Temperature shows again a substantial influence on the discharge. However, higher slope values in the CO_2 relations seem to reach a plateau. After a temperature increase of around 3.5°C, the fraction of time below Q10 stabilises just below 0.4. The minimum flow does decline with higher temperature slope values, yet the reduction gets smaller with higher slope values. This plateau-effect can be attributed to the AET reduction: with higher temperatures, PET becomes so large that most rootzone water is evaporated. As a result, the AET is strongly reduced, having only a minor influence on the resulting discharge. The combined response looks similar to the response to only temperature for both the fraction of time below Q10 and the minimum flow. However, the values are slightly reduced (with respect to temperature only) due to the reduction induced by an increase in stomatal resistance.

7.4 | Discussion

Overall, the results show that potential and actual evaporation are expected to increase with elevated atmospheric CO_2 concentrations. This can largely be attributed to the resulting increase in temperature. However, an increase in stomatal resistance partially counters the increase induced by temperature. Contrary to our hypothesis, the increase in leaf area index only had a very minor influence on the resulting evaporation and discharge. The amount of water available in the rootzone caused the actual evaporation to decrease around July. Despite this, discharge remained lower with all CO_2-driven feedbacks enabled than the original benchmark simulation. Our results show that uncertainty in the exact relation between each variable and CO_2 concentration can have substantial influence on the resulting discharge values. However, the patterns and relative contributions of the different variables showed to be consistent.

We employed a simple approach to implement the response of vegetation to an elevated CO_2 concentration. Despite that this approach has been used

before in hydrological sciences, it is a simplified representation of vegetation. We separated the effects of r_s and LAI, while in reality, a plant regulates both factors simultaneously (Zheng et al., 2019). Furthermore, other models put more emphasis on the interaction of leaves with incoming radiation (de Arellano et al., 2012), something that is not directly included in our modified Penman–Monteith equation. Additionally, with more extreme drought conditions resulting from higher temperatures, plants could potentially die from a lack of water (Schuldt et al., 2020). This is currently not accounted for. This can lead to a reduction in transpiration, and hence have a positive effect on discharge.

Comparing our results with other studies, we see similar conclusions. For example, the study by Milly & Dunne (2016) stated that PET estimations without the stomatal resistance effect are likely to be too high. We confirmed this in our study, and showed that PET estimates would be on average 0.16 mm day^{-1} too high (almost 60 mm $year^{-1}$) in the Rhine basin. Our results show that enhanced evaporation over the majority of the year reduces generated runoff, which is in line with the conclusions from Trancoso et al. (2017). However, some effects were not accounted for in our study. For example, Bounoua et al. (2010) argued that increases in evaporation will have a cooling effect (partitioning between latent heat and sensible heat). We did not account for this interaction between evaporation and temperature. Question remains whether this has any noticeable effects on a scale such as the Rhine basin. Additionally, Bounoua et al. (2010) stated that increases in evaporation will ultimately lead to changes in precipitation patterns (which was also mentioned by Notaro et al., 2007). In our study, we deliberately chose not to include changes in precipitation, in order to get a clear understanding on the importance of the specific vegetation-driven feedbacks in evaporation. As changes in precipitation patterns come with large uncertainties, getting a clear understanding on how changes in vegetation will influence the hydrological response would become too clouded. Furthermore, it has been stated that growth of plants could be stimulated when less water is required through the increase of stomatal resistance (Kruijt et al., 2008). However, we show that the effect of temperature remains dominant, leading to an overall increase in evaporation. As the CO_2-induced effect on LAI showed to be very small, we expect this effect to be even smaller (if present

at all).

In a global study, Gedney et al. (2006) concluded that an increasing trend in long-term runoff time series could not be explained by only a change in climate. They claimed that, as a result of higher CO_2 concentrations, transpiration in plants was reduced through the increase in stomatal resistance, and that this effect could be detected in river runoff. Their results, however, have been criticised. Peel & McMahon (2006) had some concerns regarding the gap-filling method, and whether the reference stations were representative. Two years later, Huntington (2008) argued that a reduction in transpiration was not the explanatory variable, and that actually increases in annual actual evapotranspiration are observed. Huntington (2008) concludes that the observed increase in runoff is more likely to be caused by increases in precipitation, and enhanced melting from ice and snow. Despite not including changes in precipitation and enhanced melting from snow and ice, our results seem to confirm this conclusion. The increase in CO_2 concentration of +400 ppm is far larger than the change in CO_2 concentration over the period in the study by Gedney et al. (2006) ($\pm$60 ppm). With smaller increases in CO_2 concentration, the vegetation effects become smaller, and hence their effects on discharge. Despite this, our results show that the changes in vegetation are important to account for in future studies.

Our results confirm and quantify the importance of CO_2-induced feedbacks on the Rhine discharge. This does, however, raise the important question on how to move forward when predicting the hydrological response on the long term. We believe that the increase of stomatal resistance should be considered in these types of studies, as it has shown to be a very important factor. It will likely not change the trend or sign of the our current predictions, as temperature remains the most dominant factor. The inclusion of this factor will likely lead to a reduction in PET estimates, which could have important implications for the predictions of hydrological extremes. Especially when droughts such as the summer drought of 2018 occur more frequently in the future, it is important to have a clear understanding on the role and response of vegetation. The relations used in our study as function of increase in CO_2 concentration contain some uncertainty. More detailed studies are therefore required to improve our understanding on how vegetation in basins such as

the Rhine respond to elevated atmospheric CO_2 concentrations. It could potentially mean that our current estimates of low flows are too low.

7.5 | Conclusions

In this study, we investigate the sensitivity of evaporation and low flows in the Rhine basin to three main CO_2-driven changes in evaporation. We simulate the year 2018 as baseline, and compare these conditions to a "future" 2018 where the atmospheric CO_2 concentration is increased with 400 ppm, in line with predictions of around 2100 following RCP8.5. It is known that an increase in atmospheric CO_2 concentration will lead to higher temperatures, but also affect vegetation through increased stomatal resistance and increased leaf area index. While the increased temperatures and increased leaf area index will raise the potential evaporation values, increased stomatal resistance will decrease the potential evaporation values. We quantified the individual and combined responses of these three processes in the Rhine basin.

We showed that with all three processes accounted for, PET is expected to increase with 150 mm year^{-1}. Temperature is the most dominant factor of the three, responsible for a fraction of 0.68 of the total change in discharge (0.70 and 0.56 for PET and AET, respectively). The increase in stomatal resistance partially countered the increase induced by the higher temperatures, and was responsible for a fraction of 0.23 of the total change in discharge (0.22 and 0.21 for PET and AET, respectively). The response of AET showed to be more complex, as it is also highly dependent on the amount of available water in the rootzone. As a result, AET values were increased throughout the year, except around July. Prior to this period, most water from the rootzone was already evaporated, leaving little water available for evaporation around July. Despite this change, discharge remained lower throughout the year.

A sensitivity analysis on the discharge response to each factor showed that our results are consistent across a range of rootzone depths and values describing the relation between each factor and increase in CO_2 concentration. The fraction of time where discharge is below the (long-term) tenth percentile score did seem to reach a plateau at around 0.35 at a temperature increase

of $\pm$4°C. Overall, this study showed that discharge is expected to decrease with 14% as a result of CO_2-induced changes in stomatal resistance, leaf area index, and temperature. When the effects of vegetation are not taken into account (especially the increase in stomatal resistance), PET values are overestimated by almost 60 mm year^{-1} (7% of average over baseline 2018 conditions), and discharge is underestimated by more than 57 m^3 s^{-1} (3% of average discharge over baseline 2018 conditions). Therefore, a correct representation of the response of vegetation, with special attention to the increase in stomatal resistance, is of vital importance in order to make reliable discharge estimates in a situation with elevated atmospheric CO_2 concentrations.


8

Synthesis

"I walked across an empty land
I knew the pathway like the back of my hand
I felt the earth beneath my feet
Sat by the river and it made me complete"

—Keane, *Somewhere Only We Know* (2004)

Several levels of hydrological variability are highlighted throughout this thesis, both in spatial and temporal aspects. The chapters range from analysing past events to simulating the hydrological response under potential future conditions. The aim of this thesis is to improve understanding of spatial and temporal aspects of hydrological variability, and how this ultimately influences the hydrological response. In this chapter, the main findings of each individual chapter are discussed first, which are also very briefly summarised in Figure 8.1. The conclusions per chapter are followed by general conclusions and how these conclusions can be interpreted in a broader sense.

8.1 | Main findings

8.1.1 | Hydrological variability during droughts

Firstly, the hydrological response to droughts is analysed in Chapter 2. This chapter showed how variability between different components of the hydrological cycle influenced drought frequency in the province Gelderland, the Netherlands. The five different variables considered (precipitation, soil moisture, vegetation, groundwater and surface water levels) all showed different drought responses. The variables showed different temporal dynamics on monthly timescales, where drought in one variable did not guarantee drought in other variables. The different dynamics can be attributed to the differences in typical processes and response times within each variable. Additionally, spatial variability within each variable also meant that droughts could occur in only a part of the region. This spatial variability caused droughts to occur more frequently (27–38% of the time, depending on the variable) than the drought definition (20% of the time) would suggest. During 73% of the time, at least one variable was in drought conditions.

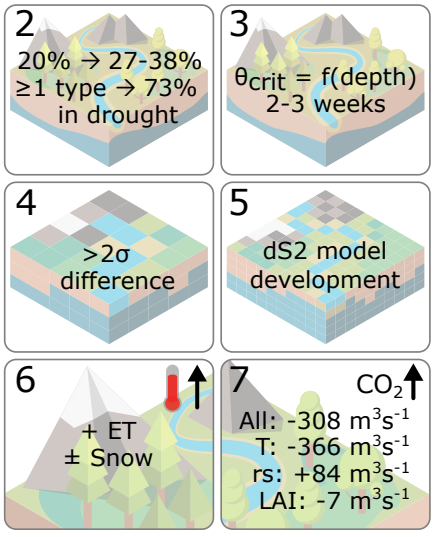

Figure 8.1 | Visual summary of the main findings in this thesis. Numbers in the top left corners represent the corresponding chapters.

Only when 3–4 variables are simultaneously in drought conditions, the actual drought frequency matches the definition. This chapter shows that the drought definition can lead to a false perception of actual drought frequency, highlighting the importance of routine drought monitoring.

The hydrological variability during droughts was further explored by investigating the interaction between vegetation productivity and soil moisture content. In Chapter 3, satellite-derived vegetation indices are compared with in situ soil moisture observations for the summer drought of 2018. The vegetation indices showed that vegetation productivity was reduced between two and three weeks after soil moisture anomalies started. This highlights the lagged response of vegetation to a lack of water. Furthermore, a piecewise linear fit showed the transition point between stable and reduced vegetation productivity, representing energy-limited and water-limited conditions, respectively. This transition point is typically described as the critical

soil moisture content. This linear fit was applied for soil moisture observations at several depths, and showed that the critical soil moisture content increased linearly with integration depth. Additionally, this critical soil moisture content at increasing depths was reached later in the year. While soil moisture content is often considered to be a constant value, this chapter highlights that the integration depth needs to be considered when quantifying this value.

8.1.2 | Simulating the hydrological response

Spatial model resolution is an important factor in capturing hydrological variability. In Chapter 4, the results of a conceptual rainfall-runoff model (SPHY) at low resolution are compared with the results of SPHY at high resolution on a seasonal scale. The high resolution model showed that both extremely positive and extremely negative anomalies could occur simultaneously within a basin. This variability is largely driven by the type of land cover, which was not captured by the coarse resolution model. A novel metric is proposed (the density-weighted distance, DWD), that can compare the single value from a coarse resolution simulation with the range of values from the high resolution model. This metric showed that the coarse resolution model missed on average two standardised anomalies during seasonal extremes. This value was higher in the Alpine (glacierised) catchments compared to the pre-Alpine (non-glacierised) catchments. These results highlight the importance of high resolution models, and that simulations from a model at coarse resolution cannot be easily transformed to represent variability that occurs within a single pixel.

In an effort to develop a distributed rainfall-runoff model, that is able to efficiently perform high resolution simulations, the dS2 model was introduced in Chapter 5. The dS2 model is based on the simple dynamical systems approach, which was extended with two modules to account for snow processes and flow routing. The implementation of a robust yet efficient numerical solver ensures that simulations on high spatial and temporal resolutions can be performed with low computational requirements. This ensures that typical spatio-temporal scales are respected, as many models still use daily time steps regardless of spatial resolution. Simulating the discharge response of

a mesoscale basin in the Swiss Alps proved that dS2 is very capable in representing the hydrological response in a region with high spatial variability. This model is used to simulate the Rhine basin in order to improve our understanding on the hydrological response to changes in temperature and CO_2 concentration in Chapter 6 and Chapter 7, respectively.

8.1.3 | Contrasting interactions in response to a changing climate

The dS2 model is used to simulate how the Rhine basin responds to temperature-driven changes in evaporation and snow processes (see Chapter 6). Simulations were performed for two decades, the 1980s and the 2010s. By swapping the individual forcing variables with those of the more recent observation period, it was possible to quantify the direct effect of each forcing variable on the discharge. As expected, precipitation played an important role in controlling the discharge patterns, but the temperature-driven changes in evaporation and snow processes were equally important. Interactions between the different variables (such as the division of precipitation between snow and rain) were responsible for most of the changes between the decades. When increasing the temperature with 2.5°C, discharge was reduced throughout the year, resulting from an increase in evaporation. Additionally, higher temperatures resulted in differences in the seasonal response of the snow processes: less precipitation was falling as snow, snow was melting earlier in the year, and the glaciers melted more during summer. The enhanced melt of the glaciers partially offset the discharge reduction resulting from the increased evaporation. However the original melt peak during spring was reduced and shifted to an earlier moment in the year, leading to an even bigger reduction in discharge. These results highlight the importance of a correct understanding of the interplay of two common variables—evaporation and snow—on the resulting discharge, especially in scenarios with increased temperatures.

The effects of CO_2-induced changes in vegetation and temperature on the discharge in the Rhine basin are quantified in Chapter 7. By using the dS2 model, multiple simulations were performed to investigate the hydrological response to the CO_2-induced effects on stomatal resistance, leaf area index and temperature. The importance of each factor is quantified by comparing

the individual and combined responses of each factor on the resulting discharge. This showed that the increase in temperature is the most important factor (reducing the average discharge with 366 m^3 s^{-1}, −17% of the average discharge during 2018), followed by the increase in stomatal resistance (increasing the average discharge with 84 m^3 s^{-1}, +4% of the average discharge during 2018). The increased leaf area index only had very minor influences on the hydrological response (with a reduction of 7 m^3 s^{-1}). Overall, the results show a decrease of 308 m^3 s^{-1} (−14% of the average discharge during 2018) on the average discharge. These results are confirmed by a sensitivity analysis, where the hydrological response is tested over a range of values determining the response of each factor. While temperature effects are often correctly accounted for, the change in stomatal resistance is not. Since stomatal resistance partially counters the effects of higher temperatures, not including this effect can potentially cause underestimations of the discharge during low flows. This chapter therefore highlights the importance of accounting for vegetation dynamics in hydrological simulations.

8.1.4 | General conclusions

The different chapters in this thesis show how hydrological variability is present across the Rhine basin. The combined conclusions from all chapters show how detailed process understanding, together with a more detailed understanding of several feedback mechanisms, can contribute to improve our understanding of the hydrological response under a changing climate. When extrapolating the conclusions according to the potential changes in the future, it is expected that discharge in the Rhine will, on average, decrease. This is largely driven by the increase in temperature, leading to changes in snowfall and -melt dynamics, and enhanced evaporation. The increase in evaporation is, however, slightly countered by the increase in stomatal resistance in vegetation. Furthermore, despite enhanced melt from glaciers being able to partially compensate for this increase in evaporation, a change in snowfall and -melt seasonality means potentially large reductions in discharge during (late) spring.

The previous conclusions rely on model simulations, where spatial resolution is shown to be an important factor for correct representation of spatial vari-

ability. The comparison of two distinct model resolutions showed that both spatial resolutions are able to represent the discharge response. Despite this, the spatial variability is largely underrepresented when using a too coarse model resolution. Ideally, a critical model resolution should be found, as described by Liang et al. (2004) and Melsen et al. (2016a). Both studies found no substantial model performance improvements at spatial resolutions finer than about 10 km $\times$ 10 km. Zappa (2002) found a finer critical resolution for a different model at 500 m $\times$ 500 m, so it is expected that the critical resolution depends on the model, but likely also on the catchment. While this thesis did not explored the critical resolution of dS2 in the Rhine basin, the selected resolution falls between the two previously mentioned resolutions (at 4 km $\times$ 4 km). Given the correct spatial patterns observed in the validation with evaporation and snow storage in Chapter 6, it appears that spatial patterns across the Rhine basin are represented at this spatial resolution.

As droughts were already occurring frequently in the downstream areas of the Rhine basin, the expected reduction in discharge means that low flows will occur more frequently. Especially in regions such as Gelderland, these reductions in discharge can amplify local droughts, as less water is available for drought measures such as irrigation. Furthermore, the increases in evaporation affects water availability throughout the basin, potentially further impacting vegetation productivity, and ultimately crop yield. In order to perform detailed simulations on the response of vegetation during droughts, the interaction between vegetation and soil moisture needs to be correctly implemented. Common methods use a single value to represent the critical soil moisture content, but it was shown that this value needs to be considered in relation with the depth of the root zone. Additionally, if models are employed for long term discharge predictions, it is vital to correctly represent the response of vegetation to a rising CO_2 concentration. Despite that the effect of rising temperatures is largest, the effect of an increase in stomatal resistance is still substantial. These two points nicely lead to the lessons learned from this thesis, and their implications.

8.2 | Lessons learned and implications

Whereas this thesis has focused at hydrological variability in the Rhine basin, the conclusions drawn in Section 8.1 are applicable in a broader spectrum. These are divided into three main topics: how to improve the capturing of hydrological variability, opportunities for hydrological models, and the implications for water management. Each topic is explained in more detail below.

8.2.1 | The best practises to capture hydrological variability

High resolution observations are ideally available to optimally capture spatial hydrological variability. The availability of data is often described as a limiting factor in hydrological studies. This is because almost every hydrological process is difficult to measure due to its spatial variation, as is also described by Sivapalan (2003). Many observations locations are required to optimally capture their full spatial variability. As an example, many rain gauges are scattered across the globe, with varying densities in different regions. However, a study by Kidd et al. (2017) estimated that the total area of the orifices of all rain gauges in the Global Precipitation Climatology Project cover only half a football field. Although rain gauge measurements should be representative for a larger area than only their orifice, this estimation gives a good perspective on the limited coverage of our measuring network. From all hydrological variables, discharge is one of the easiest to quantify. Since all water passes through a river, only a single measurement location can measure the discharge of a larger region. However, geological features cause groundwater flow to cross catchment boundaries, potentially making discharge observations not directly representative for their upstream area (Bouaziz et al., 2018). On a global scale, however, many basins are ungauged, highlighting that even one of the easier hydrological variables is lacking in coverage. As a result, performing meaningful simulations of ungauged basins is limited, as the vast majority of hydrological models needs to be calibrated (i.e. require discharge observations) in order to provide reliable estimates. Luckily, as advances are made in new interpolation techniques (such as van Osnabrugge et al., 2017), or in improved reanalysis products (such as the ERA5 dataset, Hersbach et al., 2018), or even in the number of in situ observations, we can

increase the area covered with reliable data. This means that we can provide reliable estimates for regions that are not covered with in situ sensors.

New interpolation techniques and reanalysis products are still limited by in situ observations. Fortunately, new space-borne sensors and new techniques are developed to improve the coverage and resolution of observations made by satellites (Schmugge et al., 2002). I believe that remote sensing is the way forward to get global coverage of the most important hydrological variables, such as precipitation (Sorooshian et al., 2011), evaporation (McCabe et al., 2019), and potentially discharge (provided that estimates will improve in accuracy, Birkinshaw et al., 2014). Through the development of novel algorithms and filtering techniques, the spatial coverage of space-borne sensors can hopefully be improved even further. The temporal coverage and resolution of many satellites unfortunately remains a limiting factor. Despite this, the resulting high-resolution data can be a useful source to quantify and understand hydrological variability.

Additionally, opportunistic sensing methods can be employed to improve coverage of observations. Several studies already investigated the added value of crowd-sourced data (e.g. Strobl et al., 2020; van Emmerik et al., 2020; Vos et al., 2020). This has the potential to hugely expand the observation network, especially in densely populated areas. These increases in observations help to improve our understanding of variability within the hydrological cycle, and how this relates to e.g. local characteristics. Ideally, these new insights can eventually lead to new model concepts, to extend the current suite of hydrological models. However, there is less control on the quality of the acquired observations, meaning that special filter algorithms need to be applied in order to ensure reliable observations. A combination of in situ and remotely sensed observations can potentially be used to validate and correct the crowd-sourced data points. Furthermore, not all types of crowd-sourced data lead to timeseries with consistent temporal resolutions. Despite this, it can still provide insights into the spatial variability during different conditions, especially when combined with other datasets. This increased spatial coverage can be used to improve interpolation techniques, in an effort to create a gridded dataset with a consistent temporal resolution.

8.2.2 | The role of simple hydrological models

This thesis showed that a computationally efficient hydrological model such as dS2 can be very useful to study the hydrological response. I want to highlight several topics/research directions that are important for the hydrological modelling community: the importance of new concepts, the benefit of efficient models, the added value of linking parameters to catchment characteristics, and the role of vegetation dynamics in hydrological simulations.

The majority of hydrological models are conceptual models. These models essentially simplify hydrological processes using reservoirs and interactions between these reservoirs, and are sometimes referred to as “leaky-bucket” models. Several examples of these bucket-based models are: HBV (Lindström et al., 1997), GR4J (Perrin et al., 2003), SPHY (Terink et al., 2015), and Flex-TOPO (Savenije, 2010). These models are based on varying representation of a catchments, and recent research has focused on trying to understand how these different conceptualisations and different model components affect model simulations (e.g. Bouaziz et al., 2021; de Boer-Euser et al., 2017; Clark et al., 2008). However, as they are all based on the same philosophy, I do argue that this "bucket-based" modelling is a limiting ideology, and potentially restricts the development of novel hydrological models. A similar point was also discussed by Hrachowitz & Clark (2017), who encouraged the hydrological community to make use of the different modelling strategies in order to find new or improved implementations. An example of a different modelling strategy is the simple dynamical systems approach (Kirchner, 2009). This concept is unique in that it defines a new way of conceptualising the hydrological cycle, without representing a hydrological basin by a combination of linked buckets. Additionally, this concept is based directly on discharge observations, in contrast to other bucket-based models. New concepts such as the simple dynamical systems approach can not only lead to new insights, it can also lead to new and efficient model implementations. An example of this is the vectorised approach in dS2, which allows for computationally efficient hydrological modelling at high spatio-temporal resolutions. The latter is more easily achieved with simpler hydrological models, as they require less equations (and therefore calculations) to be solved.

Computationally efficient hydrological models have a clear benefit. As recently pointed out by Loft (2020), large amounts of energy are required to run high-resolution earth system models. Due to the large computational demand of these models, large computation clusters or supercomputers are required. The electricity needed to maintain the clusters or supercomputers lead to large carbon dioxide emissions, unless the energy is provided through renewable sources. As more and more hydrological simulations are pushed towards high-performance computing, this will eventually lead to an increase in greenhouse gas emissions. With more efficient hydrological models, simulations need less powerful computers, reducing the power consumption. Efficient models allow to perform larger ensemble runs and/or sensitivity studies without increasing the computational demand, and the associated power consumption. Additionally, uncertainty and/or sensitivity studies can even be performed on normal desktops, lowering the threshold to perform these types of studies.

As mentioned earlier, most hydrological models (including dS2) require calibration before they can provide reliable discharge estimates. However, since the majority of basins across the global are ungauged (Blöschl et al., 2013a), the use of models that require calibration is limited. As a result, potential consequences of climate change in these basins are unknown. Some efforts have been made to use remotely sensed data to estimate discharge (Birkinshaw et al., 2014), but this is prone to substantial errors. Therefore, looking for models that do not require discharge data for calibration might be the solution to this problem. Imhoff et al. (2020) showed how parameters in a conceptual hydrological model (wflow_sbm) can be estimated from physical characteristics by using pedo-transfer functions. They reached good model performance, indicating that this approach could be used in many other basins across the globe. It is worthwhile to explore whether parameters from other models can be estimated with a similar approach. Naturally, this needs to be tested in basins with sufficient data availability, but it would provide many possibilities if more models can be setup without the need for calibration. For example, in Chapter 6 and Chapter 7, parameters in the dS2 model were calibrated using the slope of each pixel. This was based on other research highlighting how the simple dynamical systems approach could be related back to slope values (Rupp & Selker, 2006; Karlsen et al., 2019). More

research on trying to link the discharge sensitivity parameters with catchment characteristics (such as soil or geological characteristics) would be beneficial to dS2, as it would mean that it can be used to simulate many more basins, including ungauged basins, without a large computational cost.

Regardless of whether simulations are performed with a simple or complex hydrological model, this thesis has shown that several components need to be properly accounted for. Two clear examples are the resolution of the model, and the representation of vegetation in models. Firstly, Chapter 4 showed the importance of spatial resolution when simulating complex regions. If the aim of the study is to quantify changes in local hydrological response, it is important to select a spatial resolution that is appropriate to capture these changes. Consequently, selecting a temporal resolution appropriate for this spatial resolution is essential for correctly capturing the relevant processes (Melsen et al., 2016b). Secondly, vegetation showed to play an important role in the hydrological system. Both through the interaction with soil moisture, but also through the increase in stomatal resistance as a result of elevated CO_2 concentrations. I believe that both factors are especially important for land surface models, but the interactions between soil moisture and vegetation are less important for hydrological models, due to their (typical) simplified representation of vegetation. However, the increase of stomatal resistance in response to elevated CO_2 concentrations showed to be very important, especially when simulating climate change scenarios. Without including this process, potential evaporation estimates are likely to be too high, leading to unreliable estimations of the hydrological response. It is therefore important that the change in CO_2 concentration is provided as input in to hydrological models, such that these processes can more easily be implemented.

8.2.3 | Implications for water management

Research on hydrology extends beyond the scientific aspects. The practical aspect of hydrology, via water management, is vital as it plays an important role in providing and protecting society, especially in a country as the Netherlands. Therefore, I want to highlight two topics that I believe are important for water management: the usage of models, and the communication of

droughts between academic and operational sectors.

Simple hydrological models can also play an important role in water management. While I do not think that this should replace current operational models, simple models can be a useful tool for quick and low cost simulations. To achieve this, I believe that it is useful for water management to focus on running several hydrological models simultaneously. When relying on performing simulations on only a single model, the results can be constricted by (potentially unknown) limitations of this model. Comparing output from multiple models can give an insight in the reliability of the model results, and therefore highlight potential flaws in one of the models. Model comparison is already often performed in scientific studies, and I believe that water management can benefit from implementing a method to simultaneously run several models. Running several models can be achieved more easily when a flexible modelling environment is used, where different model concepts and equations can be run simultaneously. Transitioning to a flexible modelling environment does come with increased costs through the setup and maintenance, but I believe the benefits will outweigh the costs. A flexible modelling environment allows for easy testing and comparing of different concepts and/or equations. By including a selection of different models, these models can easily be validated with the observations, as well as providing an additional estimate on the reliability of the discharge predictions. Furthermore, decisions need to be made on which processes have to be included in the operational forecasts (short-term), and which are essential for projections for policy changes (long-term). As showed in this thesis, changes in vegetation characteristics can have a large impact on the long-term. The crossover time where this process becomes dominant enough that one should include this process is something that requires more research. A possible solution is to include this process also in short-term simulations, but this might require additional calibration and validation.

For the communication on the occurrence of droughts, Chapter 2 has shown that drought is a complex phenomenon, and different drought definitions make it even more challenging. Droughts are often associated with low water levels in lakes or rivers, but can occur in many parts of the hydrological system. Theoretical examples show how drought propagates through the

hydrological cycle, and typically start with a lack of precipitation (van Loon, 2015). However, this example does not always fully comply with reality, as different parts of the hydrological cycle could have different spatio-temporal dynamics and/or different origins of water. As a result, the occurrence of drought is not as straightforward. A potential solution to this issue would be to define a metric that combines all the different types of droughts, to determine whether action from the water managers is required. However, this requires arbitrary weighing of the different drought types. Another solution, albeit more demanding, would be to have around the clock monitoring of droughts across all components of the hydrological cycle (e.g. soil moisture, groundwater levels, surface water levels), to determine which stakeholders are affected and which actions need to be taken. While more work, this can lead to quicker and more localised measures, as this solution takes the impacts of droughts into account. With the aim to minimise these impacts across all components of the hydrological cycle, all end users could ultimately experience less impacts of droughts on a larger scale.

The chapters in this thesis showed how hydrological variability is influencing the hydrological response of the Rhine basin. It is shown that variability is present on many scales, both spatially and temporally, and that it needs to be correctly represented to provide reliable discharge estimations. While scientific studies should focus on improving hydrological understanding, communication with water management should be considered as an equally important role. Close collaborations and/or frequent interactions should provide water management sufficient insights to make decisions on potential new observation networks and/or model concepts. This way, we can ensure that hydrological variability is correctly captured, to improve how hydrology can support a safer environment.


9

- **Appendices**
- **Bibliography**
- **Summary**
- **Samenvatting**
- **Dankwoord**
- **List of publications**
- **Graduate school certificate**

Appendices

A | Additional results of Chapter 4

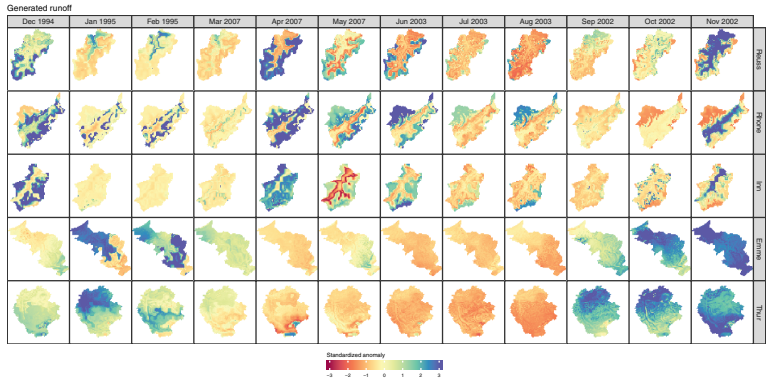

Figure A.1 | Spatial distribution of monthly anomalies of generated runoff, during the months of the selected season. Each box represents an area of ± 40 km$\times 40$ km.

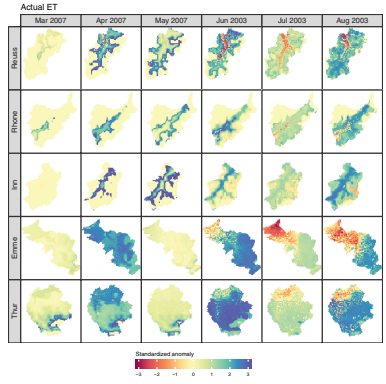

Figure A.2 | Spatial distribution of monthly anomalies of actual evapotranspiration, during the months of the selected season. Each box represents an area of ± 40 km$\times 40$ km.

B | Overview of all dS2 parameters

Table B.1 | List of dS2 parameters. All parameters after rdf only influence either the numerical stability and/or the IO operations of the model, not the model output.

Name	Description	Example value	Unit
α	gQ parameter - intersect	-2.5	-
β	gQ parameter - slope	0.85	-
γ	gQ parameter - curvature	-0.010	-
ϵ	Reduction factor for evaporation	0.89	-
τ	Travel speed of water through the catchment	2	$m\ s^{-1}$
T0	Critical temperature	0	$°C$
ddf	Degree day factor for snowmelt	2	$mm\ day^{-1}\ °C^{-1}$
rdf	Conversion factor for energy to snowmelt	0.26	$mm\ day^{-1}\ (W/m^2)^{-1}$
Qt	Threshold below which evaporation is set to zero	10^{-4}	$mm\ h^{-1}$
dt	Size of time step (Δt)	1	h
max_RAM	Maximum RAM the model is allowed to use	1024	MB
size_one_value	Size of a single value	4	bytes
LB	Factor controlling lower boundary for solver, where $Q_t \leq Q_{t-1} \cdot LB$	10^{-4}	-
max_gQ_difference	Maximum allowed difference in gQ values	2	-
dt_reduction	Factor controlling the Δt reduction	0.15	-
min_extra_dt	Number of minimum extra Δt per Δt	5	-
max_extra_dt	Number of maximum extra Δt per Δt	50	-

C | Additional results of Chapter 6

This supplement contains additional information to support the descriptions and explanations in Chapter 6. We include the parameter values resulting from the calibration procedure. We show metrics for both the calibration and validation period in all subbasins used in this study. Additionally, we explain how evaporation and snow variables responded to each incremental temperature increase, as Chapter 6 only shows the most extreme case.

C.1 | dS2 calibration results

Calibration from the 1250 Latin hypercube sampling resulted in the following parameters (note that the three g(Q) parameters are defined as a function of slope):

$$\begin{aligned}
\alpha &= 0.002472\phi - 3.725, \\
\beta &= 0.06915\phi + 0.2666, \\
\gamma &= 0.0316\phi - 0.1622, \\
\epsilon &= 1.196\ [-], \\
\mathrm{dff}_{\mathrm{snow}} &= 3.207\ [\mathrm{mm\ °C^{-1}day^{-1}}], \\
\mathrm{dff}_{\mathrm{glacier}} &= 5.523\ [\mathrm{mm\ °C^{-1}day^{-1}}],
\end{aligned}$$

where α, β, and γ are the three g(Q) parameters, ϕ represents the terrain slope in degrees, ϵ represents the the evaporation correction factor, and ddf represents the degree factor for snow and glaciers, respectively. The slope is based on Jarvis et al. (2008), and is calculated at the original resolution of $\pm$80 m. The resulting slope map is resampled to the model resolution.

In Table C.1, we show the Kling-Gupta efficiencies (KGE) for all basins used in the calibration. The location of these basins within the Rhine is presented in Figure C.1. We also included the KGE for both the 1980s and 2010s period. Due to some limitations in data availability, not all discharge observations covered the entire period. We sliced the time series to include most of the available data, yet for some stations it remained impossible to calculate the KGE.

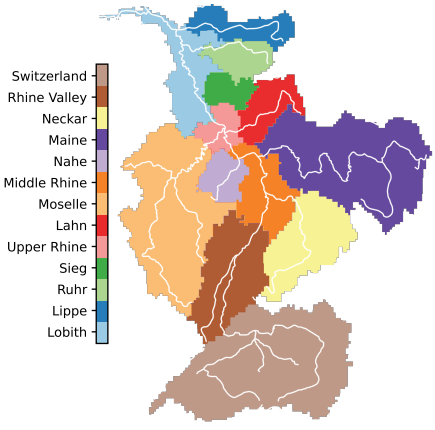

Figure C.1 | Names and areas corresponding to the (sub-)basins of the Rhine used in this study. The white line indicates the location of the main river network.

Table C.1 | Model performance statistics over all subbasins in the Rhine basins. Not all basins had sufficient data to cover the simulation periods, the percentage shows fraction of the period covered by the observations.

Basin	Area (km^2)	KGE calib	KGE 1980s	KGE 2010s
Lobith	168,448	0.90 (100%)	0.84 (18%)	0.83 (73%)
Lippe	5,520	0.44 (100%)	0.32 (9%)	0.45 (74%)
Ruhr	4,320	0.80 (100%)	0.63 (2%)	0.87 (76%)
Sieg	3,008	0.73 (100%)	0.80 (9%)	0.86 (74%)
Upper Rhine	145,984	0.87 (100%)	-	0.88 (73%)
Lahn	5,648	0.59 (99%)	0.49 (9%)	0.73 (72%)
Moselle	28,272	0.62 (100%)	0.45 (9%)	0.70 (73%)
Middle Rhine	108,672	0.87 (100%)	-	0.81 (73%)
Nahe	4,032	0.64 (100%)	-	0.76 (76%)
Maine	28,800	0.74 (100%)	0.82 (9%)	0.81 (73%)
Neckar	13,456	0.74 (99%)	-	0.78 (73%)
Rhine Valley	53,872	0.77 (100%)	-	0.75 (73%)
Switzerland	38,832	0.71 (19%)	-	0.68 (69%)

C.2 | Temperature induced changes on evaporation and snow

As shown in Chapter 6, higher temperatures substantially affect the resulting discharge, where the differences induced by changes in evaporation and snow processes are not constant over the year. To further understand how these processes influence the discharge, the changes in evaporation and snow storage are plotted in Figure C.2 and Figure C.3, respectively.

In Figure C.2, it is visible that potential evaporation will increase with higher temperatures. Despite this, the resulting actual evaporation is not bound to be higher than the 1980s, due to limitations in available soil moisture. This is clearly visible around August 17. Additionally, higher temperatures sometimes hardly change the resulting actual ET, as is the case around August 20. Finally, when sufficient moisture is available for evaporation, higher temperatures will lead to higher actual evaporation rates, as is visible around September 2. The evaporation reduction parameter, indicating the amount of water stress, shows consistently increased reduction with higher temperatures, resulting from the reduced water availability. For most pixels, this relation is non-linear, as it changes from unstressed conditions to water-stressed conditions with higher temperatures.

When investigating the response of snow processes (snowfall and melt from snow and ice) to increased temperatures, results are in line with the expectations, see Figure C.3. Less precipitation is falling as snow (Figure C.3a), which means that more precipitation is falling as rain. This has a more direct response to discharge, which explains the increased discharge during winter. Consequently, both the amount of water stored as snow and the fraction the basin covered with snow are reduced (Figure C.3b, c). Snow storages are not only reduced in terms of total water stored, but also depleted more than one month earlier (mid May 1988 versus late June 1988).

With a reduction in snow cover and snow depth in response to higher temperatures, we also see a reduction in basin-averaged snow melt rates (see Figure C.3d). This is the result of a smaller area covered with snow, and hence we see a reduction in basin-averaged snow melt rates. However, the pixels that are covered with snow melt at a faster rate due to the higher temperatures, as can be inferred from the degree-day method to determine snowmelt.

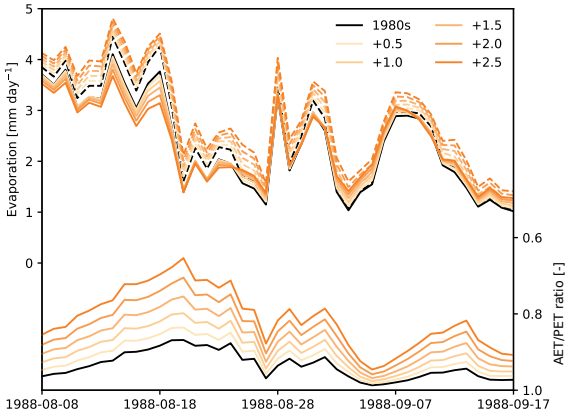

Figure C.2 | Evaporation differences under increased temperature scenarios. Top half shows potential (dashed) and actual (solid) evaporation, bottom half shows the ratio between actual and potential evaporation. All values are averaged over the entire basin.

This latter effect is visible in the melt from the glaciers (Figure C.3e). With each temperature increase, more meltwater is produced from these glaciers. Eventually, this will lead to a reduction in glacier area and volume, and hence a reduction in glacier meltwater production, but this is currently not included in the model.

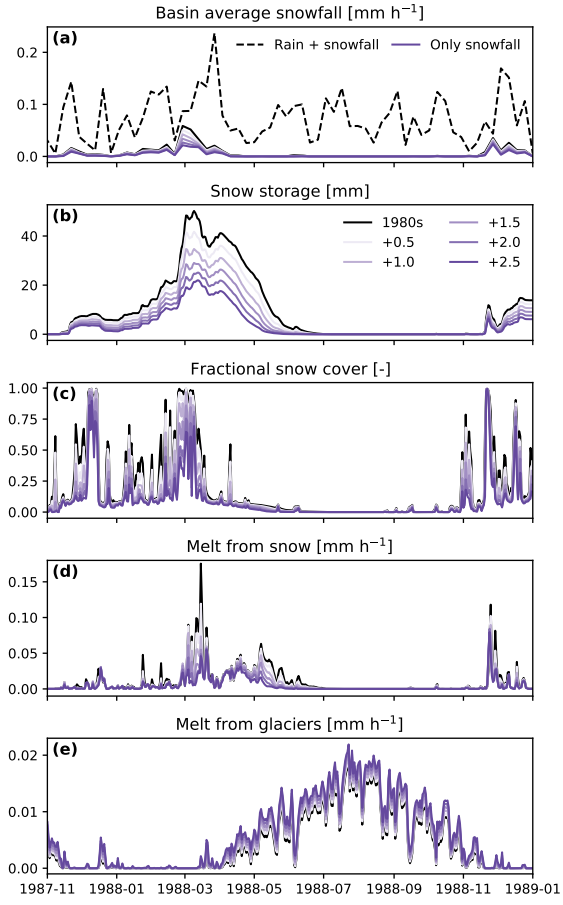

Figure C.3 | Changes in all considered snow processes under increased temperature scenarios. Panel **a** shows the amount of snowfall with respect to the total precipitation. Panel **b** shows the average amount of water stored as snow in snow-covered pixels, and panel **c** shows the fraction of the basin covered with snow. Panel **d** and **e** show the melt rates of snow and ice, respectively, averaged over the entire basin.

Bibliography

Abbott, B. W., K. Bishop, J. P. Zarnetske, C. Minaudo, F. S. Chapin, S. Krause, D. M. Hannah, L. Conner, D. Ellison, S. E. Godsey, S. Plont, J. Marçais, T. Kolbe, A. Huebner, R. J. Frei, T. Hampton, S. Gu, M. Buhman, S. Sara Sayedi, O. Ursache, M. Chapin, K. D. Henderson & G. Pinay (2019). Human domination of the global water cycle absent from depictions and perceptions. *Nature Geoscience*, 12(7), 533–540. doi: 10.1038/s41561-019-0374-y.

Abramowitz, G. (2005). Towards a benchmark for land surface models. *Geophysical Research Letters*, 32(22), L22702. doi: 10.1029/2005GL024419.

Adam, J. C., A. F. Hamlet & D. P. Lettenmaier (2009). Implications of global climate change for snowmelt hydrology in the twenty-first century. *Hydrological Processes*, 23(7), 962–972. doi: 10.1002/hyp.7201.

Adamovic, M., F. Branger, I. Braud & S. Kralisch (2016). Development of a data-driven semi-distributed hydrological model for regional scale catchments prone to Mediterranean flash floods. *Journal of Hydrology*, 541, 173–189. doi: 10.1016/j.jhydrol.2016.03.032.

Adamovic, M., I. Braud, F. Branger & J. W. Kirchner (2015). Assessing the simple dynamical systems approach in a Mediterranean context: application to the Ardèche catchment (France). *Hydrology and Earth System Sciences*, 19(5), 2427–2449. doi: 10.5194/hess-19-2427-2015.

Ainsworth, E. A. & A. Rogers (2007). The response of photosynthesis and stomatal conductance to rising CO2: mechanisms and environmental interactions. *Plant, Cell & Environment*, 30(3), 258–270. doi: 10.1111/j.1365-3040.2007.01641.x.

Albergel, C., E. Dutra, S. Munier, J. C. Calvet, J. Munoz-Sabater, P. d. Rosnay & G. Balsamo (2018). ERA-5 and ERA-Interim driven ISBA land surface model simulations: which one performs better? *Hydrology and Earth System Sciences*, 22(6), 3515–3532. doi: 10.5194/hess-22-3515-2018.

Albertson, J. D. & G. Kiely (2001). On the structure of soil moisture time series in the context of land surface models. *Journal of Hydrology*, 243(1), 101–119. doi: 10.1016/s0022-1694(00)00405-4.

Allen, R. G., L. S. Pereira, D. Raes & M. Smith (1998). *Crop evapotranspiration-Guidelines for computing crop water requirements*. FAO Irrigation and drainage paper 56, Food and Agriculture Organization of the United Nations, Rome, Italy.

Andreadis, K. M., E. A. Clark, A. W. Wood, A. F. Hamlet & D. P. Lettenmaier (2005). Twentieth-Century Drought in the Conterminous United States. *Journal of Hydrometeorology*, 6(6), 985–1001. doi: 10.1175/JHM450.1.

de Arellano, J. V. G., C. C. van Heerwaarden & J. Lelieveld (2012). Modelled suppression of boundary-layer clouds by plants in a CO_2-rich atmosphere. *Nature Geoscience*, 5(10), 701–704. doi: 10.1038/ngeo1554.

Arnold, J. G., R. Srinivasan, R. S. Muttiah & J. R. Williams (1998). Large area hydrologic modeling and assessment - Part 1: Model development. *Journal of the American Water Resources Association*, 34(1), 73–89. doi: 10.1111/j.1752-1688.1998.tb05961.x.

Bachmair, S., K. Stahl, K. Collins, J. Hannaford, M. Acreman, M. Svoboda, C. Knutson, K. H. Smith,

N. Wall, B. Fuchs, N. D. Crossman & I. C. Overton (2016). Drought indicators revisited: the need for a wider consideration of environment and society. *WIREs Water*, 3(4), 516–536. doi: 10.1002/wat2.1154.

Bachmair, S., M. Tanguy, J. Hannaford & K. Stahl (2018). How well do meteorological indicators represent agricultural and forest drought across Europe? *Environmental Research Letters*, 13(3), 034042. doi: 10.1088/1748-9326/aaafda.

Badgley, G., L. D. L. Anderegg, J. A. Berry & C. B. Field (2019). Terrestrial gross primary production: Using NIRV to scale from site to globe. *Global Change Biology*, 25(11), 3731–3740. doi: 10.1111/gcb.14729.

Badgley, G., C. B. Field & J. A. Berry (2017). Canopy near-infrared reflectance and terrestrial photosynthesis. *Science Advances*, 3(3), e1602244. doi: 10.1126/sciadv.1602244.

Bakke, S. J., M. Ionita & L. M. Tallaksen (2020). The 2018 northern European hydrological drought and its drivers in a historical perspective. *Hydrology and Earth System Sciences*, 24(11), 5621–5653. doi: 10.5194/hess-24-5621-2020.

Baldocchi, D. D., Y. Ryu, B. Dechant, E. Eichelmann, K. Hemes, S. Ma, C. R. Sanchez, R. Shortt, D. Szutu, A. Valach, J. Verfaillie, G. Badgley, Y. Zeng & J. A. Berry (2020). Outgoing Near Infrared Radiation from Vegetation Scales with Canopy Photosynthesis Across a Spectrum of Function, Structure, Physiological Capacity and Weather. *Journal of Geophysical Research: Biogeosciences*, 125(7), e2019JG005534. doi: 10.1029/2019jg005534.

Ball, J. T., I. E. Woodrow & J. A. Berry (1987). A Model Predicting Stomatal Conductance and its Contribution to the Control of Photosynthesis under Different Environmental Conditions. In J. Biggins (editor), *Progress in Photosynthesis Research: Volume 4 Proceedings of the VIIth International Congress on Photosynthesis Providence, Rhode Island, USA, August 10–15, 1986*, pages 221–224. Springer Netherlands, Dordrecht. doi: 10.1007/978-94-017-0519-6_48.

Baraer, M., B. G. Mark, J. M. McKenzie, T. Condom, J. Bury, K. I. Huh, C. Portocarrero, J. Gómez & S. Rathay (2012). Glacier recession and water resources in Peru's Cordillera Blanca. *Journal of Glaciology*, 58(207), 134–150. doi: 10.3189/2012JoG11J186.

Barnett, T. P., J. C. Adam & D. P. Lettenmaier (2005). Potential impacts of a warming climate on water availability in snow-dominated regions. *Nature*, 438, 303–309. doi: 10.1038/nature04141.

Bassiouni, M., S. P. Good, C. J. Still & C. W. Higgins (2020). Plant Water Uptake Thresholds Inferred From Satellite Soil Moisture. *Geophysical Research Letters*, 47(7), e2020GL087077. doi: 10.1029/2020gl087077.

Bastos, A., Z. Fu, P. Ciais, P. Friedlingstein, S. Sitch, J. Pongratz, U. Weber, M. Reichstein, P. Anthoni, A. Arneth, V. Haverd, A. Jain, E. Joetzjer, J. Knauer, S. Lienert, T. Loughran, P. C. McGuire, W. Obermeier, R. S. Padrón, H. Shi, H. Tian, N. Viovy & S. Zaehle (2020). Impacts of extreme summers on European ecosystems: a comparative analysis of 2003, 2010 and 2018. *Philosophical Transactions of the Royal Society B: Biological Sciences*, 375(1810), 20190507. doi: 10.1098/rstb.2019.0507.

Bavay, M., T. Grünewald & M. Lehning (2013). Response of snow cover and runoff to climate change in high Alpine catchments of Eastern Switzerland. *Advances in Water Resources*, 55, 4–16. doi:

10.1016/j.advwatres.2012.12.009.

Beniston, M., D. Farinotti, M. Stoffel, L. M. Andreassen, E. Coppola, N. Eckert, A. Fantini, F. Giacona, C. Hauck, M. Huss, H. Huwald, M. Lehning, J. I. López-Moreno, J. Magnusson, C. Marty, E. Morán-Tejéda, S. Morin, M. Naaim, A. Provenzale, A. Rabatel, D. Six, J. Stötter, U. Strasser, S. Terzago & C. Vincent (2018). The European mountain cryosphere: a review of its current state, trends, and future challenges. *The Cryosphere*, 12(2), 759–794. doi: 10.5194/tc-12-759-2018.

Beniston, M., D. B. Stephenson, O. B. Christensen, C. A. T. Ferro, C. Frei, S. Goyette, K. Halsnaes, T. Holt, K. Jylhä, B. Koffi, J. Palutikof, R. Schöll, T. Semmler & K. Woth (2007). Future extreme events in European climate: an exploration of regional climate model projections. *Climatic Change*, 81(1), 71–95. doi: 10.1007/s10584-006-9226-z.

Benninga, H. J. F., C. D. U. Carranza, M. Pezij, P. van Santen, M. van der Ploeg, D. C. M. Augustijn & R. van der Velde (2018). The Raam regional soil moisture monitoring network in the Netherlands. *Earth System Science Data*, 10(1), 61–79. doi: 10.5194/essd-10-61-2018.

Best, M. J., G. Abramowitz, H. R. Johnson, A. J. Pitman, G. Balsamo, A. Boone, M. Cuntz, B. Decharme, P. A. Dirmeyer, J. Dong, M. Ek, Z. Guo, V. Haverd, B. J. J. van den Hurk, G. S. Nearing, B. Pak, C. Peters-Lidard, J. A. Santanello, L. Stevens & N. Vuichard (2015). The Plumbing of Land Surface Models: Benchmarking Model Performance. *Journal of Hydrometeorology*, 16(3), 1425–1442. doi: 10.1175/JHM-D-14-0158.1.

Betts, R. A., P. M. Cox & F. I. Woodward (2000). Simulated responses of potential vegetation to doubled-CO2 climate change and feedbacks on near-surface temperature. *Global Ecology and Biogeography*, 9(2), 171–180. doi: 10.1046/j.1365-2699.2000.00160.x.

Beven, K. (1989). Changing ideas in hydrology — The case of physically-based models. *Journal of Hydrology*, 105(1), 157–172. doi: 10.1016/0022-1694(89)90101-7.

Beven, K. (2001). How far can we go in distributed hydrological modelling? *Hydrology and Earth System Sciences*, 5(1), 1–12. doi: 10.5194/hess-5-1-2001.

Beven, K., H. Cloke, F. Pappenberger, R. Lamb & N. Hunter (2015). Hyperresolution information and hyperresolution ignorance in modelling the hydrology of the land surface. *Science China. Earth Sciences; Dordrecht*, 58(1), 25–35. doi: 10.1007/s11430-014-5003-4.

Beven, K. J. & H. L. Cloke (2012). Comment on "Hyperresolution global land surface modeling: Meeting a grand challenge for monitoring Earth's terrestrial water" by Eric F. Wood et al. *Water Resources Research*, 48(1), W01801. doi: 10.1029/2011WR010982.

Beven, K. J. & M. J. Kirkby (1979). A physically based, variable contributing area model of basin hydrology / Un modèle à base physique de zone d'appel variable de l'hydrologie du bassin versant. *Hydrological Sciences Bulletin*, 24(1), 43–69. doi: 10.1080/02626667909491834.

Bierkens, M. F. P. (2015). Global hydrology 2015: State, trends, and directions. *Water Resources Research*, 51(7), 4923–4947. doi: 10.1002/2015WR017173.

Bierkens, M. F. P., V. A. Bell, P. Burek, N. Chaney, L. E. Condon, C. H. David, A. de Roo, P. Döll, N. Drost, J. S. Famiglietti, M. Flörke, D. J. Gochis, P. Houser, R. Hut, J. Keune, S. Kollet, R. M. Maxwell, J. T. Reager, L. Samaniego, E. Sudicky, E. H. Sutanudjaja, N. van de Giesen, H. Winsemius & E. F. Wood (2015). Hyper-resolution global hydrological modelling: what is next? *Hydrological Processes*, 29(2),

310–320. doi: 10.1002/hyp.10391.

Bierkens, M. F. P., P. A. Finke & P. d. Willigen (2000). *Upscaling and downscaling methods for environmental research*. Kluwer, Dordrecht.

Birkinshaw, S. J., P. Moore, C. G. Kilsby, G. M. O'Donnell, A. J. Hardy & P. a. M. Berry (2014). Daily discharge estimation at ungauged river sites using remote sensing. *Hydrological Processes*, 28(3), 1043–1054. doi: 10.1002/hyp.9647.

Blöschl, G. (2001). Scaling in hydrology. *Hydrological Processes*, 15(4), 709–711. doi: 10.1002/hyp.432.

Blöschl, G., G. Bloschl, M. Sivapalan, T. Wagener, H. Savenije & A. Viglione (2013a). *Runoff Prediction in Ungauged Basins: Synthesis Across Processes, Places and Scales*. Cambridge University Press. Google-Books-ID: 6muV9EdwQPgC.

Blöschl, G., T. Nester, J. Komma, J. Parajka & R. A. P. Perdigão (2013b). The June 2013 flood in the Upper Danube Basin, and comparisons with the 2002, 1954 and 1899 floods. *Hydrology and Earth System Sciences*, 17(12), 5197–5212. doi: 10.5194/hess-17-5197-2013.

Blöschl, G. & M. Sivapalan (1995). Scale issues in hydrological modelling: A review. *Hydrological Processes*, 9(3-4), 251–290. doi: 10.1002/hyp.3360090305.

de Boer-Euser, T., L. Bouaziz, J. de Niel, C. Brauer, B. Dewals, G. Drogue, F. Fenicia, B. Grelier, J. Nossent, F. Pereira, H. Savenije, G. Thirel & P. Willems (2017). Looking beyond general metrics for model comparison – lessons from an international model intercomparison study. *Hydrology and Earth System Sciences*, 21(1), 423–440. doi: 10.5194/hess-21-423-2017.

Boese, S., M. Jung, N. Carvalhais, A. J. Teuling & M. Reichstein (2019). Carbon–water flux coupling under progressive drought. *Biogeosciences*, 16(13), 2557–2572. doi: 10.5194/bg-16-2557-2019.

Bouaziz, L., A. Weerts, J. Schellekens, E. Sprokkereef, J. Stam, H. Savenije & M. Hrachowitz (2018). Redressing the balance: quantifying net intercatchment groundwater flows. *Hydrology and Earth System Sciences*, 22(12), 6415–6434. doi: 10.5194/hess-22-6415-2018.

Bouaziz, L. J. E., F. Fenicia, G. Thirel, T. de Boer-Euser, J. Buitink, C. C. Brauer, J. de Niel, B. J. Dewals, G. Drogue, B. Grelier, L. A. Melsen, S. Moustakas, J. Nossent, F. Pereira, E. Sprokkereef, J. Stam, A. H. Weerts, P. Willems, H. H. G. Savenije & M. Hrachowitz (2021). Behind the scenes of streamflow model performance. *Hydrology and Earth System Sciences*, 25(2), 1069–1095. doi: 10.5194/hess-25-1069-2021.

Bounoua, L., F. G. Hall, P. J. Sellers, A. Kumar, G. J. Collatz, C. J. Tucker & M. L. Imhoff (2010). Quantifying the negative feedback of vegetation to greenhouse warming: A modeling approach. *Geophysical Research Letters*, 37(23). doi: 10.1029/2010gl045338.

Boyle, D. P., H. V. Gupta, S. Sorooshian, V. Koren, Z. Zhang & M. Smith (2001). Toward improved streamflow forecasts: value of semidistributed modeling. *Water Resources Research*, 37(11), 2749–2759. doi: 10.1029/2000WR000207.

Braud, I., N. Varado & A. Olioso (2005). Comparison of root water uptake modules using either the surface energy balance or potential transpiration. *Journal of Hydrology*, 301(1), 267–286. doi: 10.1016/j.jhydrol.2004.06.033.

Brauer, C. C., A. J. Teuling, A. Overeem, Y. van der Velde, P. Hazenberg, P. M. M. Warmerdam & R. Uijlen-

hoet (2011). Anatomy of extraordinary rainfall and flash flood in a Dutch lowland catchment. *Hydrology and Earth System Sciences*, 15(6), 1991–2005. doi: 10.5194/hess-15-1991-2011.

Brauer, C. C., A. J. Teuling, P. J. J. F. Torfs & R. Uijlenhoet (2013). Investigating storage-discharge relations in a lowland catchment using hydrograph fitting, recession analysis, and soil moisture data. *Water Resources Research*, 49(7), 4257–4264. doi: 10.1002/wrcr.20320.

Brauer, C. C., A. J. Teuling, P. J. J. F. Torfs & R. Uijlenhoet (2014). The Wageningen Lowland Runoff Simulator (WALRUS): a lumped rainfall–runoff model for catchments with shallow groundwater. *Geoscientific Model Development*, 7(5), 2313–2332. doi: 10.5194/gmd-7-2313-2014.

Brauer, C. C., Y. van der Velde, A. J. Teuling & R. Uijlenhoet (2018). The Hupsel Brook Catchment: Insights from Five Decades of Lowland Observations. *Vadose Zone Journal*, 17(1), 180056. doi: 10.2136/vzj2018.03.0056.

Brutsaert, W. & J. P. Lopez (1998). Basin-scale geohydrologic drought flow features of riparian aquifers in the Southern Great Plains. *Water Resources Research*, 34(2), 233–240. doi: 10.1029/97WR03068.

Brönnimann, S., J. Luterbacher, T. Ewen, H. F. Diaz, R. S. Stolarski & U. Neu (2007). *Climate Variability and Extremes during the Past 100 years*. Springer Science & Business Media.

Buitink, J., T. C. van Hateren & A. J. Teuling (2021a). Hydrological System Complexity Induces a Drought Frequency Paradox. *Frontiers in Water*, 3, 42. doi: 10.3389/frwa.2021.640976.

Buitink, J., L. A. Melsen, J. W. Kirchner & A. J. Teuling (2020a). A distributed simple dynamical systems approach (dS2 v1.0) for computationally efficient hydrological modelling at high spatio-temporal resolution. *Geoscientific Model Development*, 13(12), 6093–6110. doi: 10.5194/gmd-13-6093-2020.

Buitink, J., L. A. Melsen & A. J. Teuling (2021b). Seasonal discharge response to temperature-driven changes in evaporation and snow processes in the Rhine Basin. *Earth System Dynamics*, 12(2), 387–400. doi: 10.5194/esd-12-387-2021.

Buitink, J., A. M. Swank, M. van der Ploeg, N. E. Smith, H. J. F. Benninga, F. van der Bolt, C. D. U. Carranza, G. Koren, R. van der Velde & A. J. Teuling (2020b). Anatomy of the 2018 agricultural drought in the Netherlands using in situ soil moisture and satellite vegetation indices. *Hydrology and Earth System Sciences*, 24(12), 6021–6031. doi: 10.5194/hess-24-6021-2020.

Buitink, J., R. Uijlenhoet & A. J. Teuling (2019). Evaluating seasonal hydrological extremes in meso-scale (pre-)Alpine basins at coarse 0.5° and fine hyperresolution. *Hydrology and Earth System Sciences*, 23(3), 1593–1609. doi: 10.5194/hess-23-1593-2019.

Capehart, W. J. & T. N. Carlson (1997). Decoupling of surface and near-surface soil water content: A remote sensing perspective. *Water Resources Research*, 33(6), 1383–1395. doi: 10.1029/97WR00617.

Carpenter, T. M. & K. P. Georgakakos (2006). Intercomparison of lumped versus distributed hydrologic model ensemble simulations on operational forecast scales. *Journal of Hydrology*, 329(1-2), 174–185. doi: 10.1016/j.jhydrol.2006.02.013.

Carranza, C. D. U., M. van der Ploeg & P. J. J. F. Torfs (2018). Using lagged dependence to identify

(de)coupled surface and subsurface soil moisture values. *Hydrology and Earth System Sciences*, 22(4), 2255–2267. doi: 10.5194/hess-22-2255-2018.

Cash, J. R. & A. H. Karp (1990). A Variable Order Runge-Kutta Method for Initial Value Problems with Rapidly Varying Right-hand Sides. *ACM Transactions on Mathematical Software*, 16(3), 201–222. doi: 10.1145/79505.79507.

Ciais, P., M. Reichstein, N. Viovy, A. Granier, J. Ogée, V. Allard, M. Aubinet, N. Buchmann, C. Bernhofer, A. Carrara, F. Chevallier, N. de Noblet, A. D. Friend, P. Friedlingstein, T. Grünwald, B. Heinesch, P. Keronen, A. Knohl, G. Krinner, D. Loustau, G. Manca, G. Matteucci, F. Miglietta, J. M. Ourcival, D. Papale, K. Pilegaard, S. Rambal, G. Seufert, J. F. Soussana, M. J. Sanz, E. D. Schulze, T. Vesala & R. Valentini (2005). Europe-wide reduction in primary productivity caused by the heat and drought in 2003. *Nature*, 437(7058), 529–533. doi: 10.1038/nature03972.

Clapp, R. B. & G. M. Hornberger (1978). Empirical equations for some soil hydraulic properties. *Water Resources Research*, 14(4), 601–604. doi: 10.1029/WR014i004p00601.

Clark, M. P., M. F. P. Bierkens, L. Samaniego, R. A. Woods, R. Uijlenhoet, K. E. Bennett, V. R. N. Pauwels, X. Cai, A. W. Wood & C. D. Peters-Lidard (2017). The evolution of process-based hydrologic models: historical challenges and the collective quest for physical realism. *Hydrology and Earth System Sciences*, 21(7), 3427–3440. doi: 10.5194/hess-21-3427-2017.

Clark, M. P. & D. Kavetski (2010). Ancient numerical daemons of conceptual hydrological modeling: 1. Fidelity and efficiency of time stepping schemes. *Water Resources Research*, 46(10), W10510. doi: 10.1029/2009WR008894.

Clark, M. P., B. Nijssen, J. D. Lundquist, D. Kavetski, D. E. Rupp, R. A. Woods, J. E. Freer, E. D. Gutmann, A. W. Wood, L. D. Brekke, J. R. Arnold, D. J. Gochis & R. M. Rasmussen (2015). A unified approach for process-based hydrologic modeling: 1. Modeling concept. *Water Resources Research*, 51(4), 2498–2514. doi: 10.1002/2015WR017198.

Clark, M. P., A. G. Slater, D. E. Rupp, R. A. Woods, J. A. Vrugt, H. V. Gupta, T. Wagener & L. E. Hay (2008). Framework for Understanding Structural Errors (FUSE): A modular framework to diagnose differences between hydrological models. *Water Resources Research*, 44(12), W00B02. doi: 10.1029/2007WR006735.

Collins, D. N. (2008). Climatic warming, glacier recession and runoff from Alpine basins after the Little Ice Age maximum. *Annals of Glaciology*, 48, 119–124. doi: 10.3189/172756408784700761.

Combe, M., J. V. G. de Arellano, H. G. Ouwersloot & W. Peters (2016). Plant water-stress parameterization determines the strength of land–atmosphere coupling. *Agricultural and Forest Meteorology*, 217, 61–73. doi: 10.1016/j.agrformet.2015.11.006.

Comola, F., B. Schaefli, P. D. Ronco, G. Botter, M. Bavay, A. Rinaldo & M. Lehning (2015). Scale-dependent effects of solar radiation patterns on the snow-dominated hydrologic response. *Geophysical Research Letters*, 42(10), 3895–3902. doi: 10.1002/2015GL064075.

Cornes, R. C., G. van der Schrier, E. J. M. van den Besselaar & P. D. Jones (2018). An Ensemble Version of the E-OBS Temperature and Precipitation Data Sets. *Journal of Geophysical Research: Atmospheres*, 123(17), 9391–9409. doi: 10.1029/2017JD028200.

Corzo Perez, G. A., M. H. J. van Huijgevoort, F. Voß & H. a. J. van Lanen (2011). On the spatio-temporal

analysis of hydrological droughts from global hydrological models. *Hydrology and Earth System Sciences*, 15(9), 2963–2978. doi: 10.5194/hess-15-2963-2011.

Denissen, J. M. C., A. J. Teuling, M. Reichstein & R. Orth (2020). Critical Soil Moisture Derived From Satellite Observations Over Europe. *Journal of Geophysical Research: Atmospheres*, 125(6), e2019JD031672. doi: 10.1029/2019JD031672.

Denmead, O. T. & R. H. Shaw (1962). Availability of Soil Water to Plants as Affected by Soil Moisture Content and Meteorological Conditions 1. *Agronomy Journal*, 54(5), 385–390. doi: 10.2134/agronj1962.00021962005400050005x.

Dente, L., Z. Vekerdy, Z. Su & M. Ucer (2011). *Twente soil moisture and soil temperature monitoring network*. University of Twente.

Didan, K. (2015). MOD13C2 MODIS/Terra Vegetation Indices Monthly L3 Global 0.05Deg CMG V006. doi: 10.5067/MODIS/MOD13C2.006. Type: dataset.

Dooge, J. C. I. (1986). Looking for hydrologic laws. *Water Resources Research*, 22(9S), 46S–58S. doi: 10.1029/WR022i09Sp0046S.

Dooge, J. C. I. (1988). Hydrology in perspective. *Hydrological Sciences Journal*, 33(1), 61–85. doi: 10.1080/02626668809491223.

Dorigo, W., W. Wagner, C. Albergel, F. Albrecht, G. Balsamo, L. Brocca, D. Chung, M. Ertl, M. Forkel, A. Gruber, E. Haas, P. D. Hamer, M. Hirschi, J. Ikonen, R. de Jeu, R. Kidd, W. Lahoz, Y. Y. Liu, D. Miralles, T. Mistelbauer, N. Nicolai-Shaw, R. Parinussa, C. Pratola, C. Reimer, R. van der Schalie, S. I. Seneviratne, T. Smolander & P. Lecomte (2017). ESA CCI Soil Moisture for improved Earth system understanding: State-of-the art and future directions. *Remote Sensing of Environment*, 203, 185–215. doi: 10.1016/j.rse.2017.07.001.

Dorigo, W. A., W. Wagner, R. Hohensinn, S. Hahn, C. Paulik, A. Xaver, A. Gruber, M. Drusch, S. Mecklenburg, P. van Oevelen, A. Robock & T. Jackson (2011). The International Soil Moisture Network: a data hosting facility for global in situ soil moisture measurements. *Hydrology and Earth System Sciences*, 15(5), 1675–1698. doi: 10.5194/hess-15-1675-2011.

Douville, H., S. Planton, J. F. Royer, D. B. Stephenson, S. Tyteca, L. Kergoat, S. Lafont & R. A. Betts (2000). Importance of vegetation feedbacks in doubled-CO2 climate experiments. *Journal of Geophysical Research: Atmospheres*, 105(D11), 14841–14861. doi: 10.1029/1999JD901086.

Dracup, J. A., K. S. Lee & E. G. Paulson (1980). On the definition of droughts. *Water Resources Research*, 16(2), 297–302. doi: 10.1029/wr016i002p00297.

Driessen, T. L. A., R. T. W. L. Hurkmans, W. Terink, P. Hazenberg, P. J. J. F. Torfs & R. Uijlenhoet (2010). The hydrological response of the Ourthe catchment to climate change as modelled by the HBV model. *Hydrology and Earth System Sciences*, 14(4), 651–665. doi: 10.5194/hess-14-651-2010.

van Emmerik, T., J. Seibert, B. Strobl, S. Etter, T. den Oudendammer, M. Rutten, M. S. bin Ab Razak & I. van Meerveld (2020). Crowd-Based Observations of Riverine Macroplastic Pollution. *Frontiers in Earth Science*, 8. doi: 10.3389/feart.2020.00298.

van Engelenburg, J., R. Hueting, S. Rijpkema, A. J. Teuling, R. Uijlenhoet & F. Ludwig (2018). Impact of Changes in Groundwater Extractions and Climate Change on Groundwater-Dependent Ecosys-

tems in a Complex Hydrogeological Setting. *Water Resources Management*, 32(1), 259–272. doi: 10.1007/s11269-017-1808-1.

Fatichi, S., S. Rimkus, P. Burlando, R. Bordoy & P. Molnar (2015). High-resolution distributed analysis of climate and anthropogenic changes on the hydrology of an Alpine catchment. *Journal of Hydrology*, 525, 362–382. doi: 10.1016/j.jhydrol.2015.03.036.

Feddes, R. A. (1995). *Space and Time Scale Variability and Interdependencies in Hydrological Processes*. Cambridge University Press. Google-Books-ID: tDodIEzHRxYC.

Fleig, A. K., L. M. Tallaksen, H. Hisdal & S. Demuth (2006). A global evaluation of streamflow drought characteristics. *Hydrology and Earth System Sciences*, 10(4), 535–552. doi: 10.5194/hess-10-535-2006.

FOEN (2016). Hydrological data and forecasts. Federal Office for the Environment (FOEN).

Fontrodona Bach, A., G. van der Schrier, L. A. Melsen, A. M. G. Klein Tank & A. J. Teuling (2018). Widespread and Accelerated Decrease of Observed Mean and Extreme Snow Depth Over Europe. *Geophysical Research Letters*, 45(22), 12,312–12,319. doi: 10.1029/2018GL079799.

Ford, T. W., D. B. McRoberts, S. M. Quiring & R. E. Hall (2015). On the utility of in situ soil moisture observations for flash drought early warning in Oklahoma, USA. *Geophysical Research Letters*, 42(22), 9790–9798. doi: 10.1002/2015GL066600.

Fovet, O., L. Ruiz, M. Hrachowitz, M. Faucheux & C. Gascuel-Odoux (2015). Hydrological hysteresis and its value for assessing process consistency in catchment conceptual models. *Hydrology and Earth System Sciences*, 19(1), 105–123. doi: 10.5194/hess-19-105-2015.

Franchini, M. & P. E. O'Connell (1996). An analysis of the dynamic component of the geomorphologic instantaneous unit hydrograph. *Journal of Hydrology*, 175(1), 407–428. doi: 10.1016/S0022-1694(96)80018-7.

Frankenberg, C., J. B. Fisher, J. Worden, G. Badgley, S. S. Saatchi, J. E. Lee, G. C. Toon, A. Butz, M. Jung, A. Kuze & T. Yokota (2011). New global observations of the terrestrial carbon cycle from GOSAT: Patterns of plant fluorescence with gross primary productivity. *Geophysical Research Letters*, 38(17), L17706. doi: 10.1029/2011GL048738.

Fundel, F. & M. Zappa (2011). Hydrological ensemble forecasting in mesoscale catchments: Sensitivity to initial conditions and value of reforecasts. *Water Resources Research*, 47(9), W09520. doi: 10.1029/2010WR009996.

Gao, X., Y. Xu, Z. Zhao, J. S. Pal & F. Giorgi (2006). On the role of resolution and topography in the simulation of East Asia precipitation. *Theoretical and Applied Climatology*, 86(1-4), 173–185. doi: 10.1007/s00704-005-0214-4.

Gedney, N., P. M. Cox, R. A. Betts, O. Boucher, C. Huntingford & P. A. Stott (2006). Detection of a direct carbon dioxide effect in continental river runoff records. *Nature*, 439(7078), 835–838. doi: 10.1038/nature04504.

Gedney, N., C. Huntingford, G. P. Weedon, N. Bellouin, O. Boucher & P. M. Cox (2014). Detection of solar dimming and brightening effects on Northern Hemisphere river flow. *Nature Geoscience*, 7(11), 796–800. doi: 10.1038/ngeo2263.

Geertsema, T. J., A. J. Teuling, R. Uijlenhoet, P. J. J. F. Torfs & A. J. F. Hoitink (2018). Anatomy of simultaneous flood peaks at a lowland confluence. *Hydrology and Earth System Sciences*, 22(10), 5599–5613. doi: 10.5194/hess-22-5599-2018.

Gentine, P., T. J. Troy, B. R. Lintner & K. L. Findell (2012). Scaling in Surface Hydrology: Progress and Challenges. *Journal of Contemporary Water Research & Education*, 147(1), 28–40. doi: 10.1111/j.1936-704X.2012.03105.x.

Gibbs, W. J. & J. V. Maher (1967). *Rainfall Deciles as Drought Indicators*. Bulletin No. 48. Bureau of Meteorology.

de Graaff, M. A., K. J. van Groenigen, J. Six, B. Hungate & C. van Kessel (2006). Interactions between plant growth and soil nutrient cycling under elevated CO2: a meta-analysis. *Global Change Biology*, 12(11), 2077–2091. doi: 10.1111/j.1365-2486.2006.01240.x.

Green, J. K., S. I. Seneviratne, A. M. Berg, K. L. Findell, S. Hagemann, D. M. Lawrence & P. Gentine (2019). Large influence of soil moisture on long-term terrestrial carbon uptake. *Nature*, 565(7740), 476–479. doi: 10.1038/s41586-018-0848-x.

Green, S. R. & B. E. Clothier (1995). Root water uptake by kiwifruit vines following partial wetting of the root zone. *Plant and Soil*, 173(2), 317–328. doi: 10.1007/BF00011470.

Gruber, A., W. A. Dorigo, W. Crow & W. Wagner (2017). Triple Collocation-Based Merging of Satellite Soil Moisture Retrievals. *IEEE Transactions on Geoscience and Remote Sensing*, 55(12), 6780–6792. doi: 10.1109/TGRS.2017.2734070.

Gruber, A., T. Scanlon, R. van der Schalie, W. Wagner & W. Dorigo (2019). Evolution of the ESA CCI Soil Moisture climate data records and their underlying merging methodology. *Earth System Science Data*, 11(2), 717–739. doi: 10.5194/essd-11-717-2019.

Gupta, H. V., H. Kling, K. K. Yilmaz & G. F. Martinez (2009). Decomposition of the mean squared error and NSE performance criteria: Implications for improving hydrological modelling. *Journal of Hydrology*, 377(1–2), 80–91. doi: 10.1016/j.jhydrol.2009.08.003.

Gurtz, J., M. Zappa, K. Jasper, H. Lang, M. Verbunt, A. Badoux & T. Vitvar (2003). A comparative study in modelling runoff and its components in two mountainous catchments. *Hydrological Processes*, 17(2), 297–311. doi: 10.1002/hyp.1125.

Haddeland, I., B. V. Matheussen & D. P. Lettenmaier (2002). Influence of spatial resolution on simulated streamflow in a macroscale hydrologic model. *Water Resources Research*, 38(7), 29–1 – 29–10. doi: 10.1029/2001WR000854.

Hartmann, D. L., A. M. Klein Tank, M. Rusticucci, L. V. Alexander, S. Brönnimann, Y. A. R. Charabi, F. J. Dentener, E. J. Dlugokencky, D. R. Easterling & A. Kaplan (2013). Observations: atmosphere and surface. In *Climate change 2013 the physical science basis: Working group I contribution to the fifth assessment report of the intergovernmental panel on climate change*, pages 159–254. Cambridge University Press.

van Hateren, T. C., M. Chini, P. Matgen & A. J. Teuling (2021). Ambiguous Agricultural Drought: Characterising Soil Moisture and Vegetation Droughts in Europe from Earth Observation. *Remote Sensing*, 13(10), 1990. doi: 10.3390/rs13101990.

Hayes, M., M. Svoboda, N. Wall & M. Widhalm (2011). The Lincoln Declaration on Drought Indices: Universal Meteorological Drought Index Recommended. *Bulletin of the American Meteorological Society*, 92(4), 485–488. doi: 10.1175/2010BAMS3103.1.

Heim, R. R. (2002). A Review of Twentieth-Century Drought Indices Used in the United States. *Bulletin of the American Meteorological Society*, 83(8), 1149–1166. doi: 10.1175/1520-0477-83.8.1149.

Hersbach, H., B. Bell, P. Berrisford, G. Biavati, A. Horányi, J. Muñoz Sabater, J. Nicolas, C. Peubey, R. Radu & I. Rozum (2018). ERA5 hourly data on single levels from 1979 to present.

Hidalgo, H. G., T. Das, M. D. Dettinger, D. R. Cayan, D. W. Pierce, T. P. Barnett, G. Bala, A. Mirin, A. W. Wood, C. Bonfils, B. D. Santer & T. Nozawa (2009). Detection and Attribution of Streamflow Timing Changes to Climate Change in the Western United States. *Journal of Climate*, 22(13), 3838–3855. doi: 10.1175/2009JCLI2470.1.

Hisdal, H., K. Stahl, L. M. Tallaksen & S. Demuth (2001). Have streamflow droughts in Europe become more severe or frequent? *International Journal of Climatology*, 21(3), 317–333. doi: 10.1002/joc.619.

Hrachowitz, M. & M. P. Clark (2017). HESS Opinions: The complementary merits of competing modelling philosophies in hydrology. *Hydrology and Earth System Sciences*, 21(8), 3953–3973. doi: 10.5194/hess-21-3953-2017.

van Huijgevoort, M. H. J., P. Hazenberg, H. A. J. van Lanen, A. J. Teuling, D. B. Clark, S. Folwell, S. N. Gosling, N. Hanasaki, J. Heinke, S. Koirala, T. Stacke, F. Voss, J. Sheffield & R. Uijlenhoet (2013). Global Multimodel Analysis of Drought in Runoff for the Second Half of the Twentieth Century. *Journal of Hydrometeorology*, 14(5), 1535–1552. doi: 10.1175/JHM-D-12-0186.1.

van Huijgevoort, M. H. J., H. A. J. van Lanen, A. J. Teuling & R. Uijlenhoet (2014). Identification of changes in hydrological drought characteristics from a multi-GCM driven ensemble constrained by observed discharge. *Journal of Hydrology*, 512, 421–434. doi: 10.1016/j.jhydrol.2014.02.060.

Hunink, J. E., J. P. C. Eekhout, J. d. Vente, S. Contreras, P. Droogers & A. Baille (2017). Hydrological Modelling using Satellite-Based Crop Coefficients: A Comparison of Methods at the Basin Scale. *Remote Sensing*, 9(2), 174. doi: 10.3390/rs9020174.

Huntington, T. G. (2006). Evidence for intensification of the global water cycle: Review and synthesis. *Journal of Hydrology*, 319(1-4), 83–95. doi: 10.1016/j.jhydrol.2005.07.003.

Huntington, T. G. (2008). CO2-induced suppression of transpiration cannot explain increasing runoff. *Hydrological Processes*, 22(2), 311–314. doi: 10.1002/hyp.6925.

Hurkmans, R. T. W. L., W. Terink, R. Uijlenhoet, E. J. Moors, P. A. Troch & P. H. Verburg (2009). Effects of land use changes on streamflow generation in the Rhine basin. *Water Resources Research*, 45(6), W06405. doi: 10.1029/2008WR007574.

Hurkmans, R. T. W. L., W. Terink, R. Uijlenhoet, P. Torfs, D. Jacob & P. A. Troch (2010). Changes in streamflow dynamics in the Rhine basin under three high-resolution regional climate scenarios. *Journal of Climate*, 23(3), 679–699. doi: 10.1175/2009JCLI3066.1.

Huss, M. (2011). Present and future contribution of glacier storage change to runoff from macro-

scale drainage basins in Europe. *Water Resources Research*, 47(7). doi: 10.1029/2010WR010299.

Huuskonen, A., E. Saltikoff & I. Holleman (2013). The Operational Weather Radar Network in Europe. *Bulletin of the American Meteorological Society*, 95(6), 897–907. doi: 10.1175/BAMS-D-12-00216.1.

Imhoff, R. O., W. J. van Verseveld, B. van Osnabrugge & A. H. Weerts (2020). Scaling Point-Scale (Pedo)transfer Functions to Seamless Large-Domain Parameter Estimates for High-Resolution Distributed Hydrologic Modeling: An Example for the Rhine River. *Water Resources Research*, 56(4), e2019WR026807. doi: 10.1029/2019wr026807.

Immerzeel, W. W., L. P. H. van Beek, M. Konz, A. B. Shrestha & M. F. P. Bierkens (2012). Hydrological response to climate change in a glacierized catchment in the Himalayas. *Climatic Change*, 110(3-4), 721–736. doi: 10.1007/s10584-011-0143-4.

Immerzeel, W. W., A. F. Lutz, M. Andrade, A. Bahl, H. Biemans, T. Bolch, S. Hyde, S. Brumby, B. J. Davies, A. C. Elmore, A. Emmer, M. Feng, A. Fernández, U. Haritashya, J. S. Kargel, M. Koppes, P. D. A. Kraaijenbrink, A. V. Kulkarni, P. A. Mayewski, S. Nepal, P. Pacheco, T. H. Painter, F. Pellicciotti, H. Rajaram, S. Rupper, A. Sinisalo, A. B. Shrestha, D. Viviroli, Y. Wada, C. Xiao, T. Yao & J. E. M. Baillie (2020). Importance and vulnerability of the world's water towers. *Nature*, 577(7790), 364–369. doi: 10.1038/s41586-019-1822-y.

Jacob, D., J. Petersen, B. Eggert, A. Alias, O. B. Christensen, L. M. Bouwer, A. Braun, A. Colette, M. Déqué, G. Georgievski, E. Georgopoulou, A. Gobiet, L. Menut, G. Nikulin, A. Haensler, N. Hempelmann, C. Jones, K. Keuler, S. Kovats, N. Kröner, S. Kotlarski, A. Kriegsmann, E. Martin, E. van Meijgaard, C. Moseley, S. Pfeifer, S. Preuschmann, C. Radermacher, K. Radtke, D. Rechid, M. Rounsevell, P. Samuelsson, S. Somot, J. F. Soussana, C. Teichmann, R. Valentini, R. Vautard, B. Weber & P. Yiou (2014). EURO-CORDEX: new high-resolution climate change projections for European impact research. *Regional Environmental Change*, 14(2), 563–578. doi: 10.1007/s10113-013-0499-2.

Jarvis, A., H. Reuter, A. Nelson & E. Guevara (2008). Hole-filled SRTM for the globe Version 4, available from the CGIAR-CSI SRTM 90m Database.

Jenicek, M. & O. Ledvinka (2020). Importance of snowmelt contribution to seasonal runoff and summer low flows in Czechia. *Hydrology and Earth System Sciences*, 24(7), 3475–3491. doi: 10.5194/hess-24-3475-2020.

Jennings, K. S., T. S. Winchell, B. Livneh & N. P. Molotch (2018). Spatial variation of the rain–snow temperature threshold across the Northern Hemisphere. *Nature Communications*, 9(1), 1148. doi: 10.1038/s41467-018-03629-7.

Joiner, J., L. Guanter, R. Lindstrot, M. Voigt, A. P. Vasilkov, E. M. Middleton, K. F. Huemmrich, Y. Yoshida & C. Frankenberg (2013). Global monitoring of terrestrial chlorophyll fluorescence from moderate-spectral-resolution near-infrared satellite measurements: methodology, simulations, and application to GOME-2. *Atmospheric Measurement Techniques*, 6(10), 2803–2823. doi: 10.5194/amt-6-2803-2013.

Joiner, J., Y. Yoshida, L. Guanter & E. M. Middleton (2016). New methods for the retrieval of chlorophyll red fluorescence from hyperspectral satellite instruments: simulations and application to GOME-2 and SCIAMACHY. *Atmospheric Measurement Techniques*, 9(8), 3939–3967. doi:

10.5194/amt-9-3939-2016.

Jolly, W. M., M. Dobbertin, N. E. Zimmermann & M. Reichstein (2005). Divergent vegetation growth responses to the 2003 heat wave in the Swiss Alps. *Geophysical Research Letters*, 32(18), L18409. doi: 10.1029/2005GL023252.

Kalma, J. D. & M. Sivapalan (1995). *Scale issues in hydrological modelling*. John Wiley and Sons.

Karlsen, R. H., K. Bishop, T. Grabs, M. Ottosson-Löfvenius, H. Laudon & J. Seibert (2019). The role of landscape properties, storage and evapotranspiration on variability in streamflow recessions in a boreal catchment. *Journal of Hydrology*, 570, 315–328. doi: 10.1016/j.jhydrol.2018.12.065.

Kavetski, D. & M. P. Clark (2010). Ancient numerical daemons of conceptual hydrological modeling: 2. Impact of time stepping schemes on model analysis and prediction. *Water Resources Research*, 46(10), W10511. doi: 10.1029/2009WR008896.

Kavetski, D. & M. P. Clark (2011). Numerical troubles in conceptual hydrology: Approximations, absurdities and impact on hypothesis testing. *Hydrological Processes*, 25(4), 661–670. doi: 10.1002/hyp.7899.

Keenan, T. F., I. C. Prentice, J. G. Canadell, C. A. Williams, H. Wang, M. Raupach & G. J. Collatz (2016). Recent pause in the growth rate of atmospheric CO_2 due to enhanced terrestrial carbon uptake. *Nature Communications*, 7, 13428. doi: 10.1038/ncomms13428.

Kergoat, L., S. Lafont, H. Douville, B. Berthelot, G. Dedieu, S. Planton & J. F. Royer (2002). Impact of doubled CO2 on global-scale leaf area index and evapotranspiration: Conflicting stomatal conductance and LAI responses. *Journal of Geophysical Research: Atmospheres*, 107(D24), ACL 30–1–ACL 30–16. doi: 10.1029/2001JD001245.

Kidd, C., A. Becker, G. J. Huffman, C. L. Muller, P. Joe, G. Skofronick-Jackson & D. B. Kirschbaum (2017). So, How Much of the Earth's Surface Is Covered by Rain Gauges? *Bulletin of the American Meteorological Society*, 98(1), 69–78. doi: 10.1175/BAMS-D-14-00283.1.

Kimball, B. A., J. R. Mauney, F. S. Nakayama & S. B. Idso (1993). Effects of increasing atmospheric CO2 on vegetation. *Vegetatio*, 104-105(1), 65–75. doi: 10.1007/BF00048145.

Kirchner, J. W. (2009). Catchments as simple dynamical systems: Catchment characterization, rainfall-runoff modeling, and doing hydrology backward. *Water Resources Research*, 45(2), W02429. doi: 10.1029/2008WR006912.

Kirkby, M. J. (1976). Tests of the random network model, and its application to basin hydrology. *Earth Surface Processes*, 1(3), 197–212. doi: 10.1002/esp.3290010302.

Klein Tank, A. M. G., J. B. Wijngaard, G. P. Können, R. Böhm, G. Demarée, A. Gocheva, M. Mileta, S. Pashiardis, L. Hejkrlik, C. Kern-Hansen, R. Heino, P. Bessemoulin, G. Müller-Westermeier, M. Tzanakou, S. Szalai, T. Pálsdóttir, D. Fitzgerald, S. Rubin, M. Capaldo, M. Maugeri, A. Leitass, A. Bukantis, R. Aberfeld, A. F. V. van Engelen, E. Forland, M. Mietus, F. Coelho, C. Mares, V. Razuvaev, E. Nieplova, T. Cegnar, J. A. López, B. Dahlström, A. Moberg, W. Kirchhofer, A. Ceylan, O. Pachaliuk, L. V. Alexander & P. Petrovic (2002). Daily dataset of 20th-century surface air temperature and precipitation series for the European Climate Assessment. *International Journal of Climatology*, 22(12), 1441–1453. doi: 10.1002/joc.773.

Kleine, L., D. Tetzlaff, A. Smith, H. Wang & C. Soulsby (2020). Using water stable isotopes to understand evaporation, moisture stress, and re-wetting in catchment forest and grassland soils of the summer drought of 2018. *Hydrology and Earth System Sciences*, 24(7), 3737–3752. doi: 10.5194/hess-24-3737-2020.

Klemeš, V. (1983). Conceptualization and scale in hydrology. *Journal of Hydrology*, 65(1), 1–23. doi: 10.1016/0022-1694(83)90208-1.

Kling, H. & H. Gupta (2009). On the development of regionalization relationships for lumped watershed models: The impact of ignoring sub-basin scale variability. *Journal of Hydrology*, 373(3), 337–351. doi: 10.1016/j.jhydrol.2009.04.031.

Konings, A. G., M. Piles, K. Rötzer, K. A. McColl, S. K. Chan & D. Entekhabi (2016). Vegetation optical depth and scattering albedo retrieval using time series of dual-polarized L-band radiometer observations. *Remote Sensing of Environment*, 172, 178–189. doi: 10.1016/j.rse.2015.11.009.

Koren, G., E. van Schaik, A. C. Araújo, K. F. Boersma, A. Gärtner, L. Killaars, M. L. Kooreman, B. Kruijt, I. T. van der Laan-Luijkx, C. von Randow, N. E. Smith & W. Peters (2018). Widespread reduction in sun-induced fluorescence from the Amazon during the 2015/2016 El Niño. *Philosophical Transactions of the Royal Society B: Biological Sciences*, 373(1760), 20170408. doi: 10.1098/rstb.2017.0408.

Koren, V., S. Reed, M. Smith, Z. Zhang & D. J. Seo (2004). Hydrology laboratory research modeling system (HL-RMS) of the US national weather service. *Journal of Hydrology*, 291(3), 297–318. doi: 10.1016/j.jhydrol.2003.12.039.

Koster, R. D. & M. J. Suarez (2001). Soil Moisture Memory in Climate Models. *Journal of Hydrometeorology*, 2(6), 558–570. doi: 10.1175/1525-7541(2001)002<0558:SMMICM>2.0.CO;2.

Krier, R., P. Matgen, K. Goergen, L. Pfister, L. Hoffmann, J. W. Kirchner, S. Uhlenbrook & H. H. G. Savenije (2012). Inferring catchment precipitation by doing hydrology backward: A test in 24 small and mesoscale catchments in Luxembourg. *Water Resources Research*, 48(10), W10525. doi: 10.1029/2011WR010657.

Kruijt, B., J. P. M. Witte, C. M. J. Jacobs & T. Kroon (2008). Effects of rising atmospheric CO2 on evapotranspiration and soil moisture: A practical approach for the Netherlands. *Journal of Hydrology*, 349(3), 257–267. doi: 10.1016/j.jhydrol.2007.10.052.

Kumar, R., J. L. Musuuza, A. F. van Loon, A. J. Teuling, R. Barthel, J. ten Broek, J. Mai, L. Samaniego & S. Attinger (2016). Multiscale evaluation of the Standardized Precipitation Index as a groundwater drought indicator. *Hydrology and Earth System Sciences*, 20(3), 1117–1131. doi: 10.5194/hess-20-1117-2016.

Kumar, R., V. Shankar & M. K. Jat (2015). Evaluation of root water uptake models – a review. *ISH Journal of Hydraulic Engineering*, 21(2), 115–124. doi: 10.1080/09715010.2014.981955.

Kustas, W. P., A. Rango & R. Uijlenhoet (1994). A simple energy budget algorithm for the snowmelt runoff model. *Water Resources Research*, 30(5), 1515–1527. doi: 10.1029/94WR00152.

Laio, F., A. Porporato, L. Ridolfi & I. Rodriguez-Iturbe (2001). Plants in water-controlled ecosystems: active role in hydrologic processes and response to water stress: II. Probabilistic soil moisture dynamics. *Advances in Water Resources*, 24(7), 707–723. doi: 10.1016/S0309-1708(01)00005-7.

Lammertsma, E. I., H. J. d. Boer, S. C. Dekker, D. L. Dilcher, A. F. Lotter & F. Wagner-Cremer (2011). Global CO2 rise leads to reduced maximum stomatal conductance in Florida vegetation. *Proceedings of the National Academy of Sciences*, 108(10), 4035–4040. doi: 10.1073/pnas.1100371108.

Lansu, E. M., C. C. van Heerwaarden, A. I. Stegehuis & A. J. Teuling (2020). Atmospheric Aridity and Apparent Soil Moisture Drought in European Forest During Heat Waves. *Geophysical Research Letters*, 47(6), e2020GL087091. doi: 10.1029/2020GL087091.

Leipprand, A. & D. Gerten (2006). Global effects of doubled atmospheric CO2 content on evapotranspiration, soil moisture and runoff under potential natural vegetation. *Hydrological Sciences Journal*, 51(1), 171–185. doi: 10.1623/hysj.51.1.171.

Leung, L. R. & Y. Qian (2003). The sensitivity of precipitation and snowpack simulations to model resolution via nesting in regions of complex terrain. *Journal of Hydrometeorology*, 4(6), 1025–1043. doi: 10.1175/1525-7541(2003)004<1025:TSOPAS>2.0.CO;2.

Levis, S., J. A. Foley & D. Pollard (2000). Large-Scale Vegetation Feedbacks on a Doubled CO2 Climate. *Journal of Climate*, 13(7), 1313–1325. doi: 10.1175/1520-0442(2000)013<1313:lsvfoa>2.0.co;2.

Li, X., J. Xiao, B. He, M. A. Arain, J. Beringer, A. R. Desai, C. Emmel, D. Y. Hollinger, A. Krasnova, I. Mammarella, S. M. Noe, P. S. Ortiz, A. C. Rey-Sanchez, A. V. Rocha & A. Varlagin (2018). Solar-induced chlorophyll fluorescence is strongly correlated with terrestrial photosynthesis for a wide variety of biomes: First global analysis based on OCO-2 and flux tower observations. *Global Change Biology*, 24(9), 3990–4008. doi: 10.1111/gcb.14297.

Liang, X., J. Guo & L. Leung (2004). Assessment of the effects of spatial resolutions on daily water flux simulations. *Journal of Hydrology*, 298(1-4), 287–310. doi: 10.1016/j.jhydrol.2003.07.007.

Liang, X., D. P. Lettenmaier, E. F. Wood & S. J. Burges (1994). A simple hydrologically based model of land surface water and energy fluxes for general circulation models. *Journal of Geophysical Research*, 99(D7), 14415–14428. doi: 10.1029/94JD00483.

Liang, X., E. F. Wood & D. P. Lettenmaier (1996). Surface soil moisture parameterization of the VIC-2L model: Evaluation and modification. *Global and Planetary Change*, 13(1-4), 195–206. doi: 10.1016/0921-8181(95)00046-1.

Linde, A. H. t., J. C. J. H. Aerts, A. M. R. Bakker & J. C. J. Kwadijk (2010). Simulating low-probability peak discharges for the Rhine basin using resampled climate modeling data. *Water Resources Research*, 46(3). doi: 10.1029/2009WR007707.

Lindström, G., B. Johansson, M. Persson, M. Gardelin & S. Bergström (1997). Development and test of the distributed HBV-96 hydrological model. *Journal of Hydrology*, 201(1-4), 272–288. doi: 10.1016/S0022-1694(97)00041-3.

Liu, Y., M. Hejazi, H. Li, X. Zhang & G. Leng (2018). A hydrological emulator for global applications – HE v1.0.0. *Geoscientific Model Development*, 11(3), 1077–1092. doi: 10.5194/gmd-11-1077-2018.

Lobligeois, F., V. Andréassian, C. Perrin, P. Tabary & C. Loumagne (2014). When does higher spatial resolution rainfall information improve streamflow simulation? An evaluation using 3620 flood events. *Hydrology and Earth System Sciences*, 18(2), 575–594. doi: 10.5194/hess-18-575-2014.

Loft, R. (2020). Earth System Modeling Must Become More Energy Efficient. *Eos*. doi: 10.1029/

2020eo147051.

van Loon, A. F. (2015). Hydrological drought explained. *WIREs Water*, 2(4), 359–392. doi: 10.1002/wat2.1085.

van Loon, A. F., T. Gleeson, J. Clark, A. I. J. M. van Dijk, K. Stahl, J. Hannaford, G. Di Baldassarre, A. J. Teuling, L. M. Tallaksen, R. Uijlenhoet, D. M. Hannah, J. Sheffield, M. Svoboda, B. Verbeiren, T. Wagener, S. Rangecroft, N. Wanders & H. A. J. van Lanen (2016). Drought in the Anthropocene. *Nature Geoscience*, 9(2), 89–91. doi: 10.1038/ngeo2646.

Lucas-Picher, P., M. Wulff-Nielsen, J. H. Christensen, G. Adalgeirsdóttir, R. Mottram & S. B. Simonsen (2012). Very high resolution regional climate model simulations over Greenland: Identifying added value. *Journal of Geophysical Research: Atmospheres*, 117(D2), D02108. doi: 10.1029/2011JD016267.

Luterbacher, J., D. Dietrich, E. Xoplaki, M. Grosjean & H. Wanner (2004). European Seasonal and Annual Temperature Variability, Trends, and Extremes Since 1500. *Science*, 303(5663), 1499–1503. doi: 10.1126/science.1093877.

Lutz, A. F., W. W. Immerzeel, A. Gobiet, F. Pellicciotti & M. F. P. Bierkens (2013). Comparison of climate change signals in CMIP3 and CMIP5 multi-model ensembles and implications for Central Asian glaciers. *Hydrology and Earth System Sciences*, 17(9), 3661–3677. doi: 10.5194/hess-17-3661-2013.

Lutz, A. F., W. W. Immerzeel, P. D. A. Kraaijenbrink, A. B. Shrestha & M. F. P. Bierkens (2016). Climate Change Impacts on the Upper Indus Hydrology: Sources, Shifts and Extremes. *PLOS ONE*, 11(11), e0165630. doi: 10.1371/journal.pone.0165630.

Lutz, A. F., W. W. Immerzeel, A. B. Shrestha & M. F. P. Bierkens (2014). Consistent increase in High Asia's runoff due to increasing glacier melt and precipitation. *Nature Climate Change*, 4(7), 587–592. doi: 10.1038/nclimate2237.

Lyon, S. W. & P. A. Troch (2007). Hillslope subsurface flow similarity: Real-world tests of the hillslope Péclet number. *Water Resources Research*, 43(7), W07450. doi: 10.1029/2006WR005323.

Madi, R., G. H. d. Rooij, H. Mielenz & J. Mai (2018). Parametric soil water retention models: a critical evaluation of expressions for the full moisture range. *Hydrology and Earth System Sciences*, 22(2), 1193–1219. doi: 10.5194/hess-22-1193-2018.

Makkink, G. F. (1960). Evaporation from vegetations in relation with the formula of Penman. In *Verdampingssymposium agrohydrologisch colloquium COLN en rapport inzake de lysimeters in Nederland (II)*,, pages 90–115. Commision for Hydrological Research TNO, The Hague, the Netherlands.

Marchi, L., M. Borga, E. Preciso & E. Gaume (2010). Characterisation of selected extreme flash floods in Europe and implications for flood risk management. *Journal of Hydrology*, 394(1), 118–133. doi: 10.1016/j.jhydrol.2010.07.017.

Martens, B., D. G. Miralles, H. Lievens, R. van der Schalie, R. A. M. de Jeu, D. Fernández-Prieto, H. E. Beck, W. A. Dorigo & N. E. C. Verhoest (2017). GLEAM v3: satellite-based land evaporation and root-zone soil moisture. *Geoscientific Model Development*, 10(5), 1903–1925. doi: 10.5194/gmd-10-1903-2017.

Mastrotheodoros, T., C. Pappas, P. Molnar, P. Burlando, G. Manoli, J. Parajka, R. Rigon, B. Szeles, M. Bottazzi, P. Hadjidoukas & S. Fatichi (2020). More green and less blue water in the Alps during warmer summers. *Nature Climate Change*, 10(2), 155–161. doi: 10.1038/s41558-019-0676-5.

McCabe, M. F., D. G. Miralles, T. R. H. Holmes & J. B. Fisher (2019). Advances in the Remote Sensing of Terrestrial Evaporation. *Remote Sensing*, 11(9), 1138. doi: 10.3390/rs11091138.

McDonnell, J. J., M. Sivapalan, K. Vaché, S. Dunn, G. Grant, R. Haggerty, C. Hinz, R. Hooper, J. Kirchner, M. L. Roderick, J. Selker & M. Weiler (2007). Moving beyond heterogeneity and process complexity: A new vision for watershed hydrology. *Water Resources Research*, 43(7), W07301. doi: 10.1029/2006WR005467.

McKay, M. D., R. J. Beckman & W. J. Conover (1979). A Comparison of Three Methods for Selecting Values of Input Variables in the Analysis of Output from a Computer Code. *Technometrics*, 21(2), 239–245. doi: 10.2307/1268522.

Medlyn, B. E., C. V. M. Barton, M. S. J. Broadmeadow, R. Ceulemans, P. de Angelis, M. Forstreuter, M. Freeman, S. B. Jackson, S. Kellomäki, E. Laitat, A. Rey, P. Roberntz, B. D. Sigurdsson, J. Strassemeyer, K. Wang, P. S. Curtis & P. G. Jarvis (2001). Stomatal conductance of forest species after long-term exposure to elevated CO2 concentration: a synthesis. *New Phytologist*, 149(2), 247–264. doi: 10.1046/j.1469-8137.2001.00028.x.

Melsen, L. A., N. Addor, N. Mizukami, A. J. Newman, P. J. J. F. Torfs, M. P. Clark, R. Uijlenhoet & A. J. Teuling (2018). Mapping (dis)agreement in hydrologic projections. *Hydrology and Earth System Sciences*, 22(3), 1775–1791. doi: 10.5194/hess-22-1775-2018.

Melsen, L. A., A. Teuling, P. Torfs, M. Zappa, N. Mizukami, M. Clark & R. Uijlenhoet (2016a). Representation of spatial and temporal variability in large-domain hydrological models: case study for a mesoscale pre-Alpine basin. *Hydrology and Earth System Sciences*, 20(6), 2207–2226. doi: 10.5194/hess-20-2207-2016.

Melsen, L. A., A. J. Teuling, S. W. van Berkum, P. J. J. F. Torfs & R. Uijlenhoet (2014). Catchments as simple dynamical systems: A case study on methods and data requirements for parameter identification. *Water Resources Research*, 50(7), 5577–5596. doi: 10.1002/2013WR014720.

Melsen, L. A., A. J. Teuling, P. J. J. F. Torfs, R. Uijlenhoet, N. Mizukami & M. P. Clark (2016b). HESS Opinions: The need for process-based evaluation of large-domain hyper-resolution models. *Hydrology and Earth System Sciences*, 20(3), 1069–1079. doi: 10.5194/hess-20-1069-2016.

Melsen, L. A., A. J. Teuling, P. J. J. F. Torfs, M. Zappa, N. Mizukami, P. A. Mendoza, M. P. Clark & R. Uijlenhoet (2019). Subjective modeling decisions can significantly impact the simulation of flood and drought events. *Journal of Hydrology*, 568, 1093–1104. doi: 10.1016/j.jhydrol.2018.11.046.

MeteoSwiss (2013). *Daily Mean, Minimum and Maximum Temperature: TabsD, TminD, TmaxD*. Technical report, Federal Office of Meteorology and Climatology (MeteoSwiss).

MeteoSwiss (2016). *Daily Precipitation: RhiresD*. Technical report, Federal Office of Meteorology and Climatology (MeteoSwiss).

MeteoSwiss (2017). Très chaud à la fin du mois de mai.

Middelkoop, H., K. Daamen, D. Gellens, W. Grabs, J. C. Kwadijk, H. Lang, B. W. Parmet, B. Schädler,

J. Schulla & K. Wilke (2001). Impact of climate change on hydrological regimes and water resources management in the Rhine basin. *Climatic Change*, 49(1-2), 105–128. doi: 10.1023/A:1010784727448.

Milly, P. C. D. & K. A. Dunne (2016). Potential evapotranspiration and continental drying. *Nature Climate Change*, 6(10), 946–949. doi: 10.1038/nclimate3046.

Milly, P. C. D. & K. A. Dunne (2020). Colorado River flow dwindles as warming-driven loss of reflective snow energizes evaporation. *Science*, 367(6483), 1252–1255. doi: 10.1126/science.aay9187.

Miralles, D. G., P. Gentine, S. I. Seneviratne & A. J. Teuling (2019). Land–atmospheric feedbacks during droughts and heatwaves: state of the science and current challenges. *Annals of the New York Academy of Sciences*, 1436(1), 19–35. doi: 10.1111/nyas.13912.

Mittelbach, H., F. Casini, I. Lehner, A. J. Teuling & S. I. Seneviratne (2011). Soil moisture monitoring for climate research: Evaluation of a low-cost sensor in the framework of the Swiss Soil Moisture Experiment (SwissSMEX) campaign. *Journal of Geophysical Research: Atmospheres*, 116(D5), D05111. doi: 10.1029/2010JD014907.

Moesinger, L., W. Dorigo, R. de Jeu, R. van der Schalie, T. Scanlon, I. Teubner & M. Forkel (2019). The Global Long-term Microwave Vegetation Optical Depth Climate Archive VODCA. doi: 10.5281/zenodo.2575599. Type: dataset.

Moesinger, L., W. Dorigo, R. d. Jeu, R. van der Schalie, T. Scanlon, I. Teubner & M. Forkel (2020). The global long-term microwave Vegetation Optical Depth Climate Archive (VODCA). *Earth System Science Data*, 12(1), 177–196. doi: 10.5194/essd-12-177-2020.

Mohanty, B. P., M. H. Cosh, V. Lakshmi & C. Montzka (2017). Soil Moisture Remote Sensing: State-of-the-Science. *Vadose Zone Journal*, 16(1), vzj2016.10.0105. doi: 10.2136/vzj2016.10.0105.

van der Molen, M. K., A. J. Dolman, P. Ciais, T. Eglin, N. Gobron, B. E. Law, P. Meir, W. Peters, O. L. Phillips, M. Reichstein, T. Chen, S. C. Dekker, M. Doubková, M. A. Friedl, M. Jung, B. J. J. M. van den Hurk, R. A. M. de Jeu, B. Kruijt, T. Ohta, K. T. Rebel, S. Plummer, S. I. Seneviratne, S. Sitch, A. J. Teuling, G. R. van der Werf & G. Wang (2011). Drought and ecosystem carbon cycling. *Agricultural and Forest Meteorology*, 151(7), 765–773. doi: 10.1016/j.agrformet.2011.01.018.

Monteith, J. L. (1965). Evaporation and environment. *Symposia of the Society for Experimental Biology*, 19, 205–234.

Musselman, K. N., M. P. Clark, C. Liu, K. Ikeda & R. Rasmussen (2017). Slower snowmelt in a warmer world. *Nature Climate Change*, 7(3), 214–219. doi: 10.1038/nclimate3225.

Napoli, A., A. Crespi, F. Ragone, M. Maugeri & C. Pasquero (2019). Variability of orographic enhancement of precipitation in the Alpine region. *Scientific Reports*, 9(1), 13352. doi: 10.1038/s41598-019-49974-5.

Nash, J. E. & J. V. Sutcliffe (1970). River flow forecasting through conceptual models part I — A discussion of principles. *Journal of Hydrology*, 10(3), 282–290. doi: 10.1016/0022-1694(70)90255-6.

Notaro, M., S. Vavrus & Z. Liu (2007). Global Vegetation and Climate Change due to Future Increases in CO2 as Projected by a Fully Coupled Model with Dynamic Vegetation. *Journal of Climate*, 20(1), 70–90. doi: 10.1175/JCLI3989.1.

van Osnabrugge, B., R. Uijlenhoet & A. Weerts (2019). Contribution of potential evaporation forecasts to 10-day streamflow forecast skill for the Rhine River. *Hydrology and Earth System Sciences*, 23(3), 1453–1467. doi: 10.5194/hess-23-1453-2019.

van Osnabrugge, B., A. H. Weerts & R. Uijlenhoet (2017). genRE: A Method to Extend Gridded Precipitation Climatology Data Sets in Near Real-Time for Hydrological Forecasting Purposes. *Water Resources Research*, 53(11), 9284–9303. doi: 10.1002/2017WR021201.

Otkin, J. A., M. Svoboda, E. D. Hunt, T. W. Ford, M. C. Anderson, C. Hain & J. B. Basara (2018). Flash Droughts: A Review and Assessment of the Challenges Imposed by Rapid-Onset Droughts in the United States. *Bulletin of the American Meteorological Society*, 99(5), 911–919. doi: 10.1175/BAMS-D-17-0149.1.

Pan, M. & E. F. Wood (2013). Inverse streamflow routing. *Hydrology and Earth System Sciences*, 17(11), 4577–4588. doi: 10.5194/hess-17-4577-2013.

Peel, M. C. & T. A. McMahon (2006). A quality-controlled global runoff data set. *Nature*, 444(7120), E14–E14. doi: 10.1038/nature05480.

Perrin, C., C. Michel & V. Andréassian (2003). Improvement of a parsimonious model for streamflow simulation. *Journal of Hydrology*, 279(1-4), 275–289. doi: 10.1016/S0022-1694(03)00225-7.

Peters-Lidard, C. D., M. Clark, L. Samaniego, N. E. C. Verhoest, T. van Emmerik, R. Uijlenhoet, K. Achieng, T. E. Franz & R. Woods (2017). Scaling, similarity, and the fourth paradigm for hydrology. *Hydrology and Earth System Sciences*, 21(7), 3701–3713. doi: 10.5194/hess-21-3701-2017.

Pfister, L., J. Kwadijk, A. Musy, A. Bronstert & L. Hoffmann (2004). Climate change, land use change and runoff prediction in the Rhine–Meuse basins. *River Research and Applications*, 20(3), 229–241. doi: 10.1002/rra.775.

Pijl, A., C. C. Brauer, G. Sofia, A. J. Teuling & P. Tarolli (2018). Hydrologic impacts of changing land use and climate in the Veneto lowlands of Italy. *Anthropocene*, 22, 20–30. doi: 10.1016/j.ancene.2018.04.001.

van der Ploeg, M., J. E. M. Baartman & D. A. Robinson (2018). Biophysical landscape interactions: Bridging disciplines and scale with connectivity. *Land Degradation & Development*, 29(4), 1167–1175. doi: 10.1002/ldr.2820.

Prentice, I. C., N. Dong, S. M. Gleason, V. Maire & I. J. Wright (2014). Balancing the costs of carbon gain and water transport: testing a new theoretical framework for plant functional ecology. *Ecology Letters*, 17(1), 82–91. doi: 10.1111/ele.12211.

Pryor, S. C., G. Nikulin & C. Jones (2012). Influence of spatial resolution on regional climate model derived wind climates. *Journal of Geophysical Research: Atmospheres*, 117(D3), D03117. doi: 10.1029/2011JD016822.

Purdy, A. J., J. B. Fisher, M. L. Goulden, A. Colliander, G. Halverson, K. Tu & J. S. Famiglietti (2018). SMAP soil moisture improves global evapotranspiration. *Remote Sensing of Environment*, 219, 1–14. doi: 10.1016/j.rse.2018.09.023.

Reichstein, M., M. Bahn, P. Ciais, D. Frank, M. D. Mahecha, S. I. Seneviratne, J. Zscheischler, C. Beer, N. Buchmann, D. C. Frank, D. Papale, A. Rammig, P. Smith, K. Thonicke, M. van der Velde, S. Vicca,

A. Walz & M. Wattenbach (2013). Climate extremes and the carbon cycle. *Nature*, 500(7462), 287–295. doi: 10.1038/nature12350.

Robinson, D. A., J. W. Hopmans, V. Filipovic, M. van der Ploeg, I. Lebron, S. B. Jones, S. Reinsch, N. Jarvis & M. Tuller (2019). Global environmental changes impact soil hydraulic functions through biophysical feedbacks. *Global Change Biology*, 25(6), 1895–1904. doi: 10.1111/gcb.14626.

Rodríguez-Iturbe, I. & J. B. Valdes (1979). The geomorphologic structure of hydrologic response. *Water Resources Research*, 15(6), 1409–1420. doi: 10.1029/WR015i006p01409.

Roe, G. H. (2004). Orographic precipitation. *Annual Review of Earth and Planetary Sciences*, 33(1), 645–671. doi: 10.1146/annurev.earth.33.092203.122541.

Rottler, E., T. Francke, G. Bürger & A. Bronstert (2020). Long-term changes in central European river discharge for 1869–2016: impact of changing snow covers, reservoir constructions and an intensified hydrological cycle. *Hydrology and Earth System Sciences*, 24(4), 1721–1740. doi: 10.5194/hess-24-1721-2020.

Rottler, E., K. Vormoor, T. Francke, M. Warscher, U. Strasser & A. Bronstert (2021). Elevation-dependent compensation effects in snowmelt in the Rhine River Basin upstream gauge Basel. *Hydrology Research*, 52(2), 536–557. doi: 10.2166/nh.2021.092.

Ruiz-Villanueva, V., M. Borga, D. Zoccatelli, L. Marchi, E. Gaume & U. Ehret (2012). Extreme flood response to short-duration convective rainfall in South-West Germany. *Hydrology and Earth System Sciences*, 16(5), 1543–1559. doi: 10.5194/hess-16-1543-2012.

Rupp, D. E. & J. S. Selker (2006). On the use of the Boussinesq equation for interpreting recession hydrographs from sloping aquifers. *Water Resources Research*, 42(12), W12421. doi: 10.1029/2006WR005080.

Rupp, D. E. & R. A. Woods (2008). Increased flexibility in base flow modelling using a power law transmissivity profile. *Hydrological Processes*, 22(14), 2667–2671. doi: 10.1002/hyp.6863.

Saltelli, A. (2002). Making best use of model evaluations to compute sensitivity indices. *Computer Physics Communications*, 145(2), 280–297. doi: 10.1016/S0010-4655(02)00280-1.

Saltelli, A., P. Annoni, I. Azzini, F. Campolongo, M. Ratto & S. Tarantola (2010). Variance based sensitivity analysis of model output. Design and estimator for the total sensitivity index. *Computer Physics Communications*, 181(2), 259–270. doi: 10.1016/j.cpc.2009.09.018.

Sapriza-Azuri, G., J. Jódar, V. Navarro, L. J. Slooten, J. Carrera & H. V. Gupta (2015). Impacts of rainfall spatial variability on hydrogeological response. *Water Resources Research*, 51(2), 1300–1314. doi: 10.1002/2014wr016168.

Savenije, H. H. G. (2010). HESS Opinions "Topography driven conceptual modelling (FLEX-Topo)". *Hydrology and Earth System Sciences*, 14(12), 2681–2692. doi: 10.5194/hess-14-2681-2010.

Schaaf, C. & Z. Wang (2015). MCD43A4 MODIS/Terra+ Aqua BRDF/Albedo Nadir BRDF Adjusted Ref-Daily L3 Global-500m V006 [Data set]. *NASA EOSDIS Land Processes DAAC*. doi: 10.5067/MODIS/MCD43A4.006.

Schaefli, B., B. Hingray & A. Musy (2007). Climate change and hydropower production in the Swiss Alps: quantification of potential impacts and related modelling uncertainties. *Hydrology and*

Earth System Sciences, 11(3), 1191–1205. doi: 10.5194/hess-11-1191-2007.

van Schaik, E., L. Killaars, N. E. Smith, G. Koren, L. P. H. van Beek, W. Peters & I. T. van der Laan-Luijkx (2018). Changes in surface hydrology, soil moisture and gross primary production in the Amazon during the 2015/2016 El Niño. *Philosophical Transactions of the Royal Society B: Biological Sciences*, 373(1760), 20180084. doi: 10.1098/rstb.2018.0084.

Schmidli, J. & C. Frei (2005). Trends of heavy precipitation and wet and dry spells in Switzerland during the 20th century. *International Journal of Climatology*, 25(6), 753–771. doi: 10.1002/joc.1179.

Schmugge, T. J., W. P. Kustas, J. C. Ritchie, T. J. Jackson & A. Rango (2002). Remote sensing in hydrology. *Advances in Water Resources*, 25(8), 1367–1385. doi: 10.1016/S0309-1708(02)00065-9.

Schoonjans, F., D. de Bacquer & P. Schmid (2011). Estimation of Population Percentiles. *Epidemiology*, 22(5), 750–751. doi: 10.1097/EDE.0b013e318225c1de.

Schoups, G., J. A. Vrugt, F. Fenicia & N. van de Giesen (2010). Corruption of accuracy and efficiency of Markov chain Monte Carlo simulation by inaccurate numerical implementation of conceptual hydrologic models. *Water Resources Research*, 46(10), W10530. doi: 10.1029/2009WR008648.

Schuldt, B., A. Buras, M. Arend, Y. Vitasse, C. Beierkuhnlein, A. Damm, M. Gharun, T. E. E. Grams, M. Hauck, P. Hajek, H. Hartmann, E. Hiltbrunner, G. Hoch, M. Holloway-Phillips, C. Körner, E. Larysch, T. Lübbe, D. B. Nelson, A. Rammig, A. Rigling, L. Rose, N. K. Ruehr, K. Schumann, F. Weiser, C. Werner, T. Wohlgemuth, C. S. Zang & A. Kahmen (2020). A first assessment of the impact of the extreme 2018 summer drought on Central European forests. *Basic and Applied Ecology*, 45, 86–103. doi: 10.1016/j.baae.2020.04.003.

Schuurmans, J. M. & M. F. P. Bierkens (2007). Effect of spatial distribution of daily rainfall on interior catchment response of a distributed hydrological model. *Hydrology and Earth System Sciences*, 11(2), 677–693. doi: 10.5194/hess-11-677-2007.

Seneviratne, S. I., T. Corti, E. L. Davin, M. Hirschi, E. B. Jaeger, I. Lehner, B. Orlowsky & A. J. Teuling (2010). Investigating soil moisture–climate interactions in a changing climate: A review. *Earth-Science Reviews*, 99(3), 125–161. doi: 10.1016/j.earscirev.2010.02.004.

Seneviratne, S. I., I. Lehner, J. Gurtz, A. J. Teuling, H. Lang, U. Moser, D. Grebner, L. Menzel, K. Schroff, T. Vitvar & M. Zappa (2012). Swiss prealpine Rietholzbach research catchment and lysimeter: 32 year time series and 2003 drought event. *Water Resources Research*, 48(6), W06526. doi: 10.1029/2011WR011749.

Settele, J., R. Scholes, R. Betts, S. Bunn, P. Leadley, D. Nepstad, J. Overpeck, M. Taboada, A. Fischlin, J. Moreno, T. Root, M. Musche & M. Winter (2015). Terrestrial and Inland water systems. In *Climate Change 2014 Impacts, Adaptation and Vulnerability: Part A: Global and Sectoral Aspects*, Working Group II Contribution to the IPCC Fifth Assessment Report, pages 271–360. Cambridge University Press, Cambridge, UK. doi: 10.1017/CBO9781107415379.009.

Shabalova, M. V., W. P. A. van Deursen & T. A. Buishand (2003). Assessing future discharge of the river Rhine using regional climate model integrations and a hydrological model. *Climate Research*, 23(3), 233–246. doi: 10.3354/cr023233.

Sharp, R. E. & W. J. Davies (1985). Root Growth and Water Uptake by Maize Plants in Drying Soil.

Journal of Experimental Botany, 36(9), 1441–1456. doi: 10.1093/jxb/36.9.1441.

Sheffield, J., K. M. Andreadis, E. F. Wood & D. P. Lettenmaier (2009). Global and Continental Drought in the Second Half of the Twentieth Century: Severity–Area–Duration Analysis and Temporal Variability of Large-Scale Events. *Journal of Climate*, 22(8), 1962–1981. doi: 10.1175/2008JCLI2722.1.

Sheffield, J. & E. F. Wood (2008). Global Trends and Variability in Soil Moisture and Drought Characteristics, 1950–2000, from Observation-Driven Simulations of the Terrestrial Hydrologic Cycle. *Journal of Climate*, 21(3), 432–458. doi: 10.1175/2007JCLI1822.1.

Sheffield, J., E. F. Wood & M. L. Roderick (2012). Little change in global drought over the past 60 years. *Nature*, 491(7424), 435–438. doi: 10.1038/nature11575.

Singh, A., S. Kumar, S. Akula, D. M. Lawrence & D. L. Lombardozzi (2020). Plant Growth Nullifies the Effect of Increased Water-Use Efficiency on Streamflow Under Elevated CO2 in the Southeastern United States. *Geophysical Research Letters*, 47(4), e2019GL086940. doi: 10.1029/2019GL086940.

Sippel, S., M. Reichstein, X. Ma, M. D. Mahecha, H. Lange, M. Flach & D. Frank (2018). Drought, Heat, and the Carbon Cycle: a Review. *Current Climate Change Reports*, 4(3), 266–286. doi: 10.1007/s40641-018-0103-4.

Sivapalan, M. (2003). Prediction in ungauged basins: a grand challenge for theoretical hydrology. *Hydrological Processes*, 17(15), 3163–3170. doi: 10.1002/hyp.5155.

Sivapalan, M. (2006). Pattern, Process and Function: Elements of a Unified Theory of Hydrology at the Catchment Scale, Pattern, Process and Function: Elements of a Unified Theory of Hydrology at the Catchment Scale. In *Encyclopedia of Hydrological Sciences, Encyclopedia of Hydrological Sciences*. John Wiley & Sons, Ltd, John Wiley & Sons, Ltd. doi: 10.1002/0470848944.hsa012.

Sivapalan, M., R. Grayson & R. Woods (2004). Scale and scaling in hydrology. *Hydrological Processes*, 18(8), 1369–1371. doi: 10.1002/hyp.1417.

Slette, I. J., A. K. Post, M. Awad, T. Even, A. Punzalan, S. Williams, M. D. Smith & A. K. Knapp (2019). How ecologists define drought, and why we should do better. *Global Change Biology*, 25(10), 3193–3200. doi: 10.1111/gcb.14747.

Smith, N. E., L. M. J. Kooijmans, G. Koren, E. van Schaik, A. M. van der Woude, N. Wanders, M. Ramonet, I. Xueref-Remy, L. Siebicke, G. Manca, C. Brümmer, I. T. Baker, K. D. Haynes, I. T. Luijkx & W. Peters (2020). Spring enhancement and summer reduction in carbon uptake during the 2018 drought in northwestern Europe. *Philosophical Transactions of the Royal Society B: Biological Sciences*, 375(1810), 20190509. doi: 10.1098/rstb.2019.0509.

Sobieraj, J. A., H. Elsenbeer & G. Cameron (2004). Scale dependency in spatial patterns of saturated hydraulic conductivity. *CATENA*, 55(1), 49–77. doi: 10.1016/S0341-8162(03)00090-0.

Sobol', I. M. (2001). Global sensitivity indices for nonlinear mathematical models and their Monte Carlo estimates. *Mathematics and Computers in Simulation*, 55(1), 271–280. doi: 10.1016/S0378-4754(00)00270-6.

Sorooshian, S., A. AghaKouchak, P. Arkin, J. Eylander, E. Foufoula-Georgiou, R. Harmon, J. M. H.

Hendrickx, B. Imam, R. Kuligowski, B. Skahill & G. Skofronick-Jackson (2011). Advanced Concepts on Remote Sensing of Precipitation at Multiple Scales. *Bulletin of the American Meteorological Society*, 92(10), 1353–1357. doi: 10.1175/2011BAMS3158.1.

Speich, M. J. R., L. Bernhard, A. J. Teuling & M. Zappa (2015). Application of bivariate mapping for hydrological classification and analysis of temporal change and scale effects in Switzerland. *Journal of Hydrology*, 523, 804–821. doi: 10.1016/j.jhydrol.2015.01.086.

Spence, C., X. J. Guan, R. Phillips, N. Hedstrom, R. Granger & B. Reid (2010). Storage dynamics and streamflow in a catchment with a variable contributing area. *Hydrological Processes*, 24(16), 2209–2221. doi: 10.1002/hyp.7492.

Sposito, G. (2008). *Scale Dependence and Scale Invariance in Hydrology*. Cambridge University Press. Google-Books-ID: Y5LlBfT1uPMC.

Stagge, J. H., I. Kohn, L. M. Tallaksen & K. Stahl (2015). Modeling drought impact occurrence based on meteorological drought indices in Europe. *Journal of Hydrology*, 530, 37–50. doi: 10.1016/j.jhydrol.2015.09.039.

Stahl, K., J. P. Vidal, J. Hannaford, E. Tijdeman, G. Laaha, T. Gauster & L. M. Tallaksen (2020). The challenges of hydrological drought definition, quantification and communication: an interdisciplinary perspective. In *Proceedings of the International Association of Hydrological Sciences*, volume 383, pages 291–295. Copernicus GmbH. doi: 10.5194/piahs-383-291-2020. ISSN: 2199-8981.

Stahl, K., M. Weiler, I. Kohn, D. Freudiger, J. Seibert, M. Vis, K. Gerlinger & M. Bohm (2016). *The snow and glacier melt components of streamflow of the river Rhine and its tributaries considering the influence climate change*. Technical Report I-25, International Commission for the Hydrology of the Rhine Basin, Lelystad, Netherlands.

Steinemann, A. (2003). Drought Indicators and Triggers: A Stochastic Approach to Evaluation1. *JAWRA Journal of the American Water Resources Association*, 39(5), 1217–1233. doi: 10.1111/j.1752-1688.2003.tb03704.x.

Steinemann, A., S. F. Iacobellis & D. R. Cayan (2015). Developing and Evaluating Drought Indicators for Decision-Making. *Journal of Hydrometeorology*, 16(4), 1793–1803. doi: 10.1175/JHM-D-14-0234.1.

Stocker, B. D., J. Zscheischler, T. F. Keenan, I. C. Prentice, S. I. Seneviratne & J. Peñuelas (2019). Drought impacts on terrestrial primary production underestimated by satellite monitoring. *Nature Geoscience*, 12(4), 264–270. doi: 10.1038/s41561-019-0318-6.

Stocker, T. F., D. Qin, G. K. Plattner, M. Tignor, S. K. Allen, J. Boschung, A. Nauels, Y. Xia, B. Bex & B. M. Midgley (2013). *IPCC, 2013: Climate Change 2013: The physical science basis. Contribution of Working Group I to the Fifth Assessment report of the Intergovernmental Panel on Climate Change*. Cambridge University Press, Cambridge, UK. doi: 10.1017/CBO9781107415324.

Strobl, B., S. Etter, I. van Meerveld & J. Seibert (2020). Accuracy of crowdsourced streamflow and stream level class estimates. *Hydrological Sciences Journal*, 65(5), 823–841. doi: 10.1080/02626667.2019.1578966.

Sutanudjaja, E. H., R. v. Beek, N. Wanders, Y. Wada, J. H. C. Bosmans, N. Drost, R. J. van der Ent, I. E. M.

de Graaf, J. M. Hoch, K. d. Jong, D. Karssenberg, P. López López, S. Peßenteiner, O. Schmitz, M. W. Straatsma, E. Vannametee, D. Wisser & M. F. P. Bierkens (2018). PCR-GLOBWB 2: a 5 arcmin global hydrological and water resources model. *Geoscientific Model Development*, 11(6), 2429–2453. doi: 10.5194/gmd-11-2429-2018.

Sánchez, E., C. Gallardo, M. Gaertner, A. Arribas & M. Castro (2004). Future climate extreme events in the Mediterranean simulated by a regional climate model: a first approach. *Global and Planetary Change*, 44(1-4), 163–180. doi: 10.1016/j.gloplacha.2004.06.010.

Tague, C. & G. E. Grant (2004). A geological framework for interpreting the low-flow regimes of Cascade streams, Willamette River Basin, Oregon. *Water Resources Research*, 40(4), W04303. doi: 10.1029/2003WR002629.

Takala, M., J. Pulliainen, S. J. Metsamaki & J. T. Koskinen (2009). Detection of snowmelt using spaceborne microwave radiometer data in Eurasia from 1979 to 2007. *IEEE Transactions on Geoscience and Remote Sensing*, 47(9), 2996–3007. doi: 10.1109/TGRS.2009.2018442.

Tallaksen, L. M., H. Hisdal & H. A. J. van Lanen (2009). Space–time modelling of catchment scale drought characteristics. *Journal of Hydrology*, 375(3), 363–372. doi: 10.1016/j.jhydrol.2009.06.032.

Terink, W., H. Leijnse, G. van den Eertwegh & R. Uijlenhoet (2018). Spatial resolutions in areal rainfall estimation and their impact on hydrological simulations of a lowland catchment. *Journal of Hydrology*, 563, 319–335. doi: 10.1016/j.jhydrol.2018.05.045.

Terink, W., A. F. Lutz, G. W. H. Simons, W. W. Immerzeel & P. Droogers (2015). SPHY v2.0: Spatial Processes in HYdrology. *Geoscientific Model Development*, 8(7), 2009–2034. doi: 10.5194/gmd-8-2009-2015.

Teubner, I. E., M. Forkel, G. Camps-Valls, M. Jung, D. G. Miralles, G. Tramontana, R. van der Schalie, M. Vreugdenhil, L. Mösinger & W. A. Dorigo (2019). A carbon sink-driven approach to estimate gross primary production from microwave satellite observations. *Remote Sensing of Environment*, 229, 100–113. doi: 10.1016/j.rse.2019.04.022.

Teubner, I. E., M. Forkel, M. Jung, Y. Y. Liu, D. G. Miralles, R. Parinussa, R. van der Schalie, M. Vreugdenhil, C. R. Schwalm, G. Tramontana, G. Camps-Valls & W. A. Dorigo (2018). Assessing the relationship between microwave vegetation optical depth and gross primary production. *International Journal of Applied Earth Observation and Geoinformation*, 65, 79–91. doi: 10.1016/j.jag.2017.10.006.

Teuling, A. J. (2018). A hot future for European droughts. *Nature Climate Change*, 8(5), 364–365. doi: 10.1038/s41558-018-0154-5.

Teuling, A. J., E. A. G. de Badts, F. A. Jansen, R. Fuchs, J. Buitink, A. J. Hoek van Dijke & S. M. Sterling (2019). Climate change, reforestation/afforestation, and urbanization impacts on evapotranspiration and streamflow in Europe. *Hydrology and Earth System Sciences*, 23(9), 3631–3652. doi: 10.5194/hess-23-3631-2019.

Teuling, A. J., M. Hirschi, A. Ohmura, M. Wild, M. Reichstein, P. Ciais, N. Buchmann, C. Ammann, L. Montagnani, A. D. Richardson, G. Wohlfahrt & S. I. Seneviratne (2009a). A regional perspective on trends in continental evaporation. *Geophysical Research Letters*, 36(2). doi: 10.1029/

2008GL036584.

Teuling, A. J., I. Lehner, J. W. Kirchner & S. I. Seneviratne (2010). Catchments as simple dynamical systems: Experience from a Swiss prealpine catchment. *Water Resources Research*, 46(10), W10502. doi: 10.1029/2009WR008777.

Teuling, A. J., A. F. van Loon, S. I. Seneviratne, I. Lehner, M. Aubinet, B. Heinesch, C. Bernhofer, T. Grünwald, H. Prasse & U. Spank (2013). Evapotranspiration amplifies European summer drought. *Geophysical Research Letters*, 40(10), 2071–2075. doi: 10.1002/grl.50495.

Teuling, A. J., R. Uijlenhoet, F. Hupet & P. A. Troch (2006). Impact of plant water uptake strategy on soil moisture and evapotranspiration dynamics during drydown. *Geophysical Research Letters*, 33(3), L03401. doi: 10.1029/2005GL025019.

Teuling, A. J., R. Uijlenhoet, B. van den Hurk & S. I. Seneviratne (2009b). Parameter Sensitivity in LSMs: An Analysis Using Stochastic Soil Moisture Models and ELDAS Soil Parameters. *Journal of Hydrometeorology*, 10(3), 751–765. doi: 10.1175/2008jhm1033.1.

Theurillat, J. P. & A. Guisan (2001). Potential Impact of Climate Change on Vegetation in the European Alps: A Review. *Climatic Change*, 50(1-2), 77–109. doi: 10.1023/A:1010632015572.

van Tiel, M., A. J. Teuling, N. Wanders, M. J. P. Vis, K. Stahl & A. F. van Loon (2018). The role of glacier changes and threshold definition in the characterisation of future streamflow droughts in glacierised catchments. *Hydrology and Earth System Sciences*, 22(1), 463–485. doi: 10.5194/hess-22-463-2018.

Trancoso, R., J. R. Larsen, T. R. McVicar, S. R. Phinn & C. A. McAlpine (2017). CO2-vegetation feedbacks and other climate changes implicated in reducing base flow. *Geophysical Research Letters*, 44(5), 2017GL072759. doi: 10.1002/2017GL072759.

Troch, P. A., C. Paniconi & E. E. van Loon (2003). Hillslope-storage Boussinesq model for subsurface flow and variable source areas along complex hillslopes: 1. Formulation and characteristic response. *Water Resources Research*, 39(11), 1316. doi: 10.1029/2002WR001728.

Troch, P. A., F. P. D. Troch & W. Brutsaert (1993). Effective water table depth to describe initial conditions prior to storm rainfall in humid regions. *Water Resources Research*, 29(2), 427–434. doi: 10.1029/92WR02087.

Tóth, B., M. Weynants, L. Pásztor & T. Hengl (2017). 3D soil hydraulic database of Europe at 250 m resolution. *Hydrological Processes*, 31(14), 2662–2666. doi: 10.1002/hyp.11203.

Verbunt, M., J. Gurtz, K. Jasper, H. Lang, P. Warmerdam & M. Zappa (2003). The hydrological role of snow and glaciers in alpine river basins and their distributed modeling. *Journal of Hydrology*, 282(1–4), 36–55. doi: 10.1016/S0022-1694(03)00251-8.

Viessman, W. & G. L. Lewis (2012). *Introduction to Hydrology*. Pearson Education. Google-Books-ID: Wy02uQAACAAJ.

Viviroli, D., H. H. Dürr, B. Messerli, M. Meybeck & R. Weingartner (2007). Mountains of the world, water towers for humanity: Typology, mapping, and global significance. *Water Resources Research*, 43(7), W07447. doi: 10.1029/2006wr005653.

Viviroli, D., M. Zappa, J. Gurtz & R. Weingartner (2009). An introduction to the hydrological modelling

system PREVAH and its pre- and post-processing-tools. *Environmental Modelling & Software*, 24(10), 1209–1222. doi: 10.1016/j.envsoft.2009.04.001.

Vos, L. W. d., A. M. Droste, M. J. Zander, A. Overeem, H. Leijnse, B. G. Heusinkveld, G. J. Steeneveld & R. Uijlenhoet (2020). Hydrometeorological Monitoring Using Opportunistic Sensing Networks in the Amsterdam Metropolitan Area. *Bulletin of the American Meteorological Society*, 101(2), E167–E185. doi: 10.1175/BAMS-D-19-0091.1.

Wang, K. & R. E. Dickinson (2012). A review of global terrestrial evapotranspiration: Observation, modeling, climatology, and climatic variability. *Reviews of Geophysics*, 50(2). doi: 10.1029/2011RG000373.

Wang, K., R. E. Dickinson, M. Wild & S. Liang (2010). Evidence for decadal variation in global terrestrial evapotranspiration between 1982 and 2002: 2. Results. *Journal of Geophysical Research: Atmospheres*, 115(D20), D20113. doi: 10.1029/2010JD013847.

Warren, J. M., P. J. Hanson, C. M. Iversen, J. Kumar, A. P. Walker & S. D. Wullschleger (2015). Root structural and functional dynamics in terrestrial biosphere models – evaluation and recommendations. *New Phytologist*, 205(1), 59–78. doi: 10.1111/nph.13034.

Weiler, M. & K. Beven (2015). Do we need a Community Hydrological Model? *Water Resources Research*, 51(9), 7777–7784. doi: 10.1002/2014WR016731.

West, H., N. Quinn & M. Horswell (2019). Remote sensing for drought monitoring & impact assessment: Progress, past challenges and future opportunities. *Remote Sensing of Environment*, 232, 111291. doi: 10.1016/j.rse.2019.111291.

van der Wiel, K. & R. Bintanja (2021). Contribution of climatic changes in mean and variability to monthly temperature and precipitation extremes. *Communications Earth & Environment*, 2(1), 1–11. doi: 10.1038/s43247-020-00077-4.

Wijngaard, R. R., A. F. Lutz, S. Nepal, S. Khanal, S. Pradhananga, A. B. Shrestha & W. W. Immerzeel (2017). Future changes in hydro-climatic extremes in the Upper Indus, Ganges, and Brahmaputra River basins. *PLoS ONE*, 12(12), e0190224. doi: 10.1371/journal.pone.0190224.

Wild, M. (2009). Global dimming and brightening: A review. *Journal of Geophysical Research*, 114(D10). doi: 10.1029/2008JD011470.

Wild, M., D. Folini, C. Schär, N. Loeb, E. G. Dutton & G. König-Langlo (2013). The global energy balance from a surface perspective. *Climate Dynamics*, 40(11-12), 3107–3134. doi: 10.1007/s00382-012-1569-8.

Wilhite, D. A. & M. H. Glantz (1985). Understanding: the Drought Phenomenon: The Role of Definitions. *Water International*, 10(3), 111–120. doi: 10.1080/02508068508686328.

Winterrath, T., H. Mario, T. Junghänel, A. Klameth, K. Lengfeld, E. Walawender, E. Weigl & A. Becker (2018). RADKLIM Version 2017.002: Reprocessed gauge-adjusted radar data, one-hour precipitation sums.

Wolf, A. T., J. A. Natharius, J. J. Danielson, B. S. Ward & J. K. Pender (1999). International River Basins of the World. *International Journal of Water Resources Development*, 15(4), 387–427. doi: 10.1080/07900629948682.

Wong, W. K., S. Beldring, T. Engen-Skaugen, I. Haddeland & H. Hisdal (2011). Climate Change Effects on Spatiotemporal Patterns of Hydroclimatological Summer Droughts in Norway. *Journal of Hydrometeorology*, 12(6), 1205–1220. doi: 10.1175/2011JHM1357.1.

Wood, E. F., J. K. Roundy, T. J. Troy, L. P. H. van Beek, M. F. P. Bierkens, E. Blyth, A. de Roo, P. Döll, M. Ek, J. Famiglietti, D. Gochis, N. van de Giesen, P. Houser, P. R. Jaffé, S. Kollet, B. Lehner, D. P. Lettenmaier, C. Peters-Lidard, M. Sivapalan, J. Sheffield, A. Wade & P. Whitehead (2011). Hyperresolution global land surface modeling: Meeting a grand challenge for monitoring Earth's terrestrial water. *Water Resources Research*, 47(5), W05301. doi: 10.1029/2010WR010090.

WSL (2016). CORINE Land Cover Switzerland. Swiss Federal Institute for Forest, Snow and Landscape Research (WSL).

Wu, Y., S. Liu & O. I. Abdul-Aziz (2012). Hydrological effects of the increased CO2 and climate change in the Upper Mississippi River Basin using a modified SWAT. *Climatic Change*, 110(3), 977–1003. doi: 10.1007/s10584-011-0087-8.

Yang, Y., M. L. Roderick, S. Zhang, T. R. McVicar & R. J. Donohue (2019). Hydrologic implications of vegetation response to elevated CO 2 in climate projections. *Nature Climate Change*, 9(1), 44. doi: 10.1038/s41558-018-0361-0.

Zappa, M. (2002). *Multiple-response verification of a distributed hydrologial model at different spatial scales*. Ph.D. thesis, Naturwissenschaften ETH Zürich.

Zappa, M. & C. Kan (2007). Extreme heat and runoff extremes in the Swiss Alps. *Natural Hazards and Earth System Science*, 7(3), 375–389. doi: 10.5194/nhess-7-375-2007.

Zargar, A., R. Sadiq, B. Naser & F. I. Khan (2011). A review of drought indices. *Environmental Reviews*, 19, 333–349. doi: 10.1139/a11-013.

Zheng, Y., F. Li, L. Hao, J. Yu, L. Guo, H. Zhou, C. Ma, X. Zhang & M. Xu (2019). Elevated CO2 concentration induces photosynthetic down-regulation with changes in leaf structure, non-structural carbohydrates and nitrogen content of soybean. *BMC Plant Biology*, 19(1), 255. doi: 10.1186/s12870-019-1788-9.

Zhu, C., R. H. Byrd, P. Lu & J. Nocedal (1997). Algorithm 778: L-BFGS-B: Fortran Subroutines for Large-scale Bound-constrained Optimization. *ACM Transactions on Mathematical Software*, 23(4), 550–560. doi: 10.1145/279232.279236.

Summary

Variability is present on multiple levels in the hydrological cycle, both spatially and temporally. Spatial variability can be caused by variations in catchment characteristics and by changes in dominant hydrological processes. Temporal variability occurs as a result of typical variations in diurnal and seasonal cycles, but also on longer time scales resulting from a change in climate. Spatial and temporal variability across a basin ultimately affects the hydrological response. This thesis describes how variability in different components of the hydrological cycle (precipitation, runoff generating processes, and evaporation) influence the hydrological response in the Rhine basin. The studies cover three important steps in hydrological research: understanding past events through analysis of observations (Chapter 2 and Chapter 3), conceptualising hydrology through testing and developing models (Chapter 4 and Chapter 5), and understanding the hydrological response under changing conditions (Chapter 6 and Chapter 7). The results in this thesis improve how hydrological variability resulting from variability within and across different components of the hydrological cycle is captured.

The response of five major components of the hydrological cycle to drought conditions is investigated in Chapter 2. With a special focus on the Dutch province of Gelderland, the responses of precipitation, soil moisture, vegetation, groundwater levels, and surface water levels are quantified. Droughts are defined based on a frequency-of-occurrence approach, and the actual drought frequency is tested against this definition. It is showed that each variable is more frequently in drought conditions (27–38% of the time) than expected based on the drought definition (20% of the time). This is a direct result of spatial variability within each variable. At least one variable is in drought conditions for 73% of the time, and 3–4 variables need to be simultaneously in drought conditions to have a match between actual drought frequency and the definition. This chapter shows how the drought definition does not reflect actual drought occurrence in a spatial heterogeneous region.

The interaction between soil moisture content and vegetation productivity during the summer drought of 2018 is described in Chapter 3. This chapter compares in situ soil moisture observations at several depths with satellite

derived vegetation productivity indices. It was shown that the anomaly in vegetation productivity lagged between two and three weeks behind the anomaly in soil moisture content. Furthermore, it was shown that the critical soil moisture content (indicating the transition point between energy-limited and water-limited conditions) increased linearly with integration depth. This chapter highlights the complex interaction between vegetation productivity and soil moisture content.

While it seems obvious that high spatial resolutions are required to optimally represent the spatial variability, this is not always possible. Limitations in data availability and/or computational power restrict models to be ran on high spatial resolutions. Chapter 4 compares simulations at low resolution with simulations at high resolution, using the SPHY model. While both the high and low resolution models correctly simulated the discharge, local differences were present. The high resolution model showed that both extremely positive and extremely negative anomalies can occur simultaneously in the same basin during seasonal extremes. This was not captured by the coarse resolution model. A newly proposed metric, the density-weighted distance, showed that the coarse resolution model missed on average two standardised anomalies when compared with the results from the high resolution model. This difference was larger in the basins with glaciers than in basins without glaciers. In conclusion, it was shown that results from a coarse resolution model cannot easily be translated to the results from a high resolution model.

The dS2 model is introduced in Chapter 5. This distributed rainfall-runoff model is based on the simple dynamical system approach (Kirchner, 2009), and is developed with an emphasis on computational efficiency. This allows simulations to be performed at high spatial and high temporal resolutions, without high computational costs. Snow and flow routing modules were added to ensure that the model can be applied to mesoscale basins. The dS2 model is tested to a basin in the Swiss Alps, a subbasin of the Rhine, and showed that it is able to simulate the hydrological response with high accuracy. This model is used for the simulations in the next two chapters.

The role of increasing temperatures on the discharge is described in

Chapter 6. This chapter shows how temperature-driven changes in evaporation and snow processes influence the hydrological response. Simulations of two decades (1980s and 2010s) were performed to quantify the contribution of precipitation and temperature-driven changes in evaporation and snow processes on the discharge. This showed that temperature-driven changes in evaporation and snow processes were just as important as the precipitation-driven changes. Step-wise temperature increases showed that increases in evaporation reduced discharge throughout the year, and that snow processes caused a different seasonal pattern. Higher temperatures reduced the amount of snowfall and caused the snowpacks to melt earlier in the year. Additionally, melting of the glaciers was increased over the entire year. Overall, the discharge was reduced throughout the year, and the change in snow seasonality caused a large discharge reduction during late spring and early summer. This chapter showed the importance of these temperature-driven changes on discharge simulations, as they can both counteract and amplify changes in discharge.

Chapter 7 describes how CO_2-induced changes in vegetation and temperature affect evaporation and discharge in the Rhine basin. The relative importance of CO_2-induced changes in stomatal resistance, leaf area index, and temperature are quantified. Increases in evaporation caused by temperature reduced the discharge with 17% (with respect to the average discharge over 2018). Higher stomatal resistance led to reductions in evaporation, effectively increasing the discharge with 4%. The increase in leaf area index had only a very limited effect on the discharge. Overall, discharge is expected to decrease with 14% as a result of these CO_2-induced changes. These results are confirmed in a sensitivity study. While changes in temperature are typically accounted for in hydrological studies, the changes in vegetation (and especially the increase in stomatal resistance) are not. This chapter highlights that the response of vegetation need to be accounted for, otherwise it is likely that evaporation is overestimated, and discharge is underestimated.

By combining data-analysis studies with simulation studies, this thesis showed how spatial and temporal variability influence the hydrological response. The complex interactions between different components of the hydrological cycle, as well as the contrasting responses to changing climate

conditions, need to be represented correctly in order to provide reliable discharge estimates. The results from this thesis give insight on how to capture the hydrological variability, in order to improve how hydrology can support and protect society.

Samenvatting

De hydrologische cyclus is variabel in de ruimte en in de tijd. Variabiliteit in de ruimte kan ontstaan door variaties in eigenschappen van een stroomgebied en door variaties in hydrologische processen. Variabiliteit in de tijd kan ontstaan dag- of seizoen-cycli, maar ook op langere tijdschalen door veranderingen in het klimaat. Variabiliteit in de ruimte en tijd beïnvloedt uiteindelijk het hydrologische gedrag van een stroomgebied. Dit proefschrift beschrijft hoe variabiliteit in verschillende hydrologische componenten (neerslag, afvoer-producerende processen en verdamping) de hydrologische respons beïnvloeden, met een focus op het stroomgebied van de Rijn. De hoofdstukken omvatten drie belangrijke stappen in hydrologisch onderzoek: het analyseren van gebeurtenissen in het verleden door middel van observaties (Hoofdstuk 2 en Hoofdstuk 3), het conceptualiseren van hydrologische processen door middel van modellen (Hoofdstuk 4 en Hoofdstuk 5), en het onderzoeken van de hydrologische respons als gevolg van veranderingen in het klimaat (Hoofdstuk 6 en Hoofdstuk 7). De resultaten en conclusies uit dit proefschrift vergroten de kennis over hydrologische variabiliteit veroorzaakt door variaties in en tussen de verschillende hydrologische componenten.

Het gedrag van vijf belangrijke componenten van de hydrologische cyclus tijdens droogtecondities is beschreven in Hoofdstuk 2. Het hoofdstuk analyseert het verloop van neerslag, bodemvocht, vegetatie, grondwater- en oppervlaktewaterniveaus binnen de Nederlandse provincie Gelderland. Dit onderzoek toont aan dat de theoretische definitie van droogte niet altijd overeenkomt met hoe vaak een droogte daadwerkelijk voorkomt. Elke variabele bevindt zich namelijk vaker in droogtecondities (27–38% van de tijd) dan is verwacht op basis van de definitie (20% van de tijd). Dit is een direct gevolg van de ruimtelijke variabiliteit in elke variabele. Voor bijna driekwart van de tijd (73%) bevindt minstens één variabele in Gelderland zich in droogtecondities. Pas wanneer drie tot vier variabelen zich gelijkertijd in droogtecondities bevinden, komt de droogtefrequentie in Gelderland overeen met de definitie. Dit hoofdstuk laat zien dat de definitie van droogte niet goed de werkelijke droogtefrequentie representeert in een gebied met ruimtelijke variabiliteit.

Hoofdstuk 3 beschrijft de interactie tussen bodemvocht en de productiviteit

van vegetatie tijdens de droogte van 2018. In dit hoofdstuk worden in situ observaties van bodemvocht op verschillende dieptes vergeleken met satelliet observaties van vegetatieproductiviteit. Deze analyse liet zien dat er een vertraging van twee á drie weken zit tussen een afwijking in bodemvocht en een afwijking in vegetatieproductiviteit, waarbij de vegetatie trager reageert. De bodemvochtobservaties lieten zien dat het kritische bodemvochtgehalte (het transitiepunt tussen energie-gelimiteerde en water-gelimiteerde condities) lineair toeneemt met de integratiediepte. Dit hoofdstuk benadrukt de complexe interactie tussen bodemvocht en de productiviteit van vegetatie.

De ruimtelijke resolutie van een hydrologisch model is essentieel om ruimtelijke patronen goed weer te geven. Echter is het niet altijd mogelijk om hoge ruimtelijke resoluties te gebruiken, bijvoorbeeld door beperkingen in de beschikbaarheid van data of door berperkingen in de rekenkracht van computers. Hoofdstuk 4 vergelijkt de resultaten van een model (SPHY) met een lage ruimtelijke resolutie met de resultaten van hetzelfde model met een hoge ruimtelijke resolutie. Hoewel beide simulaties de afvoer goed simuleren, zijn er grote verschillen in de ruimtelijke patronen binnen het stroomgebied. Het model met hoge resolutie laat zien dat zowel extreem negatieve als extreem positieve afwijkingen gelijktijdig voorkomen binnen een stroomgebied. Het model met lage resolutie was niet in staat om dit te simuleren. Een nieuwe index, de density-weighted distance, kwantificeert dat het model met lage resolutie gemiddeld twee genormaliseerde standaarddeviaties mist ten opzichte van het model met hoge resolutie. Deze verschillen zijn groter in de stroomgebieden met gletsjers dan in de gebieden zonder gletsjers. Dit hoofdstuk benadrukt dat de resultaten van een model met lage resolutie niet eenvoudig vertaald kunnen worden naar de resultaten van een model met hoge resolutie.

In Hoofdstuk 5 wordt het dS2 model geïntroduceerd. Dit is een ruimtelijk gedistribueerd regen-afvoer model, welke gebaseerd is op de simple dynamical systems approach (Kirchner, 2009). Door de efficiënte manier van rekenen kunnen simulaties van dit model snel en met weinig computerkracht worden uitgevoerd. Een direct gevolg hiervan is dat simulaties op een hoge ruimtelijke en temporele resoluties uitgevoerd kunnen worden, zonder dat hier enorme rekentijden tegenover staan. Modules met sneeuw en water-

routing processen zijn toegevoegd, zodat het model ook toegepast kan worden in grote stroomgebieden. Het dS2 model is getest op een stroomgebied in de Zwitserse Alpen, een sub-stroomgebied van de Rijn. Deze test liet zien dat het model in staat is om de hydrologische respons accuraat te simuleren. Het dS2 model is gebruikt om de analyses in de volgende twee hoofdstukken uit te voeren.

Het effect van temperatuur op de afvoer is beschreven in Hoofdstuk 6. In dit hoofdstuk worden temperatuurgedreven veranderingen in verdamping en sneeuwprocessen onderzocht, en hoe deze de hydrologische respons van de Rijn beïnvloeden. Twee decennia (1980's en 2010's) zijn gesimuleerd met het dS2 model. In drie andere simulatie van de 1980's zijn de tijdseries van (1) temperatuur met alleen effecten op de sneeuwprocessen, (2) temperatuur met alleen effecten op de verdamping en (3) neerslag, vervangen door de tijdseries uit de 2010's. Hierdoor is mogelijk om de effecten van deze drie variabelen op de afvoer te kwantificeren. De simulaties lieten zien dat de temperatuurgedreven veranderingen net zo belangrijk waren als de neerslaggedreven veranderingen. Stapsgewijze toenames in temperatuur lieten zien dat een toename in verdamping leidt tot lagere afvoerwaardes. Hogere temperaturen hadden verschillende effecten op de sneeuwprocessen: minder neerslag valt als sneeuw; de sneeuw die nog valt, smelt eerder in het jaar; en er wordt gedurende het hele jaar meer smeltwater geproduceerd door de gletsjers. De effecten van verdamping en sneeuwprocessen samen zorgden voor een afname in de afvoer. Extra grote verschillen waren zichtbaar in het eind van de lente en begin van de zomer, door het verschuiven en afnemen van de afvoerpiek door smeltwater van sneeuw. Dit hoofdstuk laat zien dat deze temperatuurgedreven processen erg belangrijk zijn voor afvoersimulaties, omdat deze elkaar zowel deels kunnen opheffen als elkaar kunnen versterken.

Een toename in CO_2 concentratie zorgt zowel voor hogere temperaturen als veranderingen in de vegetatie. De huidmondjes van bladeren openen minder ver, waardoor er minder water verdampt. Tegelijkertijd kunnen planten ook meer bladeren groeien doordat er meer CO_2 in de atmosfeer aanwezig is, wat zorgt voor meer verdamping. Ook de hogere temperaturen kunnen voor meer verdamping zorgen. Hoofdstuk 7 beschrijft hoe deze effecten de

afvoer van de Rijn veranderen. De toenames in verdamping als gevolg van temperatuur verlaagden de afvoer met 17% (ten opzichte van de gemiddelde afvoer over 2018). Veranderingen in de huidmondjes zorgen voor een afname in verdamping, en daardoor een toename in de afvoer van 4%. De toename in bladoppervlak had een zeer gering effect op de afvoer. Wanneer deze effecten gecombineerd werden, nam de afvoer af met 14%. Deze resultaten zijn bevestigd in een gevoeligheidsanalyse. Veranderingen in temperatuur als gevolg van een toename in CO_2 worden bijna altijd meegenomen in hydrologische onderzoeken, maar de veranderingen in vegetatie meestal niet. Dit hoofdstuk laat zien dat als de veranderingen in vegetatie niet meegenomen worden, het waarschijnlijk is dat verdamping overschat wordt, met een onderschatting van de afvoer als gevolg.

Door de combinatie van analyses op basis van observaties met analyses op basis van simulaties, laat dit proefschrift zien hoe ruimtelijk en temporele variabiliteit de hydrologische respons kan beïnvloeden. De complexe interacties tussen de verschillende componenten van de hydrologische cyclus, zoals de contrasterende reacties op een veranderend klimaat, moeten correct worden gerepresenteerd om betrouwbare afvoerinschattingen te kunnen maken. De resultaten van dit proefschrift geven inzicht in hoe de hydrologische variabiliteit gerepresenteerd moeten worden: een beter hydrologisch begrip verbetert hoe hydrologie de samenleving kan ondersteunen en beschermen.

Dankwoord

"I thought it was impossible,
But you make it possible"

—Nothing But Thieves, *Impossible* (2020)

Ondanks dat het schijven van een proefschrift vaak als een eenzame "reis" beschreven wordt, is het een reis die alleen dankzij ondersteuning van anderen haalbaar is. Zonder deze mensen zou ik nooit deze reis begonnen zijn, plezier hebben gehad gedurende de reis, en/of deze reis succesvol kunnen afronden. Graag wil ik in dit hoofdstuk even stil staan bij deze mensen, om ze te bedanken voor hun wijze woorden, ondersteuning, en/of ontspanning.

Allereerst wil ik graag mijn directe begeleiding, Lieke en Ryan, bedanken voor hun ideeën, suggesties en tijd wanneer ik weer eens vastgelopen was. Ik kreeg altijd erg veel energie en nieuwe ideeën van onze meetings, ondanks dat (of misschien juist doordat..?) we ook de nodige zijstapjes maakten en roddels bespraken. Een goede kop koffie en een gebakje konden natuurlijk niet ontbreken. Ryan, bedankt dat jij mij het doen van een PhD serieus hebt laten overwegen: zonder jouw woorden aan het eind van mijn masterscriptie hadden de afgelopen jaren er voor mij waarschijnlijk compleet anders uitgezien. Lieke, ondanks dat je niet vanaf het begin (direct) betrokken was, ben ik je heel dankbaar voor jouw altijd positieve feedback en waardevolle suggesties.

Naast mijn (co-) promotoren zijn er nog een aantal personen die een cruciale rol hebben gespeeld gedurende mijn promotie-traject. Remko, onwijs bedankt voor je betrokkenheid als leerstoelhouder van HWM en jouw bijdrage aan mijn eerste paper. Paul, bedankt voor jouw ondersteuning en voorbeelden bij de ontwikkeling van scripts. Ook bedankt voor de afleiding via mooie plaatjes of leuke dingen "om even in Google in te tikken." James Kirchner and Martin Clark, thank you both for your quick responses to help finding and solving the "numerical deamons" in the dS2 model. I am sure that the dS2 model would not be in it's current state if it wasn't for both of your sugges-

tions and expertise. Een aantal hoofdstukken in dit proefschrift hadden er totaal anders uitgezien zonder het (voorbereidend) werk van Anne, Tessa en Christoph. Anne, bedankt dat ik jouw werk kon overnemen en bedankt voor alle uitleg om jouw MATLAB scriptjes uit te pluizen. Tessa, ondanks dat we onder een behoorlijk krappe planning stonden voor het "droogte paper", heel erg bedankt dat je zo snel hebt kunnen bijspringen om de data aan te leveren en het paper kritisch hebt kunnen aanpassen. Christoph, jouw master thesis bleek uiteindelijk een cruciaal onderdeel te worden van de laatste twee hoofdstukken in dit proefschrift. Bedankt voor jouw scherpe en nauwkeurige analyses, zonder het BETA model waren deze twee hoofdstukken een stuk lastiger geworden!

Dit project was niet mogelijk geweest zonder de financiering van Rijkswaterstaat. Ik wil graag de commissie vanuit Rijkswaterstaat (in het bijzonder Eric Sprokkereef, Hendrik Buiteveld, Wim Werkman, Henk Looijen, Jasper Stam, Klaas Groen en Charlotte Schmidt) bedanken voor hun feedback en suggesties tijdens onze voortgangsbijeenkomsten. Ondanks dat deze bijeenkomsten maar één keer per jaar waren, was het altijd heel prettig om jullie reacties, ideeën en suggesties te horen. Ik denk dat het onwijs belangrijk is om de connecties met universiteiten op deze manier in stand te houden, omdat beide partijen veel van elkaar kunnen leren.

Naast de inhoudelijke samenwerkingen, wil ik ook graag iedereen bedanken die de hele "reis" leuker, gezellig en plezierig hebben gemaakt. De IJslanddreamteams uit 2017, 2018 en 2019 kunnen hierbij niet ontbreken: Roel, Ryan, Victor, Lotte, Monica, Tjitske, Lieke, Tessa en Bram, bedankt dat wij samen de studenten door het prachtige IJsland konden begeleiden. We hebben er een hoop mooie verhalen aan overgehouden: van allerlei autoproblemen tot mysterieuze ingrediënten in het avondeten. Sony, who would have thought that the plans we made at the start of our contracts actually happened? Thanks for joining me for a week to cruise around the United States in a Mustang, it really was an amazing experience.

Ook kunnen mijn kantoor-kamergenoten niet ontbreken: Tommy, Timo, Tjitske, Femke, Linda en Iris. Tommy, bedankt voor alle gezelligheid, discussies en het delen van slechte emails. Timo, het was gezellig om samen met jou

aan het zelfde bureau-eilandje te zitten en om je (bijna) elke maand ervan te overtuigen om de kalender op de goede maand te zetten. Tjitske, onwijs bedankt voor de gezellige tijd op kantoor en daarbuiten. Ook bedankt voor jouw perspectief en adviezen zowel in persoonlijke als werkgerelateerde situaties. Ik hoop dat we nog een keer een herkansing krijgen voor de walvistour, zodat je mij niet meer de schuld hoeft te geven voor het missen daarvan (onterecht, het parkeren in Reykjavik was misschien niet voor herhaling vatbaar, maar het was wel efficiënt). Hopelijk was je mij nog niet zat als collega, want ik kom ook gezellig naar het "verre westen". Ik hoop dat we samen nog veel hapjes gaan eten en veel kilometers samen op de fiets zitten. Ik vind het fijn dat mij als paranimf wilt bijstaan! Femke, bedankt voor de thee, gezellige praatjes en gekke huppeltjes. De avontuurlijke expedities door Wageningen samen met Linda en mij, of de verhalen van jouw bushcraft-avonturen, waren altijd fantastisch. Linda, heel erg bedankt voor alle offline en online koffiepauzes, belwandelingen, hardlooprondjes en vooral slechte woordgrappen. Bedankt dat ik jou altijd kon lastig vallen voor feedback op tekst, grafieken, of infographics. Ik ben blij dat je mijn paranimf wilt zijn! Iris, ondanks dat we ruim een jaar in hetzelfde kantoor zaten, hebben we maar korte tijd ook daadwerkelijk tegelijkertijd in hetzelfde kantoor gewerkt. Bedankt voor de gezelligheid en de kritische blik op mijn pomodoro timer (hoewel de kookwekker uiteindelijk voor meer afleiding zorgde dan serieus gebruikt werd). Het was zelfs zo gezellig dat we regelmatig allebei met noise-cancelling koptelefoons op zaten te werken. Verder wil ik ook graag alle andere HWM-collega's bedanken voor alle lunches, borrels en HWM uitjes. Ik kijk ook nog vaak met plezier terug naar de schrijfweek, in het bijzonder naar het maken van de stapels tosti's samen met Jelte. Het was fijn om in een hechte en gezellige groep collega's te werken. Ik wens de hele groep veel succes toe en ik ben benieuwd wat de toekomst brengt.

I would also like to thank Annemerel, Job, Kamonashish, and Viola for the two and a half years that we spend together representing the PhD candidates of WIMEK via the WIMEK PhD Council. It was a very enjoyable and valuable experience to re-establish the WIMEK PhD Council within WIMEK, push important issues to the board of WIMEK, organise documentary evenings and barbecues, and start the logo competition. Our monthly meetings always were a nice break from the "regular PhD stuff."

Ook wil ik graag iedereen bedanken die voor de nodige ontspanning buiten de werkuren heeft gezorgd. Allereerst wil ik de hele *Ciao Bella*-club bedanken voor alle weekendjes weg, feestjes, borrels, (mannen)dagen. Ik kijk uit naar het volgende weekendje weg! Uit deze groep zijn er een paar mensen die ik in het bijzonder wil bedanken. Allereerst Erwin, bedankt dat we elkaar altijd konden lastig vallen met goede muziek, Fiesta-dingen, lekkere biertjes en alle klus-avonturen. Ook wil ik jou en Maaike bedanken voor alle gastvrijheid en relaxte dagen samen. Uiteraard kan Frederik ook niet ontbreken. Bedankt voor de vele leuke gesprekken en discussies, maar natuurlijk ook bedankt voor het (nog veel meer) slap geouwehoer over niks. Ondanks dat we dit elke keer zeggen, hoop ik echt dat we regelmatiger afspreken, onder het genot van een biertje natuurlijk. Vincent, Walter en Martine, bedankt voor de gezellige etentjes. Ondanks dat we elkaar niet super vaak spreken, ben ik ook de *Hydrology VIP* groep (Lisette, Sander, Niek, Bas en Maren) dankbaar voor de gezellige dagjes uit, pubquizzen en etentjes.

Daarnaast wil ik ook de hele Almere-club bedanken. Dymar en Julia, bedankt voor alle gezellige etentjes, uitjes, feestjes en dat jullie deur altijd open staat. Dymar, bedankt voor de relaxte middagen en avonden op de bank, het terras, of waar dan ook. Uiteraard ook bedankt voor talloze avondjes vermaak en—om even je eigen woorden te gebruiken—"alle overwinningen." David, jij ook bedankt voor het vermaak in de avonden, maar ook voor een luisterend oor en al je geniale spreekbeurten. Ik hoop dat er nog vele etentjes komen met de "bois". De *Austria Schnitzel* groep (Dymar, Ryan, Gabe, Kyron, Stef, Tom, Glenn en Mike) wil ik graag bedanken voor de gezelligheid tijdens het kijken van de Formule 1 races, zowel op de bank als op de tribunes. Ik ben benieuwd welke circuits we in de toekomst kunnen afstrepen! Natuurlijk kunnen Rhianne en Guillaume ook niet ontbreken, voor de talloze middagen waarbij het kopje koffie naadloos overging in drankjes (en bitterballen) op het terras. Ook bedankt voor alle gastvrijheid en de altijd heerlijke gerechten. Brian en David, bedankt voor de gezellige bijpraat-middagen, feestjes en barbecues. Brian, bedankt dat je al mijn koffie-verhalen aanhoort; ik zal mijn ogen en oren ophouden als er weer een proeverij voorbij komt.

Als laatst—maar zeker niet *least*—wil ik graag mijn familie bedanken. Mam en Pap, bedankt voor jullie interesse en luisterend oor als ik weer even een

verhaal kwijt moest. Ik weet niet hoeveel jullie begrijpen van de inhoud van dit boekje—en dat doet er ook niet toe—, zonder jullie had deze er (letterlijk en figuurlijk) totaal anders uitgezien. Laura, ondanks de grote afstand, ben ik erg trots om zo'n stoere zus te hebben. Ik hoop dat jij en Hernany snel naar Nederland kunnen komen en anders kom ik snel weer jullie kant op: we hebben tenslotte nog een feest te vieren! Henk-Jan, Erna, Jasper, Jurrien en Esra, ondanks dat we elkaar niet heel regelmatig zien, is het altijd erg gezellig. Ook beide oma's bedankt voor alle goede zorgen.

Voor iedereen die ik hierboven direct en indirect heb genoemd (en iedereen die ik vergeten ben te noemen), ik hoop dat we elkaar nog vaak gaan en blijven zien. Ik ben benieuwd en kijk uit naar de toekomst!

Joost Buitink
Wageningen, september 2021

List of publications

Peer-reviewed journal papers | In this thesis

Buitink, J., Uijlenhoet, R., and Teuling, A. J. (2019). Evaluating seasonal hydrological extremes in mesoscale (pre-)Alpine basins at coarse 0.5° and fine hyperresolution, *Hydrology and Earth System Sciences*, 23, 1593–1609, doi:10.5194/hess-23-1593-2019.

Buitink, J., Melsen, L. A., Kirchner, J. W., and Teuling, A. J. (2020). A distributed simple dynamical systems approach (dS2 v1.0) for computationally efficient hydrological modelling at high spatio-temporal resolution, *Geoscientific Model Development*, 13, 6093–6110, doi:10.5194/gmd-13-6093-2020.

Buitink, J., Swank, A. M., van der Ploeg, M., Smith, N. E., Benninga, H.-J. F., van der Bolt, F., Carranza, C. D. U., Koren, G., van der Velde, R., and Teuling, A. J. (2020). Anatomy of the 2018 agricultural drought in the Netherlands using in situ soil moisture and satellite vegetation indices, *Hydrology and Earth System Sciences*, 24, 6021–6031, doi:10.5194/hess-24-6021-2020.

Buitink, J., Melsen, L. A., and Teuling, A. J. (2021): Seasonal discharge response to temperature-driven changes in evaporation and snow processes in the Rhine Basin, *Earth System Dynamics*, 12, 387–400, doi:10.5194/esd-12-387-2021.

Buitink, J., van Hateren T. C., Teuling A. J. (2021): Hydrological system complexity induces a drought frequency paradox, *Frontiers in Water*, 3, 42, doi:10.3389/frwa.2021.640976

Peer-reviewed journal papers | Other

Teuling, A. J., de Badts, E. A. G., Jansen, F. A., Fuchs, R., Buitink, J., Hoek van Dijke, A. J., and Sterling, S. M. (2019). Climate change, reforestation/afforestation, and urbanization impacts on evapotranspiration and streamflow in Europe, *Hydrology and Earth System Sciences*, 23, 3631–3652, doi:10.5194/hess-23-3631-2019.

Straatsma, M., Droogers P., Hunink, J., Berendrecht, W., Buitink, J., Buytaert, W., Karssenberg, D., Schmitz, O., Sutanudjaja, E. W., L.P.H. van Beek, Vitolo, C., and Bierkens, M. F. P. (2020). Global to regional scale evaluation of adaptation measures to reduce the future water gap, *Environmental Modelling & Software*, 124, 104578, doi:10.1016/j.envsoft.2019.104578

Bouaziz, L. J. E., Fenicia, F., Thirel, G., de Boer-Euser, T., Buitink, J., Brauer, C. C., De Niel, J., Dewals, B. J., Drogue, G., Grelier, B., Melsen, L. A., Moustakas, S., Nossent, J., Pereira, F., Sprokkereef, E., Stam, J., Weerts, A. H., Willems, P., Savenije, H. H. G., and Hrachowitz, M. (2021). Behind the scenes of streamflow model performance, *Hydrology and Earth System Sciences*, 25, 1069–1095, doi:10.5194/hess-25-1069-2021.

Netherlands Research School for the
Socio-Economic and Natural Sciences of the Environment

D I P L O M A

for specialised PhD training

The Netherlands research school for the
Socio-Economic and Natural Sciences of the Environment
(SENSE) declares that

Joost Buitink

born on 3rd July 1993 in Almere, The Netherlands

has successfully fulfilled all requirements of the
educational PhD programme of SENSE.

Wageningen, 20th October 2021

Chair of the SENSE board

Prof. dr. Martin Wassen

The SENSE Director

Prof. Philipp Pattberg

The SENSE Research School has been accredited by the Royal Netherlands Academy of Arts and Sciences (KNAW)

KONINKLIJKE NEDERLANDSE
AKADEMIE VAN WETENSCHAPPEN

The SENSE Research School declares that **Joost Buitink** has successfully fulfilled all requirements of the educational PhD programme of SENSE with a work load of 45.6 EC, including the following activities:

SENSE PhD Courses

- Environmental research in context (2017)
- Research in context activity: 'Infographic and supporting article to share research results on the occurrence of droughts' (2021)

Other PhD and Advanced MSc Courses

- Workshop 'Improving the theoretical underpinnings of hydrologic models', University of Sopron (2018)
- Scientific writing, Wageningen Graduate Schools (2018)
- Brain training, Wageningen Graduate Schools (2018)
- Career Orientation, Wageningen Graduate Schools (2019)
- Principles of catchment scale hydrological models, University of Padova (2019)

Selection of Management and Didactic Skills Training

- Stakeholder meetings (2016-2020)
- Member of WIMEK PhD council (2017-2020)
- Member of WIMEK Education Committee (2018-2020)
- Supervising five MSc students with thesis (2016-2021)
- Assisting practicals of the BSc course 'Water Quality and Quantity' (2016-2019)
- Teaching in the MSc course 'Catchment Hydrology' (2017-2019)
- Teaching in the BSc course 'Water 2' (2017-2019)

Oral Presentations

- *A simple dynamical systems approach to computationally efficient distributed hydrological modelling.* EGU General Assembly, 8-13 April 2018, Vienna, Austria
- *The distributed simple dynamical systems model (dS2) - Computationally efficient hydrological modelling.* 6th Symposium on the hydrological modelling of the Meuse basin in Liège, 13 September 2019, Liege, Belgium
- *dS2 model.* Boussinesq meeting, 17 October 2019, Amsterdam, The Netherlands

SENSE coordinator PhD education

Dr. ir. Peter Vermeulen

The presented research was financially supported by the Directorate-General for Public Works and Water Management (Rijkswaterstaat), and was carried out at the Hydrology and Quantitative Water Management Group, Department of Environmental Sciences, Wageningen University & Research.

Financial support from Wageningen University for printing this thesis is gratefully acknowledged.

Cover design	James Jardine | jamesjardine.nl
Layout	Joost Buitink, using LaTeX 2_ε
Printed by	ProefschriftMaken | www.proefschriftmaken.nl